

Cardiff University
Cardiff Marine Energy Research Group
(CMERG)

**Technical and Economic Feasibility Analysis of a
Horizontal Axis Tidal Turbine when Operating in Low
Velocity Conditions**

A Thesis submitted for the Degree of Doctor of Philosophy

By
Tattiana Hernández-Madrigal

20th July 2020

Acknowledgements

This project was done with the financial support from Cardiff University and Costa Rica's Ministerio de Ciencia, Tecnología y Telecomunicaciones (Ministry of Science, Technology, and Telecommunications, MICTT).

I would like to thank my supervisors: Prof. Tim O'Doherty, Dr. Allan Mason-Jones, and Dr. Daphne O'Doherty for their support and guidance during the duration of my PhD. I am forever grateful for being part of CMERG.

Work related to the power plant procedures in Costa Rica and the UK, and the LCOE method selection was done with support from Sam Wright-Green and Alex Vidal-Hiscock. Data from Costa Rica was provided by Dr. Rodrigo Rojas-Morales and Kenneth Lobo-Méndez from Instituto Costarricense de Electricidad (Costa Rican's Institute of Electricity, ICE). Many thanks for their input.

This PhD would not have been finished without the reassurance provided by my family in Costa Rica, and friends in Cardiff. Special thanks to Edith, Andrea, and Tony for becoming my *away* family. Enormous gratitude to Nati for bringing a safe haven with her, the coincidence of us being in the same city kept me sane.

A distinct acknowledgement to Shaun for making Wales a second home to me, for the encouragement during the hardest times, and for the creative writing advice to make my thesis readable. Diolch!

This work is dedicated to my Mam.

Como todos mis logros, ésto es por y para usted mi madrecita Lupita.

Abstract

Current global warming requires the de-carbonisation of electricity production with the use of renewable energy sources. This thesis assessed if the economically feasible tidal stream known locations could be expanded with the use of a modified Horizontal Axis Tidal Turbine (HATT) .

Cardiff Marine Energy Research Group's (CMERG) well characterised HATT, designed to operate in high velocities (6 knots), was adapted to operate in low velocity conditions (≤ 1.2 m/second). Using the Gulf of Nicoya site's conditions in Costa Rica for reference, the analysis was made with Computational Fluid Dynamics (CFD) using the ANSYS CFX, and ICEM packages.

Initially, the 5 m radius rotor's geometry was changed using the rotor solidity parameters. Ten single rotor turbine (SRT) configurations were modelled, and the pitch angle at which they had the maximum power output was found for all geometries. From the results, a solidity based performance prediction tool was proposed for SRTs.

Using the SRT results, a contra-rotating rotors turbine (CRT) matching and selection process was proposed. The procedure considered the SRT geometry characteristics, their torque and power output, rotational velocities, blade interference, and estimated cost. A CRT was modelled with CFD to validate the prediction values, and results showed that the expected net performance characteristics were not obtained but the technical restrictions were kept during operation.

Finally, an economic study based on the levelised cost of energy (LCOE) was made to determine the CRT's feasibility when operating in the set conditions. It was found that, though technically feasible, the proposed modifications would not make the SRT nor the CRT economically feasible to compete, currently, in the renewable energy market in the UK and Costa Rica. Based on the results, cost reduction opportunities were given for the device to be en par with commercially ready technologies.

Contents

Chapter 1	Introduction	1
1.1	Marine Energy Resources	3
1.1.1	Ocean Thermal Energy	3
1.1.2	Salinity Gradient	4
1.1.3	Tidal Range	5
1.1.4	Ocean Currents	7
1.1.5	Offshore Wind	8
1.1.6	Waves	9
1.1.7	Tidal Stream	12
1.2	Justification	15
1.2.1	Tidal Stream Energy in the UK	16
1.2.2	Tidal Stream Energy in Costa Rica	17
1.3	Aims and Objectives	19
1.4	Thesis Outline	20
Chapter 2	Tidal Stream Turbines Technology	21
2.1	Tidal Stream Technology Background	21
2.1.1	First Generation Technology	22
2.1.2	Second Generation Technology	24
2.1.3	Third Generation Technology	26
2.2	HATT Theory	27
2.2.1	HATT's Performance	29
2.3	HATT Development Projects	30
2.3.1	Device Components	31
2.3.2	Logistics	33
2.3.3	Economic Feasibility	38
Chapter 3	Numerical Modelling	39
3.1	Modelling Background	39

3.2	Computational Fluid Dynamics Theory	42
3.2.1	Reynolds Averaged Navier-Stokes (RANS) Model	43
3.2.2	SST - $k - \omega$ Turbulence Model	45
3.2.3	Wall Functions	48
3.2.4	Modelling Approach	50
3.3	Geometry	51
3.3.1	Baseline Turbine Geometry	52
3.3.2	Domain Description	53
3.4	Mesh	54
3.4.1	Sea Mesh	55
3.4.2	MFR Mesh	56
3.4.3	Quality	59
3.5	Model Set up	60
3.5.1	Boundary Conditions	61
3.5.2	Analysis Type	63
3.6	Convergence	64
3.7	Post-Processing	64
3.8	Model Validation	65
3.8.1	Mesh Independence	65
3.8.2	Y plus	68
3.8.3	Mesh Validation	68
Chapter 4	Single Rotor Turbine Optimisation	71
4.1	Solidity Background	71
4.1.1	Solidity in the Tidal Energy Sector	73
4.2	Rotor Geometry Theory	75
4.2.1	Solidity Definition	76
4.2.2	Lift Coefficient and Solidity	76
4.3	Geometry Variations	77
4.3.1	Solidity Cases	77
4.3.2	Set-up	83

4.4	Single Rotor Turbines Results	84
4.4.1	Performance Variation Based on Tip Pitch Angle	85
4.4.2	Single Rotor Turbines at Peak Power Coefficient Performance	89
4.5	Performance Predictions for Solidity Cases	91
4.6	Single Rotor Turbines Feasibility in Low Speed Conditions	95
Chapter 5	Contra-Rotating Rotors Turbine Configuration	97
5.1	Contra-Rotating Tidal Stream Turbines Background	98
5.1.1	CoRMaT's CRT	98
5.1.2	Kyushu Institute of Technology's CRT	99
5.1.3	Other CRT Studies	102
5.2	Contra-Rotating Tidal Stream Turbines Theory	104
5.2.1	Efficiency Limit	104
5.2.2	Power Output	105
5.2.3	Power Coefficients	105
5.2.4	Torque	106
5.2.5	Rotational Velocity	106
5.2.6	Inlet Velocities	107
5.3	Contra-Rotating Rotor Selection	107
5.3.1	Single Rotor Options	108
5.3.2	Single Rotor Matching	109
5.3.3	CRT Selection	109
5.4	Contra-Rotating CFD Model	113
5.4.1	Contra-Rotating Geometry	113
5.4.2	Contra-Rotating Mesh	114
5.4.3	Contra-Rotating Model Set-up	115
5.5	Contra-Rotating Model Results	116
Chapter 6	Economic Feasibility	123
6.1	Economic Feasibility Background for TSTs	123
6.2	Economic Feasibility Theory	128
6.2.1	Expected Cash Flow	128
6.2.2	Net Present Value	129

6.2.3	Internal Rate of Return	129
6.2.4	Weighted Average Capital Cost	130
6.2.5	Progress Ratio	131
6.2.6	Levelised Cost of Energy	131
6.2.7	Sensitivity Analysis	134
6.3	Economic Analysis Procedure	135
6.4	Reference LCOE Calculation	138
6.4.1	Capital Expenditures (CAPEX)	139
6.4.2	Operational Expenditures (OPEX)	141
6.4.3	Energy Produced	141
6.4.4	SRT Reference LCOE Results	142
6.4.5	CRT Reference LCOE Results	144
6.4.6	Reference LCOE Sensitivity Analysis	146
6.5	Detailed LCOE Calculation	151
6.5.1	General Assumptions	152
6.5.2	Capital Expenses	153
6.5.3	Operational Expenses	166
6.5.4	Annual Energy Production	168
6.5.5	CRT Detailed LCOE Results	169
6.6	Cost Reduction Opportunities	174
6.6.1	Sensitivity Analysis	174
6.6.2	LCOE Forecast	179
6.6.3	LCOE Improvement Suggestions	180
6.7	Applications to Costa Rica	182
Chapter 7	Conclusions and Recommendations	187
7.1	Conclusions	187
7.1.1	Single Rotor Turbines	187
7.1.2	Contra-Rotating Rotors Turbine	189
7.1.3	Levelised Cost of Energy for SRT and CRT	190
7.2	Recommendations and Further Work	193

Appendix A Turbines' Geometry Details	195
A.1 Baseline Turbine Blade Chord Length Variation	195
A.2 Modified Blades Details	197
A.2.1 Chord Length Calculations	197
A.2.2 Modified Blades Chord Length Variation	198
Appendix B Single Rotor Turbines Performance Curves	203
B.1 Case (i) Turbines	203
B.1.1 Turbine B Performance Curves	203
B.1.2 Turbine C Performance Curves	205
B.1.3 Turbine D Performance Curves	207
B.2 Case (ii) Turbines	209
B.2.1 Turbine b Performance Curves	209
B.2.2 Turbine c Performance Curves	211
B.2.3 Turbine d Performance Curves	213
B.3 Case (iii) Turbines	215
B.3.1 Turbine A _b Performance Curves	215
B.3.2 Turbine A _c Performance Curves	217
B.3.3 Turbine A _d Performance Curves	219
Appendix C Detailed LCOE Calculation Tables	221
C.1 Capital Expenses	221
C.1.1 Development Costs	221
C.1.2 Infrastructure	222
C.1.3 Mooring	224
C.1.4 Power Take Off	224
C.1.5 Installation	228
C.2 Operational Expenses	230
Appendix D Detailed LCOE Sensitivity Analysis Charts	231
D.1 Detailed LCOE Sensitivity Analysis Results for 1 Unit TSP	231
D.2 Detailed LCOE Sensitivity Analysis Results for 10 Units TSP	234
D.3 Detailed LCOE Sensitivity Analysis Results for 50 Units TSP	237

Appendix E Matlab Codes	241
E.1 Contra-Rotating Rotors Matching Script	241
E.2 Contra-Rotating Rotors Selection Script	252
E.3 Single Rotor Turbines LCOE Calculation	254
E.4 Contra-Rotating Rotors Turbines LCOE Calculation	256

List of Figures

1.1	Global Renewable Energy Consumption by Region in 2016. Source: Adapted from ESMAP (2019)	2
1.2	Global Renewable Energy Generation Plan to 2050. Source: IRENA (2019)	2
1.3	Global Ocean Average Temperature Difference Between 20 m and 1000 m Depth. Source: IPCC (2012)	4
1.4	Salinity Gradient Energy Extraction Technologies. Source: IPCC (2012)	5
1.5	Tidal Impoundment. Source: Aqua-RET Project (2012)	5
1.6	Global Tidal Amplitude Prediction. Source: IPCC (2012)	6
1.7	Tidal Range Energy Extraction. Source: Aqua-RET Project (2012)	6
1.8	Global Surface Ocean Currents. Source: IPCC (2012)	7
1.9	Offshore Wind Characteristics. Source: Aqua-RET Project (2012)	8
1.10	Offshore Wind Energy Extraction Technologies. Source: Aqua-RET Project (2012)	8
1.11	Global Wind Power Capacity by Region. Source: REN21 (2018)	9
1.12	Wave Energy Extraction. Source: Aqua-RET Project (2012)	9
1.13	Global Wave Energy Prediction. Source: IPCC (2012)	10
1.14	Wave Energy Research and Development Efforts. Source: Adapted from World Energy Council (2016a)	10
1.15	Wave Energy Extraction Technologies. Source: Aqua-RET Project (2012)	11
1.16	Tidal Stream Characteristics. Source: Aqua-RET Project (2012)	12
1.17	Tidal Stream Extraction Technologies. Source: Aqua-RET Project (2012)	13
1.18	Tidal Stream Installed Capacity in Development. Source: World Energy Council (2016a)	14
1.19	Renewable Electricity Consumption per Country in 2018. Source: Adapted from ESMAP (2018)	15
1.20	Practical Tidal Energy Sites in the UK. Source: Adapted from Carbon Trust Marine Energy Accelerator (2011)	16
1.21	UK's Electricity Generation Matrix in 2017. Source: Adapted from DBEIS (2018)	17
1.22	Tidal Energy Sites in Costa Rica. Source: Adapted from Brito e Melo (2013)	18

1.23	Costa Rica’s Electricity Generation Matrix in 2015. Source: Adapted from Instituto Costarricense de Electricidad (2017)	19
2.1	Tidal Stream Technologies Research and Development Efforts. Source: Adapted from World Energy Council (2016a)	21
2.2	First Generation Commercial Tidal Turbines	23
2.3	Second Generation Commercial Tidal Turbines	25
2.4	Third Generation Commercial Tidal Turbines	26
2.5	Power Extraction Flow Conditions. Source: Adapted from Hau et al. (2006)	28
3.1	CFD Modelling Process	51
3.2	Baseline Turbine Geometry	52
3.3	Fluid Domains Used to Model the Turbine in Sea Water	54
3.4	Volume Shapes Used to Create the Mesh. Source: Adapted from Bakker et al. (2002)	55
3.5	Sea Domain’s Mesh	56
3.6	MFR Domain’s Mesh	58
3.7	Final Mesh with Two Domains Merged	60
3.8	Boundary Conditions of the Sea Domain	61
3.9	Boundary Conditions of the MFR Domain: Turbine	62
3.10	Mesh Independence Wake Recovery Study for the Sea Domain-1 Mesh	66
3.11	Sea Domain-2 Mesh Validation	67
3.12	Numerical Models’ Mesh Validation with Experimental Results. Source: Adapted from Hernandez-Madrigal et al. (2017)	69
4.1	Effect of Changing Solidity in Wind Turbines. Source: Adapted from Burton et al. (2011)	72
4.2	Aerofoil Diagram. Source: Adapted from Greaves et al. (2018)	75
4.3	Blade A Geometry	79
4.4	Blade A’s Pitch Angle Distribution	79
4.5	Case (i) Single Rotor Turbine Geometries	80
4.6	Blade A - Chord Length Measurement Planes	80
4.7	Case (ii) Single Rotor Turbine Blades	81
4.8	Case (ii) Single Rotor Turbine Geometries	82

4.9	Blades' Chord Length Distribution	82
4.10	Case (iii) Single Rotor Turbine Geometries	83
4.11	Turbine C's Performance Coefficients	84
4.12	Turbine C's Torque and Power Output	85
4.13	Power Coefficient - Tip Pitch Angle Variation	87
4.14	Thrust Coefficient - Tip Pitch Angle Variation	87
4.15	Torque Coefficient - Tip Pitch Angle Variation	88
4.16	Tip Speed Ratio - Tip Pitch Angle Variation	88
4.17	Rotors with Peak C_p - Performance Coefficients	89
4.18	Rotors with Peak C_p - Torque and Power Output	91
4.19	Peak C_p Performance Prediction - Case (i): Constant Chord Length	92
4.20	Peak C_p Performance Prediction - Case (ii): Constant Solidity	93
4.21	Peak C_p Performance Prediction - Case (iii): Constant Number of Blades	94
5.1	CoRMaT's CRT Diagram. Source: Adapted from Clarke et al. (2008b)	98
5.2	Kyushu's CRT Diagram. Source: Adapted from Kawashima et al. (2017)	99
5.3	Barbarelli's CRT Diagram. Source: Barbarelli et al. (2014c)	103
5.4	CMERG's CRT Diagram. Source: D. O'Doherty et al. (2009)	104
5.5	CRT Selection Process	108
5.6	Kyushu's CRT Generator Diagram. Source: Adapted from Kawashima et al. (2017)	110
5.7	CoRMaT's CRT Generator Diagram. Source: Adapted from Clarke et al. (2010)	111
5.8	Contra-Rotating Models' Diagram	113
5.9	Contra-Rotating Models' Mesh	115
5.10	Contra-Rotating Models' Steady State Geometry	115
5.11	Transient Torque Variation	117
5.12	Contra-Rotating Rotors Transient Absolute Total Torque Variation	118
5.13	Contra-Rotating Rotors Transient Total Thrust Variation	119
5.14	Contra-Rotating Rotors Total Torque Difference	121
6.1	LCOE for Tidal Stream Turbines based on Technology's Deployment Stage. Source: Ocean Energy Systems et al. (2015)	127
6.2	Cash Flow Diagram	129
6.3	NPV - IRR Decision Making Process. Source: Adapted from Bishop (2012)	130

6.4	Tidal Stream Farm in the United Kingdom	136
6.5	LCOE Calculation Process	137
6.6	Breakdown of Capital Costs. Source: Adapted from Vazquez et al. (2016b)	139
6.7	Single Rotor Diagram for $LCOE_{Ref}$	142
6.8	Power v $LCOE_{Ref}$ for SRT Selection	143
6.9	Contra-Rotating Rotor Diagram for LCOE	144
6.10	Power v $LCOE_{Ref}$ for CRT Selection	145
6.11	$LCOE_{Ref}$ Sensitivity Analysis for Selected Rotors	148
6.12	$LCOE_{Ref}$ Costs Comparison	149
6.13	$LCOE_{Ref}$ Annual Production Comparison	150
6.14	Marine Energy Conversion Reference Models. Source: Neary et al. (2014a)	151
6.15	CRT Array Configuration. Source: Adapted from Neary et al. (2014a)	157
6.16	Riser Cable Diagram. Source: Adapted from Neary et al. (2014a)	157
6.17	CRT Mooring System. Source: Adapted from Neary et al. (2014a)	158
6.18	$LCOE_{Det}$ Costs	170
6.19	$LCOE_{Det}$ Costs per Unit	171
6.20	$LCOE_{Det}$ Capital Expenses Breakdown	172
6.21	$LCOE_{Det}$ Annual Operational Expenses Breakdown	173
6.22	$LCOE_{Det}$ Sensitivity Analysis for a 50 Units TSP	175
6.23	$LCOE_{Det}$ Power Related Sensitivity Analysis for a 50 Units TSP	176
6.24	$LCOE_{Det}$ CAPEX and OPEX Main Components Sensitivity Analysis for a 50 Units TSP	177
6.25	Forecast $LCOE_{Det}$ Costs	180
6.26	Tidal Stream Farm Location in Costa Rica. Source: Esri (2018)	183
B.1	Turbine B's Performance Coefficients	203
B.2	Turbine B's Torque and Power Output	204
B.3	Turbine C's Performance Coefficients	205
B.4	Turbine C's Torque and Power Output	206
B.5	Turbine D's Performance Coefficients	207
B.6	Turbine D's Torque and Power Output	208
B.7	Turbine b's Performance Coefficients	209

B.8	Turbine b's Torque and Power Output	210
B.9	Turbine c's Performance Coefficients	211
B.10	Turbine c's Torque and Power Output	212
B.11	Turbine d's Performance Coefficients	213
B.12	Turbine d's Torque and Power Output	214
B.13	Turbine A_b 's Performance Coefficients	215
B.14	Turbine A_b 's Torque and Power Output	216
B.15	Turbine A_c 's Performance Coefficients	217
B.16	Turbine A_c 's Torque and Power Output	218
B.17	Turbine A_d 's Performance Coefficients	219
B.18	Turbine A_d 's Torque and Power Output	220
D.1	$LCOE_{Det}$ Sensitivity Analysis for a 1 Unit TSP	231
D.2	$LCOE_{Det}$ Power Related Sensitivity Analysis for a 1 Unit TSP	232
D.3	$LCOE_{Det}$ CAPEX Components Sensitivity Analysis for a 1 Unit TSP	232
D.4	$LCOE_{Det}$ OPEX Components Sensitivity Analysis for a 1 Unit TSP	233
D.5	$LCOE_{Det}$ Sensitivity Analysis for a 10 Units TSP	234
D.6	$LCOE_{Det}$ Power Related Sensitivity Analysis for a 10 Units TSP	235
D.7	$LCOE_{Det}$ CAPEX Components Sensitivity Analysis for a 10 Units TSP	235
D.8	$LCOE_{Det}$ OPEX Components Sensitivity Analysis for a 10 Units TSP	236
D.9	$LCOE_{Det}$ Sensitivity Analysis for a 50 Units TSP	237
D.10	$LCOE_{Det}$ Power Related Sensitivity Analysis for a 50 Units TSP	238
D.11	$LCOE_{Det}$ CAPEX Components Sensitivity Analysis for a 50 Units TSP	238
D.12	$LCOE_{Det}$ OPEX Components Sensitivity Analysis for a 50 Units TSP	239

List of Tables

3.1	Coefficients for SST - k - omega Turbulence Model. Source: ANSYS (2016a)	47
3.2	MFR Maximum Surface Element Size	57
3.3	Mesh Characteristics	59
3.4	Mesh Independence Study for Sea Domain-1	66
3.5	Mesh Independence Study for MFR Domain	67
4.1	Single Rotor Turbine Variations Cases	78
4.2	Single Rotor Turbines with Peak Power	90
4.3	Optimised Single Rotor Turbine Specifications	96
5.1	Possible CRT Blade Number Configurations	109
5.2	Contra-Rotating Turbine Theoretical Specifications	112
5.3	Selected CRT Model Steady State Results	116
5.4	CRT Model Torque and Thrust Standard Deviations	119
5.5	CRT Model Transient Results	119
6.1	LCOE Costs per MWh. Source: Adapted from Ocean Energy Systems et al. (2015)	127
6.2	LCOE Assumptions Summary	138
6.3	Optimum Single Rotor Turbine Specifications	144
6.4	Contra-Rotating Rotor Turbine LCOE _{Ref} Results	146
6.5	Development Costs for CRT	155
6.6	Infrastructure Costs for CRT	157
6.7	Moorings Costs for CRT	159
6.8	Power Take Off Costs for CRT	163
6.9	Device Structural Components Costs for CRT	164
6.10	Installation Costs for CRT	165
6.11	Other Capital Costs for CRT	166
6.12	Capital Expenses Summary for CRT	166
6.13	Annual Operational Expenses Summary for CRT	168
6.14	Annual Energy Production for CRT	169

6.15	Contra-Rotating Turbine LCOE _{Det} Summary	169
A.1	Blade A Details - 5 m Radius Turbine. Source: Mason-Jones et al. (2012)	195
A.2	Blade A Details - 6 m Radius Turbine	196
A.3	Blade b Details - 5 m Radius Turbine	198
A.4	Blade c Details - 5 m Radius Turbine	199
A.5	Blade c Details - 6 m Radius Turbine	200
A.6	Blade d Details - 5 m Radius Turbine	201
C.1	Siting and Scoping Costs for CRT	221
C.2	Pre-Installation Studies Costs for CRT	221
C.3	Post-Installation Capital Costs for CRT	222
C.4	Documentation and Process Costs for CRT	222
C.5	Trunk Cable Length	222
C.6	Trunk Cable Specifications Assumed for CRT	223
C.7	Trunk Cable Costs for CRT	223
C.8	Riser Cable Length	223
C.9	Riser Cable Costs for CRT	223
C.10	Mooring Lines and Chain Costs for CRT	224
C.11	Anchors Costs for CRT	224
C.12	Generator Costs for CRT	224
C.13	Power Take Off Mounting Costs for CRT	225
C.14	Other Power Take Off Costs for CRT	225
C.15	Rotor Costs for CRT	226
C.16	Permanent Magnet Generator for CRT Specifications	227
C.17	Mooring Installation Costs for CRT	228
C.18	Trunk Cable Installation Costs for CRT	228
C.19	Riser Cable Installation Costs for CRT	229
C.20	Device Installation Costs for CRT	229
C.21	Marine Operations Costs for CRT	230
C.22	Shoreside Operations Costs for CRT	230
C.23	Replacement Parts Costs for CRT	230

Nomenclature

Latin Letters

Symbols	Description	Units
A	Aerofoil Area	m^2
AEP	Annual Energy Production	MW h
c_{ave}, c	Averaged Blade Chord Length	m
F	Axial Force Exerted by the Turbine (Thrust)	kN
A_{BR}	Back Rotor Area for Contra-Rotating Turbine	m^2
D_{BR}	Back Rotor Diameter for Contra-Rotating Turbine	m
P_{BR}	Back Rotor Power for Contra-Rotating Turbine	kW
R_{BR}	Back Rotor Radius for Contra-Rotating Turbine	m
T_{BR}	Back Rotor Torque for Contra-Rotating Turbine	kN·m
S	CRT Blade Surface Area	m^2
$CAPEX$	Capital Expenditures	£
C_C	Cable Cost	£
A_F	Cross-Section Flow Area	m^2
$Blade_{mold}$	CRT Blades Masters and Molds Cost	\$ ₂₀₀₁
$depth$	Depth of the Power Plant's Location	m
$LCOE_{Det}$	Detailed Levelised Cost of Energy	£/MWh
r	Discount Rate	%
L	Distance Between Contra-Rotating Rotors	m
F_D	Drag Aerodynamic Force Component	N
C_D	Drag Coefficient	-
E_n	Electricity Generated in Year n	MW h
C_F	Foundation Cost	£
A_{FR}	Front Rotor Area for Contra-Rotating Turbine	m^2
D_{FR}	Front Rotor Diameter for Contra-Rotating Turbine	m
P_{FR}	Front Rotor Power for Contra-Rotating Turbine	kW

Continued on next page

Latin Letters– Continued from previous page

Symbols	Description	Units
R_{FR}	Front Rotor Radius for Contra-Rotating Turbine	m
T_{FR}	Front Rotor Torque for Contra-Rotating Turbine	kN·m
F_n	Fuel Expenditure in Year n	£
η_{Gen}	Generator's Efficiency	%
D_h	Hub Diameter	m
P	Hydrostatic Pressure	Pa
P_H	Hydraulic Power	kW
IRR	Internal Rate of Return	%
I_n	Investment Made in Year n	£
$LCOE$	Levelised Cost of Energy	£/MWh
F_L	Lift Aerodynamic Force Component	N
C_L	Lift Coefficient	-
$c(r)$	Local Blade Chord Length	m
M_n	Maintenance Expenditures in Year n	£
\dot{m}	Mass Flow Rate	kg/s
m	Mass of Water	kg
NPV	Net Present Value	£
N_D	Number of Turbines	-
$OPEX$	Operational Expenditures	£
C_P	Power Coefficient	-
P	Pressure	Pa
$LCOE_{Ref}$	Reference Levelised Cost of Energy	£/MWh
C_R	Rotor Cost	£
u_T	Rotor Tangential Velocity	m/s
$dist$	Shortest Distance to Shore from Power Plant	m
u	Stream Flow Velocity	m/s
\mathbf{U}	Time Averaged Velocity Vector	m/s
U, V, W	Time Averaged Velocity Components in x, y, z Directions	m/s
C_θ	Torque Coefficient	-

Continued on next page

Latin Letters– Continued from previous page

Symbols	Description	Units
t	Time	s
$TotPow$	Total Power Output in Power Plant	kW
η_T	Transmission Efficiency	%
LT	TSEP Lifetime	years
Av	Turbine's Availability	%
D	Turbine Diameter	m
R	Turbine Radius	m
P	Turbine Power Output	kW
T	Turbine Torque	kN·m
u, v, w	Velocity Components in x, y, z Directions	m/s
u', v', w'	Velocity Components Fluctuations in x, y, z Directions	m/s
\mathbf{u}	Velocity Vector	m/s
\mathbf{u}'	Velocity Vector Fluctuations	m/s
V	Volume of Water	m ³
$WACC$	Weighted Average Cost of Capital	%
K_E	Water's Kinetic Energy	kN·m
n	Year Counter	-

Greek Symbols

Symbols	Description	Units
α	Angle of Attack	°
σ_{ave}	Averaged (Blade) Solidity	%
ω_{BR}	Back Rotor Rotational Velocity for Contra-Rotating Turbine	rad/s
β	Blade Pitch Angle	°
$\lambda_{(C_R+C_C+C_F)}$	CAPEX Associated to Rotor, Cable, and Foundation	£
μ	Dynamic Viscosity, Radial Position	N·s/m ² , -
ω_{FR}	Front Rotor Rotational Velocity for Contra-Rotating Turbine	rad/s

Continued on next page

Greek Symbols– Continued from previous page

Symbols	Description	Units
θ	Inflow Velocity Angle	°
ν	Kinematic Viscosity	m ² s
σ_r	Local (Chord) Solidity	%
ω	Rotational Velocity	rad/s
σ	Rotor (Blade) Solidity	%
λ	Tip Speed Ratio (TSR)	-
ω_{tot}	Total Rotational Velocity for Contra-Rotating Turbine	rad/s
ρ	Water Density	kg/m ³

Acronyms

Symbols	Description
AEM	Anion Exchange Membrane
BR	Back Rotor of a CRT
BSL	Baseline $k - \omega$ Turbulent Model
BC	Boundary Conditions
BEMT	Blade Element Momentum Theory
<i>LE</i>	Blade's Leading Edge
<i>TE</i>	Blade's Trailing Edge
CCS	Carbon Capture and Storage
CMERG	Cardiff Marine Energy Research Group
CEM	Cation Exchange Membrane
CFC	Chlorofluorocarbon
CCGT	Combined Cycle Gas Turbine
CFD	Computational Fluid Dynamics
CAD	Computer-Aided Design
CRT	Contra-Rotating Rotors Turbine
DCO	Development Consent Order

Continued on next page

Acronyms– Continued from previous page

Symbols	Description
DDPMG	Direct Drive Permanent Magnet Generator
DRT	Double Rotors Turbine
EMEC	European Marine Energy Centre
ESMAP	Energy Sector Management Assistance Program
EIA	Environmental Impact Assessment
EsIA	Environmental Impact Study
ES	Environmental Statement
CFIA	Colegio Federado de Ingenieros y Arquitectos
FSI	Fluid Structure Interaction
FR	Front Rotor of a CRT
FORCE	Fundy Ocean Research Center for Energy
IGCC	Gasification Combined Cycle
GGI	General Grid Interface
HATT	Horizontal Axis Tidal Turbine
HAWT	Horizontal Axis Wind Turbine
MMO	Marine Management Organisation
MFR	Multiple Frame of Reference
OSWC	Oscillating Wave Surge Converters
OTEC	Ocean Thermal Energy Conversion
OWC	Oscillating Wave Converters
PV	Photo Voltaic
PTO	Power Take Off
PRO	Pressure-Retarded Osmosis
PWR	Pressurised Water Reactor
ARESEP	Regulatory Authority of Public Services
R&D	Research and Development
RED	Reversed Electro Dialysis
RANS	Reynolds Averaged Navier-Stokes Equations
RMI	Reference Model 1 from Neary et al. (2014a)

Continued on next page

Acronyms– Continued from previous page

Symbols	Description
RM4	Reference Model 4 from Neary et al. (2014a)
SETENA	Secretaría Técnica Nacional
SRT	Single Rotor Turbine
SDG	Sustainable Development Goals
SME	Sustainable Marine Energy
DJCO	Sworn Declaration of Environmental Commitment
TKE	Turbulent Kinetic Energy
TSEP	Tidal Stream Energy Projects
TST	Tidal Stream Turbine
UFS	Universal Floating System
VATT	Vertical Axis Tidal Turbine
VAWT	Vertical Axis Wind Turbine

Chapter 1

Introduction

Climate change is the long-term variation in the average weather patterns that have come to define Earth's local, regional and global climates (NASA 2019). The changes observed during the last century have been as a result of global warming, which has been further influenced by human activities. The global temperature increase (greenhouse effect) causes variations in the Earth's physical, biological, and human systems, such as: change in ecosystems and desertification, melting of poles and rising sea level, acidification of the oceans, extreme weather phenomena, extinction of species, and massive migrations (ACCIONA 2019).

The greenhouse effect is primarily driven by fossil fuels burning, such as coal, natural gas, and oil (National Geographic 2019). Some actions to mitigate the global warming include: (a) more investment in renewable energies, (b) transition to a low-carbon economy, (c) promoting energy efficiency, (d) electrification of industrial processes, (e) implementation of efficient transportation means, and (f) carbon pricing (ACCIONA 2019). In September 2015 world leaders adopted the Paris Agreement on climate change, which included the 2030 Agenda for Sustainable Development and its 17 Sustainable Development Goals (SDG), related to: (1) end poverty in all its forms, (2) zero hunger, (3) health, (4) education, (5) gender equality and women's empowerment, (6) water and sanitation, (7) energy, (8) economic growth, (9) infrastructure, industrialization, (10) inequality, (11) cities, (12) sustainable consumption and production, (13) climate change, (14) oceans, (15) biodiversity, forests, desertification (16) peace, justice and strong institutions, and (17) partnerships (United Nations 2019). The research presented in this thesis relates directly to goal 7, specifically target 7.2: *By 2030, increase substantially the share of renewable energy in the global energy mix* (United Nations 2019), where renewable energy refers to the use of this sources for transportation, heating, and electricity generation. The topic of interest in this project is with the latter.

Worldwide, the share of renewable energy for electricity production grew by 1% to reach 24% in 2016. As shown in [Figure 1.1](#), according to World Bank's Energy Sector Management Assistance Program (ESMAP), the main source used was hydropower (i.e. 68%), followed by

wind, bioenergy, solar, geothermal, and ocean technologies (i.e. others) (ESMAP 2019). Wind and solar PV generation has been growing rapidly since 2010 due to policy support and cost reductions, and it is expected to keep this trend to 2030. Nonetheless, a more rapid decarbonization of the electricity sector is needed because fossil fuels still account for the majority of generation globally (ESMAP 2019).

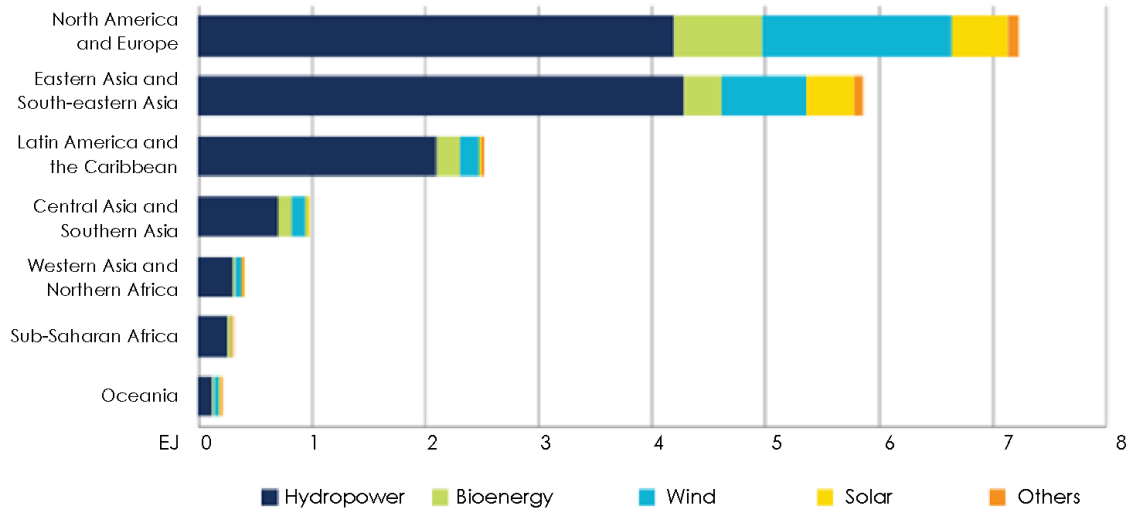


Figure 1.1: Global Renewable Energy Consumption by Region in 2016. Source: Adapted from ESMAP (2019)

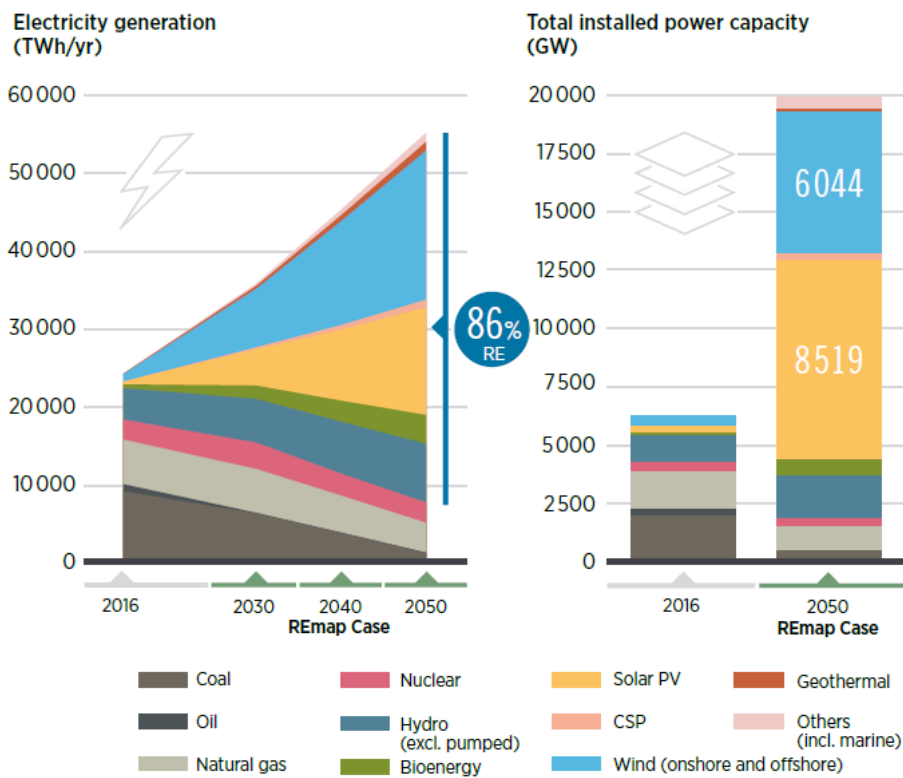


Figure 1.2: Global Renewable Energy Generation Plan to 2050. Source: IRENA (2019)

To meet the Paris Agreements objectives IRENA (2019) suggests an acceleration of the global energy system transformation from now to 2050. This requires renewable sourced electricity to progressively become the central energy carrier for transportation, heating, and cooking. Figure 1.2 shows that the increase in demand implies scaling up conventional renewable sources like wind and solar, and diversifying the matrix with other sources, such as marine energy, to reduce the dependency on fossil fuels (IRENA 2019). Though still at research and development stage, and not yet commercially available, marine energy technologies are promising (IRENA 2018).

The next section describes the current marine energy situation in the world, followed by a description on how marine resources can be used to produce electricity. This thesis focuses on the energy extraction from tidal stream currents with a horizontal axis tidal turbine (HATT), which is justified within Section 1.2 along with the main research objectives.

1.1 Marine Energy Resources

The world's surface is two thirds water, and 70% of it is found in the oceans. Earth's rotation, the sun's influence, the relative moon's motion around the planet, and wind circulation create opportunities to generate electricity extracting energy from the available marine resources: thermal and salinity gradients, tidal range, ocean currents, wind, waves, and tidal stream (Borthwick 2016). The different energy extraction methods for each source are described next.

1.1.1 Ocean Thermal Energy

Ocean Thermal Energy Conversion (OTEC) uses a temperature difference of at least 20 °C, between the top water surface layers and the deep water (~1000 m), to produce electricity using a heat exchanger with an evaporator and a condenser (Borthwick 2016). The open conversion type uses water for working fluid, the closed system uses ammonia, propane or chlorofluorocarbon (CFC), and the hybrid system works as the closed scheme but the discharged seawater is evaporated and condensed before discharge (World Energy Council 2016a).

The global resource potential, illustrated in Figure 1.3, has been estimated to be 30 000 TWh/year - 90 000 TWh/year. The source is considered to be continuously available contributing to the base-load power supply (IPCC 2012), but due to its high costs, OTEC has only been tested in small scale plants (Borthwick 2016).

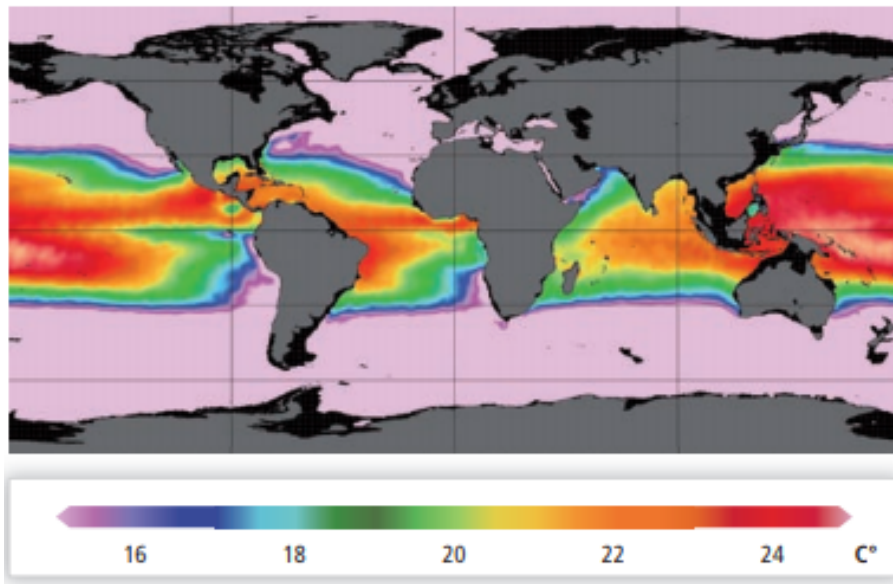


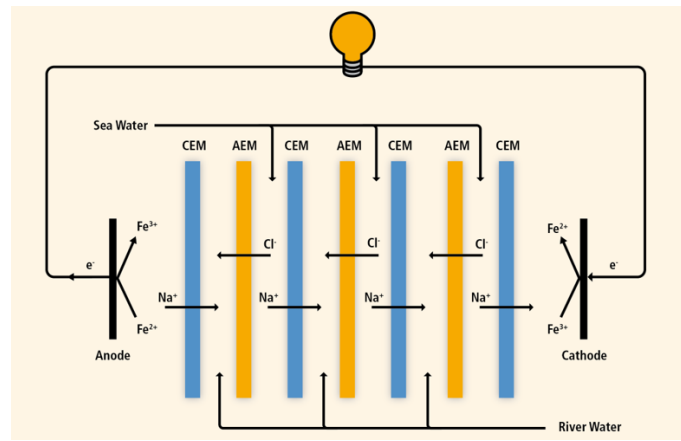
Figure 1.3: Global Ocean Average Temperature Difference Between 20 m and 1000 m Depth.
Source: IPCC (2012)

1.1.2 Salinity Gradient

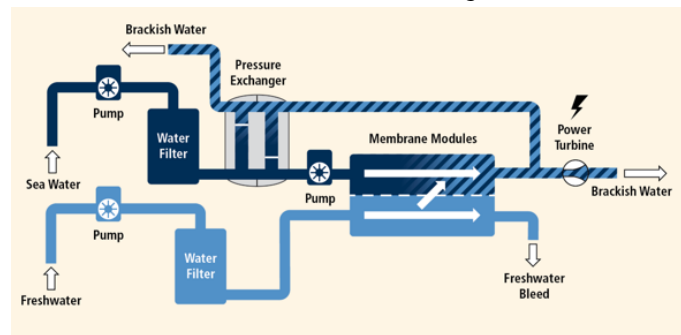
The technical global power generation using salinity gradients is 1650 TWh/year (IPCC 2012). Electricity can be generated with the heat released during the mixing of freshwater and seawater using reversed electro dialysis (RED), and pressure-retarded osmosis (PRO). Both of these approaches have presented technical issues that need to be addressed before full implementation (Borthwick 2016).

RED (Figure 1.4a) harnesses the voltage generated due to the chemical potential difference created in an alternating series of anion and cation exchange membranes, AEM and CEM respectively (IPCC 2012).

PRO, also known as osmotic power, uses the chemical potential as pressure to produce electricity. The natural occurring osmosis between freshwater and seawater is controlled by pressurizing the latter to approximately half the osmotic pressure (12 bar-13 bar), forcing freshwater to pass through a membrane into the pressurized seawater. One third of the resulting brackish water passes through a hydropower turbine generating electricity, whilst the rest passes through a pressure exchanger (to pressurize the incoming seawater). The brackish water is then returned to the river or sea, depending on where they would naturally have mixed (IPCC 2012). A diagram of this process is presented in Figure 1.4b.



(a) Reversed Electro Dialysis



(b) Pressure-Retarded Osmosis

Figure 1.4: Salinity Gradient Energy Extraction Technologies. Source: IPCC (2012)

1.1.3 Tidal Range

Tidal range technologies harvest the potential energy created by the difference in head between ebb tide and flood tide, caused by the gravitational pull of the moon and sun on the seas, as described in Figure 1.5 (Aquaret Consortium 2008b).

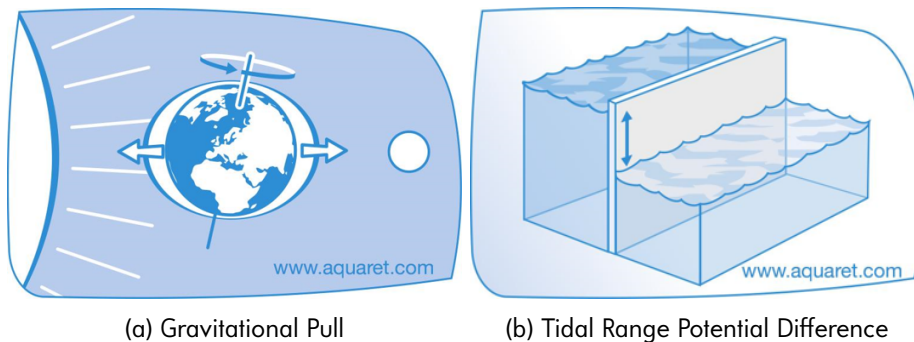


Figure 1.5: Tidal Impoundment. Source: Aqua-RET Project (2012)

The world map of tidal amplitude is shown in Figure 1.6. This energy extraction has been commercially used since 1966, with power plants functioning in France, Canada, China, Iran, Russia, and South Korea (IRENA 2014), adding to 629 MW of operating capacity at the end of

2017 (REN21 2018). Tidal range can be forecast with a high level of accuracy, and there is no resource risk due to climate change (IPCC 2012), but their impact on local estuarine environment, and socio-economic activities has limited their development (World Energy Council 2016a).

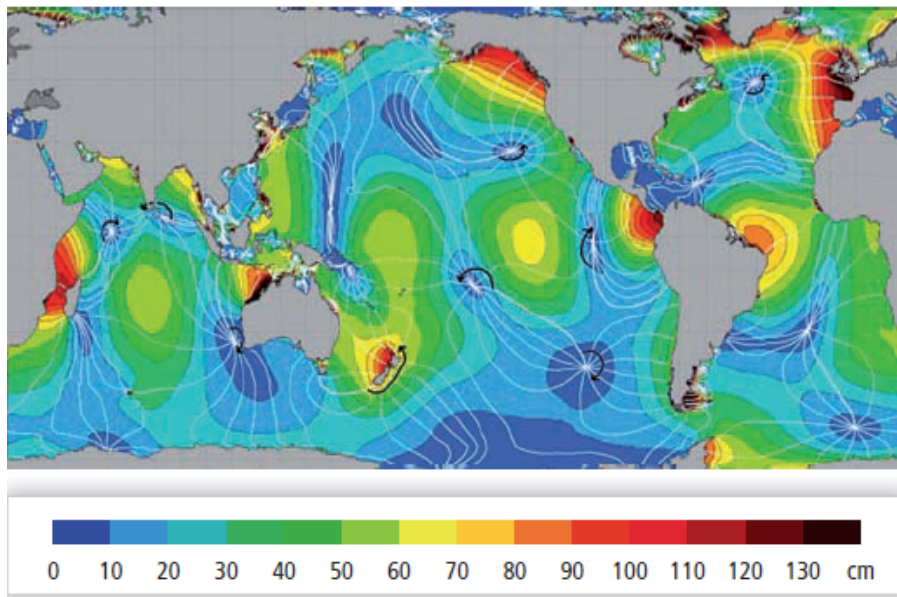


Figure 1.6: Global Tidal Amplitude Prediction. Source: IPCC (2012)

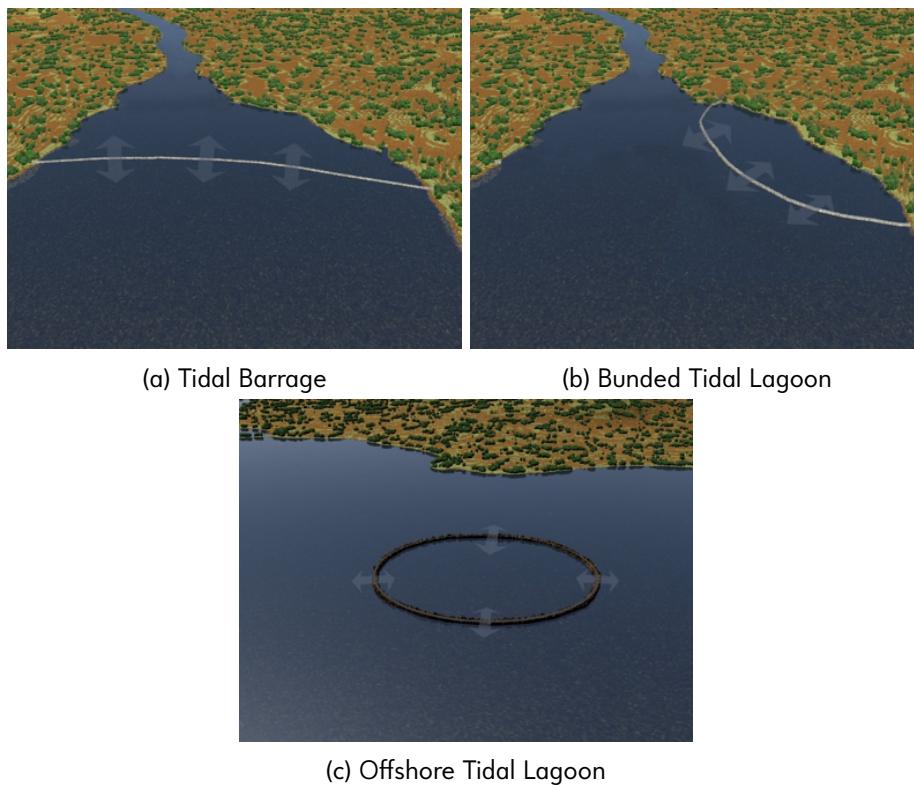


Figure 1.7: Tidal Range Energy Extraction. Source: Aqua-RET Project (2012)

Tidal range technologies to produce electricity consist in building impoundments for tides'

large volumes of water to create a head difference. The water flows in and out of the basin producing electricity with a hydroelectric turbine during ebb and/or flood tide (Borthwick 2016). The impoundments can be made with barrages building a dam across a estuary (Figure 1.7a) and lagoons that can be bounded near estuaries and basins (Figure 1.7b), or completely artificial offshore (Figure 1.7c). Their commercial development has been delayed due to the high uncertainty it brings a first of a kind project, but efforts on showing their technical and economic feasibility have been made with projects like Swansea's Tidal Lagoon in the UK. Nonetheless, financial support from public or private investors is needed for said project to be deployed and prove their capability (Thomas 2019).

1.1.4 Ocean Currents

Ocean currents are derived from wind-driven, and thermohaline ocean circulation. The continuous flows exist in the open ocean, always move in the same direction, and have low variability (IPCC 2012), providing a mean value of velocities different to zero over at least one year (Segura et al. 2017). Their advantages include stability, availability, predictability, and no visual impact. But research has proven technical difficulties, and potentially costly deployment (Shirasawa et al. 2016).

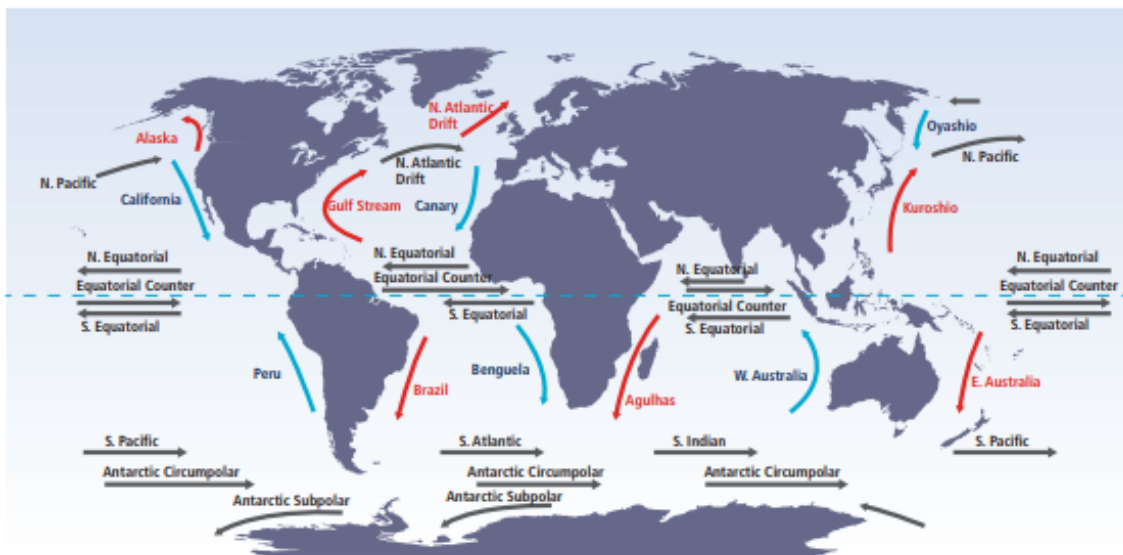


Figure 1.8: Global Surface Ocean Currents. Source: IPCC (2012)

The locations of identified ocean currents in the planet are shown in Figure 1.8. The ocean technology used to extract this energy is similar to the one required for tidal flows, but infrastructure might differ (IPCC 2012). Due to their lower velocity and deeper locations, second

generation tidal stream technology (explained in [Section 2.1.2](#)), like the Kuroshio power plant proposal by Chen (2010), could be more suitable for this resource.

1.1.5 Offshore Wind

Atmospheric wind is the movement of air that circle the Earth caused by the unevenly heated surfaces, and rotation of the planet. Specifically, offshore wind is the movement of air caused by the heating rate difference between land and water: during the day air over land expands, rises and is replaced by cooler sea air, creating sea-breezes on coastlines which are then reversed during the night. The lack of obstacles, and lower friction on the water surface makes offshore wind generally faster than onshore wind (Aquaret Consortium 2008a). [Figure 1.9](#) illustrates this behaviour.

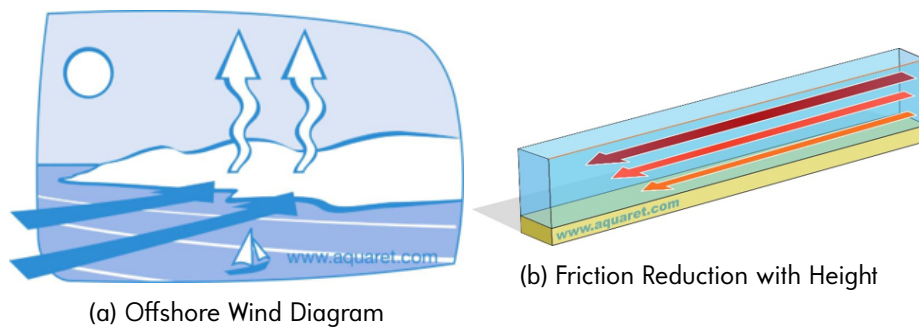


Figure 1.9: Offshore Wind Characteristics. Source: Aqua-RET Project (2012)

Offshore wind energy technology is based on the experience learned from onshore development. Turbines extract the kinetic energy in the wind and convert it to electricity using rotating blades. Two basic configurations are used for this purpose: horizontal axis wind turbine, HAWT ([Figure 1.10a](#)), and vertical axis wind turbine, VAWT ([Figure 1.10b](#)) (Aquaret Consortium 2008a). The most used configuration is the three-bladed HAWT (Borthwick 2016).

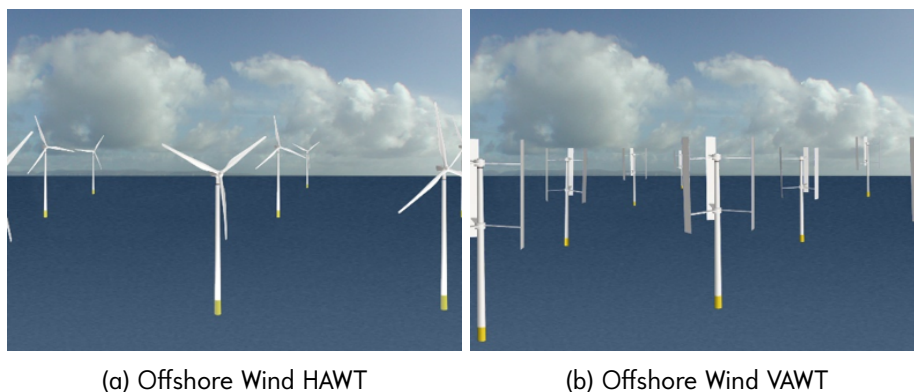


Figure 1.10: Offshore Wind Energy Extraction Technologies. Source: Aqua-RET Project (2012)

The technology is currently used in offshore wind farms, with rotors typically larger than onshore, with capacities of up to 6 MW per turbine (World Energy Council 2016b). Offshore wind rotors have a higher capacity factor, and greater potential for deployment than onshore technology because they can: have larger swept area, be located in regions with higher wind speeds, be used in very large wind farms, and have less siting issues (IRENA 2012).

Figure 1.11 shows the global offshore wind capacity increase from 1.1GW installed in 2007 to 18.8 MW in 2017, with most of the new installations made in Asia. Even though there is a rapid implementation of offshore wind technologies, new devices must reduce installation and maintenance costs (World Energy Council 2016b; Borthwick 2016).

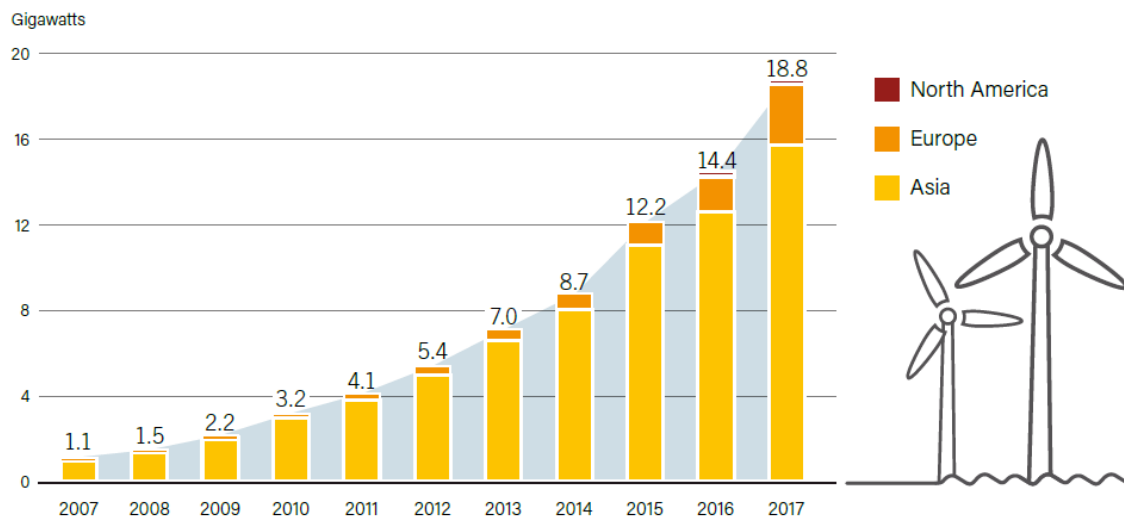


Figure 1.11: Global Wind Power Capacity by Region. Source: REN21 (2018)

1.1.6 Waves

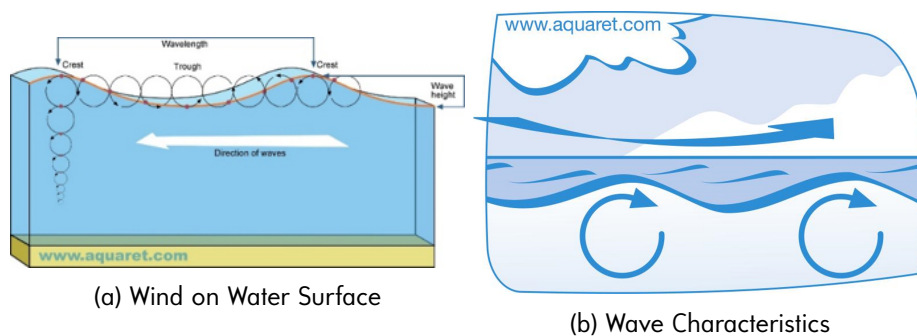


Figure 1.12: Wave Energy Extraction. Source: Aqua-RET Project (2012)

Waves are the movement of water caused by winds blowing over water near the sea surface. Wave energy devices harness the kinetic energy carried in the movement, which varies with

period, height and wave length (Aquaret Consortium 2008c). Figure 1.12 describes the wave characteristics, and wave creation process.

The global resource prediction is shown in Figure 1.13 in kW/m. Deep sea waves offer large energy fluxes under predictable conditions over periods of days (A.S Bahaj 2011). The total theoretical wave energy resource in the world is 32 000 TWh/year, but the technical potential depends on the extraction technologies (IPCC 2012).

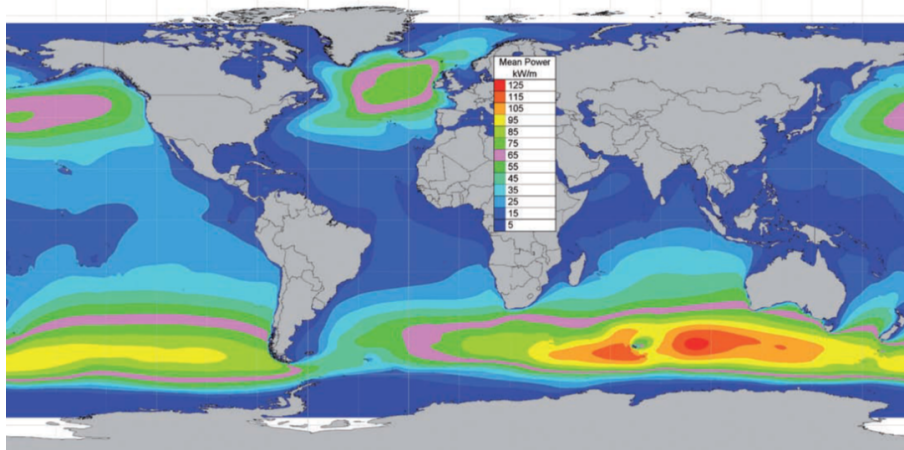


Figure 1.13: Global Wave Energy Prediction. Source: IPCC (2012)

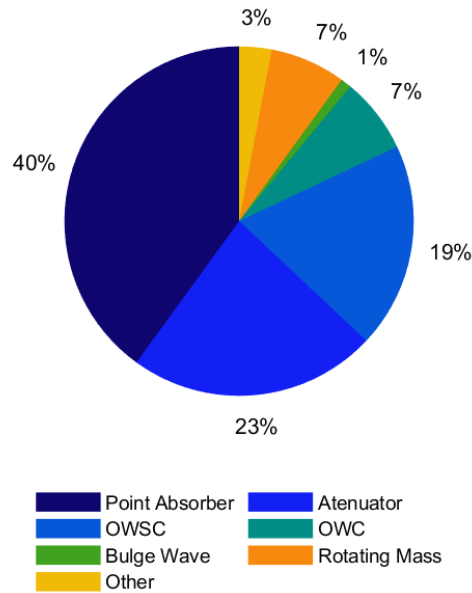


Figure 1.14: Wave Energy Research and Development Efforts. Source: Adapted from World Energy Council (2016a)

The possible configurations have not converged to an optimum wave energy converter. As shown in Figure 1.14, research and development efforts are focused on several technologies, with

the key priority in the sector to improve power take off (PTO) systems (World Energy Council 2016a). The main methods used are described next.

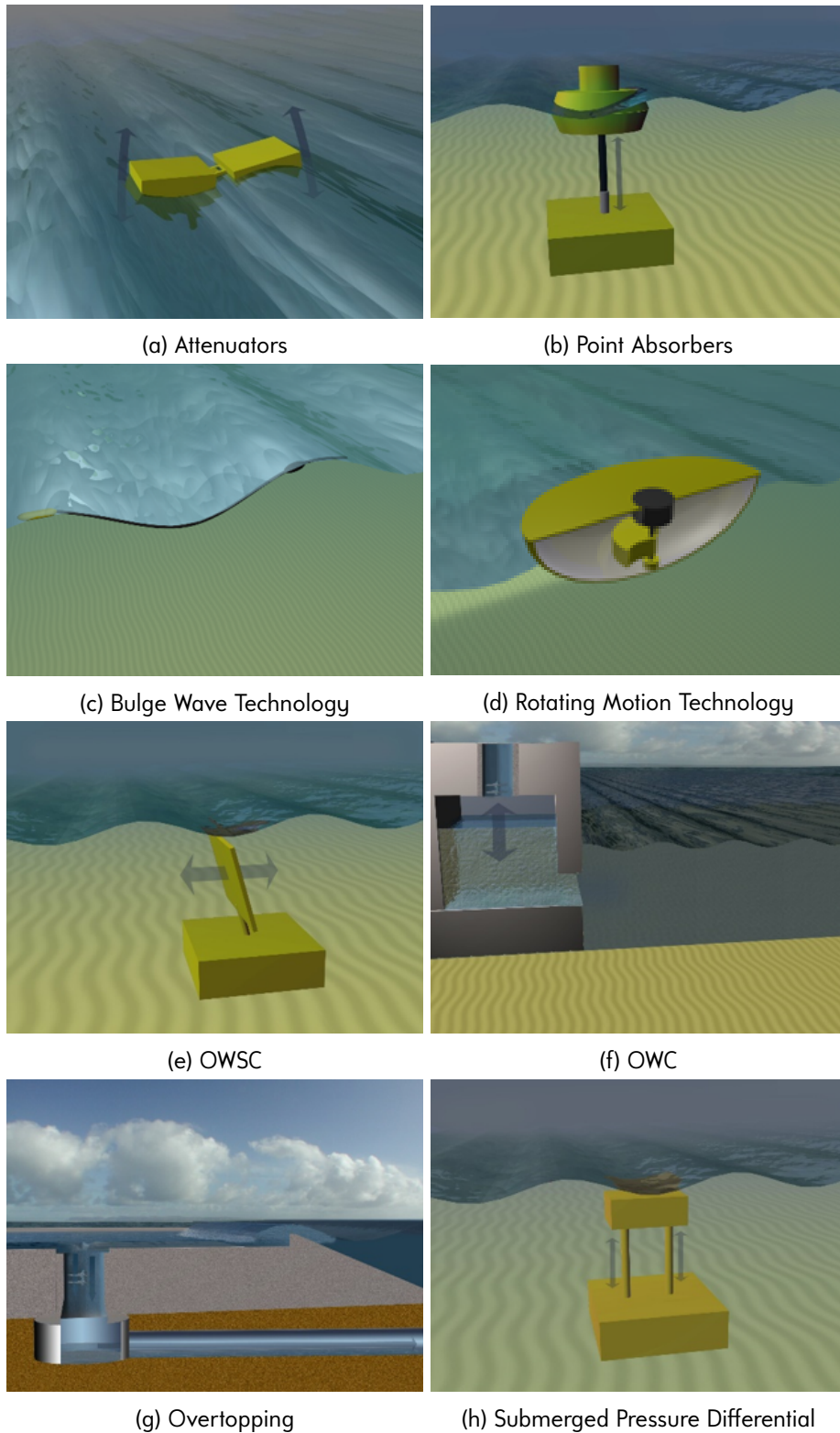


Figure 1.15: Wave Energy Extraction Technologies. Source: Aqua-RET Project (2012)

Wave energy can be extracted by floating devices, such as attenuators (Figure 1.15a) and

point absorbers (Figure 1.15b) that absorb energy as waves past them. Rubber tubes moored to the seabed that also float and head into the waves to produce electricity are categorised as bulge wave technology (Figure 1.15c), and floating devices that heave and sway in the waves can produce electricity by moving an eccentric weight or gyroscope (Figure 1.15d).

The oscillating water motion can produce electricity with near-surface collectors like wave surge converters, OWSC (Figure 1.15e), or with partially submerged open to the sea below water surface water columns, OWC (Figure 1.15f). Other methods include overtopping devices (Figure 1.15g) that collect the waves' water in a reservoir and release it back to the sea through conventional low head turbines, and submerged pressure differential devices (Figure 1.15h).

1.1.7 Tidal Stream

As explained in Section 1.1.3, and described in Figure 1.16a, tidal energy is generated from the gravitational and centrifugal forces among the Earth, moon, and sun (Segura et al. 2017). In most coastal locations two high, and two low tides are experienced ('semi-diurnal') every 24 hours 50 minutes (IPCC 2012). This variation creates tidal streams with zero mean velocities, over time periods of half a day and a day, that can be used to extract electricity (Segura et al. 2017).

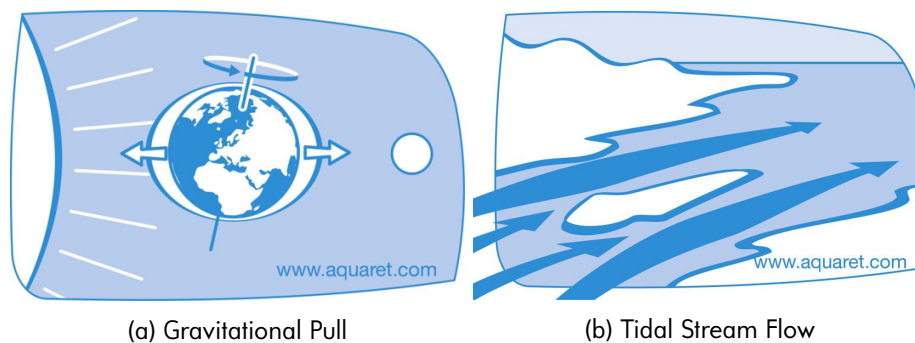


Figure 1.16: Tidal Stream Characteristics. Source: Aqua-RET Project (2012)

The major tidal currents locations in the world are: Artic Ocean, English Channel, Irish Sea, Skagerrak-Kattegat, Hebrides, Gulf of Mexico, Gulf of St. Lawrence, Bay of Fundy, Amazon, Rio de la Plata, Straits of Magellan, Gibraltar, Messina, Sicily, and Bosports (O'Rourke et al. 2010). Hydrokinetic energy converters have been developed to increase the number locations where it could be used, allowing the technology adaptation to also extract energy from ocean currents, and river streams (Laws et al. 2016).

As detailed by Segura et al. (2017), tidal stream energy extraction has the following advant-

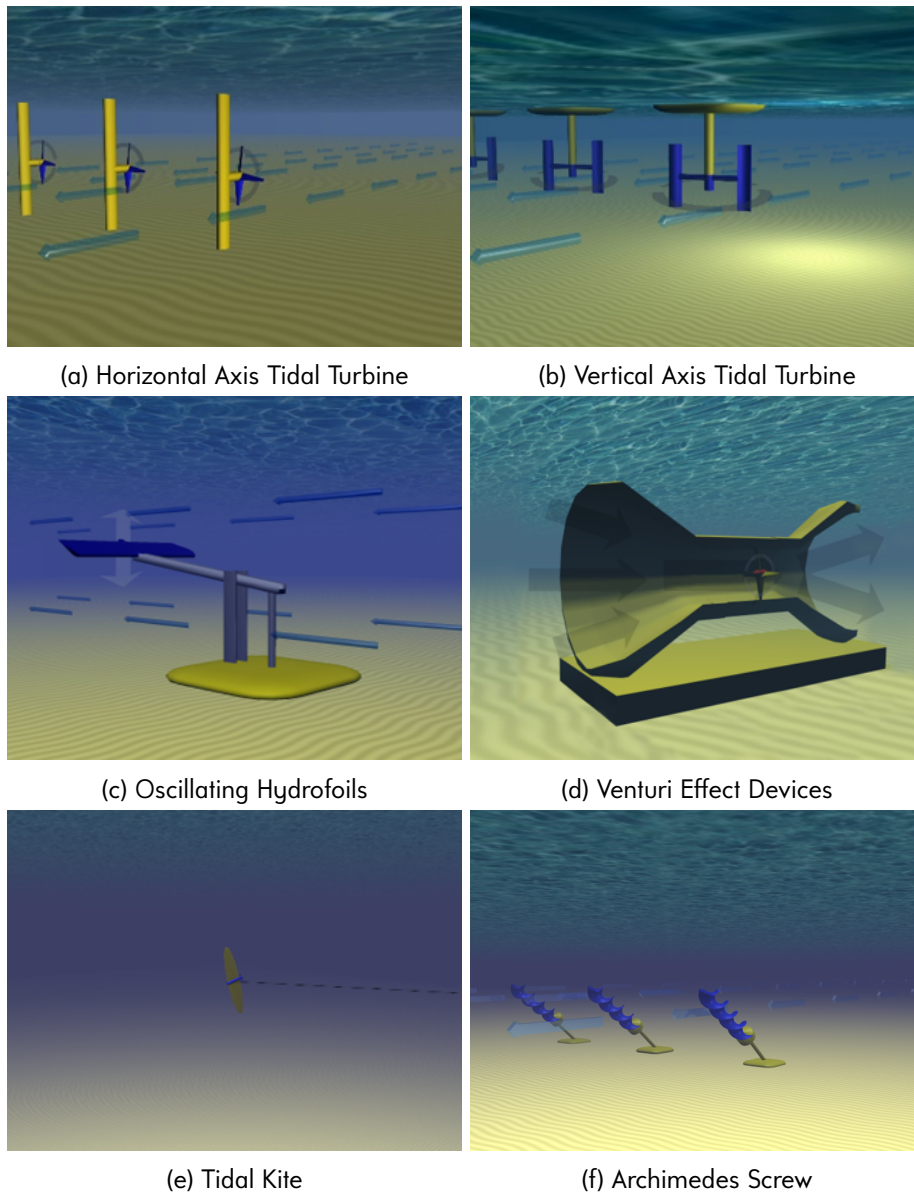


Figure 1.17: Tidal Stream Extraction Technologies. Source: Aqua-RET Project (2012)

ages: accurate and constant high load factors, can be used as a base-load supplier due to its forecasting and reliability, and lower environmental impact compared to other renewable sources. These benefits have led to different designs that would harness the available resource. The main device categories to extract tidal stream energy are horizontal axis tidal turbines, HATT, vertical axis tidal turbines, VATT, reciprocating hydrofoils, and venturi effect devices. Other technologies are kite, and rotating screw shaped devices (World Energy Council 2016a).

With influence from the wind industry, HATT (Figure 1.17a) and VATT (Figure 1.17b) designs use blades that rotate with the flow more slowly than wind turbines due to the water's higher density. They can be located in the free flow, or enclosed in venturi shaped ducts (Figure 1.17d) (IRENA 2014). Reciprocating devices (Figure 1.17c) move up and down as the tidal stream flows

on either side of the blade (IRENA 2014), the motion operates hydraulic cylinders that pump fluid through a motor, which then converts electricity through a generator (World Energy Council 2016a). The helical screw, also known as 'Archimedes' screw (Figure 1.17e), draws energy from the tides as water flows up across the helix (Segura et al. 2017), and the tidal kite flies through the flow with a small HATT turbine attached to its wing (Figure 1.17f) (World Energy Council 2016a).

Other technological aspects affecting the performance and costs of tidal stream devices are support structure, array formation, and electrical connections to shore (IRENA 2014). Research is made to determine the best configuration to generate electricity with this source. Testing facilities, such as EMEC in Scotland and FORCE in Canada (World Energy Council 2016a), have allowed for prototype deployment in locations where: assistance is provided for developers to get devices in the water, a pathway is provided for project development, research and development (R&D) is encouraged, early introduction of renewable energy is encouraged, and opportunities are provided for rural development in coastal areas (Aqua-RET Project 2012).

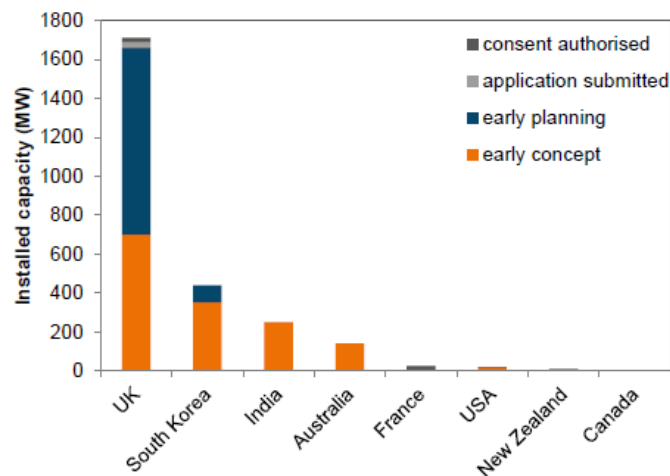


Figure 1.18: Tidal Stream Installed Capacity in Development.

Source: World Energy Council (2016a)

Pre-commercial demonstration represent the world installed capacity of tidal stream power plants. Figure 1.18 shows that most of the devices are currently being planned and tested in the United Kingdom (UK) (World Energy Council 2016a) due to their high resource availability (~29 TWh/year) (Carbon Trust Marine Energy Accelerator 2011), and economic support (e.g. Contracts for Difference, CfD) from the government to develop research and industry. Their commitment to lead the sector is evidenced with their installed operational capacity (9 MW), the largest in the world (CAELULUM et al. 2017).

Research in this thesis presents a feasibility study of adapting a tidal stream turbine (TST) to operate in low velocity conditions, when it was initially designed to work in high velocity tidal conditions, like the ones found in the UK.

1.2 Justification

The global goal to increase electricity generation with the use of renewable energies requires countries to implement alternative sources in their electricity matrix. This thesis relates to the use of tidal stream energy in the UK and Costa Rica.

Figure 1.19 shows the percentage of electricity produced by renewable sources per country. In 2016 Costa Rica generated 99% of its electricity with renewable energy, whereas 25% of the UK's electricity was produced using these sources. Though neither of them uses tidal stream technology in their matrix as of the time of this publication, both countries have considered the implementation of TST devices based on their resource. A brief description of each country's context is given next, providing details of their matrix composition with support of Figure 1.21 and Figure 1.23.

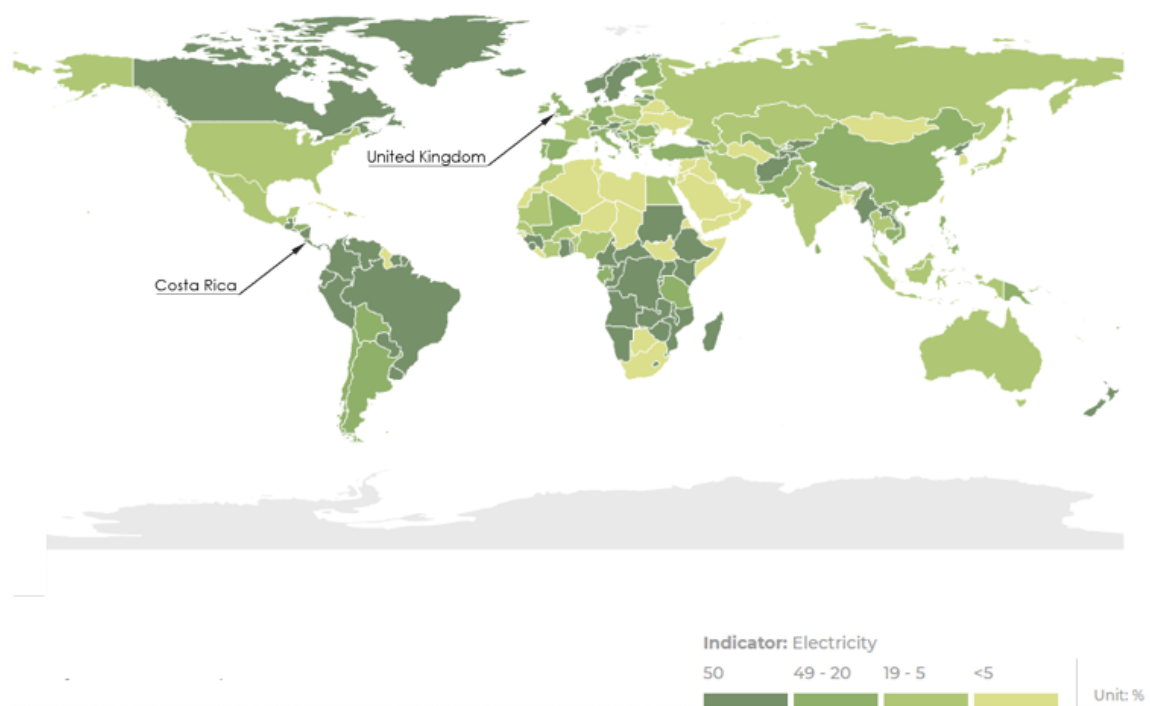


Figure 1.19: Renewable Electricity Consumption per Country in 2018.
Source: Adapted from ESMAP (2018)

1.2.1 Tidal Stream Energy in the UK

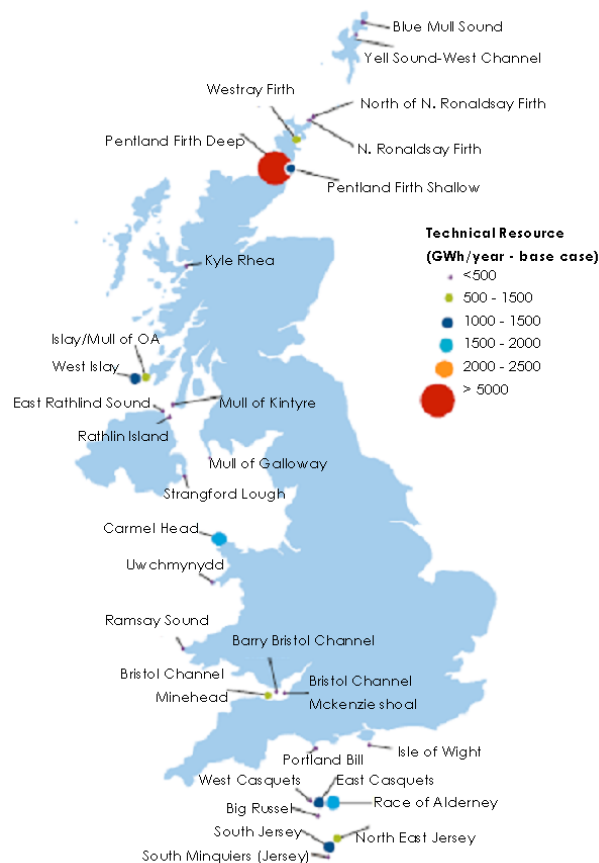


Figure 1.20: Practical Tidal Energy Sites in the UK.
 Source: Adapted from Carbon Trust Marine Energy Accelerator (2011)

The main source of electricity generation in the UK are fossil fuels, as shown in Figure 1.21. Though the use of renewable sources (e.g. wind, solar, and hydro) has increased (DBEIS 2018), other sources can be added to their matrix.

Tidal characterisation in the UK done by Carbon Trust Marine Energy Accelerator (2011) estimated ~ 29 TWh/year of technical resource, and a practical ~ 20.6 TWh/year generation potential, using baseline assumptions on acceptable environmental and economic impacts of extraction. The UK's high resource availability (Figure 1.20) has led the country to consider tidal energy as part of their electricity matrix between 2020 and 2050 (UK Government 2013). Therefore, the government's support and investment in R&D has led them to the creation of testing sites, commercial prototypes, and academic research providing scientific data and surveys to develop marine energy in the UK.

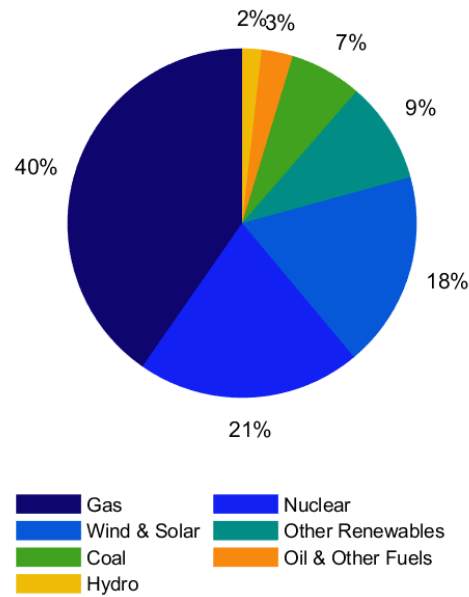


Figure 1.21: UK's Electricity Generation Matrix in 2017. Source: Adapted from DBEIS (2018)

1.2.2 Tidal Stream Energy in Costa Rica

Costa Rica's electricity matrix makes a contrast with the UK's. The base-load generation is supported by geothermal energy, and other renewable sources supply the demand. Though fossil fuels only represent 1% in the electricity matrix, as shown in Figure 1.23, the demand is expected to gradually increase until 2040 (Instituto Costarricense de Electricidad 2017).

To supply the demand increase, the electricity matrix is expected to diversify introducing new technologies, such as marine energy devices, as they are commercially ready to be deployed (Instituto Costarricense de Electricidad 2017). This research analyses the feasibility of adapting a tidal stream turbine to operate using the expected available resource in Costa Rica.

Due to the availability of other renewable sources in Costa Rica, marine energy has not been studied as much as in the UK. A preliminary survey determined that 45.5% (Costa Rica Limpia 2016) of the population confirmed that marine energy should be used to produce electricity. This percentage shows that, if developments of this kind are proposed once there is technology feasible for the country's conditions, the public might support them.

Though limited by lack of data and in detailed resource characterisation, preliminary studies by Brito e Melo (2013) have shown the expected resource characteristics in the country, determining the tidal velocities around the coast in Costa Rica. Figure 1.22 presents the predicted results from the resource study: a practical potential of 4.1GWh/year with the technology available at

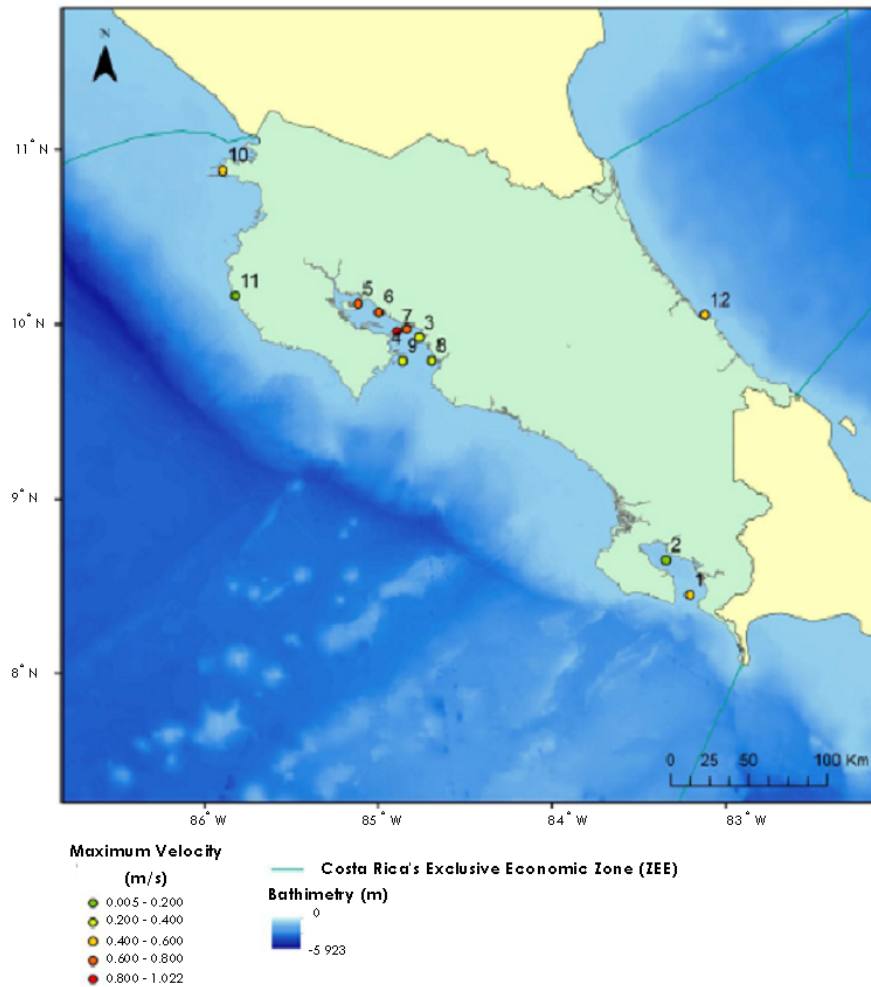


Figure 1.22: Tidal Energy Sites in Costa Rica.
Source: Adapted from Brito e Melo (2013)

the time of publication (Brito e Melo 2013).

The location considered for this research is marked with number 7, where the maximum velocity measured was 1.02 m/s, with depth of 33 m. This data was obtained with a drifter during two days, and a full resource characterisation of the area was recommended by the author to validate the results (Brito e Melo 2013).

This thesis proposes a tidal turbine design that could operate in the selected location, modifying a design proposed by Cardiff University's Cardiff Marine Energy Research Group (CMERG). The models presented in this work assume a velocity of 1.2 m/s in site, to be in agreement with the turbine's Reynolds number independence analysed by Mason-Jones et al. (2012).

Based on the expertise from the United Kingdom and motivated by the resource characteristics from Costa Rica, the work presented in this thesis aims to provide a method that adapts a well characterised HATT, designed to operate in high energy sites, to be technical and eco-

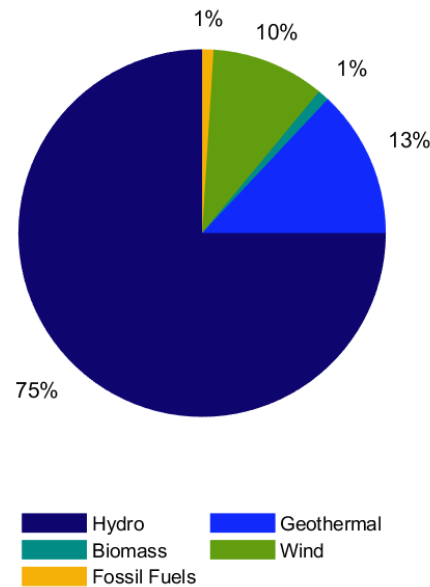


Figure 1.23: Costa Rica's Electricity Generation Matrix in 2015.

Source: Adapted from Instituto Costarricense de Electricidad (2017)

nomically feasible when operating in sites with low velocity tides. The suggested approach can then be applied to other HATT configurations.

1.3 Aims and Objectives

The aims of this thesis are: **i)** to provide a methodology to adapt the geometry of a horizontal axis tidal stream turbine to operate in low speed flows when it was designed to do so in higher velocity conditions, and **ii)** to determine the technical and economic feasibility of the proposed modified rotors if they were to be deployed in the UK and Costa Rica. They are to be achieved using the following objectives:

Objective 1 - To find the maximum power output configuration of single rotor horizontal axis tidal turbines when modified, based on solidity, to operate in low speed flows.

Objective 2 - To determine how solidity affects a horizontal axis tidal turbine's performance when modified to operate in low speed flows.

Objective 3 - To create a methodology that outlines technically feasible contra-rotating rotors turbines configurations based on their individual performance as single rotor horizontal axis tidal turbines.

Objective 4 - To determine if a horizontal axis tidal turbine can be modified to be technically and economically feasible when operating in low speed flows.

Objective 5 - To establish a baseline economic feasibility study for a tidal stream power plant, with low velocity conditions, in Costa Rica and in the United Kingdom.

1.4 Thesis Outline

- [Chapter 2](#) provides an update on HATT technology, and the physics behind it. The components of a tidal stream power plant are also described.
- [Chapter 3](#) explains the numerical method used to model the HATT geometries analysed in [Chapter 4](#), and [Chapter 5](#).
- [Chapter 4](#) compares the performance of single rotor HATT that were modified based on their solidity. A single rotor HATT is proposed to operate in low velocity flow conditions.
- [Chapter 5](#) describes the contra-rotating rotors selection method, using results from [Chapter 4](#). A contra-rotating HATT is proposed to operate in low velocity flow conditions.
- [Chapter 6](#) explains the economic feasibility study used for the proposed turbines. Results of their applicability in the UK and Costa Rica are presented.
- [Chapter 7](#) summarises the thesis' conclusions, and provides a baseline for future work.

Chapter 2

Tidal Stream Turbines Technology

As explained in [Chapter 1](#), this thesis focuses on horizontal axis tidal stream turbines and a method that could adapt a design that is meant to operate in high speed velocities (>2 m/s) to be functional in conditions with lower flow velocities. To give context of the research topic this chapter provides an overview of tidal stream technology, their operation theory, and how they can be used in a tidal stream power plant.

2.1 Tidal Stream Technology Background

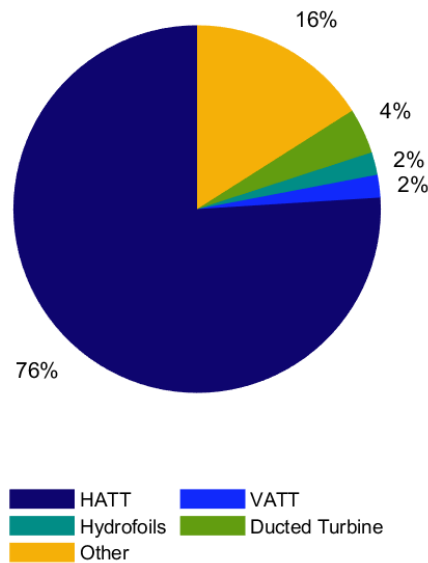


Figure 2.1: Tidal Stream Technologies Research and Development Efforts.
Source: Adapted from World Energy Council (2016a)

In [Figure 2.1](#) the R&D efforts for the different technologies are shown. According to World Energy Council (2016a) the main commercial scale application of tidal stream devices are HATT with 76%, and the other 24% is dedicated to other configurations like vertical axis tidal turbines, oscillating hydrofoils, and ducted turbines. Due to the majority of designs being open HATT,

such as the one analysed in this thesis, their application is studied more in depth.

These technologies can be divided in three main categories based on their foundation method: (a) first, (b) second, and (c) third generation (World Energy Council 2016a; Segura et al. 2017). Each of them are described next, with a few examples of commercial and academic configurations.

2.1.1 First Generation Technology

First generation devices consist of bottom mounted designs (World Energy Council 2016a), moored to the sea floor with monopile, piloted, or gravity based foundations (Segura et al. 2017). These technologies are expensive due to high uncertainties, but are installed in shallow waters (< 30 m (Vazquez et al. 2017)) to reduce risk (Carbon Trust Marine Energy Accelerator 2011).

Geometries different to the HATT, such as the transverse flow design from Kepler Energy (McAdam et al. 2013; Kepler Energy 2013) and ORPC's TidGen Power System (ORPC Inc. 2019), oscillating hydrofoils (Xu et al. 2015; Kinsey et al. 2010), and vertical axis tidal turbines have been proposed with seabed foundations (Blue Energy Canada Inc 2019; Lam et al. 2013; Kirke et al. 2008; Torresi et al. 2013). Seabed ducted HATT have also been considered as alternatives to accelerate the flow, and make the flow going through the turbine more uniform (Chen 2013). Research on this configurations has led to improve the duct shape (Fleming et al. 2016), determine their technical feasibility in lower velocities (Elbatran et al. 2016), analyse dual rotor configurations (Luquet et al. 2013), and to compare their efficiency from bare to ducted (Belloni 2013; Laurens et al. 2016).

HATT open rotor configurations are the most widely used due to their higher conversion efficiency, capability to maintain stability, and less fatigue loading (Chen 2013). Their design (Mason-Jones et al. 2012; Beam et al. 2012; H. Liu et al. 2016; Batten et al. 2006; O'Doherty et al. 2010), characteristics (Frost et al. 2017; Morris et al. 2016b; Wang et al. 2017), array configurations (D. O'Doherty et al. 2011; Myers et al. 2011), environmental impact (Pacheco et al. 2016), and economics (Vazquez et al. 2016a) have been widely studied. Commercial devices with this characteristics are shown in figures (2.2a) to (2.2d).

Andritz Hydro Hammerfest (ANDRITZ HYDRO Hammerfest 2019) has two commercially ready devices: the 21 m diameter *HS100* displayed in Figure 2.2a, and the *MK1 Turbine*. They are both capable to operate in depths of 35 m to 100 m, use an induction generator and have 21 m open

rotors with 3 blades. Their nominal rated power capacity vary from 1 MW to 2 MW.

Nova Innovation has also developed two turbine designs that operate in velocities of up to 2 m/s with rated power of 100 kW: *Nova M100-D* and *Nova M100* (Nova Innovation Ltd 2019). The former is shown in Figure 2.2b, which has a direct drive generator, unlike its counterpart that uses a geared drivetrain. They are both rated to produce 100 kW with their two bi-directional bladed rotors.

Sabella is another developer using direct drive generator technology (Sabella SAS 2019). Their 6 bladed *D10* 10 m diameter rotor, shown in Figure 2.2c, is designed to operate in tidal conditions of 4 m/s and produce up to 1 MW. On the contrary, Simec Atlantis turbines use a planetary gearbox connected to a generator (SIMEC Atlantis Energy 2019). Their devices are a combination of technologies previously developed by Marine Current Turbines SeaGen and Atlantis: the fully submersible 1.5 MW three bladed *AR1500* (Figure 2.2d) that operates in 3 m/s - 5 m/s tidal speeds, and the dual three bladed 2 MW *SeaGen-S* for locations with 1 m/s - 2.5 m/s flow velocities (SIMEC Atlantis Energy 2019).



(a) Andritz Hydro Hammerfest Turbine.
Source: ANDRITZ HYDRO Hammerfest (2019)



(b) Nova Innovation M100-D Turbine.
Source: Nova Innovation Ltd (2019)



(c) Sabella D-10 Turbine.
Source: Sabella SAS (2019)



(d) SIMEC Atlantis AR-1500 Turbine.
Source: SIMEC Atlantis Energy (2019)

Figure 2.2: First Generation Commercial Tidal Turbines

2.1.2 Second Generation Technology

Second generation technologies are those looking to capitalise on lower installation costs and faster flowing water designs located in the mid/high water column (World Energy Council 2016a), when compared to first generation technology. The devices can either be fully submerged with mooring lines to be located in the desired operation depth, or can float interacting with the free surface and joined to the seabed with mooring or anchoring lines (Segura et al. 2017). These technologies are intended for deeper sites at a lower cost (Carbon Trust Marine Energy Accelerator 2011).

Designs using this approach are mostly HATT that have been proved to be successful technology, though have a greater operational range than their first generation prototypes. Some commercial designs include *CoRMAT*'s (Figure 2.3a) contra-rotating turbine designed in Strathclyde University (Clarke et al. 2007a) and developed by Nautricity. *CoRMAT*'s configuration has a rated power of 0.5 MW - 2 MW and can be installed in depths of 8 m - 500 m (Nautricity Ltd 2019). With a three bladed front rotor and a two bladed back rotor, the configuration uses a direct drive permanent magnet generator and is moored to the seabed with a single point tensioned mooring system (Clarke et al. 2009a). More tethered contra-rotating configurations have also been proposed by Kawashima et al. (2017) and Barbarelli et al. (2014c).

Floating platforms are also used as an alternative to install HATT, which ease the maintenance and installation process. Orbital Marine Power has developed the *Orbital O2* following their success with FloTEC's *SR2000* prototype (Orbital Marine Power 2019). Displayed in Figure 2.3b, the two 16 m HATT two bladed rotors connect to direct drive permanent magnet generators and have a rated 2 MW power output.

As an integrated power solution, Tocardo has developed the semi-submersible U-shaped *Universal Foundation System (UFS)* that can be used offshore holding five *T2* turbines connected to direct drive permanent magnet generators (Tocardo B.V. 2019). The HATT are made with two bladed bi-directional rotors, have a combined rated power capacity of 1.5 MW, and have been previously tested in the Eastern Scheldt storm surge barrier.

Initially a platform developer, Sustainable Marine Energy (SME) has now combined Schottel's tidal energy assets to offer integrated tidal solutions. Figure 2.3d shows SME's *PLAT-O*, a moored buoyant mid-water column platform with four HATT rotors connected to a two-stage planetary gearbox and an induction generator, that have a combined maximum power output of 280 kW. Their relatively smaller generation installations are made with the intent to reduce capital and

operation costs for developers (SME Ltd 2019). Similarly, Bluewater Energy has developed the *Blue TEC Modular* platform for HATT tidal turbines working in tidal velocities of at least ~ 2 m/s, and in depth ranges of 20 m-1000 m (Bluewater 2019). Its effectiveness has been tested with 1-4 rotors of power ratings from 100 kW-2.5 MW with devices from Tocardo and Schottel Hydro, as shown in Figure 2.3e, proving its capability to be used with different turbine designs.



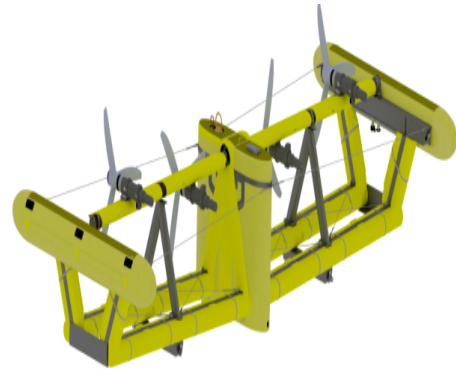
(a) Nautricity's CoRMaT Turbine.
Source: Nautricity Ltd (2019)



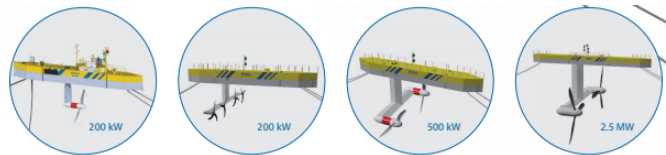
(b) Orbital Marine O2 Turbines.
Source: Orbital Marine Power (2019)



(c) Tocardo UFS T2 Turbines.
Source: Tocardo B.V. (2019)



(d) SME PLAT-O Turbines.
Source: SME Ltd (2019)



(e) Bluewater Energy BlueTEC Platform.
Source: Bluewater (2019)

Figure 2.3: Second Generation Commercial Tidal Turbines

This thesis considers CMERG HATT (Mason-Jones 2010) in a second generation arrangement. The proposed configuration aims to reduce installation costs (Walker et al. 2015), making the device more economically feasible.

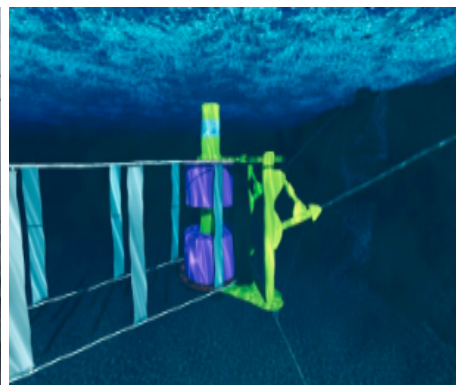
2.1.3 Third Generation Technology

Third generation technologies are those devices using an energy extraction method that differs from the horizontal and vertical axis tidal turbines. They seek to move the PTO mechanism through the flow rather than having the swept area as the prime mover (World Energy Council 2016a), and to harness energy from small velocity streams (Segura et al. 2017). These alternative concepts are meant to allow new areas of resource to be exploited in a more cost-effective manner (Carbon Trust Marine Energy Accelerator 2011), such as the device proposed by Akimoto et al. (2012): a turbine with a floating axis configuration which captures the tidal current in both directions which can be used in rivers, tidal stream, and current stream conditions. This preliminary concept could produce up to 2 MW.

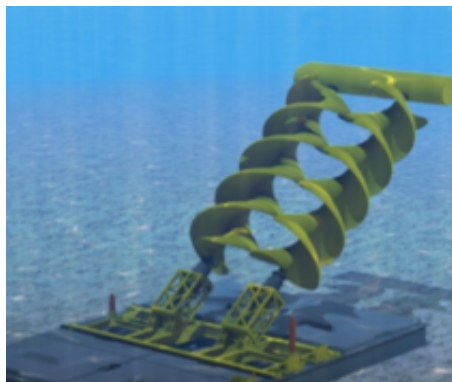
Third generation commercial alternatives have been developed by Minesto, Tidal Sails, and Flumill. Minesto's Deep Green technology is used in their *DG500*, shown in Figure 2.4a: a 500 kW rudder steered wing with an attached 1.5 m diameter 5 bladed turbine (kite), that pushes through the water following an eight-shaped trajectory in tidal velocities of 1.2 m/s-2.4 m/s with depths



(a) Minesto Deep Green Technology.
Source: Minesto AB (2019)



(b) Tidal Sails Beam Reach Technology.
Source: Tidal Sails AS (2019)



(c) Flumill Technology.
Source: Flumill (2014)

Figure 2.4: Third Generation Commercial Tidal Turbines

of 60 m-120 m (Minesto AB 2019).

The Norwegian company Tidal Sails invented the *Bam Reach*, the platform with slow moving sails from Figure 2.4b, which is located 15 m below the surface and can produce 6 MW. The device generates electricity by moving sails across the flow, that pulls two steel wire rope loops rotating four freely suspended direct drive generators (Tidal Sails AS 2019). The *Bam Reach* can have 4-600 sails and 500 m long loops whilst operating in 2 m/s flow velocities.

Another alternative commercial configuration is *Flumill* from a company with the same name. The twin Archimedes screws in Figure 2.4c have a rated power output of 2 MW, and can operate in tidal speeds of 2 m/s-8 m/s. The system is bidirectional and self regulating, with two turbines that slowly rotate opposite to each other using permanent magnet synchronous generators (Laws et al. 2016; Chen 2013; Flumill 2014).

The listed devices above are used as the main current working technologies. Many other configurations have been described previously by Segura et al. (2017), Chen (2013), Laws et al. (2016), Borthwick (2016) and ORE Catapult (2015).

As mentioned in Section 2.1.2, this thesis is based on the analysis of a HATT, therefore the theory and project characteristics for a device of this type are explained next.

2.2 HATT Theory

Rotors are used to produce electricity from the flow because of their rotational form that suits conventional electricity generating systems, and their blades' capacity to concentrate the energy available in the swept area by occupying a small percentage of it (Jamieson 2011). HATT rotor design is based on the physical principals of open flow actuator disk theory, which is also used for wind energy extraction turbine design. This theory is described next.

The available kinetic energy K_E in the open flow is determined by equation (2.1) (Hardisty 2009), where m is the mass of water, and u is the free stream flow velocity at time t . At the same time, the kinetic energy that passes through a flow cross-section area A_F depends on the water's mass flow rate \dot{m} (Hau et al. 2006) described in equation (2.2) where ρ is the fluid's density.

$$K_E = \frac{1}{2}mu(t)^2 \quad (2.1)$$

$$\dot{m} = \rho \cdot u \cdot A_F \quad (2.2)$$

Substituting the mass with the mass flow rate in equation (2.1), the hydraulic available power P_H (energy rate) in a flow cross-section area A_F is determined using equation (2.3).

$$P_H = \frac{1}{2} \cdot \rho \cdot u^3 \cdot A_F \quad (2.3)$$

The mechanical energy that can be extracted from the free stream flow by a turbine depends on flow power difference between before ($u_1, A_{F,1}$) and after ($u_2, A_{F,2}$) the converter (Hau et al. 2006), as shown in Figure 2.5, and described in equation (2.4) which is based on Bernoulli's equation.

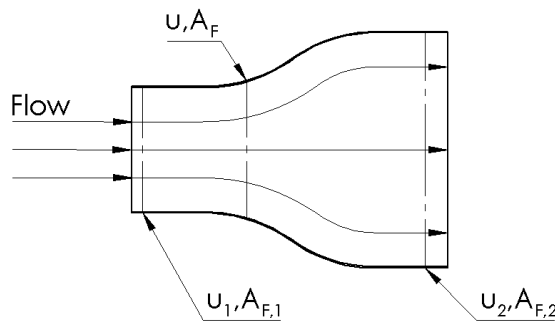


Figure 2.5: Power Extraction Flow Conditions. Source: Adapted from Hau et al. (2006)

$$P_H = \frac{1}{2} \cdot \rho \cdot (u_1^3 \cdot A_{F,1} - u_2^3 \cdot A_{F,2}) \quad (2.4)$$

Due to mass conservation (equation (2.5)), and the constant cross-section for a free flow HATT, the mechanical power output is given by equation (2.6).

$$\rho \cdot u_1 \cdot A_{F,1} = \rho \cdot u_2 \cdot A_{F,2} \quad (2.5)$$

$$P_H = \frac{1}{2} \cdot \rho \cdot \dot{m} \cdot (u_1^3 - u_2^3) \quad (2.6)$$

The flow velocity u_2 depends on how much power the device extracts from the flow (Hau et al. 2006). Equation (2.7) shows the correlation between turbine's power output P , the force F exerted by the turbine (thrust), and the velocity u_T at which the device makes the fluid move.

$$P = F \cdot u_T = \dot{m} \cdot (u_1 - u_2) \cdot u_T \quad (2.7)$$

Velocity u_T depends on the rotational velocity ω and the radius r at which this is measured. To obtain the total power output by a HATT with radius R , equation (2.7) can also be expressed as equation (2.8), where T is the turbine's torque. The torque is produced by forces on the blades that appear from pressure differences on each side of the aerofoil. The turbine resists incoming flow slowing the fluid ahead of the rotor plane, which increases the static pressure following Bernoulli's equation. The pressure difference across the rotor plane, dependant on blade shape, is created allowing energy extraction by the rotor (Jamieson 2011).

$$P = F \cdot \omega \cdot R = T \cdot \omega \quad (2.8)$$

Equation (2.8) is used to compute the power output from the rotor geometries modelled in this thesis.

2.2.1 HATT's Performance

The parameter that relates turbine's power output with the free flow available power in an area A with the same HATT's radius R is called power coefficient, C_P , and it is shown in equation (2.9). For reference on how much power is extracted by the turbine, the velocity u is obtained from the flow immediately before the device. Based on BEMT, the power coefficient (equation (2.9)) for a single rotor turbine can be written as equation (2.10), introducing the axial induction factor, a (equation (2.11)), that relates the upstream flow velocity u_1 with the flow velocity at the turbine u . The maximum theoretical power coefficient for a single rotor HATT of 59% is achieved when $a = \frac{1}{3}$, also known as the Lanchester-Betz Limit (equation (2.12)) (Burton et al. 2011). The turbines' characterisation presented in this thesis was done using equation (2.9).

$$C_P = \frac{T \cdot \omega}{1/2 \cdot \rho \cdot \pi \cdot R^2 \cdot u^3} \quad (2.9)$$

$$C_{P,SRT}(a) = 4a(1 - a)^2 \quad (2.10)$$

$$u = u_1(1 - a) \quad (2.11)$$

$$C_{P,SRT,max} = \frac{16}{27} = 0.593 \quad (2.12)$$

The turbines' thrust F , and torque T are also normalised to the upstream rotor area and flow velocity with thrust and torque coefficients, C_T (equation (2.13)) and C_θ (equation (2.14)) respectively.

$$C_T = \frac{F}{1/2 \cdot \rho \cdot \pi \cdot R^2 \cdot u^2} \quad (2.13)$$

$$C_\theta = \frac{T}{1/2 \cdot \rho \cdot \pi \cdot R^2 \cdot u^2 \cdot R} \quad (2.14)$$

These non-dimensional parameters (performance coefficients) characterise a HATT, allowing to predict a device's performance. Rotors are characterised with plot curves for each performance coefficient at different velocities, using the tip speed ratio (TSR) λ shown in equation (2.15). The non-dimensional variable relates a HATT's velocity u_T at the blade tip to the upstream flow velocity u .

$$\lambda = \frac{u_T}{u} = \frac{\omega \cdot R}{u} \quad (2.15)$$

These performance coefficients are used in this thesis to compare rotors with different geometries, to determine what configuration is more suitable for low speed flow conditions, and to predict scaled rotors' power, torque, and thrust outputs.

2.3 HATT Development Projects

For a HATT to be used in a commercial deployment, the rotor's technical specifications is only one variable to account for project development. As stated by Uihlein et al. (2016), resource assessment, environmental impact, socio-economic impacts, grid integration, installation, operation, maintenance, and regulatory affairs must also be considered for a device to be deployed in a commercial array. This thesis focuses on device's characteristics, and its likely applicability, based on cost estimation, assuming all other logistics aspects have been accounted.

This section describes the parameters analysed in this research for a HATT power plant.

2.3.1 Device Components

The main components of a turbine are rotor, device train, generator, transmission cables, instrumentation and control, and supporting structure (Hardisty 2009). These are described next.

2.3.1.1 Rotor

The rotor is considered the main mechanical component of a turbine, its efficiency will determine how much power will be extracted from the fluid. The design constraints considered in this research are radius, blade geometry, and number of blades. The hub connects blades to the rotor's shaft, and contains the hub bearings and pitch control mechanism (Hau et al. 2006).

The rotor size determines the swept area covered by the turbine, which has an effect on power output, as shown in equation (2.6). Also, the number of devices installed in a power plant depend on rotor's size. Their physical characteristics will constraint the location depending on its bathymetry (Vazquez et al. 2016a) and flow velocity profile.

As mentioned in Section 2.2, the number of blades and their design influence how much power is extracted from a specific site. The rotor's geometry depends on the aerofoil shape used for the blade, which will affect the turbine's performance based on its lift to drag ratio (Hau et al. 2006).

2.3.1.2 Drive Train

The drive train refers to the mechanical rotating parts from the hub to the electric generator: rotor shaft, gearbox, and generator drive shaft. They convert the rotor's mechanical rotational motion into electrical energy, and are housed inside the nacelle (Hau et al. 2006).

The nacelle also houses the turbine's generator, yawing system, sensors, instrumentation for performance monitoring, industrial controllers, and feedback systems (Hardisty 2009).

The gearbox's mechanism that converts the rotor's low rotational velocity to match the generator high rotational speed. Second generation technologies are considering devices where no gearbox is needed to reduce capital, and operation costs (Johnstone et al. 2013; Carbon Trust Marine Energy Accelerator 2011) because they require maintenance on a regular basis, and can have a significant effect on system's reliability (Alcorn et al. 2013).

2.3.1.3 Generator

The generator converts the rotor's mechanical energy to electricity. Traditional designs following wind energy technology are used for first generation tidal turbines (Segura et al. 2017; Benelghali et al. 2012), but second generation devices are designed to reduce costs and uncertainty by removing the gearbox from the drive train, which led them to use permanent magnet direct drive generators (PMDDG) (Benelghali et al. 2012; Keysan et al. 2010, 2011; Johnstone et al. 2013; Kanemoto et al. 2000).

Direct-drive systems must be designed to meet the low speed-high torque characteristics of a turbine, and the use of permanent magnets reduces the system weight whilst increasing the efficiency (Alcorn et al. 2013). For the purpose of this research where low flow velocities are modelled, directly driven generators were considered.

2.3.1.4 Cables

The cables represent an important cost due to the distance to shore where the operations plant will be located. They are placed at the bottom of the sea to connect with the grid in land. Installation (and materials), mobilisation, seabed conditions, downtime, availability of equipment (Alcorn et al. 2013), maintenance, and connection (Segura et al. 2017) are some of the factors to consider when placing the cables that carry electricity and data to control each device in the power plant array.

For low velocity conditions, such as the ones analysed in this thesis, the installation process should be simpler than the procedure followed in high energetic sites. The flow characteristics should be less harsh (e.g. less scour), hence reducing the overall cable related costs.

2.3.1.5 Support Structure

The foundation/mooring of a tidal turbine depends on the loads that it must withstand. The design itself of the support structure affects the turbine's efficiency (Segura et al. 2017), and would have a significant effect on the costs (SI Ocean 2013; ORE Catapult 2018a; Sanchez et al. 2014).

Instead of using gravity based foundations (Keysan et al. 2011), new designs use floating platforms (Akimoto et al. 2012; Keysan et al. 2010), and tethering cables (Clarke et al. 2010; Barbarelli et al. 2014a) to support the turbines. These second generation (Carbon Trust Marine Energy Accelerator 2011) configurations have reduced the cost and eased the installation

process, as well as increased the power output since the velocities are higher near the water body surface, therefore showing a better production to capital investment ratio (Sanchez et al. 2014): generating more power at a lower (or same) cost .

2.3.2 Logistics

For the development of a fully operating HATT power plant, the logistics involved at different stages of its lifetime must be considered. In this section, the planning processes involved are described.

2.3.2.1 Resource Assessment

To propose a tidal energy extraction plant, a resource assessment is needed to estimate the flow velocities of a specific location. The tidal current energy depends on seawater density, velocity, velocity availability factor, neap/spring factor, peak spring-tide velocity (Uihlein et al. 2016), velocity profile, and flatness of bed. Numerical models allow to predict tides' characteristics for some regions, but a full resource characterisation requires measurements taken with instrumentation on site that provides a full bathymetry scan, and validates the forecast done.

2.3.2.2 Location Selection

A site location is made once the resource is well characterised. Flow data, depth, distance to shore, weather patterns, and device selection are the technical parameters that narrow the possibilities on where devices could be placed. To make a final decision, issues such as tourism activities, boat routes, installation and maintenance windows, environmental restrictions, communities affected directly and indirectly, road and port access, legislation, and permits must be accounted (Segura et al. 2017; Vazquez et al. 2016a). The effect a development of this kind would have to the immediate community must be addressed for the power plant to be deployed (Johnson et al. 2013).

2.3.2.3 Permissions

Once the site location has been chosen, permits and consents must be granted by the authorised organisation. Each country has different regulations that must be met, and depending on their requirements several institutions could be involved in the process. This procedure could include, but not be limited to, field survey and formulation, environmental impact assessment (EIA),

applications for permits, leases, and legal work (Hardisty 2009). This stage of the developing process could take years, and could be costly. A clear understanding of the requirements could avoid delays and unnecessary fees.

This project analysed the feasibility of a well characterised HATT to operate in conditions like the ones predicted for Costa Rica, and the cost prediction described in Chapter 6 was based in the UK situation. As a reference, the permissions process that must be followed in the UK and Costa Rica (Hernandez-Madrigal et al. 2016) are described next.

2.3.2.3.1 Procedure in the UK

According to the Planning Act 2008, for a marine power plant larger than 100 MW it must be determined if it is classified as a National Significant Infrastructure Project (NSIP). NSIPs are large scale developments related to energy, transport, water, waste water, and general waste. Power plants qualify as a NSIP if they produce over 100 MW or 50 MW for onshore wind farms. Once a project is considered a NSIP, the permits required for its development are granted through a Development Consent Order (DCO) managed by the UK Planning Inspectorate and granted by the Secretary of State. The developers must determine if they require other permit, such as the Marine Licence. The consultees involved with a specific project can be found on the Regulations (UK Government 2008). Other organisations include: (a) Safety Zone Scheme (DBEIS 2011), (b) Crown Estate Land (Kerr et al. 2014), (c) Local Planning Authorities (Vantoch-Wood et al. 2012), (d) Local Port Harbour Authority, and (e) National Grid.

Marine power plants in the UK are considered as EIA developments according to Schedule 1 of The Infrastructure Planning (Environmental Impact Assessment) Regulations 2009 UK Government (2009). Hence, an Environmental Statement (ES) must be done for a power plant to be built. The developer can request a scope of the ES, which will detail what information must be included in the statement. Developers may include a list of consultees to create the application (UK Government 2009).

The Secretary of State determines what items have to be included in the EIA, as part of the ES, which could include: coastal processes, sediment, transport and contamination; marine water quality; intertidal and sub-tidal benthic ecology; fish, including recreational and commercial fisheries; marine mammals; coastal birds; terrestrial ecology; seascape, landscape and visual assessment; navigation and marine transport assessment; onshore transport assessment; air quality; hydrology and flood risk; land quality and hydrogeology; noise and vibration; marine

archaeology; terrestrial archaeology and historic landscape; economy, tourism and recreation; and mitigation and monitoring (UK's National Infrastructure Planning 2016).

When there is a plan to develop an offshore electricity generation project between 1 MW and 100 MW, the required planning permission is given by the Secretary of State. A similar procedure to the DCO's must be followed, and the application is managed by the Department of Business, Energy and Industrial Strategy (DBEIS) (UK Government 1989). A marine licence is also required and given by the Marine Management Organisation (MMO), and other permits required must be obtained depending on the relevant consultees recommendations (Vantoch-Wood et al. 2012).

For projects smaller than 1 MW a consultation must be made to the respective marine authority and the MMO to determine what procedures to follow in regards to the specific characteristics of the development (Argyll Tidal Ltd et al. 2013).

2.3.2.3.2 Procedure in Costa Rica

The developer has to make a feasibility study and determine the project's scope, as any other renewable energy project. Developers must submit a Document of Environmental Evaluation (DI) to the Secretaría Técnica Nacional Ambiental (Environmental Technical Secretary, SETENA) (SETENA 2016) which must include: basic engineering, geology, a quick archaeological study of the project area; basic characterisation of the project area and its influence areas; climate data of the project area; and an evaluation using a matrix with marks that show: consumption and effects of the water, energy, and flora and fauna; negative and positive impacts on air, soil and humans; and other risks (Gobierno de Costa Rica 2016). The DI has guidelines for the developer to complete an electronic form that indicates the significance of each assessed impact, and the mitigations planned for them.

All electricity generation projects are considered as high impact projects, therefore the developer must prepare an EIA (Ossenbach-Sauter et al. 2010) once SETENA has decided if their project is environmentally viable. This assessment is made with three tools created specifically for the report: Estudio de Impacto Ambiental (Environmental Impact Study, EslA), Plan-Pronóstico de Gestión Ambiental (Plan-Forecast of Environmental Management, PPGA) and Declaración Jurada de Compromiso Ambiental (Sworn Declaration of Environmental Commitment, DJCA).

The local government provides signature receipt of the EIA, which can then be submitted to SETENA. SETENA has a maximum of 12 weeks to determine a resolution, which could be extended up to 24 months due to added/modified information requested during revision. Once

the project is approved, SETENA announces the preparation of the DJCA and establishes a warranty deposit value for environmental fulfilment that can vary from 1% to 4% of the total cost of the project (Ossenbach-Sauter et al. 2010).

The developer must request an authorisation from the *Autoridad Reguladora de Servicios Públicos* (Regulatory Authority of Public Services, ARESEP) to provide the public service of electricity generation. ARESEP's *Dirección de Servicios de Energía* (Directorate of Energy Services) is in charge of handling this request where the developer must show the environmental viability resolution given by SETENA, information of the developer, maps, and location of the project. After all documentation has been validated, the Directorate calls for a public meeting through ARESEP's *Dirección de Protección al Usuario* (Directorate of User Protection), where the general public can attend in support or opposition to the project. For situations where citizens do not have the resources to provide a technical study that justifies a concern they might have, ARESEP provides a technical expert to make the study. ARESEP's executive board then analyses minutes and reports from public feedback, and gives a resolution considering all stakeholders' inputs. The developer also has to apply for a electricity tariff approval, given by ARESEP and its Directorate of Energy Services after a second public meeting (Ossenbach-Sauter et al. 2010).

To get construction permits the developer must validate plans with different authorities depending on the characteristics and location of the project. For renewable energy projects the developer must contact the *Colegio Federado de Ingenieros y Arquitectos* (Federate College of Engineers and Architects, CFIA), Ministry of Public Works and Transportation, Health Ministry, local Municipality, Fire Brigade, Costa Rican Institute of Tourism, and any other relevant consultee that those entities might recommend (Ossenbach-Sauter et al. 2010).

Once all relevant organisations have approved the project's plans, the developer must request a soil use permit given by the municipality. The developer then must submit all previous authorised documentation to receive a sanitary functioning permit from the Health Ministry to start operations (Ossenbach-Sauter et al. 2010).

In the absence of a regulation plan no marine renewable energy power plant can be developed in Costa Rica. Likewise there is no procedure for marine energy power plants' licences (CFIA 2014).

Another factor to consider when planning these projects is the corruption involved in the permitting process. The Latin American countries are considered as highly corrupted according to the Corruption Perceptions Index (Transparency International 2018), and Costa Rica is not the

exception: it is ranked 6th within the region and 44th in the world (May-Grosser 2020) with a score of 56 which is higher than the average 43. Though the country went up the ranking 4 positions in 2019 due to the increase in corruption in other countries, there is still preferential treatment and conflict of interests that might affect the development of tidal stream energy projects.

2.3.2.4 Installation

Installation logistics depend on the device been used, the weather patterns, distance to shore, depth, available vessels to carry the devices from inland to the array site, and mooring system (Vazquez et al. 2016b). Due to the complexity of all the variables involved in the installation procedure, the costs can represent up to 27% of a device's lifetime cost (SI Ocean 2013). Different installation methods are studied to reduce the costs, and normalise the process in marine energy industry (A.S Bahaj 2011; Carbon Trust Marine Energy Accelerator 2011; Segura et al. 2017; Uihlein et al. 2016).

For low velocity conditions, this costs could also be reduced with the use of a device that requires a smaller vessel to install and give maintenance services.

2.3.2.5 Operation and Maintenance

Operations include maintaining a constant check on the various systems of the power plant, servicing for the whole equipment, insurance, power measurement, telecommunications with the turbines, and administration (Hardisty 2009). Device maintenance must be done to keep the optimum conditions during a device's lifetime, and planning must consider weather conditions to know the repair time windows and procedures to ensure economic viability of the projects (Uihlein et al. 2016; Borthwick 2016; ORE Catapult 2018a; A.S Bahaj 2011).

Reducing downtime, achieving high availability, and being able to access devices without delay is crucial to reduce maintenance costs (Carbon Trust Marine Energy Accelerator 2011). Some strategies used to achieve this are: designing cost-effective-redundant systems which need little maintenance, and automating the performance of emersion and immersion manoeuvres (Segura et al. 2017). Having suitable local port infrastructure also enables lower maintenance costs for devices that are taken to shore as part of the maintenance plan (SI Ocean 2013).

The time when operation and maintenance can be performed could be higher in sites with

low velocity conditions, where weather and wave windows are longer (Carbon Trust Marine Energy Accelerator 2011).

2.3.3 Economic Feasibility

All the aspects described above have an effect on a power plant's economic feasibility, which is based on how much energy can be sold whilst generating a profit.

The present project analyses the technical and economic feasibility for a HATT when operating in low speed conditions. The technical specifications of the device are analysed in [Chapter 4](#) and [Chapter 5](#), whereas the levelised cost of energy (LCOE) is calculated in [Chapter 6](#). The results will determine whether the proposed configurations are feasible to be deployed in sea conditions similar to the ones in Costa Rica. The following chapter ([Chapter 3](#)) describes the methodology followed to model the analysed rotor configurations.

Chapter 3

Numerical Modelling

This chapter provides a background on numerical modelling of tidal stream turbines, then explains the basics of Computational Fluid Dynamics (CFD), and the modelling approach that was followed to obtain the results for each case considered when making changes to CMERG's turbine. The CMERG rotor has been optimised and validated to operate at speeds above 1 m/s (Mason-Jones et al. 2012; Morris et al. 2015; Frost et al. 2015). The specific alterations made to the geometry are explained in [Chapter 4](#) and [Chapter 5](#).

3.1 Modelling Background

Research presented in this thesis is based on results provided by numerical modelling of a HATT, that was designed using the Blade Element Momentum Theory (BEMT) and validated with CFD. The BEMT is based on a combination of momentum and blade element theories, used as the initial design proposal for tidal turbines to determine the spanwise and chordwise loads affecting a turbine. BEMT results can be validated with experimental data only (Batten et al. 2007; A.S. Bahaj et al. 2007; Batten et al. 2008), or using CFD and experimental validation to corroborate their performance (Goundar et al. 2013; Mason-Jones 2010; J. Lee et al. 2012; Noruzi et al. 2015). Schluntz et al. (2015) used a coupled Reynolds Averaged Navier-Stokes with Blade Element Momentum (RANS-BEM) method to optimise a rotor geometry according to four blockage values of an infinite tidal fence and found that the maximum power output is obtained when the highest solidity rotor operates in the highest blockage domain. CFD with BEMT modelling has also been used to model turbines as an enhanced actuator disk, which has allowed to analyse the wake effect on turbine arrays (Edmunds et al. 2014), blade tip losses (Edmunds et al. 2017b), power shedding (Edmunds et al. 2017a), and the model's capability when comparing results with experimental data (Edmunds et al. 2017c).

CFD's capability has been increasing in the years, and the computational cost associated with it has decreased. The tool is now used widely to predict complex fluid behaviour without the

need of experimental resources, such as flow separation and its impact in hydrodynamic efficiency of HATTs (Shi et al. 2013), but considering physical model tests to validate final numerical results. The purpose of this research is to adapt a rotor geometry to a specific set of conditions, and CFD allows the understanding of a device's hydrodynamics for comparison between laboratory and full size prototypes predictions. Gorle et al. (2016) modelled a vertical axis H-Darrieus in two dimensions and compared the results to 3D towing tank experiments. Belloni (2013) modelled an open centre HATT to compare the free flow turbine design to its performance when located within a duct, which accelerates the flow introducing blockage effects. By modelling a duct with an actuator disk, with the help of FLUENT CFD solver, Fleming et al. (2016) proved that the duct would reduce the disc power but the power density was increased when compared to a free flow rotor, and that both thin and cambered profiles have pros and cons to consider when designing a device. Different diffuser configurations are also being analysed with the help of CFD to determine which method is the most appropriate for the technology. For instance, Cresswell et al. (2015) determined that wake recovery for an optimised duct with a turbine was less than half at 9 blade radii downstream compared to a bared rotor. Similar analysis by Luquet et al. (2013) showed that an optimised rotor within a divergent optimised duct, validated with experimental results, had a predicted $C_p=0.41$ considering the velocity just before the rotor and a $C_p=0.75$ when the free stream velocity is used. When considering low speed flow conditions, as the ones analysed in this project, an efficient accelerating method could be considered to expand upon the results presented in this thesis.

CFD is also used to analyse more complex (and computational expensive) situations like with Fluid Structure Interaction (FSI), wake analysis, array modelling, and contra-rotating configurations like the one proposed in Chapter 5. In FSI simulations, the hydrodynamics results from CFD are the boundary conditions in structural calculations and/or vice versa. Singh et al. (2014) used FSI to do a cavitation analysis in their design, and Morris et al. (2016a) studied the effect of blade deformation on kinetic energy extraction.

To have an initial understanding of a turbine's wake behaviour basic tidal stream numerical modelling, that lasts a few days per model, considers the RANS equations with the common turbulence models ($k - \epsilon$ and SST- $k - \omega$). A more detailed wake analysis with a simpler turbulence model for a single turbine was studied by Masters et al. (2013), where a non-uniform flow, imposed by a negative gradient on the top surface of the boundary conditions, determined that flow acceleration causes a faster wake recovery. More time consuming simulations have

been done by Ebdon et al. (2016, 2017), where a more detailed wake analysis was made using Detached Eddy Simulation (DES) and models can last weeks to converge.

To determine turbine array configurations, it is necessary to understand wake behaviour. Numerical models, so far, are limited to the hardware's capability when analysing turbines arrays. Nonetheless, some studies have been done with the aid of CFD, considering their limitations, and have allowed different aspects of array configurations to be understood. D. O'Doherty et al. (2011) considered two array arrangements of four turbines to determine how the power output was affected depending on the distance between two rows of turbines; the results showed that the second row should be located at least 5D downstream from the first one, and that when using a counter-rotating approach between rows the second line of turbines could extract about 88% of the front rotors' power.

Low velocity flow conditions have not been considered thoroughly in the design of tidal stream turbines, due to their power output limitations. Using CFD, a baseline understanding is proposed for single rotor and contra-rotating turbines, which could then be extended to wake analysis, and array configurations. Previous research done by Clarke et al. (2007b) proposed a scale contra-rotating turbine that was designed with BEMT, optimised with FLUENT, and experimentally validated in test tanks (Clarke et al. 2007a) and in real sea conditions (Clarke et al. 2010). Huang et al. (2016d) modelled with CFD a bi-directional contra-rotating rotor using symmetric blades, which then were optimised using a multi-objective optimisation method to increase the lift-drag ratio, and validated again with ANSYS CFX. More HATT contra-rotating performance CFD studies have been done by N. Lee et al. (2015), whereas Barbarelli et al. (2016) proposed a design of a two concentric contra-rotating rotors anchored to the coast, using an iterative procedure based on zero-dimensional approach to characterise the device, and validated the results using FLUENT.

The geometry used to create the models analysed in Chapter 4 and Chapter 5 was designed by Egarr et al. (2004), where a 4 bladed rotor simulation and sea based experimental validation was used to propose a more cost effective 3 bladed rotor, which was modelled in a 5 rotor array (Egarr et al. 2005) with results limited to the computational capacity of the study. CMERG's 3 bladed rotor's pitch angle was optimised and characterised with experimental validation by T. O'Doherty et al. (2009). Then with the use of BEMT the blade shape was modified and the results were validated with CFD and experimental data (Tedds et al. 2011) to obtain the non-dimensional characteristics of the device (Mason-Jones et al. 2012). These results have been

used to do further research in HATT design's fluid dynamics. Morris et al. (2015) used this design to analyse how the solidity affects performance characteristics when comparing 2, 3, and 4 bladed devices in high speed conditions, and evaluated the swirl in each of those devices (Morris et al. 2016b). More studies have provided a general understanding the effect of flow misalignment (Frost et al. 2017), profiled flow and surface gravity waves (Tatum et al. 2016) have on tidal stream turbines.

This chapter explains the CFD modelling method used to analyse CMERG's turbine performance when the geometry is being optimised to operate in low speed conditions. Previous modelling approaches followed by Frost (2016), Morris (2014), Mason-Jones (2010), Goundar et al. (2013), Noruzi et al. (2015), and Jo et al. (2014) were used as reference.

In Chapter 4 an adaptation of CMERG's turbine is done following learned lessons on solidity (Morris 2014), and in Chapter 5 a contra-rotating configuration is proposed using previous simulations done with this rotor by D. O'Doherty et al. (2009) as a design reference, where modified rotors were used for both rows of the contra-rotating configuration.

3.2 Computational Fluid Dynamics Theory

CFD is the analysis of systems involving fluid flow, heat transfer and associated phenomena such as chemical reactions by means of computer-based simulation. The technique is very powerful and spans a wide range of industrial and non-industrial application areas such as aerodynamics of aircraft and vehicles, hydrodynamics of ships, turbomachinery and marine engineering (Versteeg et al. 2007). For the specifics of tidal stream turbines, previous research (J. Lee et al. 2012) has determined that CFD is useful for more detailed flow features around a turbine and a more accurate performance estimation. This method was adopted for this research where a trial and error was made to determine the optimum geometry configuration of the CMERG turbine in low speed conditions.

The software used to run the simulations presented here is the commercial package ANSYS CFX 16.0, which uses the Finite Element Volume Method to solve the Navier-Stokes equations in conjunction with the turbulence models required to determine the turbines' technical characteristics. The fluctuating and complex effects of turbulence on the flow can be seen with CFX using one of the turbulence models that have been specifically developed to account for the effects of turbulence without recourse to a prohibitively fine mesh and direct numerical sim-

ulation (ANSYS 2016a). ANSYS CFX has the option to use Eddy Viscosity, Reynolds Stress, and ANSYS CFX Transition turbulence models; plus the possibility to do Large Eddy and Detached Eddy Simulations. Due to the complexity of these project's studied cases, the turbulence models used are *SST - $k - \omega$* and *Reynolds Stress*, which are described below.

3.2.1 Reynolds Averaged Navier-Stokes (RANS) Model

RANS equations are made to include the turbulence fluctuations in time by considering their variation with respect to a mean value, therefore modelling turbulence effects without a need for resolution of the fluctuations. These variations to the original Navier-Stokes equations create additional unknown terms called 'turbulent' or 'Reynolds' stresses that need to be modelled with additional equations to achieve "closure" (ANSYS 2016a).

For incompressible flows, such as the water where turbines are located, the instantaneous continuity equation (3.1), and Navier-Stokes momentum equations (3.2a - 3.2c) are given in a Cartesian co-ordinate system, where the velocity vector \mathbf{u} has the x , y , and z component: u , v , and w , respectively; p refers to the hydrostatic pressure, and ν and μ are the kinematic and dynamic viscosity, respectively (Versteeg et al. 2007).

$$\nabla \cdot \mathbf{u} = \frac{\partial u}{\partial x} + \frac{\partial v}{\partial y} + \frac{\partial w}{\partial z} = 0 \quad (3.1)$$

$$\frac{\partial u}{\partial t} + \nabla \cdot (u\mathbf{u}) = -\frac{1}{\rho} \frac{\partial p}{\partial x} + \nu \nabla \cdot (\nabla(u)) \quad (3.2a)$$

$$\frac{\partial v}{\partial t} + \nabla \cdot (v\mathbf{u}) = -\frac{1}{\rho} \frac{\partial p}{\partial y} + \nu \nabla \cdot (\nabla(v)) \quad (3.2b)$$

$$\frac{\partial w}{\partial t} + \nabla \cdot (w\mathbf{u}) = -\frac{1}{\rho} \frac{\partial p}{\partial z} + \nu \nabla \cdot (\nabla(w)) \quad (3.2c)$$

To obtain the RANS equations, the velocity is separated in its time averaged (U) and fluctuations (u') components as shown in equations (3.3) and (3.4a - 3.4c), where the former presents variables in vector style and the latter in Cartesian format.

$$\mathbf{u} = \mathbf{U} + \mathbf{u}' \quad (3.3)$$

$$u = U + u' \quad (3.4a)$$

$$v = V + v' \quad (3.4b)$$

$$w = W + w' \quad (3.4c)$$

$$p = P + p' \quad (3.4d)$$

The velocity is density-weighted averaged (Favre-averaged) for incompressible flows. It is represented by \tilde{U} and inserted in the original continuity and Navier-Stokes equations. The final RANS model, where the overbar indicates time-averaged variables is shown in equations (3.5) and (3.6a - 3.6c) (Versteeg et al. 2007).

$$\frac{\partial \bar{\rho}}{\partial t} + \frac{\partial(\bar{\rho}\tilde{U})}{\partial x_i} = 0 \quad (3.5)$$

$$\frac{\partial(\bar{\rho}\tilde{U})}{\partial t} + \nabla \cdot (\bar{\rho}\tilde{U}\tilde{U}) = -\frac{\partial \bar{P}}{\partial x} + \nabla \cdot (\mu \nabla \tilde{U}) + \left[-\frac{\partial \tau_{xx}}{\partial x} - \frac{\partial \tau_{xy}}{\partial y} - \frac{\partial \tau_{xw}}{\partial z} \right] + S_{Mx} \quad (3.6a)$$

$$\frac{\partial(\bar{\rho}\tilde{V})}{\partial t} + \nabla \cdot (\bar{\rho}\tilde{V}\tilde{U}) = -\frac{\partial \bar{P}}{\partial y} + \nabla \cdot (\mu \nabla \tilde{V}) + \left[-\frac{\partial \tau_{xy}}{\partial x} - \frac{\partial \tau_{yy}}{\partial y} - \frac{\partial \tau_{yw}}{\partial z} \right] + S_{My} \quad (3.6b)$$

$$\frac{\partial(\bar{\rho}\tilde{W})}{\partial t} + \nabla \cdot (\bar{\rho}\tilde{W}\tilde{U}) = -\frac{\partial \bar{P}}{\partial z} + \nabla \cdot (\mu \nabla \tilde{W}) + \left[-\frac{\partial \tau_{xz}}{\partial x} - \frac{\partial \tau_{yz}}{\partial y} - \frac{\partial \tau_{zw}}{\partial z} \right] + S_{Mz} \quad (3.6c)$$

Equations (3.7a - 3.7c) show the normal stresses created by the RANS model, which involve the respective variances of the x -, y -, and z -velocity fluctuations. The Reynolds (shear) stresses are created by the momentum exchange due to eddies' convective transport, which causes the faster moving fluid layers to be decelerated and the slower ones to be accelerated. They are associated with correlations between different velocity components, and illustrated in equations (3.8a - 3.8c) (Versteeg et al. 2007).

$$\tau_{xx} = -\rho \overline{u'^2} \quad (3.7a)$$

$$\tau_{yy} = -\rho \overline{v'^2} \quad (3.7b)$$

$$\tau_{zz} = -\rho \overline{w'^2} \quad (3.7c)$$

$$\tau_{xy} = \tau_{yx} = -\rho \overline{u'v'} \quad (3.8a)$$

$$\tau_{xz} = \tau_{zx} = -\rho \overline{w'w'} \quad (3.8b)$$

$$\tau_{yz} = \tau_{zy} = -\rho \overline{v'w'} \quad (3.8c)$$

3.2.1.1 Rotational Forces

The variables S_{Mx} , S_{My} , and S_{Mz} included in equations (3.6a - 3.6c) refer to the source terms added, in their respective Cartesian components, to the RANS equations depending on the model's characteristics. To simulate the rotation of a tidal turbine at a constant angular velocity ω , with a location vector \mathbf{r} , a rotational Multiple Frame of Reference (MFR) is used in ANSYS CFX. Additional sources of momentum ($S_{M,rot}$) that account for the Coriolis (S_{Cor}) and centrifugal (S_{cfg}) forces must then be considered (ANSYS 2016a); they are defined in equations (3.9a - 3.9c). The MFR domain is described in Section 3.3.2 and its set up is detailed in Section 3.5.

$$S_{M,rot} = S_{Cor} + S_{cfg} \quad (3.9a)$$

$$S_{Cor} = -2\rho\omega \times \mathbf{U} \quad (3.9b)$$

$$S_{cfg} = -\rho\omega \times (\omega \times \mathbf{r}) \quad (3.9c)$$

Following ANSYS CFX guidelines (ANSYS 2016a) an alternate rotation model was used in the simulations, since the absolute frame flow is essentially a constant flow parallel to the axis of rotation. When using this setting the flow solver advects the absolute instead of the relative frame velocity, reducing the numerical error to zero as the absolute frame flow becomes axially constant. By doing this the Coriolis source term changes as shown in equation (3.10).

$$S_{Cor} = -\rho\omega \times \mathbf{U} \quad (3.10)$$

3.2.2 SST - $k - \omega$ Turbulence Model

As explained in Section 3.2.1, to close the RANS equations, a turbulence model that accounts for the flow's kinetic energy must be included. For the purpose of this research the SST- $k - \omega$ Eddy Viscosity Model (SST, from here onwards) is used. SST has been used in previous research by Morris (2014) where the results were compared to those obtained with the Reynolds Stress turbulence Model (RSM) and experimental data, showing that SST provided a closer match to the real values. Frost (2016) also used this turbulence model when running simulations with

ANSYS CFX, finding that transient results differed to experimental values by 3%.

The SST - $k-\omega$ is a two-equation turbulence model based on the eddy viscosity hypothesis, which assumes that the Reynolds stresses can be related to the mean velocity gradients, and eddy (turbulent) viscosity by the gradient diffusion hypothesis (ANSYS 2016a). Equation (3.11) shows this relationship, where μ_t is the eddy viscosity, k is the kinetic energy per unit of mass, and δ_{ij} is the Kronecker delta ($\delta_{ij} = 1$ if $i = j$ and $\delta_{ij} = 0$ if $i \neq j$). To explain the mathematics behind this model the suffix notation is used (Versteeg et al. 2007).

$$\tau_{ij} = -\overline{\rho u'_i u'_j} = \mu_t \left(\frac{\partial U_i}{\partial x_j} + \frac{\partial U_j}{\partial x_i} \right) - \frac{2}{3} \delta_{ij} \left(\rho k + \mu_t \frac{\partial U_k}{\partial x_k} \right) \quad (3.11)$$

The eddy diffusivity hypothesis relates the Reynolds fluxes of a scalar linearly to the mean scalar gradient. Equations (3.12) and (3.13) show this relationship where Γ_t is the eddy diffusivity and Pr_t is the turbulent Prandtl number (ANSYS 2016a).

$$-\overline{\rho u'_i \varphi'} = \Gamma_t \frac{\partial \Phi}{\partial x_i} \quad (3.12)$$

$$\Gamma_t = \frac{\mu_t}{Pr_t} \quad (3.13)$$

The model accounts for the turbulent shear stress transport and gives highly accurate predictions of the onset and amount of flow separation under adverse pressure gradients. Versteeg et al. (2007) created it by transforming the $k - \epsilon$ model into a $k - \omega$ model in the near-wall region and the standard $k - \epsilon$ model in the fully turbulent region far from the wall. The transport equations (3.14) and (3.15) are taken from the hybrid Baseline (BSL) $k - \omega$ turbulent model (ANSYS 2016a), but the limiter of the eddy viscosity in equation (3.16) allows to predict the onset and amount of flow separation from smooth surfaces (ANSYS 2016a).

$$\frac{\partial(\rho k)}{\partial t} = \frac{\partial}{\partial x_j} (\rho U_j k) = \frac{\partial}{\partial x_j} \left[\left(\mu + \frac{\mu_t}{\sigma_{k3}} \right) \frac{\partial k}{\partial x_j} \right] + P_k - \beta' \rho k \omega + P_{kb} \quad (3.14)$$

$$\begin{aligned} \frac{\partial(\rho \omega)}{\partial t} = \frac{\partial}{\partial x_j} (\rho U_j \omega) = \frac{\partial}{\partial x_j} \left[\left(\mu + \frac{\mu_t}{\sigma_{\omega 3}} \right) \frac{\partial \omega}{\partial x_j} \right] \\ + (1 - F_1) 2\rho \frac{1}{\sigma_{\omega 2} \omega} \frac{\partial k}{\partial x_j} \frac{\partial \omega}{\partial x_j} + \alpha_3 \frac{\omega}{k} P_k - \beta_3 \rho k \omega^2 + P_{\omega b} \end{aligned} \quad (3.15)$$

$$\nu_t = \frac{a_1 k}{\max(a_1 \omega, S F_2)} \quad (3.16)$$

Where μ_t refers to the turbulent kinematic viscosity that relates to ν_t as described in equations (3.17a - 3.17b). These model includes two Blending Functions: F_1 , equals to one near the surface and decreases to zero as it reaches the edge of the boundary layer where the $k - \epsilon$ model is recovered, and F_2 , which restricts the limiter to the wall boundary layer, as the underlying assumptions are not correct for free shear flows. The other variables included are: an invariant measure of the strain rate S , the production rate of turbulence P_k (equation (3.18)) due to viscous forces, the buoyancy production terms P_{kb} and $P_{\omega b}$ (equations (3.19a - 3.19b)) that consider the dissipation coefficient C_3 , and the equations coefficients that are found in Table 3.1. The coefficients not listed in Table 3.1 can be obtained using equation (3.20) where Φ refers to the coefficient in question.

Table 3.1: Coefficients for SST - k - omega Turbulence Model. Source: ANSYS (2016a)

Symbol	Value
β'	0.09
α_1	5/9
β_1	0.075
σ_{k1}	1.176
σ_{ω_1}	2
α_2	0.44
β_2	0.0828
σ_{k2}	1
σ_{ω_2}	1/0.856

$$\mu_t = \rho \frac{k}{\omega} \quad (3.17a)$$

$$\nu_t = \frac{\mu_t}{\rho} \quad (3.17b)$$

$$P_k = \mu_t \left(\frac{\partial U_i}{\partial x_j} + \frac{\partial U_j}{\partial x_i} \right) \frac{\partial U_i}{\partial x_j} - \frac{2}{3} \frac{\partial U_k}{\partial x_k} \left(3\mu_t \frac{\partial U_k}{\partial x_k} + \rho k \right) \quad (3.18)$$

$$P_{kb} = -\frac{\mu_t}{\rho \sigma_p} g_i \frac{\partial \rho}{\partial x_i} \quad (3.19a)$$

$$P_{\omega b} = \frac{\omega}{k} ((\alpha_3 + 1) C_3 \max(P_{kb}, 0) - P_{kb}) \quad (3.19b)$$

$$\Phi_3 = F_1 \Phi_1 + (1 - F_1) \Phi_2 \quad (3.20)$$

3.2.3 Wall Functions

Boundary Layer Theory explains how the flow behaves when encounters a solid body, stating that velocity is 0 m/s when on the surface and it changes rapidly to the maximum value in the middle of the water column (Schlichting 1979). The *law of the wall* is used to describe how the flow is influenced by viscous effects close to a surface (wall) and does not depend on free stream parameters (Versteeg et al. 2007). Equation (3.21) defines the dimensionless variables u^+ and y^+ which relate the flow velocity and distance from the wall with the density ρ , viscosity μ and the wall shear stress τ_w .

$$u^+ = \frac{U}{u_\tau} = f\left(\frac{\rho u_\tau y}{\mu}\right) = f(y^+) \quad (3.21)$$

Fluid in contact with a smooth wall, such as the fluid flowing around the turbine, can be divided in three different layers: (i) the viscous sub-layer which is the fluid in direct contact with the surface, (ii) the log law layer that refers to the turbulent region close to a smooth wall, and (iii) the outer layer far from the wall, where the inertia dominates (Versteeg et al. 2007). In order to reduce the need for a refined mesh in the whole domain a wall-function approach is used by ANSYS CFX (equations (3.22) to (3.24)), where the viscosity sublayer region is bridged to provide near-wall boundary conditions for the mean flow and turbulence transport equations. The near wall velocity is represented by u^+ , the friction velocity by u_τ , the known velocity tangent to the wall at a distance Δy by U_t , the dimensionless distance from the wall by y^+ , the wall shear stress by τ_w , the von Karman constant by κ , and the wall roughness dependant log-layer constant by C (ANSYS 2016a).

$$u^+ = \frac{U_t}{u_\tau} = \frac{1}{\kappa} \ln(y^+) + C \quad (3.22)$$

$$y^+ = \frac{\rho \Delta y u_\tau}{\mu} \quad (3.23)$$

$$u_\tau = \sqrt{\frac{\tau_w}{\rho}} \quad (3.24)$$

The inconsistencies created by the wall-function approach when having fine meshes are overcome with ANSYS CFX's *Scalable Wall Function*, which allows to perform a consistent mesh refinement independent of the Reynolds number of the application. This method limits the y^* (equation (3.25)) created for the logarithmic region where the near-wall velocity U_t approaches zero and the velocity scale u^* (equation(3.26)) is used instead of u_τ . The limitation of y^* is given by \tilde{y}^* in equation (3.27) meaning that all mesh points are outside the viscous sublayer and all fine mesh inconsistencies are avoided (ANSYS 2016a).

$$y^* = \frac{\rho \Delta y u^*}{\mu} \quad (3.25)$$

$$u^* = C_\mu^{1/4} k^{1/2} \quad (3.26)$$

$$\tilde{y}^* = \max(y^*, 11.06) \quad (3.27)$$

The SST– $k - \omega$ turbulence model offers an *Automatic Near-Wall Treatment* that blends the wall value for ω between the logarithmic and the near wall formulation, allowing a consistent y^+ insensitive mesh refinement from coarse to fine placing points inside the viscous sublayer (ANSYS 2016a). The treatment modifies the flux terms F_k and F_U , for the kinetic energy and momentum equations, respectively, as detailed below in equations (3.28) to (3.33):

$$F_U = -\rho u_\tau u^* \quad (3.28)$$

$$u^* = \sqrt[4]{\left(\sqrt{\frac{\mu}{\rho}} \left|\frac{\Delta U}{\Delta y}\right|\right)^4 + (\sqrt{a_1 k})^4} \quad (3.29)$$

$$u_\tau = \sqrt[4]{(u_\tau^{vis})^4 + (u_\tau^{log})^4} \quad (3.30)$$

$$u_\tau^{vis} = \sqrt{\frac{\mu}{\rho} \left|\frac{\Delta U}{\Delta y}\right|} \quad (3.31)$$

$$u_\tau^{log} = \frac{U}{\frac{1}{\kappa \log(y^+)} + C} \quad (3.32)$$

$$F_k = 0 \quad (3.33)$$

Equations (3.34) to (3.36) detail the blending made to avoid cyclic convergence behaviour in the ω – equation when a transition happens between the analytical expressions for ω in the logarithmic region, ω_l , and in the sublayer, ω_s .

$$\omega_l = \frac{u^*}{a_1 \kappa y} = \frac{1}{a_1 \kappa \nu} \frac{u^{*2}}{y^+} \quad (3.34)$$

$$\omega_s = \frac{6\nu}{\beta(\Delta y)^2} \quad (3.35)$$

$$\omega_\omega = \omega_s \sqrt{1 + \left(\frac{\omega_l}{\omega_s}\right)^2} \quad (3.36)$$

3.2.4 Modelling Approach

As mentioned in [Section 1.3](#), the first aim of the present research is to adapt the geometry of a well characterised tidal stream turbine rotor so to determine if it is economically feasible for it to operate in low speed conditions (1.2 m/s). CFD was used to model multiple variations of the geometry and to determine their performance characteristics. These data were obtained with ANSYS CFX solving the equations described in [Section 3.2.1](#), [Section 3.2.2](#), and [Section 3.2.3](#) for all the models analysed in this thesis.

The initial modifications to geometry were made based on the solidity variable, as detailed in [Chapter 4](#), and from those results a contra-rotating configuration was considered in [Chapter 5](#), with the purpose to analyse the feasibility of adapting a turbine to operate in low speed flows, similar to the ones found in Costa Rica.

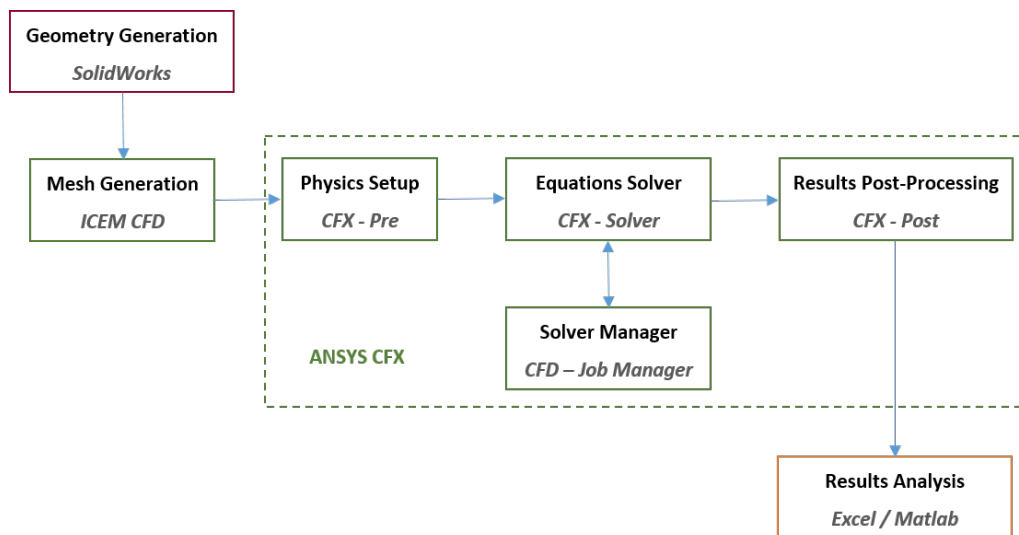


Figure 3.1: CFD Modelling Process

The method used to model and understand the turbine's variations done in this thesis is shown in [Figure 3.1](#). The geometry was created using SolidWorks, it was then exported to ANSYS ICEM CFD for meshing. Once the mesh was completed, it was imported in ANSYS CFX to create the set-up with each model's specifics, then run in the solver application, and the extracted results were analysed with Matlab and Microsoft Excel. CFD provided an approximation of the flow behaviour once the turbine was modified, located, and rotated in water without the need of experiments, reducing the cost and time of physical tests. The next sections discuss the steps followed to model the different scenarios studied in this thesis.

3.3 Geometry

The basic physical characteristics of a model are given by the geometry, which is done with a Computer-Aided Design (CAD) Software and represents the fluid that is studied. The model's geometry gets simplified depending on the computational capacity, results, and accuracy that are required for each project. Before setting up a model with the use of CFD, the theoretical characteristics must be known to determine how much simplification can be done whilst capturing the most relevant details, and to analyse the final results considering the model's limitations. Geometries used in this project were divided in two main sections: the turbine with its immediate rotating surroundings and the farfield water representing the rest of the sea water where the turbine was located.

3.3.1 Baseline Turbine Geometry

The baseline turbine used for the research was designed by Mason-Jones (2010) and has been experimentally validated by Morris (2014) and Frost (2016) when compared to CFD results. The original geometry is a three bladed 10 m diameter horizontal axis tidal stream turbine that has been characterised to operate in conditions of 6 knots (Mason-Jones 2010). The blade's original design was made by Egarr et al. (2004), and then modified by Mason-Jones (2010) to obtain the geometry used in this project. The blade uses a variant of the Wortmann FX63-137 aerofoil, which has a blade tip pitch angle of 6° , a chord length variation from 1598 mm at the root to 643 mm at the tip, and a 35° twist. In order to build the blades needed for this research it was necessary to obtain the aerofoil points, at different distances from the hub. Using SolidWorks the blade was segmented in different planes, then the curve was extracted from each of those planes and stored in separate files, which were post-processed in Matlab to obtain the chord length at each plane. To finish the original geometry, three blades were attached at 120° from each other, to the 1.8 m diameter hub. The chord details extracted for each of the planes, which are reference to create some of the turbines' blades found in Chapter 4, are included in Appendix A.1 with their respective twist and location.

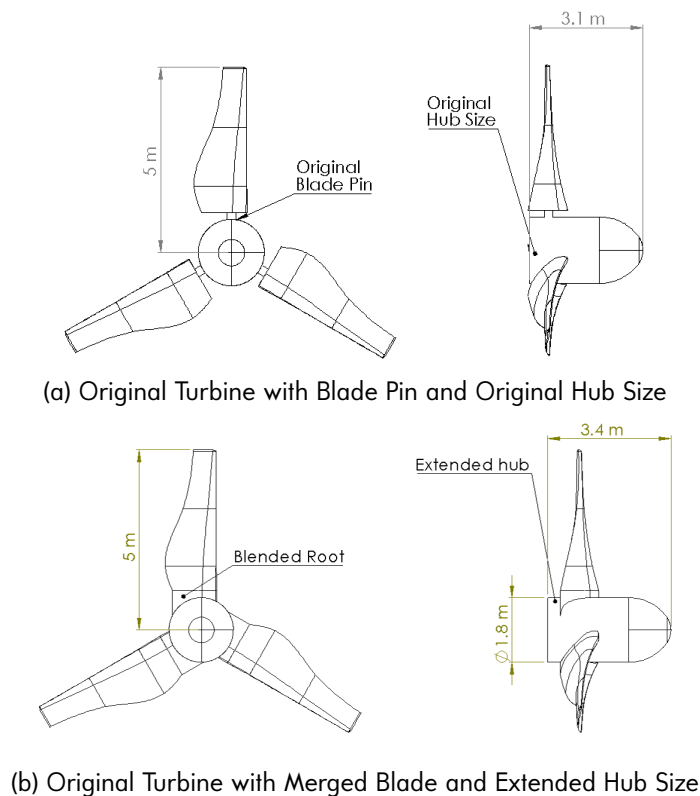


Figure 3.2: Baseline Turbine Geometry

As shown in [Figure 3.2](#) the following changes were made to the original turbine ([Figure 3.2a](#)) to create the *Baseline Geometry* ([Figure 3.2b](#)), which adapted to the scope of this project:-

- (i) The base of the blade was extruded and merged with the hub. This geometry adaptation has been validated with experimental data by Frost (2016).
- (ii) The hub size was increased by 350 mm from the back to make space for the higher pitch blade geometries analysed in the following chapters.
- (iii) The turbine's models did not include a stanchion, they are aimed to provide the rotor's performance characteristics regardless of the supporting structure used.

Once the turbine's geometry was successfully modified, it was located inside a cylinder with a radius 2 m larger than the rotor to simulate the immediate flow surrounding the device, which represents the Multiple Frame of Reference (MFR) domain as it is explained in the next section.

3.3.2 Domain Description

The CFD numerical models in this research were created to simulate the body of sea water's behaviour before and after the rotation caused by the turbine. This volume of fluid was represented by the domain, where boundary conditions and physics characteristics of the models were set. The shape and size were selected according to the conditions that needed to be represented, which in this case show similitude to Costa Rican tidal resource described in [Section 1.2.2](#), and following previous characterisation of the device in order to keep the results validated with experimental data.

Following previous research by Mason-Jones (2010), Morris (2014, and) and Frost (2016) the two geometrical domains shown in [Figure 3.3](#) were made to set up the turbine models. Their description are as follows:-

1. **Sea Domain:** Represents the tides with constant flow velocity affected only by the turbine's rotation that is located within the MFR Domain ([Figure 3.3a](#)). The MFR Domain is located within the cylinder space left in the Sea Domain box. The sea is made in a $10D \times 10D \times 40D$ rectangular prism for the initial validation studies (Sea Domain-1) (Hernandez-Madrigal et al. 2017), and then reduced to a $10D \times 10D \times 22D$ rectangular prism for the rest (Sea Domain-2) ([Figure 3.3b](#)). For the purpose of this chapter, the Sea Domain-2 is used to illustrate the meshing and set up process.

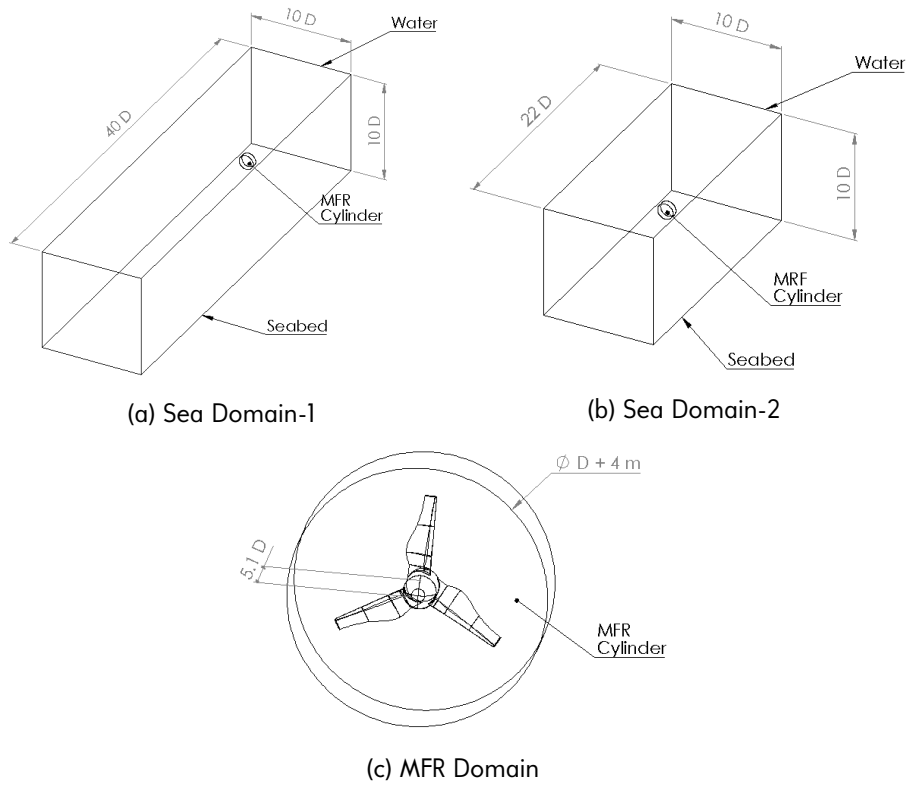


Figure 3.3: Fluid Domains Used to Model the Turbine in Sea Water

2. **MFR Domain:** The MFR is made to simulate the turbine's rotation in a small volume of fluid reducing the computational cost of having the whole sea water rotating. It represents the immediate water surrounding the turbine in a cylinder shape (Figure 3.3c), that fits exactly in the Sea Domain's cylinder space, with a radius 2 m larger than the turbine's to capture the blades' tip interaction with the fluid. This distance is kept to make sure the flow's rotational behaviour, from the interaction with the turbine, is captured within the MFR boundaries to then merge with the Sea Domain data.

These domains were created separately, then the meshes were merged and a Domain Interface was created, as explained in Section 3.5.1.3, where the fluid volumes were connected. The MFR is located 5D from the wall boundaries to avoid seabed and waves interaction with the turbine, and to obtain the performance characteristics of the rotors without any boundary interference.

3.4 Mesh

Once the turbine and domains' geometries were finished, the mesh was created with the software package ICEM CFD due to its flexibility when setting the parameters required to character-

ise the fluid that is being modelled. The mesh used in this study was made by small volumes of fluid with Tetrahedron ('tet'), Hexahedral ('hex'), and Prism shapes, illustrated in Figure 3.4, that adapted to the models' geometry. ANSYS CFX stores all the solution variables and fluid properties at the nodes (mesh vertices), creates control volumes around each of them using the medial dual, and solves the RANS and turbulence equations integrating them over each control volume (ANSYS 2016a).

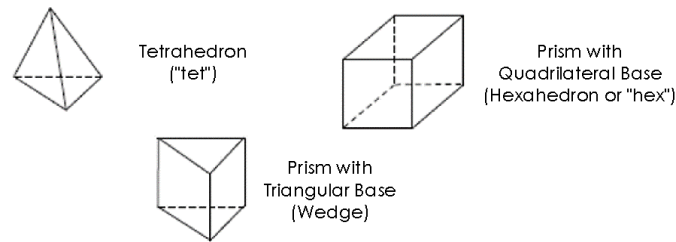


Figure 3.4: Volume Shapes Used to Create the Mesh.
Source: Adapted from Bakker et al. (2002)

The Sea Domain was meshed using Hex shape volumes and the MFR's mesh was made with Tet and Prism volumes. The surface fluid behaviour for both domains were captured with prism elements that adapt to the geometries' characteristics, and hexahedral or tetrahedral elements filling the volume in between the boundaries. The mesh details for each domain are explained next.

3.4.1 Sea Mesh

Due to the simple rectangular shape of the Sea Domain an hexahedron mesh is used to represent the farfield water. The benefits from using this method are:-

- (i) Reduces the computational cost by capturing the fluid characteristics with less elements.
- (ii) An O-grid (*O-type mesh either around a localized geometry feature or globally around an object* (ANSYS 2016b)) was created to make a mesh transition from rotating domain, MFR, to a steady one, capturing the limited wake characteristics offered by RANS, with less elements.
- (iii) The elements aligned with the main flow direction have a higher aspect ratio, allowing the mesh to adapt in the areas of interest without losing accuracy in the results.

The four main sections of the Sea Domain shown in Figure 3.5 are: (a) Domain Inflow, (b) Turbine Area, (c) Domain Outflow, and (d) Seabed Inflation. The inflow represents the water

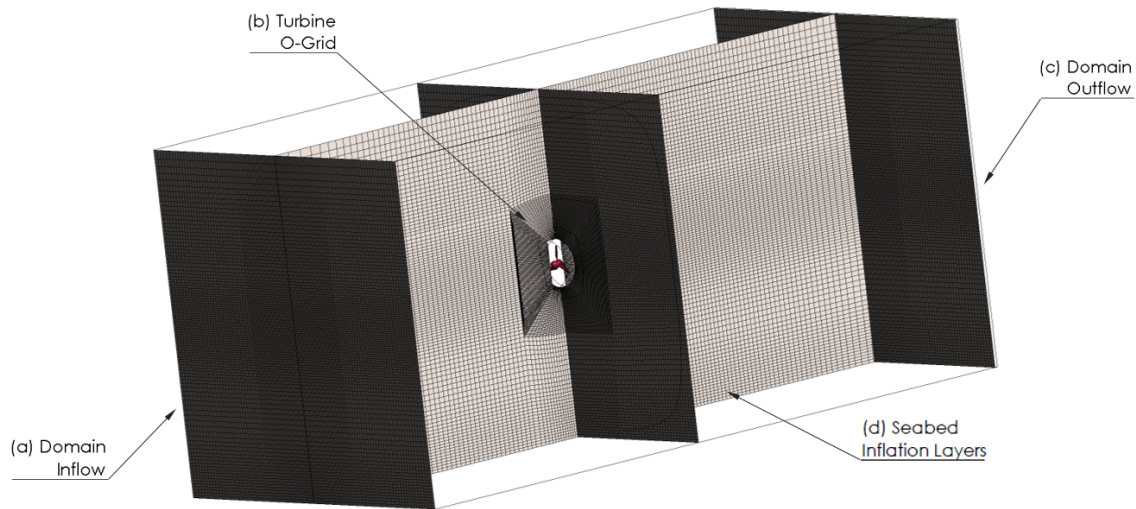


Figure 3.5: Sea Domain's Mesh

inlet to the domain and transitions from a coarse mesh aligned with the flow to the refined O-grid surrounded turbine area. After the turbine the fine O-grid and surroundings transition to the coarser water outflow, where the mesh again aligns with the fluid direction. Finally, the Sea Domain includes a surface boundary layer at the seabed, as show in [Figure 3.3](#), with inflation layers added to capture the rapid variation of the fluid characteristics, determined by the Boundary Layer Theory (Schlichting 1979).

These mesh characteristics, summarised in [Table 3.3](#) on page 59, apply for the two Sea Domains used in the thesis. The main difference between the two meshes is the domain's length so to reduce the number of elements (approximately by a third) and to improve the transition between the MFR's cylinder to the water outflow. In the contra-rotating cases, the Sea Domain-2 was modified to consider the two MFRs required for the models ([Section 5.4.1](#)).

3.4.2 MFR Mesh

The Multiple Frame of Reference enables the analysis of cases where one domain is rotating relative to another (ANSYS 2016a), just like the turbine located in the Sea Domain. To build the MFR domain a cylinder was created around the rotor leaving 2 m from the blade tip to the cylinder farfield, 0.5 m from the front of the hub to the front of the cylinder and 0.15 m from the back of the hub to the back of the cylinder. The space between the rotor and the MFR limits was left to have enough mesh elements to model the boundary layer, and capture the device's rotation.

The MFR mesh was created using a periodic symmetry approach that ensures nodes from

one boundary have identical coordinates to the corresponding nodes on the second boundary (ANSYS 2016b). The turbine and cylinder were divided in N_B (number of blades) equal portions and only one of them was kept to create the mesh. Once the mesh of that portion was completed, it was copied N_B-1 times and rotated to complete the whole circular shape with periodic walls that had matching nodes on each side of the mesh. The portion of a cylinder covered 120° , 90° , or 72° depending on whether the turbine had 3, 4, or 5 blades, respectively. For the 2 bladed rotors and 5 bladed rotors with high pitch angles the whole cylinder was modelled at once.

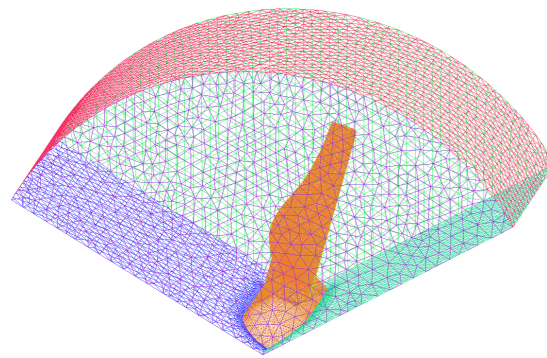
The following characteristics apply for all the rotors modelled:-

- (i) The global element size for the domain was limited to 7 cm. This value was determined as the largest element size parameter that would provide the expected CFD results from previous validated studies made by Frost (2016) and Ordonez Sanchez et al. (2016).
- (ii) The maximum element size for the volumes included in the MFR domain were set as detailed in Table 3.2.

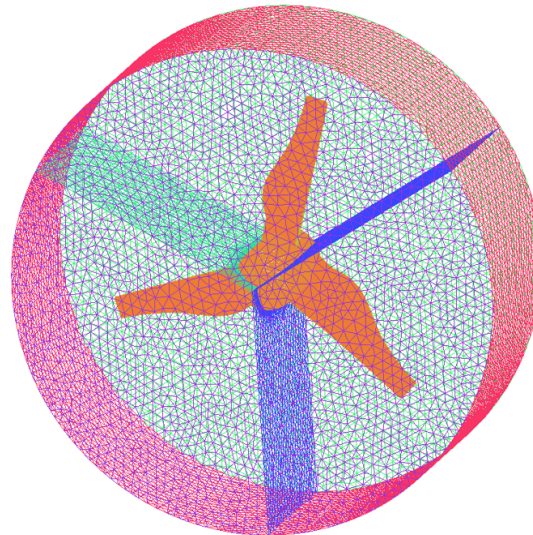
Table 3.2: MFR Maximum Surface Element Size

Part Name	Maximum Size
Blades Surface	3 cm
Hub Surface	5 cm
Farfield Surface	7 cm
MFR Volume	7 cm

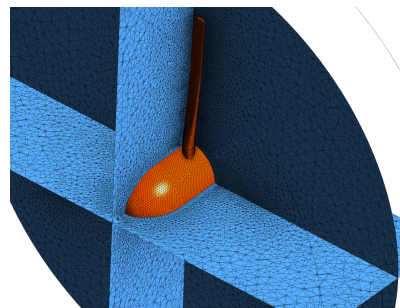
- (iii) The periodic walls were set when the geometric limitation was used to make sure the elements matched from one portion next to the other. They are set to be 'Internal Walls' and ANSYS CFX recognised them as such when the model was set up.
- (iv) To capture the boundary layer behaviour from the rotor's surface, 5 inflation layers were created with a height ratio increase of 1.1. They were made with prism elements because the fluid near a surface is aligned to the shape, and their geometry helps to capture the trailing edge and blade tip shedding.
- (v) The volume of fluid between the rotor and MFR surfaces was made with tetrahedral elements due to the geometry's complexity. The Delaunay approach was used to create a



(a) MFR's Mesh- 120°



(b) MFR's Mesh - 360°



(c) MFR's Mesh Detail - 360°

Figure 3.6: MFR Domain's Mesh

smooth transition in the volume element size (ANSYS 2016b) and density region from the turbine's surface to the MFR boundaries meshes.

The parameters mentioned above are shown in Figure 3.6, where the MFR domain shows the near 3.5 million elements mesh for the Baseline Turbine. This value changed depending on the number of blades, pitch angle, number of rotors, and rotor radius of the model simulated.

3.4.3 Quality

Once the meshes were created, a quality analysis was made to assure solver accuracy and optimise computational time (Bakker et al. 2002). For this project the metrics considered were the *Quality* and *Aspect Ratio* given by ICEM CFD, where a value of 1 is considered as high quality cells. For the specific cases of Hexa elements, the aspect ratio can go as high as 11 when the long edge of the element is parallel to the main direction of the fluid. As can be seen in [Table 3.3](#), the meshes created for this research have most of their elements in a range close to 1. The results obtained were validated with experimental data, as will be explained in [Section 3.8](#).

Table 3.3: Mesh Characteristics

Domain Name	Number of Elements	Aspect Ratio 0.6 – 1	Quality 0.8 – 1
Sea Domain-1	2,819,862	35 %	99%
Sea Domain-2	2,078,839	82 %	90%
MFR Domain	3,349,734	94 %	91%

Once the quality metrics met the required standards, the two domains' meshes were merged and exported to ANSYS CFX so that the model was prepared for solving. [Figure 3.7](#) shows how the final mesh looked once all the parts were put together. The Baseline Turbine has been used as a reference for the procedure followed with the other geometries. For the Contra-Rotating Configuration an additional Domain was created, as explained in [Section 3.5.1.3](#).

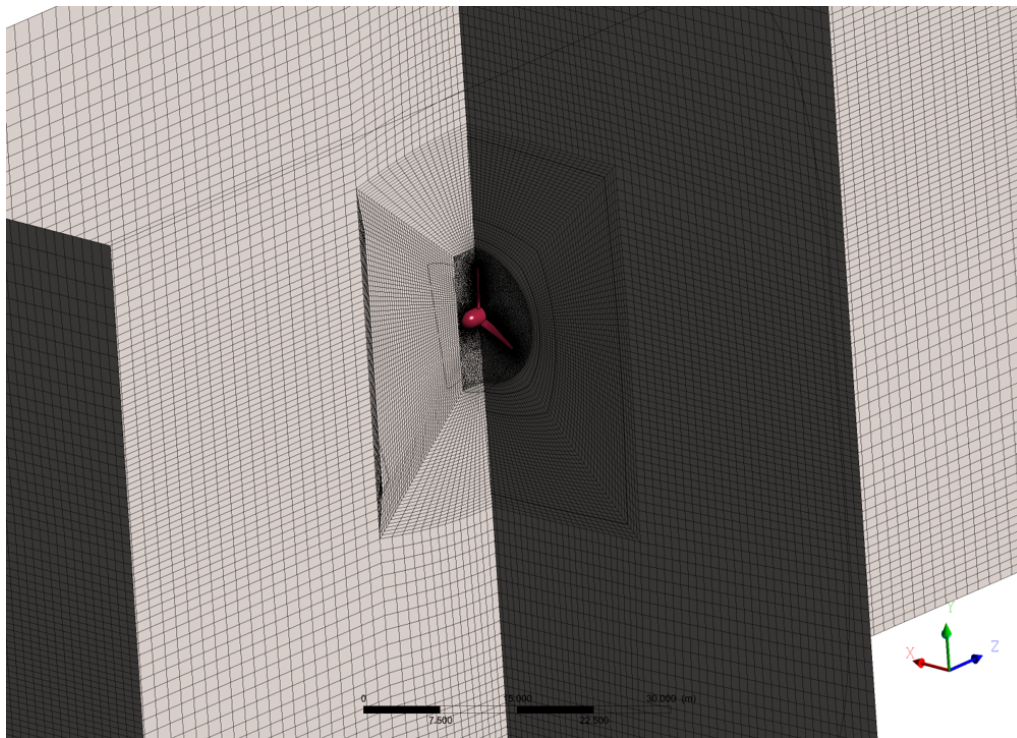


Figure 3.7: Final Mesh with Two Domains Merged

3.5 Model Set up

Using [Figure 3.1](#) as guideline, the physics set-up was made with the final mesh created for each model by importing it to CFX-Pre from ICEM-CFD. The Sea and MFR Domains were labelled to recognise their regions, and the fluid physics were attributed to each of them.

Water at 25 °C was selected to replicate the experimental data conditions from Frost (2016) and Ordonez Sanchez et al. (2016) that validate the models presented in this thesis, with a reference pressure of 0 Pa applied to the Sea and MFR Domains. The models were considered Isothermal, Non Buoyant, and with no Mesh Deformation. As explained in [Section 3.2.2](#) SST- $k-\omega$ turbulence model was used.

The Sea Domain was set up with a stationary frame of reference, whereas the MFR was defined with a rotating frame of reference around the Z axis at a constant angular velocity, and used the Alternate Rotation Model explained in [Section 3.2.1.1](#). For the Contra-Rotating models, two MFR Domains were included and each of them had rotational velocity and direction specified.

3.5.1 Boundary Conditions

Once the domains characteristics were set, the Boundary Conditions (BC) were located in the surfaces that limit their geometries. The BC provide known initial conditions to solve the RANS equations. They were set for each of the domains as detailed below.

3.5.1.1 Sea Domain's Boundary Conditions

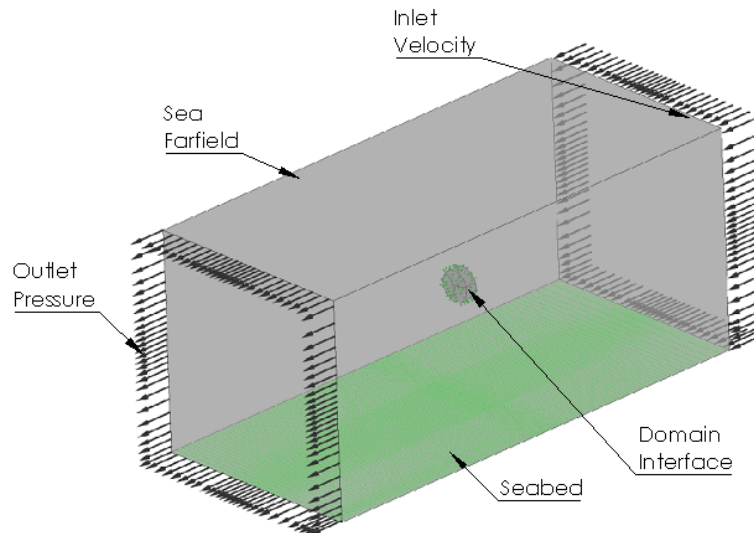


Figure 3.8: Boundary Conditions of the Sea Domain

The Sea Domains included the BC attributed to the locations that represent the seabed, water inflow and outflow, and the surrounding sea water outside the domain. The BC's specifics are shown in [Figure 3.1](#) and listed next:-

- (i) **Inlet:** The inlet condition describes a constant flow with a velocity of 1.2 m/s parallel to the negative Z-axis, as shown in [Figure 3.8](#). This value was taken as a reference from what is expected to be found in Costa Rican conditions.
- (ii) **Outlet:** The outlet parameter is set to a subsonic flow regime with a relative static pressure of 0 Pa. The final dynamic pressure depends on the fluid velocity after the simulation. The location of this BC is shown in [Figure 3.8](#).
- (iii) **Seabed:** The domain's ground floor highlighted in [Figure 3.8](#) is set as a Non-Slip Wall. The rotor's location in the Sea Domain makes this boundary's effect negligible on the turbine's performance, hence the default CFX settings are kept.

- (iv) **Farfield Sea:** The rest three surfaces in Figure 3.8 were set as Free-Slip walls to represent the water surrounding the domain, with no friction to the volume of fluid.

3.5.1.2 MFR Domain's Boundary Conditions

The rotating Multiple Frame of Reference in a cylinder had the turbine boundary condition, which is composed of the hub and blades that varied with each of the analysed geometries. The surfaces highlighted in Figure 3.9, that simulate the turbine geometry, were set as Non-Slip Smooth Walls.

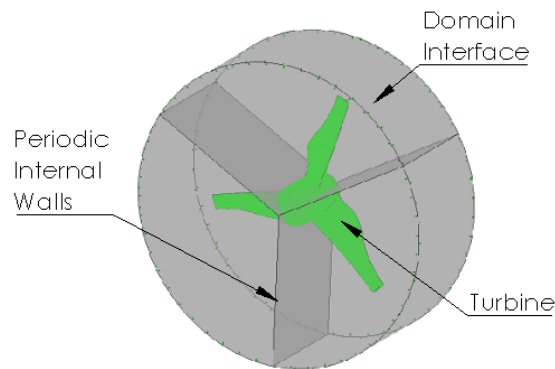


Figure 3.9: Boundary Conditions of the MFR Domain: Turbine

3.5.1.3 Domain Interfaces

The final boundary conditions needed in the model were domain interfaces, set as General Grid Interface (GGI) in ANSYS CFX. The algorithm was used to treat the fluxes between two surfaces where meshes from two different domains coincide, such as the cylinder shape in the Sea and MFR. The GGI treatment offered by the software is characterised by: (a) strict conservation maintained across the interface; (b) it is fully implicit; (c) the interface is applicable to incompressible, subsonic, transonic, supersonic flows, and all model options; (d) the interface accounts internally for pitch change by scaling the local flows; and (e) any number of GGI connections can be made in a domain (ANSYS 2016a).

The simulations run in this thesis required the use of Interface Models to account the interaction between the stationary Hexa meshed cylinder in the Sea Domain (Figure 3.8), and the rotating Tetra meshed cylinder in the MFR Domain (Figure 3.9). Another Domain Interface was also used to consider the interaction between two rotating domains in the Contra-Rotating simulations. The interface models used were *Frozen Rotor*, and *Transient Rotor-Stator*:-

- (i) **Frozen Rotor:** This parameter was used to model rotational behaviour in the steady state simulations, considering the interaction between the two frames. The frame of reference changes but the relative orientation of the interface's components is fixed (ANSYS 2016a). In the set-up, no pitch change was considered and there was no additional interface model included. All the geometry configurations were modelled using this approach for every interface included in the steady state simulations.
- (ii) **Transient Rotor-Stator:** This model simulated the transient relative motion between the components on each side of the GGI, and accounted for all the interaction effects by updating the interface position in each timestep (ANSYS 2016a). The Contra-Rotating rotors considered in Chapter 5 considered this approach for every interface included in the transient simulations, using their steady state models with Frozen Rotor interfaces as the initial values.

3.5.2 Analysis Type

To solve the RANS equations with their respective turbulence equations, ANSYS CFX has two methods: Steady, and Transient States. All the single rotor geometries created were run in Steady State to determine the basic performance coefficients for each arrangement. The Contra-Rotating Rotors were first modelled in Steady State conditions to use them as initial parameters for their Transient Simulations, where the interaction between the two rotors was monitored.

3.5.2.1 Steady State

The steady state method was used to obtain the turbines' performance coefficients because they were assumed to be settled once the device was rotating continuously after the unsteady start up and before being fully stopped. Steady state conditions were defined as those where the model's characteristics do not change with time. ANSYS CFX applied a false timestep as means of under relaxing the equations when iterating towards the final solution (ANSYS 2016a).

To set up the steady state simulations a conservative auto timescale option was selected, which calculates the time scaled based on the models' inherent characteristics: boundary and flow conditions, physics, and geometry.

3.5.2.2 Transient State

Unlike the steady state where a pseudo-time was used to solve the RANS equations; in the transient conditions, time duration and timestep values were given. For the contra-rotating simulations, where the transient models were used, the total time was set to the equivalent of 11 rotations made by the slowest blade row, each time step moved 0.05 rad, and the maximum number of iterations per time step (coefficient loops) were limited to 10. The initial time for each transient simulation was set to be automatic with value at 0 s. The final time values and models' specifics for the transient Contra-Rotating simulations are detailed in [Chapter 5](#).

3.6 Convergence

CFX-Solver was the software used to run the numerical simulations prepared with the parameters mentioned above. To determine when the results reached convergence, the residuals were monitored.

For steady state models a residual target was set to 1×10^{-20} , which was never reached because their RMS values would stabilise and stay constant at a higher value than the target (asymptotically to the x-axis) or would oscillate repeatedly around that number. Convergence was considered when the residuals showed a trend parallel to the number of iterations axis, not by reaching a set target.

For the transient models a residual target was set again to 1×10^{-20} , and the Steady State results for each model were used as the initial conditions. To determine the models' convergence, monitor points were created to keep track of the thrust and torque in the turbines' blades and hub, because they were needed to obtain the contra-rotating turbines' performance coefficients. The simulations ran for a specific number of rotations assuring that the monitor points would reach a stable value.

3.7 Post-Processing

Once the simulations converged, the results were analysed using CFD-Post. This software was used to extract the values required to determine the performance characteristics of each geometry considered, which were the torque and force (thrust) on the z-axis acting on the turbine during operation. They were both obtained using the Function Calculator provided by the soft-

ware, which calculates the parameter value over the surface in question (e.g. blade, hub, etc.). For the steady state simulations one number was given, whereas for the transient models, the data were given for each timestep. More details on how these data were post-processed can be found in [Chapter 5](#).

3.8 Model Validation

This section describes the modelling validation for the process established in this chapter. The mesh independence approach is first explained, followed by the experimental comparison.

3.8.1 Mesh Independence

In order to achieve reliable results a mesh independence study was made for each of the domains, and the final selected meshes described in [Section 3.4](#) were used to run all simulations. The mesh independence study determines what is the best mesh that can be used considering: (a) computational cost, and (b) results accuracy. The final mesh should have the least number of elements whilst keeping the results as close as possible to those obtained with experimental data.

The Sea Domain-1 mesh was selected by analysing the wake recovery for the 4 different refinements listed in [Section 3.4](#). A basic turbine mesh, shown in [Figure 3.10](#), was added to these simulations for wake velocity comparison. The wake mesh independence study was made for comparison to determine the convergence in results regardless of the number of elements added. The accuracy of the wake recovery was not considered as part of the study due to the turbulent kinetic energy (TKE) dissipation caused by the SST model and the simplicity of the turbulence input BC, which overestimates the wake extent downstream, as discussed by [Frost \(2016\)](#), [Morris \(2014\)](#) and [Mason-Jones \(2010\)](#). For the purpose of this research the data extracted from the CFD simulations was based on the turbine's near field, which provides the required information to compute a HATT's performance characteristics .

The Sea Domain-1 (C) option was selected as the final mesh for the domain, due to the computational time, number of elements, and wake results. Option (A) would provide a limited characterisation of the fluid due its coarse mesh, option (B) has less elements than (C) but it would be more computational expensive, and option (D) provides a similar wake recovery to (C) but with more than double number of elements in the mesh. Option (C)'s mesh characteristics

were selected for this research.

Table 3.4: Mesh Independence Study for Sea Domain-1

Mesh Version	Number of Elements	Simulation Time
Sea Domain-1 (A)	261 396	64 h
Sea Domain-1 (B)	1 701 400	142 h
Sea Domain-1 (C)*	2 819 862	114 h
Sea Domain-1 (D)	5 969 904	124 h

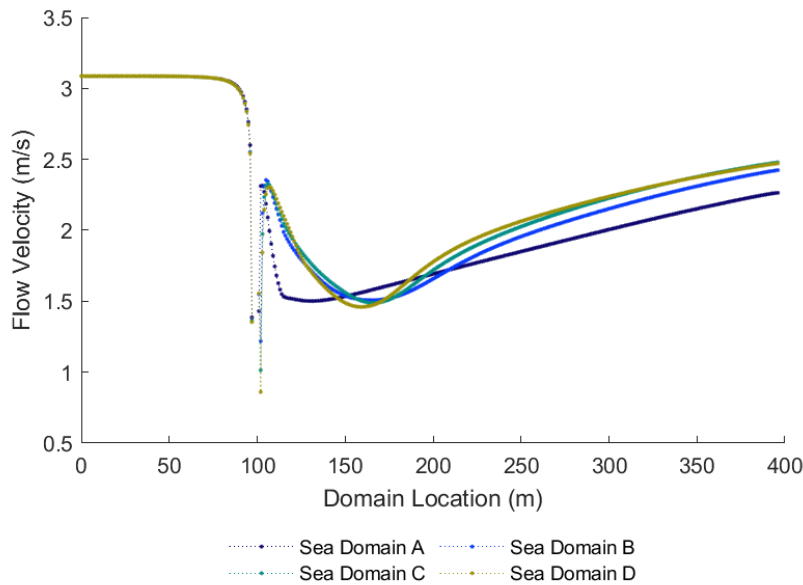


Figure 3.10: Mesh Independence Wake Recovery Study for the Sea Domain-1 Mesh

The turbine mesh was validated comparing the results to previous numerical studies, as mentioned by Hernandez-Madriral et al. (2017). The MFR mesh variations were merged to the Sea Domain-1 selected mesh and the power coefficient was calculated with the torque output, as explained in Section 2.2.1. Two mesh configurations were considered for the analysis: MFR(A) with tetrahedral elements only and a wake region for the trailing edge, and MFR(B) with tetrahedral and prism elements that diffused from turbine surface to the farfield.

From the results obtained for each of the options listed in Table 3.5, MFR (B) was selected for the models. The results provided by the tets+prism mesh differed by 5% from the results given by Frost et al. (2017), attributed to the MFR Domain (B) mesh refinement and the lack of stanchion effects in the fluid. The results provided by the MFR Domain (A) mesh differed

by 12%, thus the tetrahedral with prisms approach was selected as the optimum. Both cases were modelled at the peak design conditions: 3.086 m/s (6 knots) inlet velocity with a rotational speed of 2.25 rad/s [$\lambda=3.65$].

Table 3.5: Mesh Independence Study for MFR Domain

Mesh Version	Number of Elements	Simulation Time	Power Coefficient
MFR Domain (A)	1,044,783	115 h	0.38
MFR Domain (B)*	3,349,734	96 h	0.45

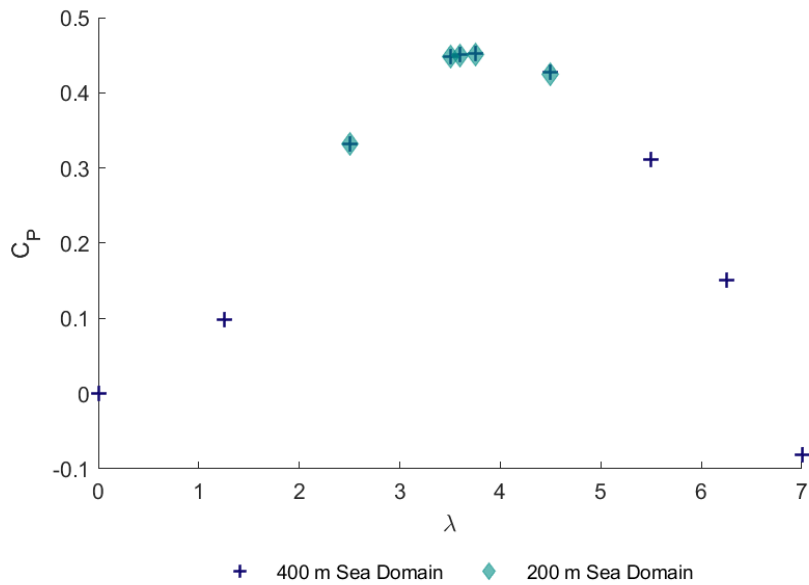


Figure 3.11: Sea Domain-2 Mesh Validation

The Sea Domain-2 mesh was an adaptation of the Sea Domain-1's to a smaller geometry, which was done to reduce the computational time by having less elements. To validate the Sea Domain-2 mesh the original baseline geometry was modelled at different tip speed ratios, and it was compared to the results acquired with the Sea Domain-1. The power curve characterising CMERG's turbine was virtually the same in both circumstances for peak operation points, as shown in Figure 3.11. With a variation of less than 1% between results, this mesh was considered validated for the simulations where it was used.

3.8.2 Y^+ plus

Based on the wall-function approach explained in [Section 3.2.3](#), the dimensionless distance from the wall y^+ is limited by the Reynolds number of the model (ANSYS 2016a). For the turbine studied in this project the y^+ varied from ~ 11 to ~ 1300 : the highest values were found at the hub behind the blade root; the front of the hub and middle of the blade have values between 200 and 500, and the blade's tip and root show a y^+ of ~ 700 . Following previous research by Frost (2016), these results were considered acceptable.

3.8.3 Mesh Validation

Mason-Jones et al. (2012) proved that a full size HATT, like the rotors modelled with CFD in this thesis, can be characterised with reduced sized devices in experimental conditions as long as they are Reynolds independent. To make sure that the results obtained from the simulations were accurate, a validation was done comparing the numerical results with the experimental data from Frost (2016) and Ordonez Sanchez et al. (2016). Ordonez Sanchez et al. (2016) fixed the 1 m scaled CMERG turbine to a motor and towed it at 1 m/s in *INSEAN Marine Technology Research Institute's* tow tank to obtain the device's performance coefficients. To compute the power coefficient (C_p) they calculated the turbine's torque based on the current required by the motor to hold and drive the rotor at each tested rotational velocity.

The original baseline geometry's C_p obtained from the experimental data and from the proposed CFD model are shown in [Figure 3.12](#) for comparison. The CFD model overestimated the power coefficient values with a difference of 7% at the peak of the model's C_p - λ curve. Given that the current model did not account for the supporting structure used during the experiments, with these results the mesh was considered accurate for the purpose of this research.

The results from the mesh independence analysis in conjunction with the experimental data comparison validated the modelling approach used for the geometries analysed in the following chapters. In [Chapter 4](#) a solidity analysis is made for single rotor turbines, and in [Chapter 5](#) contra-rotating rotor devices are compared. All of the geometries were created with the intention to determine their technical feasibility when operating in a test site with low speed flow conditions.

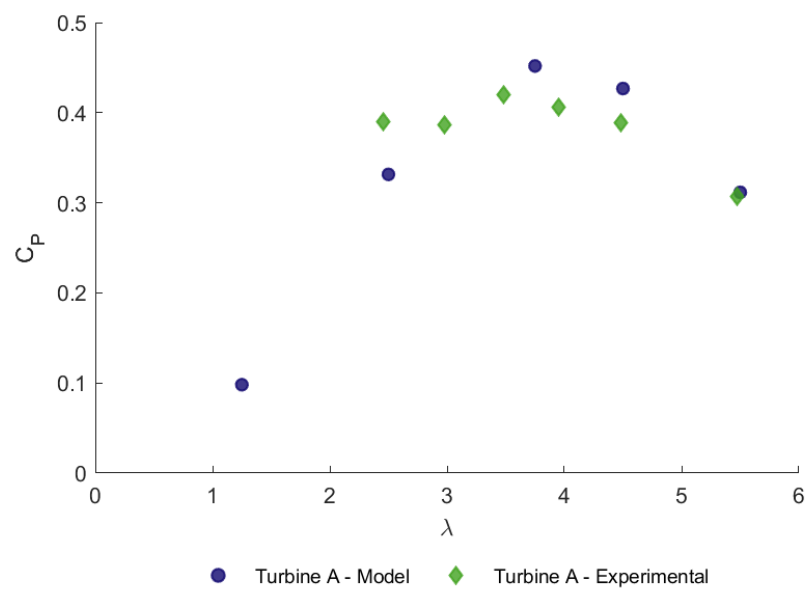


Figure 3.12: Numerical Models' Mesh Validation with Experimental Results.
Source: Adapted from Hernandez-Madrigal et al. (2017)

Chapter 4

Single Rotor Turbine Optimisation

The Single Rotor Turbine (SRT), designed by CMERG, was modified using solidity as a variable geometry parameter. The device was modelled using ANSYS CFX to simulate tidal conditions with constant inflow velocity of 1.2 m/s, such as the ones expected in Costa Rica detailed in [Chapter 1](#).

All the simulations shown in this chapter were run to find the optimum configuration of a SRT when operating in low speed conditions, based on power output, since a variation from the optimum solidity could cause a significant efficiency drop (Fraenkel 2014). The geometry variations were made taking into account that a larger solidity absorbs more fluid power until it becomes extremely large to produce substantial drag (P. Liu et al. 2012).

This chapter provides the solidity background, theory, and results of the numerical study for the SRT optimisation. A tool is proposed in [Section 4.5](#) to predict the turbines' performance based on the results from the solidity study.

4.1 Solidity Background

Solidity describes the fraction of a turbine's swept area that is solid, it is dependant upon number of blades and their width (Hardisty 2009). The wind energy sector has widely used solidity as a rotor design parameter, and as the physics are the same, their studies are used as reference on how solidity can also be applied to Horizontal Axis Tidal Turbines' design.

Rotor Solidity is defined by (Hau et al. 2006) as the total blade planform area covered in the rotor swept area, where 'planform' vaguely limits the blade surface that should be considered. Manwell (2009) introduces the local solidity definition in the Blade Element Momentum Theory (BEMT) for wind rotor design, and the optimum blade rotor solidity calculation is proposed relating the blade's chord length to the tip speed ratio λ . An extended distinction between chord and blade solidity is made by Burton et al. (2011) when explaining the Rotor Blade Theory (BEMT). Local chord solidity is used to create the optimal blade design (ignoring drag and tip loss)

at variable speed conditions and maintain the maximum power coefficient regardless of wind speed; whereas blade solidity is the primary characteristic in determining rotor performance with local blade solidity being the parameter that mostly affects stall delay.

As explained in Section 2.2.1, a device's power output is not dependant on the number of blades. However, they influence the turbine's power coefficient and the rotational velocity range of operation (Hau et al. 2006). Burton et al. (2011) describes how torque and thrust coefficients increase with solidity in the operational tip speed ratio range, and the effect of solidity on power extraction when varying the number of blades (Figure 4.1). When there is low solidity the maximum C_p is lower due to high drag losses, but the C_p does not vary much over a wider tip speed ratio range. Rotors with high tip speed ratio need technologically complex and expensive rotor blades (Burton et al. 2011). In contrast, when there is a high solidity the turbine's power is very sensitive to tip speed ratio changes (Burton et al. 2011).

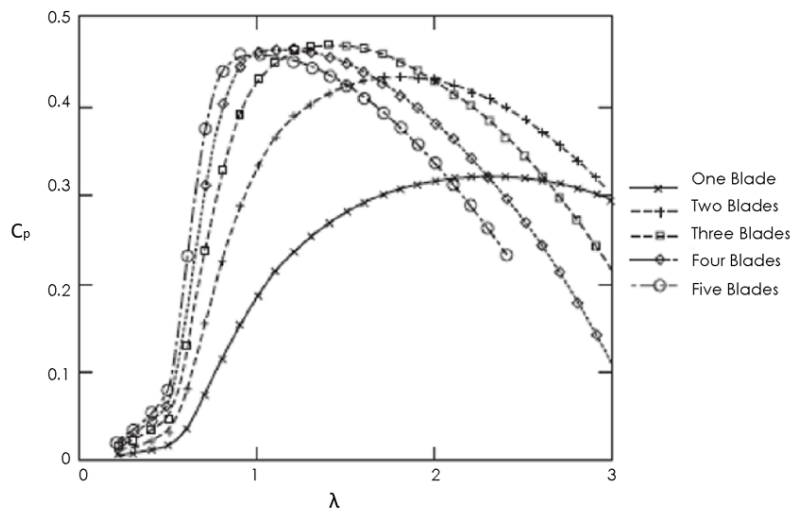


Figure 4.1: Effect of Changing Solidity in Wind Turbines.
Source: Adapted from Burton et al. (2011)

The magnitude by which the number of blades affect the power output is small compared to the blade's pitch angle variation. Positive pitch angle changes from the optimum design decrease the angle of incidence, whereas negative changes has the opposite effect and may cause stalling. The configuration for various operation conditions must include adjustments of the rotational speed (Burton et al. 2011).

The wind energy sector has used solidity as a design parameter for various turbines' configurations. Eriksson et al. (2008) showed how solidity is defined for vertical and horizontal axis turbines, then compared three different design concepts: (a) HAWT, (b) Darrieus VAWT, and

(c) H-rotor VAWT. Eriksson et al. (2008) proved that blades of a VAWT are not necessarily much larger than those of a HAWT, and provided typical turbine solidity values ranging from 13% to 30% in VAWT, and from 5% to 7% in HAWT.

The rotor performance of HAWT when solidity and number of blades vary was analysed by Duquette et al. (2003) using BEMT and Wake Theory, which provided an aerodynamic reference of how the C_p - λ behave with geometry variations. Experimental results of a constant chord, untwisted blade, fixed pitch angle rotor contradicted theoretical predictions by showing that an increase of blade number, whilst keeping solidity constant, would not increase power output but confirmed that when solidity was higher, so was the C_p (Duquette et al. 2003). Duquette et al. (2003) also determined how the blade's pitch angle increment would decrease the tip speed ratio operation range and increase the maximum power output.

Even though HAWT are commercially more successful than vertical axis wind turbines (Jamieson 2011), solidity's influence in VAWT has been widely studied. Mohamed (2013) analysed a H-Darrieus VAWT using CFD with experimental validation, and determined that its self-starting capability increased with solidity, which could be used to enhance a VAWT's initial design (Eboibi et al. 2016). Experimental investigation by Eboibi et al. (2016) compared how the variation in chord length of a VAWT's blades affects the power coefficient of a turbine at different tip speed ratios λ whilst keeping the same Reynolds Number. It was found that higher solidity produces steeper C_p - λ curves and overall C_p values, probably related to earlier start of dynamic stall in the lower solidity VAWT. Rezaeiha et al. (2017) determined that the stall and power performance variations of a low solidity VAWT could be reduced finding an optimum fixed pitch angle, or no pitch angle in some cases.

4.1.1 Solidity in the Tidal Energy Sector

Tidal stream technology has also considered solidity as a design parameter to propose vertical and horizontal axis rotor configurations. Shiono et al. (2000) made a solidity analysis of a Darrieus water turbine operating in tidal flows, which showed that when the solidity decreased (with constant number of blades) so did the power output, and the turbine's efficiency peaked at larger tip speed ratios. Shiono et al. (2000) also determined that as more blades were added (with constant solidity) the torque and efficiency would drop. Similarly, Hyun et al. (2012) found that a Darrieus rotor's efficiency would decrease with a higher solidity, but the power coefficient had less fluctuations during each rotation than those with lower solidity values. When

analysing the two-dimensional Darrieus cross-flow turbine's performance, Consul et al. (2009) found that higher solidity configurations at low tip speed ratios can increase the power output by decreasing the angle of attack, whereas at high tip speed ratios this variation would cause the opposite.

Horizontal axis tidal turbines (HATT), such as CMERG's design, are the most developed configuration for tidal stream energy extraction (Fraenkel 2014). Various geometries and configurations have been proposed in search of commercially competitive rotors, and solidity is one of the parameters that developers and researchers have considered when designing HATT. P. Liu et al. (2012) determined that the highest power output was obtained with an optimum rotor solidity value, when this changed the turbine's efficiency decreased. P. Liu et al. (2012) introduced the pitch ratio ($pitch/Diameter$) term as a turbine's performance parameter when numerically optimising a bi-directional rotor design, and further experimental results showed that as the ratio increases, whilst keeping constant solidity, so does the power coefficient (P. Liu et al. 2014). The *pitch* term used by P. Liu et al. (2014, 2012) refers to the hydrodynamics propeller definition: the distance that a propeller theoretically (i.e. without slip) advances during one revolution (Wärtsilä 2019).

Other applications of solidity in HATT include using the parameter to model the blockage ratio in long tidal fences (Schluntz et al. 2015), where it was determined that rotors in high local blockage flows require greater solidity and lower blade twist to achieve maximum efficiency, contrary to rotors operating in unblocked flow. The HATT CMERG rotor analysed in this research was modelled by Morris (2014) in configurations with 2, 3, and 4 blades operating in flow conditions of 6 knott. The numerical simulations were made to confirm the optimum pitch angle for each configuration (Morris 2014), and to understand the solidity effects in the wake (Morris et al. 2016b). The performance characteristics of the device were also analysed (Morris et al. 2015). The power output increased with the number of blades, as expected, and the loading in each blade increased when the solidity was reduced. The blade deflection and its effect on rotor's performance for each solidity case were detailed by Morris et al. (2016a).

This thesis extends initial studies made with solidity variations of CMERG's geometry operating in low speed conditions (Hernandez-Madrigal et al. 2017). The next section provides the theory used in the research.

4.2 Rotor Geometry Theory

To optimise the CMERG's turbine solidity was used as the main driving parameter, and to modify the geometry some basic aerodynamic terms related to solidity were considered. They are listed below and shown in the aerofoil shape from Figure 4.2:-

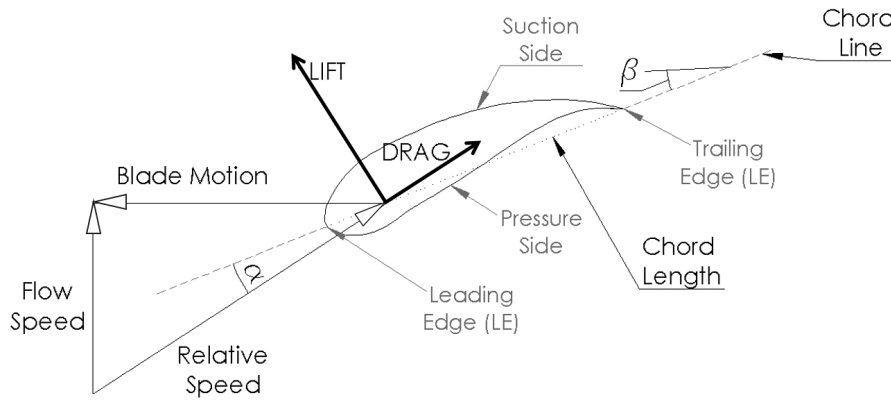


Figure 4.2: Aerofoil Diagram. Source: Adapted from Greaves et al. (2018)

- (i) **Chord Length, c** : Distance along the chord line which goes from the aerofoil's leading edge to the trailing edge.
- (ii) **Drag Coefficient, C_D** : Relates the drag F_D (aerodynamic force component acting in the same direction as the undisturbed stream motion) to the dynamic pressure of the free-stream incompressible flow (Houghton et al. 2003). Equation (4.1) considers the tidal stream velocity u and the aerofoil area A .

$$C_D = \frac{F_D}{\frac{1}{2}\rho u^2 A} \quad (4.1)$$

- (iii) **Lift Coefficient, C_L** : Relates the lift F_L (aerodynamic force component acting in perpendicular direction to the undisturbed stream motion), in equation (4.2), to the dynamic pressure of the free-stream incompressible flow (Houghton et al. 2003).

$$C_L = \frac{F_L}{\frac{1}{2}\rho u^2 A} \quad (4.2)$$

- (iv) **Pitch Angle, β** : Angle measured between the chord line and the plane of rotation (Burton et al. 2011).

- (v) **Angle of Attack, α** : Angle measured between the chord line and the relative flow direction (Burton et al. 2011).

4.2.1 Solidity Definition

As mentioned above, solidity is the ratio of the planform area of the blades to the swept area of a turbine (Manwell 2009). The rotor (blade) solidity σ_R can be obtained with equation (4.3), using the radius dependant chord length $c(r)$. The local (chord) solidity σ_r (equation (4.4)) is integrated over the blade span from the hub radius r_h to the turbine radius R , where N_B refers to the number of blades (Jamieson 2011).

$$\sigma_R = \frac{N_B}{\pi R^2} \int_{r_h}^R c(r) dr \quad (4.3)$$

$$\sigma_r = \frac{N_B c(r)}{2\pi r} \quad (4.4)$$

Other method to characterise a rotor is using the average (blade) solidity σ assuming the blade is modelled as a set of N blade sections with equal span and c_i representing the chord length at each of those sections (Manwell 2009). For the scope of this research, the rotor solidity of the horizontal axis tidal stream turbines was measured using equation (4.5) proposed by Eriksson et al. (2008), where c is the average blade chord length given by equation (4.6).

$$\sigma = \frac{N_B c}{\pi R} \quad (4.5)$$

$$c = \frac{1}{N} \sum_{i=1}^N c_i \quad (4.6)$$

4.2.2 Lift Coefficient and Solidity

The chord solidity σ_r defined in equation (4.4) can also be expressed as equation (4.7) where the total blade chord length at a given radius $c(r)$ is divided by the circumference at that ratio, with μ as the non-dimensional radial position (equation (4.8)) (Burton et al. 2011).

$$\sigma_r = \frac{N_B c(r)}{2\pi \mu R} \quad (4.7)$$

$$\mu = \frac{r}{R} \quad (4.8)$$

For the purpose of this thesis a turbine's optimum operation is defined as the condition where the maximum power coefficient is obtained for a specific configuration which, as detailed in [Section 2.2.1](#), is achieved when $a = \frac{1}{3}$. This can be described for each blade geometry with equation (4.9) that relates σ_r and C_L with $a = \frac{1}{3}$, and the local speed ratio $\lambda\mu$ (speed ratio where $\mu = 1$). The pitch angle β can then also be obtained using equations (4.10) and (4.11), where θ is the angle between the relative velocity and the rotation plane, the inflow angle (Burton et al. 2011).

$$\sigma_r \lambda C_L = \frac{\frac{8}{9}}{\sqrt{\left[1 - \frac{1}{3}\right]^2 + \lambda^2 \mu^2 \left[1 + \frac{2}{9\lambda^2 \mu^2}\right]^2}} \quad (4.9)$$

$$\beta = \theta - \alpha \quad (4.10)$$

$$\tan \theta = \left[\frac{1 - \frac{1}{3}}{\lambda \mu \left(1 + \frac{2}{9\lambda^2 \mu^2}\right)} \right] \quad (4.11)$$

4.3 Geometry Variations

To find the optimum geometry of CMERG's turbine when operating at low velocity conditions, the variables defining solidity involved in equation (4.5) were used as modification parameters. The CFD models were all run using a constant 5 m radius rotor, and the turbines were analysed using the non-dimensional performance (power, torque, and thrust) coefficients. The modifications made were based on constant chord length, constant number of blades, and constant solidity. The initial constant values were taken from CMERG's original well characterised turbine (baseline geometry), described in [Section 3.3.1](#) and shown in [Figure 3.2b](#).

4.3.1 Solidity Cases

The SRT geometries analysed in this chapter are listed in [Table 4.1](#). The changes made to the baseline geometry were done considering the variables in equations (4.5) and (4.6), and were divided in the three cases: (i) constant chord length, (ii) constant solidity, and (iii) constant number of blades. The *constant* reference values which were taken from the original geometry,

Table 4.1: Single Rotor Turbine Variations Cases

Reference Variable	Turbine Label	Solidity σ	Blades N_B	Chord c	Pitch Angle β	Blade Label
Geometry	A	21%	3	1.107 m	6°	A
(i) <u>Chord</u>	B	14%	2	1.107 m	2°, 3°, 4°, 5°, 6°, 7°	A
	C	28%	4	1.107 m	9°, 9.2°, 10°, 11°, 14°, 18°	A
	D	35%	5	1.107 m	10°, 11°, 12°, 13°, 14°, 16°	A
(ii) <u>Solidity</u>	b	21%	2	1.661 m	2°, 3°, 4°, 6°, 7°	b
	c	21%	4	0.830 m	5°, 6°, 8°, 9°, 10°, 11°, 12°	c
	d	21%	5	0.664 m	5°, 6°, 8°, 9°, 10°, 11°, 12°, 13°, 14°	d
(iii) <u>Blades</u>	A _b	32%	3	1.661 m	7°, 8°, 9°, 10°, 11°	b
	A _c	16%	3	0.830 m	3°, 4°, 5°, 6°	c
	A _d	13%	3	0.664 m	2°, 2.5°, 3°, 4°, 5°	d

Turbine A, are detailed in the first line of [Table 4.1](#). These parameters are also specified with bold text for the new rotors where they were used. Variations made to the baseline rotor were done by changing the blades (number, shape, and position), the hub was only modified in length so that the new blades' roots could be extended and merged with it, as explained in [Section 3.3.1](#).

The different rotors geometries were modelled to find their maximum power configuration, following the procedure explained in [Section 3.2.4](#). The pitch angles listed in [Table 4.1](#) were modelled to find the maximum power coefficient for each turbine, determining its optimum setting. The optimum pitch angles for Turbine B and Turbine C were previously studied by Morris (2014), hence the angles analysed in this thesis were selected to validate those results. For Turbine C's configuration, Morris (2014) found that a 0.2° increment over 9° reduced the thrust loads whilst increasing the power output. This research aims to confirm the results for low velocity conditions, validating the Reynolds independence study made by Mason-Jones (2010) for the same geometry.

Details on the geometry specifics for all cases listed in [Table 4.1](#) are given next.

4.3.1.1 Case (i): Constant Blade Chord Length Rotors

The first case consisted in modifying the original geometry by changing the number of blades N_B but keeping constant chord lengths c_i . The blade used to create Case (i)'s rotors was Blade A ([Figure 4.3](#)), taken from the original baseline geometry and has an average chord

length $c_A = 1.107$ m. The pitch angle distribution along the blade is shown in Figure 4.4, and the full geometry details can be found in Appendix A.

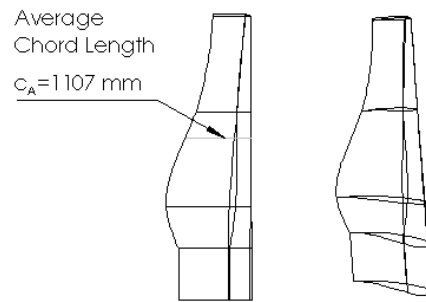


Figure 4.3: Blade A Geometry

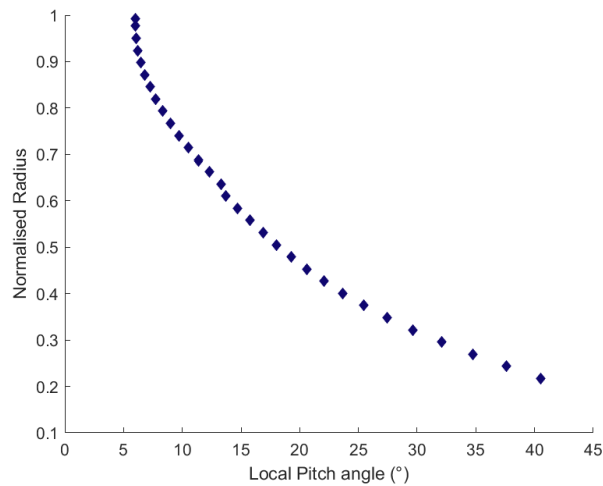


Figure 4.4: Blade A's Pitch Angle Distribution

This case's geometries are labelled *Turbine B*, *Turbine C*, and *Turbine D*. They have solidity values of 14 %, 28%, and 35%, that depend on blade number: 2, 4, or 5, respectively. Figure 4.5 presents the rotors as they were modelled in ANSYS CFX and equations (4.12a - 4.12c) summarise the parameters used to create them: different number of blades, hence different solidity.

$$c_B = c_C = c_D = c_A = 1.107 \text{ m} \quad (4.12a)$$

$$N_{B,A} = 2 ; N_{B,C} = 4 ; N_{B,D} = 5 \quad (4.12b)$$

$$\sigma_B = 14\% ; \sigma_C = 28\% ; \sigma_D = 35\% \quad (4.12c)$$

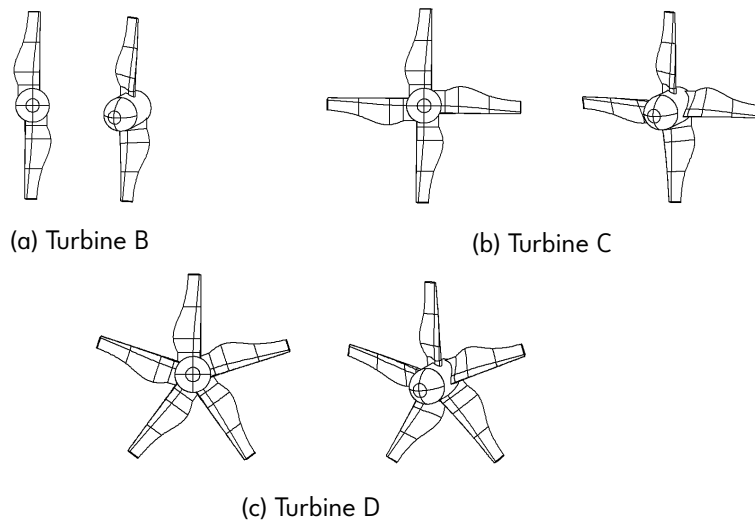


Figure 4.5: Case (i) Single Rotor Turbine Geometries

4.3.1.2 Case (ii): Constant Solidity Rotors

Case (ii) consists of three turbines with equal solidity as Turbine A: *Turbine b* with 2 blades, *Turbine c* with 4 blades, and *Turbine d* with 5 blades. Each configuration has a different blade that was made by modifying the chord lengths taken from Blade A at 32 different radial planes (Figure 4.6). Using Blade A as reference, the new aerofoils at each plane were created extracting the pressure and suction sides' curves, and normalising their shape by the respective $c_{A,i}$ found in Table A.1 of Appendix A.

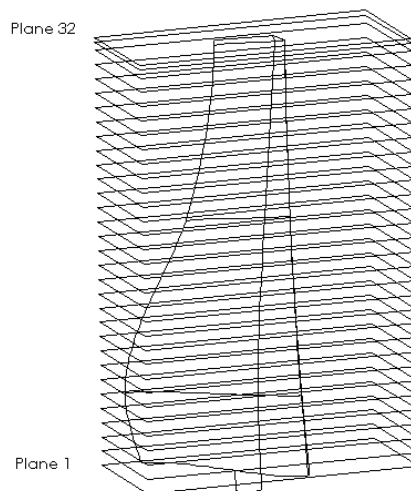


Figure 4.6: Blade A - Chord Length Measurement Planes

The new blades created, and shown in Figure 4.7, were labelled as the turbine that uses them: *Blade b*, *Blade c*, and *Blade d*, corresponding to Turbine b, Turbine c, and Turbine d respectively. To replicate the blade shape, but with different chord lengths, the non-dimensional

aerofoil curves were scaled with the modified chord length obtained for each specific blade.

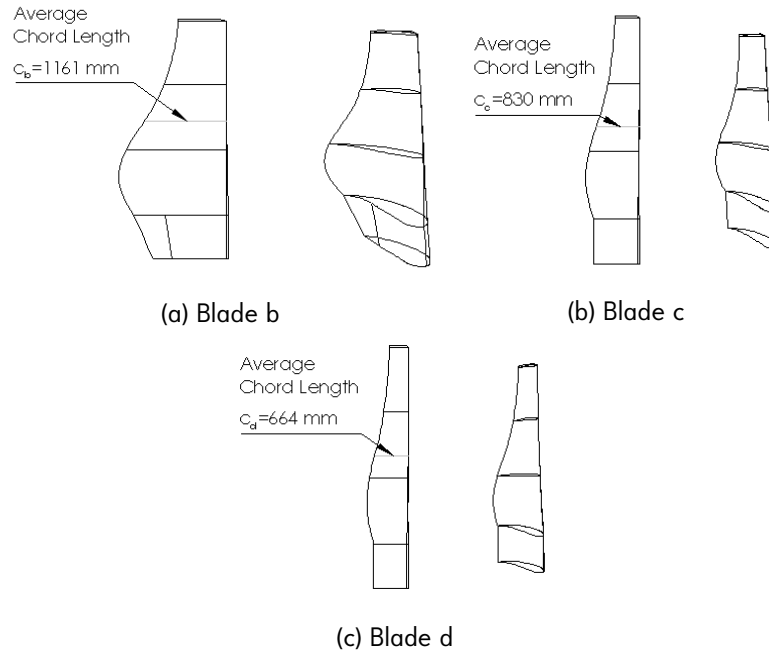


Figure 4.7: Case (ii) Single Rotor Turbine Blades

For guidance, equations (4.13a - 4.13c) explain how the new chord length was calculated for blade b. The solidities from Turbine A and Turbine b were equalled to obtain the ratio between number of blades and blade A's chord length shown in equation (4.13c).

$$\sigma_b = \sigma_A \quad (4.13a)$$

$$\frac{N_{B,b} c_{b,i}}{\pi R} = \frac{N_{B,A} c_{A,i}}{\pi R} \quad (4.13b)$$

$$c_{b,i} = \frac{N_{B,A} c_{A,i}}{N_{B,b}} \quad (4.13c)$$

The same approach was followed for blade c and blade d. The modified chord length expressions (equations (4.14a - 4.14d)) were then used to create the modified aerofoils that gave shape to blades b, c, and d. Once they were completed, the rotors were created using different number of blades, and different average chord length values, as shown in equation (4.14).

$$\sigma_b = \sigma_c = \sigma_d = \sigma_A = 21\% \quad (4.14a)$$

$$N_{B,b} = 2 ; N_{B,c} = 4 ; N_{B,d} = 5 \quad (4.14b)$$

$$c_{b,i} = \frac{3c_{A,i}}{2} ; c_{c,i} = \frac{3c_{A,i}}{4} ; c_{d,i} = \frac{3c_{A,i}}{5} \quad (4.14c)$$

$$c_b = \frac{3c_A}{2} = 1.661 \text{ m} ; c_c = \frac{3c_A}{4} = 0.830 \text{ m} ; c_d = \frac{3c_A}{5} = 0.664 \text{ m} \quad (4.14d)$$

The final geometry for turbines b, c, and d is shown in Figure 4.8. Due to the hub's geometry constraints, when merging the blade to the hub, Turbine b's blade root is extruded following the blade's trailing edge line instead of a straight line parallel to the pin.

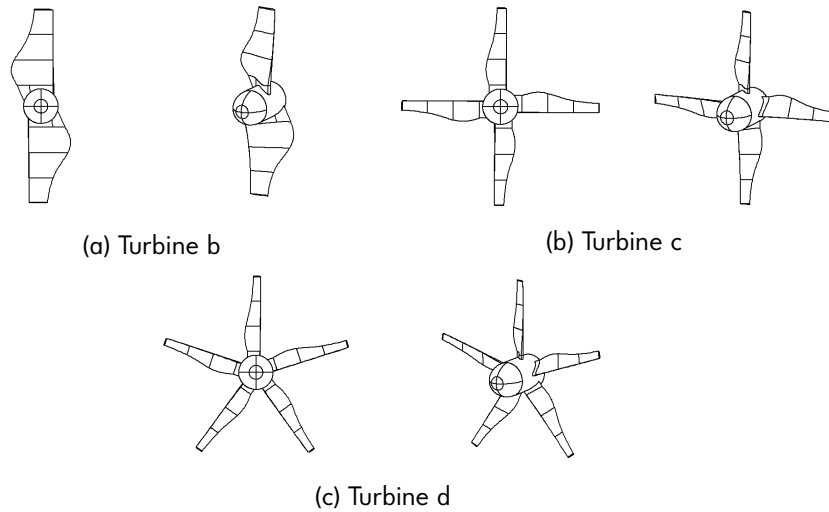


Figure 4.8: Case (ii) Single Rotor Turbine Geometries

A direct comparison of the blades' chord length is shown in Figure 4.9, whereas the chord length ratio calculation steps, and chord length details for each of the blades' aerofoils can be found in Appendix A.

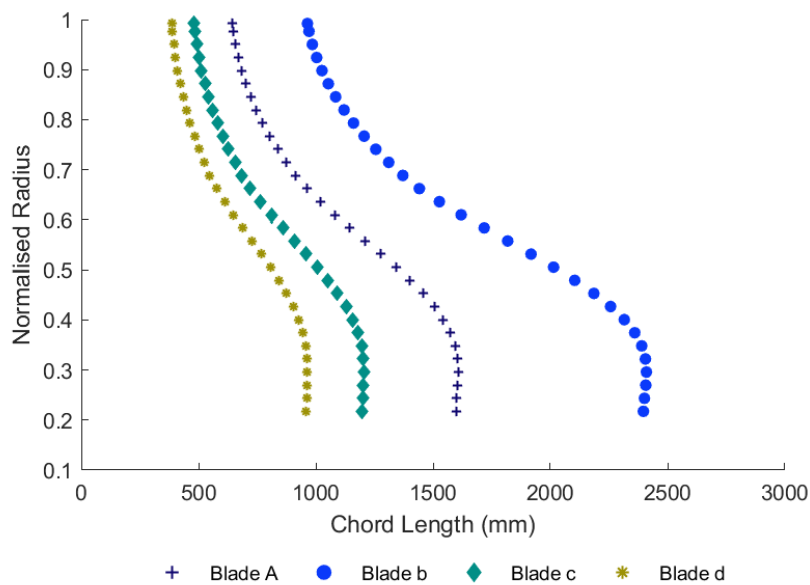


Figure 4.9: Blades' Chord Length Distribution

4.3.1.3 Case (iii): Constant Number of Blades Rotors

The last case consists of three rotors with constant number of blades: Turbine A_b , Turbine A_c , and Turbine A_d . The subscripts refer to the blade from Case (ii) that was used to create each three bladed rotor (Figure 4.7). Equations (4.15a - 4.15c) show the parameters that describe these turbines geometries, where a constant number of blades causes different solidities that change depending on the average chord length. The rotors modelled in Case (iii) are shown in Figure 4.10.

$$N_{B,A_b} = N_{B,A_c} = N_{B,A_d} = N_{B,A} = 3 \quad (4.15a)$$

$$c_{A_b} = 1.661 \text{ m} ; c_{A_c} = 0.830 \text{ m} ; c_{A_d} = 0.664 \text{ m} \quad (4.15b)$$

$$\sigma_{A_b} = 32\% ; \sigma_{A_c} = 16\% ; \sigma_{A_d} = 13\% \quad (4.15c)$$

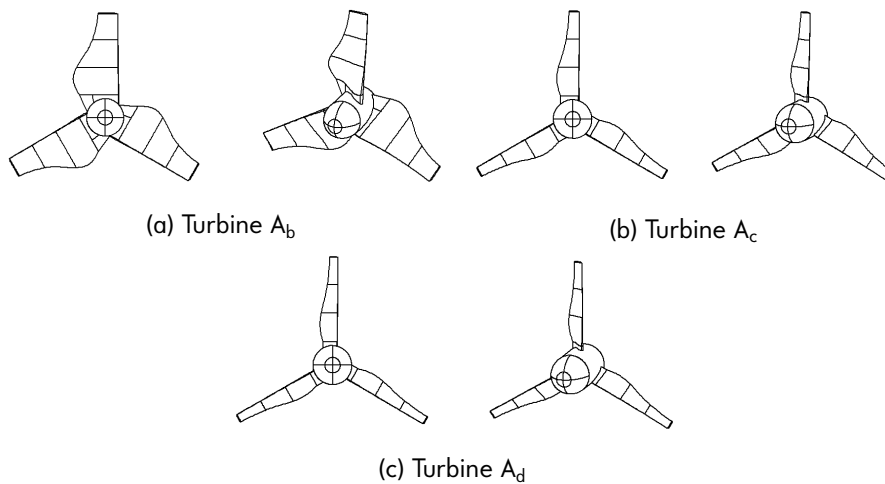


Figure 4.10: Case (iii) Single Rotor Turbine Geometries

4.3.2 Set-up

The models set-up were made following the procedure for steady state analysis shown in Section 3.5.

The turbines from Case (i) were run using the 400 m sea domain, and to reduce computational time, all the others were run using the 220 m sea domain. The MFRs mesh were done using the periodic setting, similar to the one shown in Figure 3.6a, but with different angles, depending on the number of blades: 120° for the three bladed rotors, 90° for the 4 bladed rotors, and 72° for some of the 5 bladed rotors. Due to geometry constraints, the 5 bladed rotors with high pitch

angles were meshed as one piece. Likewise, the two bladed rotors were meshed as a whole.

4.4 Single Rotor Turbines Results

The SRT geometries were analysed to understand their behaviour when operating with an inflow velocity of 1.2 m/s. Turbine A was modelled only at a tip pitch angle of 6°, and it was used as the reference parameter. The other 9 turbines were modelled at different tip pitch angles to determine the optimum blade configuration for each geometry, based on highest power coefficient.

The performance coefficients for each turbine were plotted as shown in Figure 4.11. The results show the power, thrust, and torque coefficients for every tip pitch angle considered when modelling Turbine C. To complete the performance study, the power to thrust coefficients ratio curve was also included.

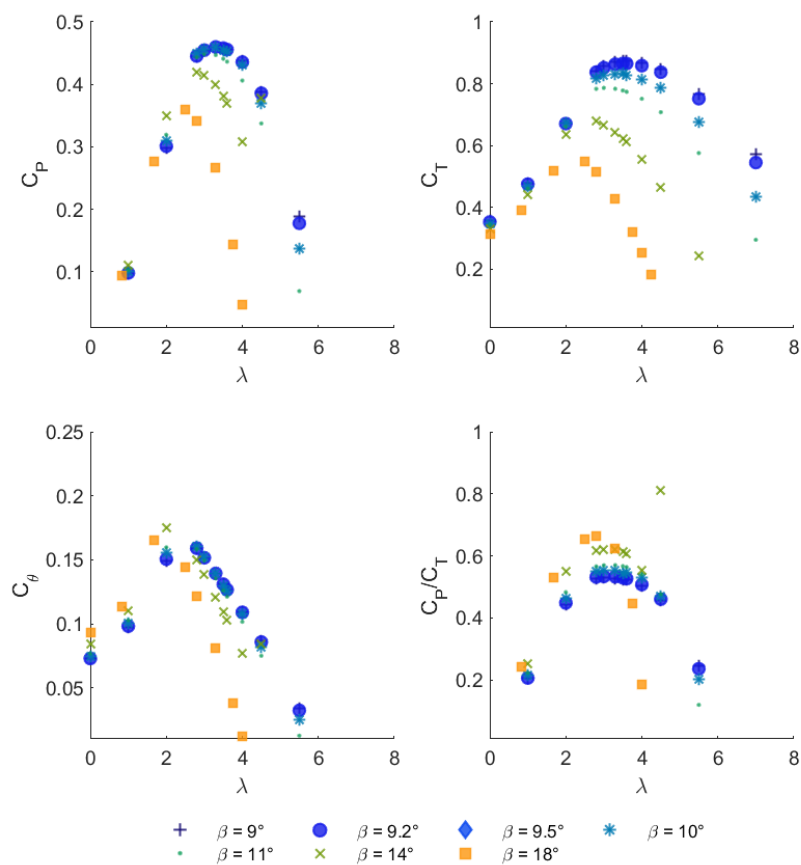


Figure 4.11: Turbine C's Performance Coefficients

Figure 4.11 illustrates the data obtained for each turbine, although the tip pitch angle was varied following Table 4.1. The objective of this solidity variation analysis was to determine

CMERG's turbine's feasibility when operating on low speed velocities. To understand which geometry was the most suitable under said conditions, the non-dimensionalised parameters provided a guidance of the different geometries' performance characteristics with plots as those shown in Figure 4.12 for Turbine C as reference.

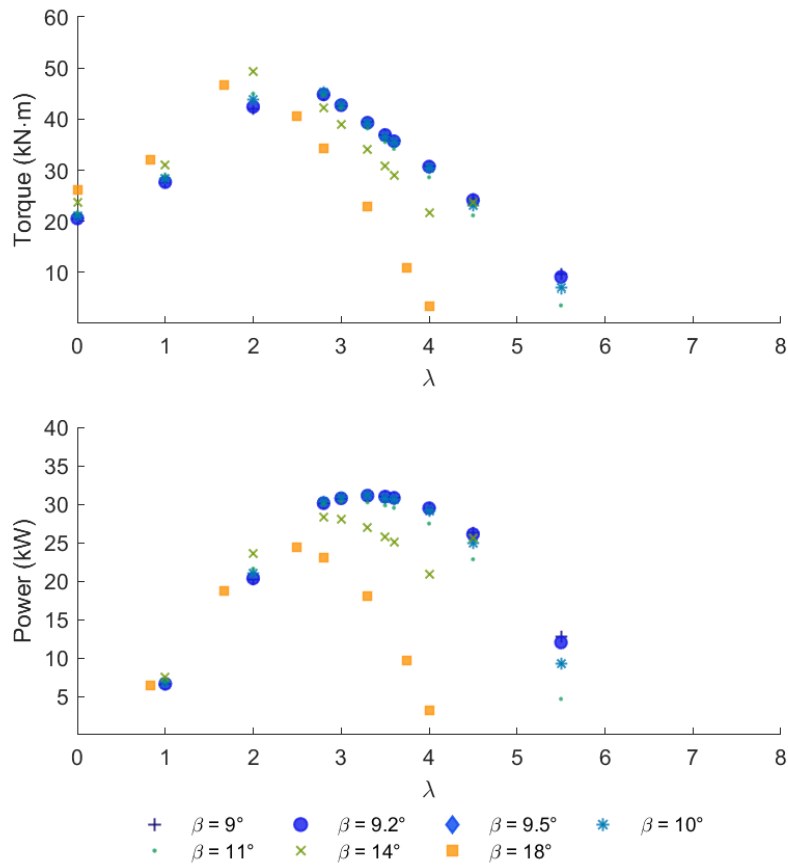


Figure 4.12: Turbine C's Torque and Power Output

The performance and output curves for the other 8 geometries analysed in this chapter are included in Appendix B.

4.4.1 Performance Variation Based on Tip Pitch Angle

Building upon research by Hernandez-Madriral et al. (2017), the influence of the tip pitch angle on the performance coefficients for the different turbines was analysed. The results shown in the following figures refer to the rotor configurations when peak C_p was achieved. The power coefficient, shown in Figure 4.13, varied up to 22% when the pitch angle was changed up to 9°. This compromise in power output can be compensated by the thrust reduction that is seen in Figure 4.14, where the same variation in pitch angle had a reduction in loads of 37%.

These results are useful during the design of variable pitch devices that can be adapted to the flow velocity and angle of attack. Compromise in power could reduce the installation and production costs of the stanchion needed to hold the turbine, increasing the feasibility of a particular design.

For both power and thrust coefficients, the range of values stayed constant regardless of the turbine configuration. The main variation found was the angle at which those values were achieved. With the exception of Turbine d, where a significant load reduction was found for all the modelled angles, the results showed that solidity did not have a major impact on the turbines' performance.

Figure 4.15 shows how the torque coefficient changed for each turbine configuration. Although the pitch angle variation for a specific rotor did not have a significant effect on the torque output, the geometry characteristics did have an influence. The highest torque found for the turbines operating at peak C_p was given by Turbine A.

Following on the feasibility of a SRT, when selecting a generator that would match a variable pitch angle turbine, the reduced variation in torque ($\sim 5\%$) would ease the different power plant's components operation.

The variation of the tip speed ratio, at which the maximum power output was obtained from the rotors, with respect to the modelled pitch angles is shown in Figure 4.16. The plot illustrates how the configurations with lower solidity had their maximum power output when rotating at higher velocities ($\lambda \geq 4$), whereas the pitch angle at which this happened increased with the solidity.

The figure also shows how λ remained constant for various tip pitch angles followed by a sudden change in the rotational speed with 1° variation. This behaviour suggests that the blades' pitch could be slightly changed without changing the rotor's rotational speed and the turbine would still be operating in peak power conditions for that specific geometry configuration. Nonetheless, for this to be effective a turbine must be well characterised to determine when the sudden change in β requires a different λ to operate with the highest C_p possible.

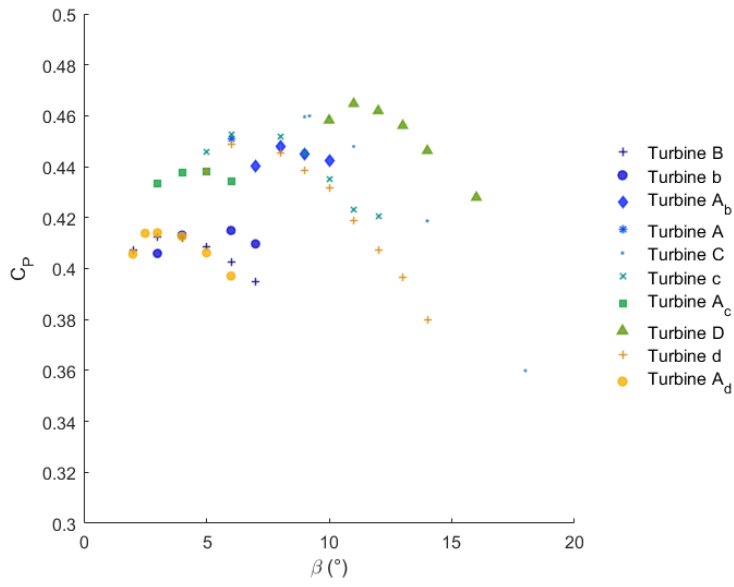


Figure 4.13: Power Coefficient - Tip Pitch Angle Variation

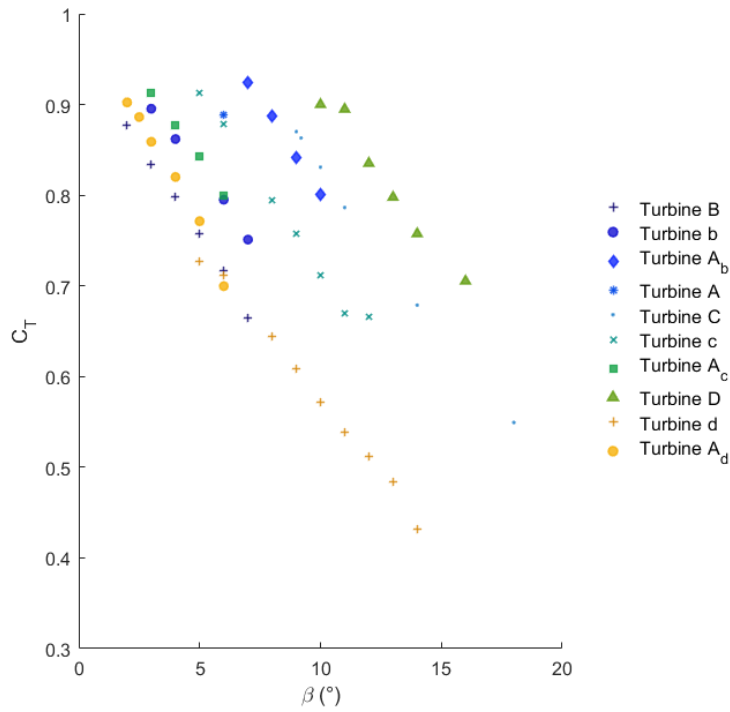


Figure 4.14: Thrust Coefficient - Tip Pitch Angle Variation

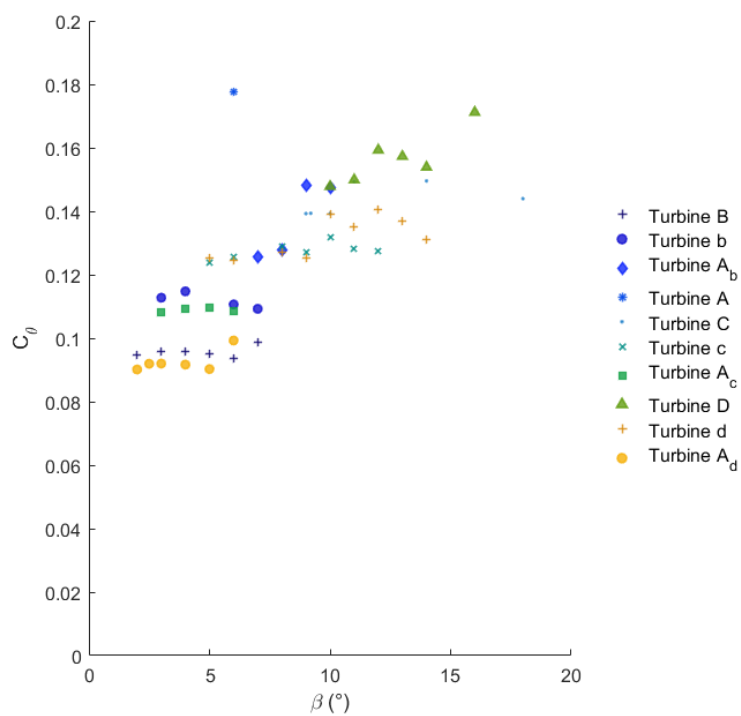


Figure 4.15: Torque Coefficient - Tip Pitch Angle Variation

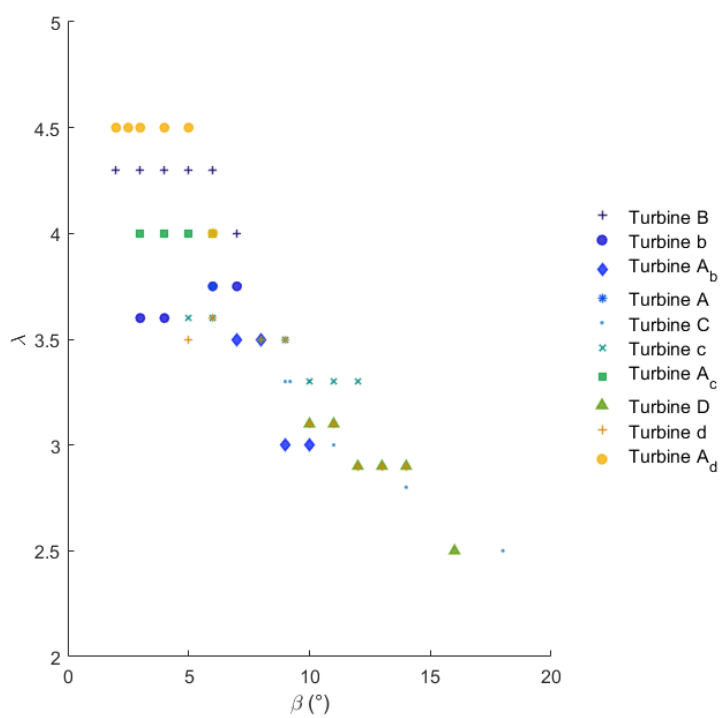


Figure 4.16: Tip Speed Ratio - Tip Pitch Angle Variation

4.4.2 Single Rotor Turbines at Peak Power Coefficient Performance

The full operation curves for the turbine geometry configurations at which the maximum power coefficient was found are shown in Figure 4.17. As expected from previous studies, with higher solidity the range of rotational speed decreased, but the peak power output increased. With a lower solidity, the λ operation was larger with a slightly lower power coefficient, but the highest power output was achieved over a wider option of rotational velocities.

The thrust coefficient increased with the solidity due to the larger surface area obstructing the flow. However, at peak power operation conditions the variation was fairly constant, with all turbines having a thrust coefficient of ~ 0.8 . The ratio of power to thrust coefficient showed that the only rotor having a noticeable improvement from the reference Turbine A, based on said parameter, was Turbine d.

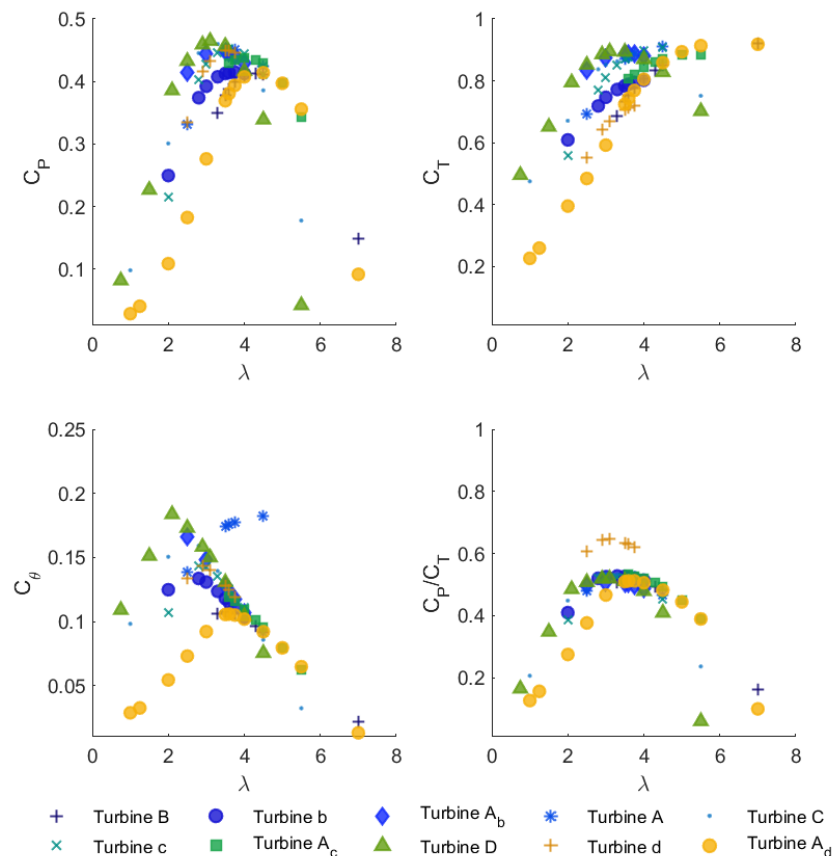


Figure 4.17: Rotors with Peak C_p - Performance Coefficients

The results also showed that depending on solidity, the peak torque coefficient could vary up to 74% from 0.106 for Turbine A_d to 0.184 for Turbine D. The increase in peak value was achieved in a shorter range of tip speed ratio, just as with the power coefficient.

The peak power coefficient for each of the turbine geometries modelled was found with their correspondent torque, and thrust coefficients. The specific pitch angles (α), and tip speed ratios (λ) at which this occurred are listed in Table 4.2.

As expected from previous results by Morris (2014), Turbine B and Turbine C had their maximum power output at 3° and 9.2° tip pitch angles. The geometries from case (ii), with the same solidity value as the original Turbine A, had the maximum C_p at the same pitch angle of 6°, which agrees with the theory explained in Section 4.2.2.

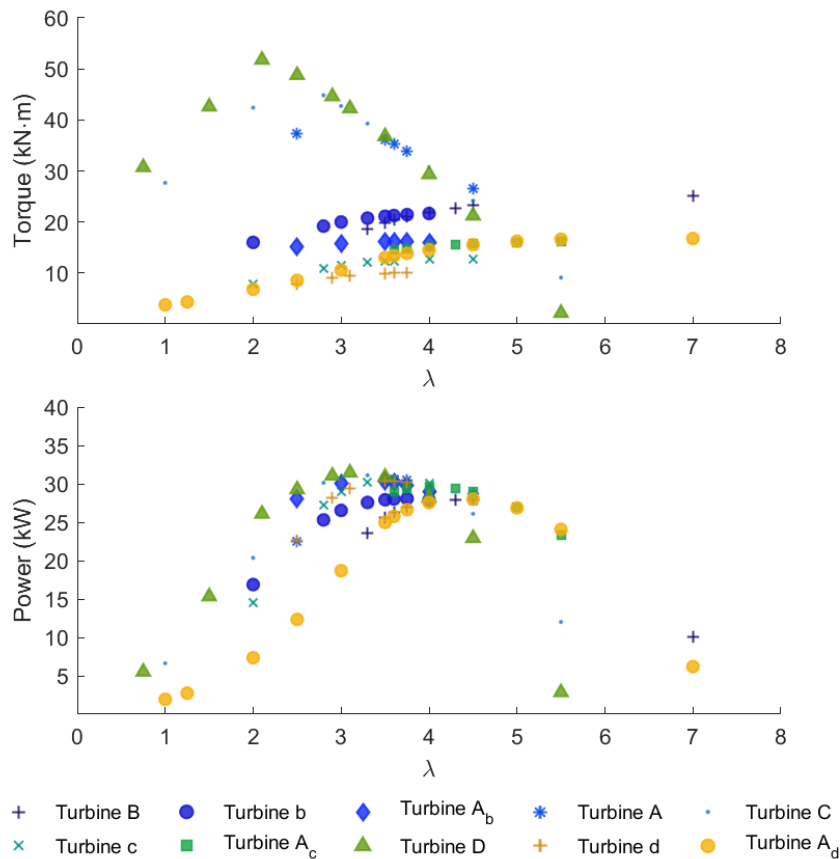
Solidity is related to the optimum lift coefficient, therefore if it is set constant so should be C_L and θ , as stated in equations (4.9) to (4.11). The results for case (ii) showed that the relative flow angle matched for Turbine A and Turbine b, whereas for Turbine c and Turbine d, θ differed only by 4% from the reference rotor.

Table 4.2: Single Rotor Turbines with Peak Power

Turbine	Pitch Angle	λ	Peak C_p	C_T	C_θ	θ
A	6°	3.75	0.451	0.889	0.178	9.9°
B	3°	4.3	0.413	0.834	0.096	8.7°
C	9.2°	3.3	0.460	0.863	0.139	11.2°
D	11°	3.1	0.465	0.895	0.150	11.9°
b	6°	3.75	0.415	0.795	0.111	9.9°
c	6°	3.6	0.453	0.878	0.126	10.3°
d	6°	3.6	0.449	0.712	0.125	10.3°
A _b	8°	3.5	0.448	0.888	0.128	10.6°
A _c	5°	4	0.438	0.843	0.110	9.3°
A _d	3°	4.5	0.414	0.859	0.092	8.3°

The final selection of a turbine, if economically feasible, must consider the device's operation curves. The net power and torque output are plotted in Figure 4.18 for the different rotors operating with their peak C_p blade configuration. The highest power output was 31.4 kW given by Turbine D, which represented 3% higher than the power generated by Turbine A (30.5 kW). The lowest power output 27.9 kW was given by Turbine B, 8.5% lower than Turbine A.

The torque output, required for the start up of a device and to match a generator specifications, varied from the lowest output given by Turbine d (10.04 kN·m) to the highest value given by Turbine D (42.3 kN·m), a difference of 75% and 7% respectively, with reference to Turbine A (39.3 kN·m). These values were considered at peak C_p operation point.

Figure 4.18: Rotors with Peak C_p - Torque and Power Output

4.5 Performance Predictions for Solidity Cases

Once the peak power configuration was found for each of the cases listed in Table 4.1 their performance variation with respect to solidity or number of blades was analysed. In this section a tool is proposed to predict the tip speed ratio (λ), power (C_p), thrust (C_T), and torque (C_θ) coefficients for the configuration that has maximum power output. The results from Table 4.2 were used to determine the prediction trends shown in Figure 4.19, Figure 4.20, and Figure 4.21, where the performance parameters were normalised using the maximum value of each set. The following plots were made using the steady state values of torque and thrust obtained from the CFD simulations. These parameters suffice to initially characterise a turbine but do not capture the rotors' transient behaviour.

Prediction curves were created to use as a guideline that could be improved with more solidity values to complete the set of points. With the available results, third order polynomial curves were fit to the all the rotors' cases. The results were verified using the original data points and the resulting matching values were highlighted as shown in Figure 4.19, Figure 4.20, and

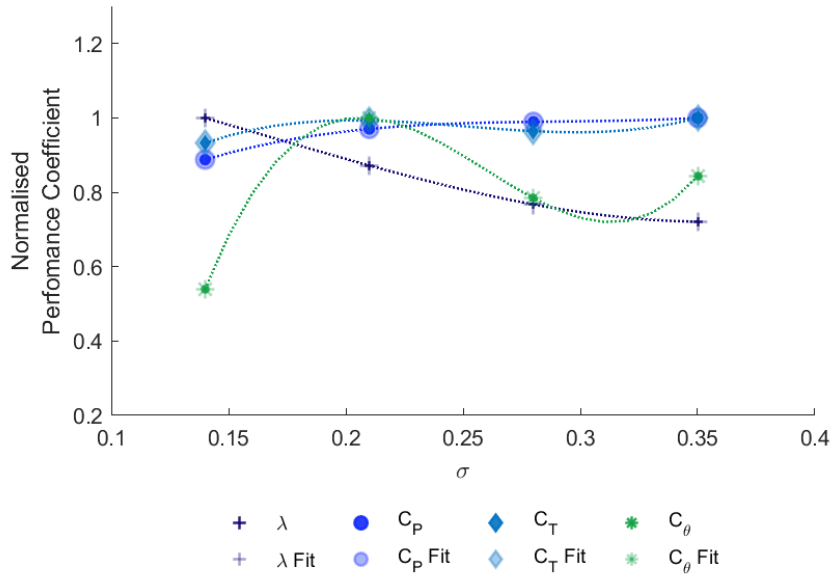


Figure 4.19: Peak C_p Performance Prediction - Case (i): Constant Chord Length

Figure 4.21.

Case (i) turbines were created by keeping the same blade chord length for the rotors whilst varying the number of blades, changing their solidity too. The turbines' performance at peak power output is presented in Figure 4.19, and compared against rotor's solidity. Results showed that thrust and power coefficients did not vary drastically with respect to the solidity, whereas the torque output decreased when the number of blades changed from the design conditions. Also, the rotational speed at which peak power occurred decreased with solidity, as was predicted by Morris (2014).

For a SRT in low velocity conditions, the original Turbine A design would have the optimum characteristics, due to the high torque required for start up. From Figure 4.19 it can be seen that if the number of blades was increased the power increase implied a compromise on torque and rotational speed, which then would need to be compensated with a gearbox and/or larger generator.

Equations (4.16a - 4.16d) list the polynomials for the curves that matched the results from case (i), where the sub-index i refers to the case and its constraints when setting the models.

$$\lambda_i = 16.9503\sigma_i^3 + 26.5457\sigma_i^2 + 74.6158\sigma_i + 462.2333 \quad (4.16a)$$

$$C_{p,i} = -8.3057\sigma_i^3 - 23.1970\sigma_i^2 - 56.1388\sigma_i - 360.1909 \quad (4.16b)$$

$$C_{t,i} = -0.4983\sigma_i^3 + 6.8278\sigma_i^2 + 13.5713\sigma_i + 89.6064 \quad (4.16c)$$

$$C_{\theta,i} = 1.1861\sigma_i^3 + 0.3138\sigma_i^2 - 0.0721\sigma_i - 6.2136 \quad (4.16d)$$

The performance coefficients were also plotted for the peak power output configurations of case (ii). These results are displayed in Figure 4.20, where the x-axis shows the number of blades for each of the rotors, instead of solidity because this was kept constant (21%). The variables were normalised using the maximum value of the set, and third degree polynomial curves were found to fit the parameters' trends.

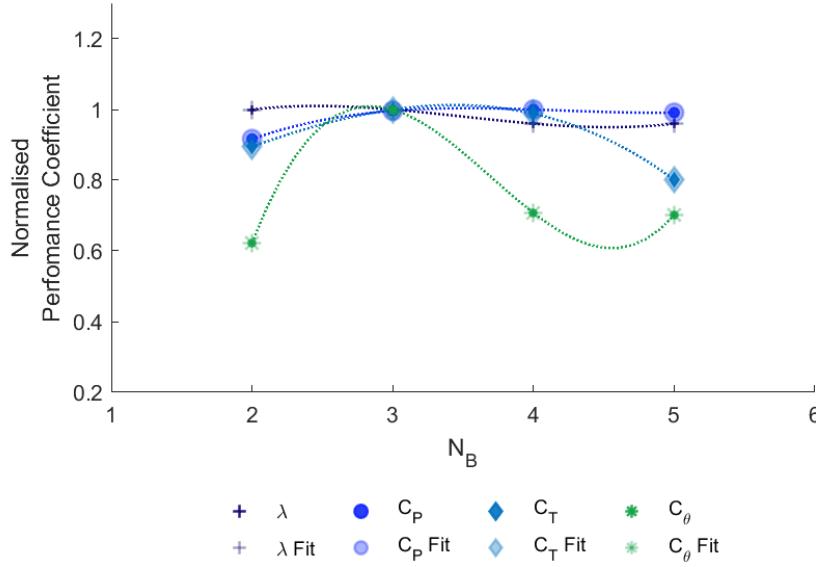


Figure 4.20: Peak Cp Performance Prediction - Case (ii): Constant Solidity

Regardless of blade number, the power and lambda at which the peak power output was obtained was relatively similar, as explained in Section 4.4.2. The torque coefficient had a noticeable maximum for Turbine A, which agrees with the initial design parameters of the turbine, and remained relatively constant for Turbine B, Turbine C, and Turbine D. The thrust coefficient showed a steady trend when blades change from 2 to 4, and a sudden drop was seen for the 5 bladed rotor, which could be attributed to the smaller surface area per blade. The set of equations for the case (ii) polynomial curves are shown in equations (4.17a - 4.17d).

$$\lambda_{ii} = 0.0133\sigma_{ii}^3 + 0.0106\sigma_{ii}^2 - 0.0096\sigma_{ii} + 0.1594 \quad (4.17a)$$

$$C_{p,ii} = -0.1400\sigma_{ii}^3 - 0.1332\sigma_{ii}^2 + 0.0282\sigma_{ii} - 1.7695 \quad (4.17b)$$

$$C_{t,ii} = 0.4467\sigma_{ii}^3 + 0.5446\sigma_{ii}^2 + 0.1477\sigma_{ii} + 6.1967 \quad (4.17c)$$

$$C_{\theta,ii} = 0.5600\sigma_{ii}^3 + 0.2756\sigma_{ii}^2 + 0.5635\sigma_{ii} - 5.9678 \quad (4.17d)$$

The last set of curves was created for the results from case (iii)'s rotors, and it is shown in Figure 4.21. When the blade number was kept constant, the peak power output increased with the solidity, and the tip speed ratio at which this occurred decreased. This behaviour was consistent with the results found for case (ii).

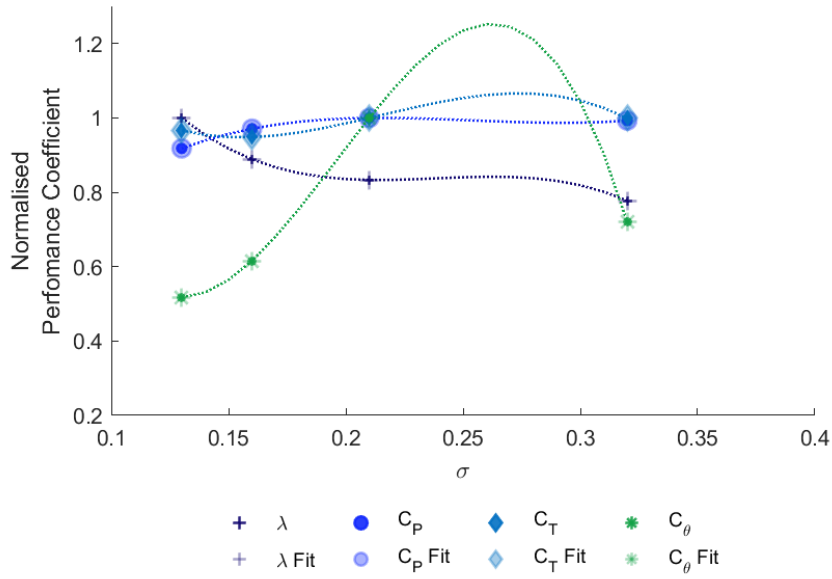


Figure 4.21: Peak C_p Performance Prediction - Case (iii): Constant Number of Blades

On the contrary, torque and thrust coefficients decreased when the solidity differed from Turbine A's. The polynomial curves that fit their trends had a more complex shape than the ones found for the previous cases, with predictions surpassing the normalised unit boundary on the y-axis. These results showed that further work is needed to obtain more data (solidity points) to create a more reliable set of equations (4.18a - 4.18d).

$$\lambda_{iii} = -150.6291\sigma_{iii}^3 + 56.6341\sigma_{iii}^2 - 141.9903\sigma_{iii} - 626.2855 \quad (4.18a)$$

$$C_{p,iii} = 107.7220\sigma_{iii}^3 - 43.1022\sigma_{iii}^2 + 91.4638\sigma_{iii} + 368.2147 \quad (4.18b)$$

$$C_{t,iii} = -25.4082\sigma_{iii}^3 + 10.6779\sigma_{iii}^2 - 18.1409\sigma_{iii} - 63.8629 \quad (4.18c)$$

$$C_{\theta,iii} = 2.8135\sigma_{iii}^3 + 0.1340\sigma_{iii}^2 + 2.0910\sigma_{iii} + 3.9730 \quad (4.18d)$$

The prediction curves created for each case are useful for this specific blade shape to determine what performance could be expected in peak power conditions if the solidity is known. The polynomials listed in this section were found by trial and error, selecting the lowest degree that would capture all the data points obtained from the simulations' results. However, these equations were found to describe the trends found with the solidity values modelled in this chapter and further research could improve the suggested tool by: (i) characterising more turbine geometries to validate the predicted results, and determine their applicability on other HATT; and (ii) including more solidity points that would allow a better understanding of the relationship between solidity and performance coefficients, and provide more accurate curves (and equations) to describe said relationship.

4.6 Single Rotor Turbines Feasibility in Low Speed Conditions

When considering a device that could work in low speed conditions the power output is one of the main factors to analyse. Once the technical specifications are assessed, their capital, installation, and operation costs will have a significant input to determine whether a project is developed or not. In this chapter it was determined that the maximum power output of a 5 m rotor, with the blade shape from CMERG, and operating with an inflow tide velocity of 1.2 m/s was ~30 kW. However, when the rotors' radius is changed the power output can be increased using the performance coefficients previously calculated.

This section analyses the economic feasibility of the modelled SRT rotors by considering different radii of the geometries (0.5 m, 1 m, 1.5 m, 2 m, 2.5 m, 3 m, 3.5 m, 4 m, 4.5 m, 5 m, 5.5 m, 6 m, 6.5 m, 7 m, and 7.5 m). They were considered as if they were to be used in a hypothetical power plant and their respective LCOE (levelised cost of energy) was obtained as described in [Section 6.4](#) to determine what would be the optimum rotor to install, based on their power output and cost.

The 200 results with highest power to LCOE ratio were summarised in [Figure 6.7](#), and the turbine with the highest ratio was selected as the optimum configuration. The rotor specifications of the chosen SRT are listed in [Table 4.3](#).

From these results it was found that the technology's cost was within the commercial stage range of £ 88/MWh - £ 188/MWh provided by Ocean Energy Systems et al. (2015). Nonetheless, the reference LCOE method used to obtain the value mentioned above did not account for the

Table 4.3: Optimised Single Rotor Turbine Specifications

Variable	Symbol	Value
Radius	R	7.5 m
Number of Blades	N_B	5
Blade Label	-	A
Tip Pitch Angle	β	11°
Rotational Speed	ω	0.496 rad/s
Power	P	70.78 kW
Power Coefficient	C_P	0.47
levelised Cost of Energy		$LCOE$ £164.4 /MWh

fact that the size of the selected device would require more complex installation, maintenance, and operation logistics: the vessels required to provide this service are scarce, and have limited capability incrementing the costs depending on the device's geometry (size and weight).

An alternative HATT configuration, such as a contra-rotating rotors turbine could address those issues. It has been proven (Johnstone et al. 2013; Jung et al. 2019) that a contra-rotating tidal stream device can be self-balancing with a near zero reaction torque, which means that a tethered foundation (instead of a mono-pile gravity based) could be used reducing and simplifying costs and logistics. Furthermore, when two rotors are located in tandem the power output from one turbine could be increased when compared to a SRT (Newman 1983), and a contra-rotating configuration would not require a gearbox if connected to a direct drive train reducing capital and maintenance costs. To determine if all these factors, combined, could lead to a decrease of the LCOE making the proposed HATT more competitive with other renewable energy technologies, the following chapter analyses a second generation technology contra-rotating configuration for low speed conditions.

Chapter 5

Contra-Rotating Rotors Turbine Configuration

As explained in [Section 4.6](#), a modified (and optimised) 15 m diameter SRT could be competitive with other commercially ready technologies when operating in low velocity conditions. However, the device would require a large vessel for its deployment and maintenance, and a mono-pile structure that complicates operation logistics. To address those issues, this chapter considers horizontal axis Contra-Rotating Turbine (CRT) arrangements as a solution for low speed conditions due to their technical characteristics that can be translated to lower capital costs, and an increase in the possible maximum power output (Newman 1983). Clarke et al. (2007a) listed the main benefits of using a contra-rotating device for tidal stream energy extraction:-

- (i) A simple supporting structure can be used because there is near-zero reaction torque on it.
- (ii) The possibility of not needing a gear drive to the generator because the rotational speeds are higher than the relative SRT.
- (iii) Power output is higher than the relative SRT.

This chapter includes a background and theory summary on contra-rotating configurations for tidal stream turbines. Then a rotor set-up procedure, and performance results are given to determine their technical and economical feasibility if installed in conditions similar to the ones in Costa Rica. The modelled turbines were operating in 1.2 m/s tide velocities, and were made by pairing the single rotor turbines analysed in [Chapter 4](#) that matched a specific set of parameters.

For description purposes, the CRT are labelled depending on the number of blades in the front rotor, *FR*, and the back rotor, *BR*. The format used is *FR – BR CRT*.

5.1 Contra-Rotating Tidal Stream Turbines Background

Contra-rotating TST have the advantage of a balanced inertia moment that allows a TST to be moored with a floating buoy (Kanemoto et al. 2000). This benefit over SRT has led research to contra-rotating devices in the tidal stream energy sector, where a few contra-rotating configurations are available for reference. This chapter's objective is to propose a CRT using the SRT geometries analysed in Chapter 4 with two fully developed HATT CRT designs used as guidance: Nautricity's CoRMaT with research from Strathclyde University, and the Counter-Rotating Type Tidal Stream Tandem Propellers design from the Kyushu Institute of Technology. Other contra-rotating tidal stream energy extraction alternatives are briefly considered.

5.1.1 CoRMaT's CRT

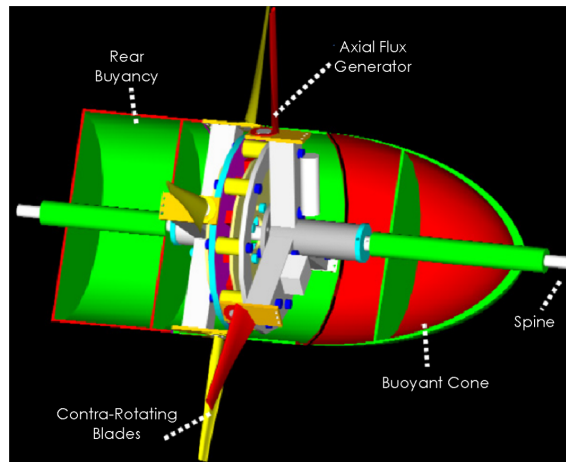


Figure 5.1: CoRMaT's CRT Diagram. Source: Adapted from Clarke et al. (2008b)

Clarke et al. (2007a) proposed an initial design (Figure 5.1) of a 3 – 4 CRT that has blade profiles made with the *NRELS814* aerofoil, and both rotors have the same tip speed ratio, torque, and axial thrust loads. Clarke et al. (2007a) experimentally validated the 1/30th scale rotor's performance, and determined that a small increase in pitch angle (for both rotors) could maximise power output, but when comparing the CRT with a SRT the peak C_p values were similar for both configurations. Further studies (Clarke et al. 2007b) determined the optimum distance between rotors should not be larger than the design value (0.073D), which is based on the assumption that rotors are in close proximity. The same turbine, at 1/10th scale, was modelled with Computational Fluid Dynamics (CFD) by Clarke et al. (2007b) to optimise the interblade spacing and it was determined that the CRT's wake impact on the environment is less than the one caused by a SRT. Experimental data from sea measurements confirmed that

the reactive torque was offset by the contra-rotating nature of the device.

Further work was dedicated to the design and sea testing of the tethering structure and contra-rotating generator for a 1 m diameter CRT (Clarke et al. 2009b). The turbine was connected to a submersible Direct Drive Permanent Magnet Generator (DDPMG), which does not require a gearbox to transmit the low rotational velocities, and uses sea water as the cooling fluid (Clarke et al. 2008b). The mooring system was made using a tensioned cable attached to the sea bed, and a floating buoy that would keep the rotor in the operating depth range (Clarke et al. 2009a). Positive sea test results led to the proposal of a commercial 250 kW configuration with a single point mooring that would reduce cost of installation, allow free yawing and alignment with the tidal flow, and facilitate turbine deployment in deeper waters (Clarke et al. 2010).

Clarke et al. (2010)'s determined CorMaT's commercial characteristics: (a) no gearbox to reduce maintenance costs; (b) fixed pitch rotor blades; (c) contra-rotating rotors; and (d) contra-rotating direct drive permanent magnet generator. These guidelines were applied in the design process for the CRT proposed in this chapter. The next section introduces Kyushu Institute of Technology's CRT, which was also used for reference in the design of this research's CRT.

5.1.2 Kyushu Institute of Technology's CRT

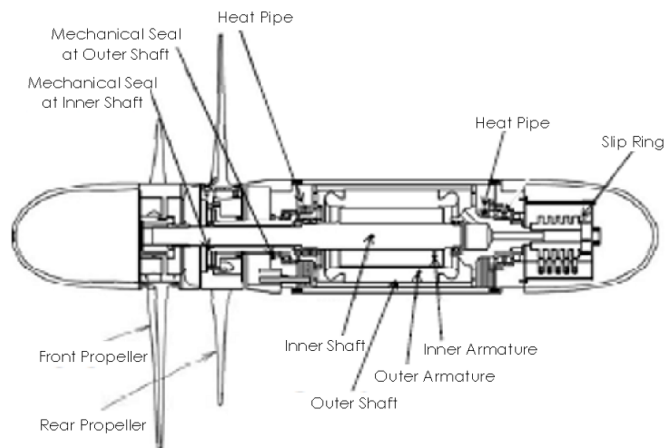


Figure 5.2: Kyushu's CRT Diagram. Source: Adapted from Kawashima et al. (2017)

The development of Kyushu's CRT (Figure 5.2) involved using lessons learned from the wind energy sector. Usui et al. (2013a) experimentally modelled a 3 – 5 CRT, made with a combination of the NACA0015 (for $R > 0.5R$) and the MEL002 (for $R > 0.6R$) aerofoils, originally designed for wind energy extraction (Kubo et al. 2010, 2008), in a water tow tank. Unlike the turbine

used by Clarke et al. (2008a) where both rotors have the same radius, Usui et al. (2013a)'s CRT has a back rotor to front rotor diameter ratio of 0.84. The design of this turbine was made using the peculiar generator designed by Kanemoto et al. (2000), which has a double rotational armature without the conventional stator, and the FR and BR have the same rotational torque output but in opposite directions (Kubo et al. 2008).

The number of blades were selected by analysing the effect this variable would have in the power output. The FR with 3 blades was chosen because there was no real output variation when the number was changed, and 2 blades do not have counter-rotation. On the contrary, the effect of BR's blade number on the CRT performance was noticeable: the power output increased with the number of blades, but the FR's rotational velocity decreased and the total torque increased. The optimum number of blades for the BR was found to be 5 for this CRT. The blade twist and sizes were obtained by Kubo et al. (2008), where combinations of two blade profiles with various diameter ratios were tested, and it was found that the BR's blade shape, pitch angle, and size are the main factors to consider when calculating the maximum power coefficient of the CRT. When the diameter ratio varied from 0.84 the contra-rotation nature of the device disappeared. Kubo et al. (2008) also determined that the axial distance between the rotors had to be the smallest possible considering the bending moments and vibrations of the blades. More details of the turbine design were given by Galal et al. (2008) and Huang et al. (2016a).

In the study made by Usui et al. (2013a) the CRT was attached to a pillar to determine how three different pitch angle configurations would affect the turbine's performance characteristics, and drag effect on the pillar axial force and downstream waves. The power output was higher when operating under wind flow, and the drag increased with the pitch angle causing higher loads on the pillar and larger waves (Usui et al. 2013a). Single cable mooring for the CRT was considered by Usui et al. (2014, 2013b). Usui et al. (2014) experimentally tested the CRT's unsteady motion when located in a water tank moored with one cable attached to a floating pile. Initial results demonstrated that a CRT would keep horizontal posture regardless of the flow velocity, and the rotational velocities balanced the turbine.

More numerical simulations were done by Huang et al. (2015a) to optimize (with statistical methods) the front rotor blades' pitch angle distribution minimising the thrust load whilst maximising power output. The optimum blade increased the power coefficient by 1% over the low tip speed ratio (TSR) area, whereas the thrust coefficient showed a slight decrease in the high

TSR region. CFD validation results showed that the optimum configuration reduced flow separation and vortices on the blades. The optimum blade setting angles (tip pitch angle (Kubo et al. 2008)) for the front and back rotors of the 3 – 5 *CRT* were obtained by Huang et al. (2016b). The maximum power output was found when there was no change in the front blade setting angle, and the back blade setting angle was increased by 7°. Experimental results in a wind tunnel confirmed the performance improvement with the optimisation (C_p increased from 0.35 to 0.41), and also showed an over prediction of the power output given by CFD results. To determine the optimum pitch angle for both rotors and the axial distance between them, more experimental wind tunnel tests were made. Wei et al. (2015) compared eight combination groups of blade pitch angles (using the blade setting angle as reference) and axial distances for the 3 – 5 *CRT*. The results showed that increasing the FR blades' pitch angle to match the single rotor's value was the optimum configuration for the FR (from 36.5° to 41.5°). The BR blades' optimum pitch angle was found by increasing the initial condition until finding the angle until which the power output would start decreasing again (from 27.5° to 34.5°). It was determined that for the pitch angles equal and larger than the optimum configurations, an increase in axial distance enhanced the FR power output, whereas not showing significant variation on the BR. Similarly, the blades yaw angle for the FR and BR, and their axial location on the hub, were optimised to obtain the maximum power output by Jung et al. (2019) using the response surface method, and the adaptive single objective method. Results showed a 5% increase of the power coefficient, but that more research needs to be done on the multiple variable input optimisation methods.

A prototype 3 – 5 *CRT* with a 1 m diameter FR, and a 0.95 m diameter BR was experimentally tested offshore by Samura et al. (2019). A modified synchronous generator with double rotatable armatures (Kanemoto et al. 2000) was used, which has been previously used for tidal range (Kanemoto et al. 2010b) and wind (Kanemoto et al. 2010a) energy extraction. At a fairly constant 1 m/s the rotational speeds and torque, power output and angular velocity were measured. Results showed that velocities of both rotors could be adjusted to obtain the desired output, with a maximum $C_p=0.42$, with a fully operational device. Samura et al. (2019) did not specify why they used a 0.95 ratio for this analysis, instead of the 0.84 previously used by Kubo et al. (2008).

New blades were made by Huang et al. (2015c) using the *KIT001* aerofoil with different thickness, to improve the 3 – 5 *CRT*'s performance ($C_p= 0.43$). Experimental testing was done

with the new blades, and a CFD numerical model was proposed simulating the CRT operation in water conditions using ANSYS CFX 14.0. Results showed a slight over prediction of the performance characteristics, but overall similar behaviour to the experimental values. Pressure distribution, and streamlines on the rotors' blades showed when flow separation occurred, and how the stagnation point moved to the suction side during high tip speed ratios (λ). Velocity contours and profiles were also analysed to understand wake behaviour, and recovery. This turbine was designed as a trade-off between maximising the Reynolds number and not incurring excessive tunnel blockage correction (Huang et al. 2016c). Wei et al. (2016) presented the design methodology, and detailed the blade selection approach, where one FR configuration was combined with three different BR diameter options: same as the FR, 3% larger, and 9% larger. Wind tunnel experimental data provided power coefficient results for the three arrangements, and it was determined that the larger FR/BR diameter ratio had the highest power output, and a relatively wider λ operation range.

Once the turbine design was completed, research was done to understand the CRT behaviour. A bi-directional 3 – 5 CRT configuration was proposed (Huang et al. 2016d; Funami et al. 2017) as an improved alternative of a CRT. Fluid behaviour studies have also been made, such as cavitation modelling (Huang et al. 2015b), vorticity prediction (Jung et al. 2017), scaling effects (P. Liu et al. 2018), and the performance under oblique flow conditions (N. Lee et al. 2019).

Kyushu's CRT optimised configuration for tidal stream turbine has taken years to develop. This chapter presents a method to adapt a well characterised HATT into a CRT that could be economically feasible, based on some findings from Kyushu's research.

5.1.3 Other CRT Studies

Research by N. Lee et al. (2015) and Kim et al. (2016) proposed a 0.5 m dual 3 – 3 CRT with both rotors rotating at the same velocity in opposite directions, and had BEMT created blade profiles using the *NACA* – 63421 aerofoil. The expected power coefficient, experimentally validated, for this device is $C_p=0.46$.

Amelio et al. (2012) developed an innovative 8 blades open centre HATT with buoys, and a deflector instead of the traditional hub to stabilise the device. It could be anchored using a steel rope connected to rigid rod hinged to the coast (Barbarelli et al. 2014b) with no need for sea bed support. The increased power/weight ratio output of an open centre turbine (0.9 kW/kg) in comparison to a 'traditional' full length blade device (0.3 kW/kg) was pointed by Barbarelli



Figure 5.3: Barbarelli's CRT Diagram. Source: Barbarelli et al. (2014c)

et al. (2019). To improve the SRT design, a 6 – 6 *CRT* configuration (Figure 5.3) was proposed (Barbarelli et al. 2014c), and analysed in equilibrium conditions (Barbarelli et al. 2014a). Barbarelli et al. (2014a) modelled the machine with *blades that are connected by circular rings sliding through the stator: the two rotors -external and internal- rotate in opposite directions to produce equal torque*. The generator coils are located in the stator, whereas magnets are placed in the rotors' blades. The external and internal rotors have different C_p values of 0.46 and 0.43 respectively (Barbarelli et al. 2014a), but an overall $C_p=0.4$ was used in the techno-economic evaluation of the turbine (Barbarelli et al. 2018).

CMERG's turbine geometry used in this project has previously been considered in the contra-rotating configuration as two 10 m rotors assembled in a mirrored 3 – 3 *CRT*. Figure 5.4 shows the geometry D. O'Doherty et al. (2009) modelled using CFD in conditions with 3.1 m/s inlet velocity, the FR rotating at 2.25 rad/s, and changing the rotational velocity of the BR from 0.7 rad/s to 2.25 rad/s. These conditions were repeated for two axial distances ($1D_h$, $2D_h$) between rotors using the hub diameter ($1D_h$) as reference. At the closest proximity ($1D_h$) the power coefficient increased from 0.4 to 0.46, whilst at $3D_h$ the power output was reduced. Results showed that by keeping both rotors with the same pitch angle at the optimised 6° the torque outputs did not match. The BR blades' size and angle should be modified to obtain zero torque reaction from the turbine's contra-rotation. This would imply a considerable increase in the axial thrust that must be accounted for when designing the supporting tethering cables' loads.

The CRT configuration proposed in this chapter follows up on the results made by D. O'Doherty et al. (2009). Its technical and economic feasibility is analysed considering that the use of contra-rotating tidal stream turbines as second generation technology can eliminate the need



Figure 5.4: CMERG's CRT Diagram. Source: D. O'Doherty et al. (2009)

of a stanchion as supporting structure, simplifying installation logistics and reducing costs due to (Johnstone et al. 2013):-

- (i) No need for gearbox because the rotational velocity is doubled with the two rotors.
- (ii) Higher overall drive-train/take off efficiency ($\sim 90\%$) with the DDPMG compared to gearbox and generator combination ($\sim 80\%$).
- (iii) Simpler manufacturing costs because rotor blades are mounted directly onto the generator elements.
- (iv) Reduced maintenance requirement.

5.2 Contra-Rotating Tidal Stream Turbines Theory

This section details the theory considered to propose a technically feasible CRT.

5.2.1 Efficiency Limit

In Section 2.2.1 (page 29) the maximum theoretical power coefficient for a single rotor horizontal axis turbine, known as the Lanchester-Betz limit, was described. This occurs when the axial flow induction factor $a = \frac{1}{3}$ is used in equation (2.10) equating to $C_{P,SRT,max} = 0.593$ (Burton et al. 2011). Similarly, Newman (1983) determined that for Double Rotor Turbines (DRT), the limit increases to 64% (equation (5.1b)), when the induction factors for the front and back rotors, $a_1 = \frac{1}{5}$ and $a_2 = \frac{3}{5}$ respectively, are used in equation (5.1a).

$$C_{P,DRT}(a) = 4 [a_1(1 - a_1)^2 + (1 - a_2)^2(a_2 - 2a_1)] \quad (5.1a)$$

$$C_{P,DRT,max} = \frac{16}{25} = 0.64 \quad (5.1b)$$

This value is obtained when the DRT is analysed as two actuator discs in tandem (one behind the other) with the same axis of rotation and assumes one-dimensional flow at the second disc (Newman 1983, 1986), where the minimum spacing between discs should be in the order of one rotor's diameter (Draper et al. 2014). When a CRT is analysed as a 'single blockage' device, such as the configurations analysed in this chapter, the Lanchester-Betz limit (59%) applies as the maximum theoretical power coefficient.

5.2.2 Power Output

The total power output of a CRT (P_{tot}) is given by the sum of power output given by front (P_{FR}) and back rotors (P_{BR}), as shown in equation (5.2). The power of each rotor is given by equations (5.3a - 5.3b), where the torques, T_{FR} and T_{BR} are extracted from the CFD simulation results, and the rotational velocities, ω_{FR} and ω_{BR} , were given as simulation parameters.

$$P_{tot} = P_{FR} + P_{BR} \quad (5.2)$$

$$P_{FR} = T_{FR} \cdot \omega_{FR} \quad (5.3a)$$

$$P_{BR} = T_{BR} \cdot \omega_{BR} \quad (5.3b)$$

5.2.3 Power Coefficients

The definition of power coefficient for devices in open flow conditions is given in Section 2.2.1. To determine the efficiency of a CRT turbine, the C_p of each rotor can be calculated using equations (5.4a - 5.4b), where u is the inlet flow velocity before reaching the CRT, and the areas (A_{BR} , A_{FR}) of each rotor are used.

$$C_{P,FR} = \frac{P_{FR}}{\frac{1}{2}\rho A_{FR}u^3} \quad (5.4a)$$

$$C_{P,BR} = \frac{P_{BR}}{\frac{1}{2}\rho A_{BR}u^3} \quad (5.4b)$$

$$C_{P,sum} = C_{P,FR} + C_{P,BR} \quad (5.5)$$

Huang et al. (2016a) measured their CRT's total power coefficient ($C_{P,sum}$) adding the individual values, as shown in equation (5.5). Clarke et al. (2007a) and Wei et al. (2016) calculated the CRT's power coefficient ($C_{P,tot}$) using the overall power output, as defined in equation (5.6). When both rotors of the CRT have different diameters the area A is calculated using the largest rotor's radius. For the purpose of this thesis, CRT's power coefficient is obtained using equation (5.6).

$$C_{P,tot} = \frac{P_{FR} + P_{BR}}{\frac{1}{2}\rho Au^3} \quad (5.6)$$

5.2.4 Torque

One advantage of a CRT over a SRT is its near-zero net torque reaction (Clarke et al. 2007a; Huang et al. 2016a), which in practice is achieved with contra-rotating generator that acts as a differential. This characteristic is described by setting each of the rotors torque output equal in magnitude, but in opposite directions. Equation (5.7) illustrates the condition.

$$T_{FR} = -T_{BR} \quad (5.7)$$

5.2.5 Rotational Velocity

As shown in Section 2.2.1, to characterise a HATT, the power coefficient is analysed at different tip speed ratios. For a CRT, the non-dimensionalised tip speed ratio is the sum of each rotors' λ , as shown in equation (5.8) (Clarke et al. 2007a; Huang et al. 2016a).

$$\lambda_{tot} = \lambda_{FR} + \lambda_{BR} \quad (5.8)$$

The tip speed ratio for each rotor is calculated with equations (5.9a - 5.9b) that account for each rotor's rotational speed.

$$\lambda_{FR} = \frac{\omega_{FR} R_{FR}}{u} \quad (5.9a)$$

$$\lambda_{BR} = \frac{\omega_{BR} R_{BR}}{u} \quad (5.9b)$$

Assuming the FR's direction as positive, the total rotational speed of the CRT ω_{tot} is defined as the difference between each rotor's rotational speed (ω_{FR} , ω_{BR}). Equation (5.10) shows the calculation.

$$\omega_{tot} = \omega_{FR} - \omega_{BR} \quad (5.10)$$

5.2.6 Inlet Velocities

The inlet velocity of the CRT u is constant at 1.2 m/s with the direction parallel to the flow, for all the cases analysed in this research. This parameter is considered constant for the turbine and rotors' characterisation.

5.3 Contra-Rotating Rotor Selection

Following the guidelines stated in the previous section and lessons learned from literature review, a contra-rotating turbine is proposed using the rotors analysed in [Chapter 4](#). The following rotors' parameters were taken into account in the selection process for CRT configurations:-

- (i) Blade design.
- (ii) Tip speed ratio.
- (iii) Pitch angles.
- (iv) Size.
- (v) Number of blades.
- (vi) Torque
- (vii) Rotational speed.
- (viii) Power output.
- (ix) Levelised cost of energy (LCOE).

To determine possible contra-rotating configurations the following steps were taken: (a) single rotor possibilities, (b) rotor matching, and (c) rotor selection. Two Matlab codes, shown in [Appendix E](#), were written; one to determine all the possible geometry configurations ([Section E.1](#)), and one to select options that were technically feasible ([Section E.2](#)).

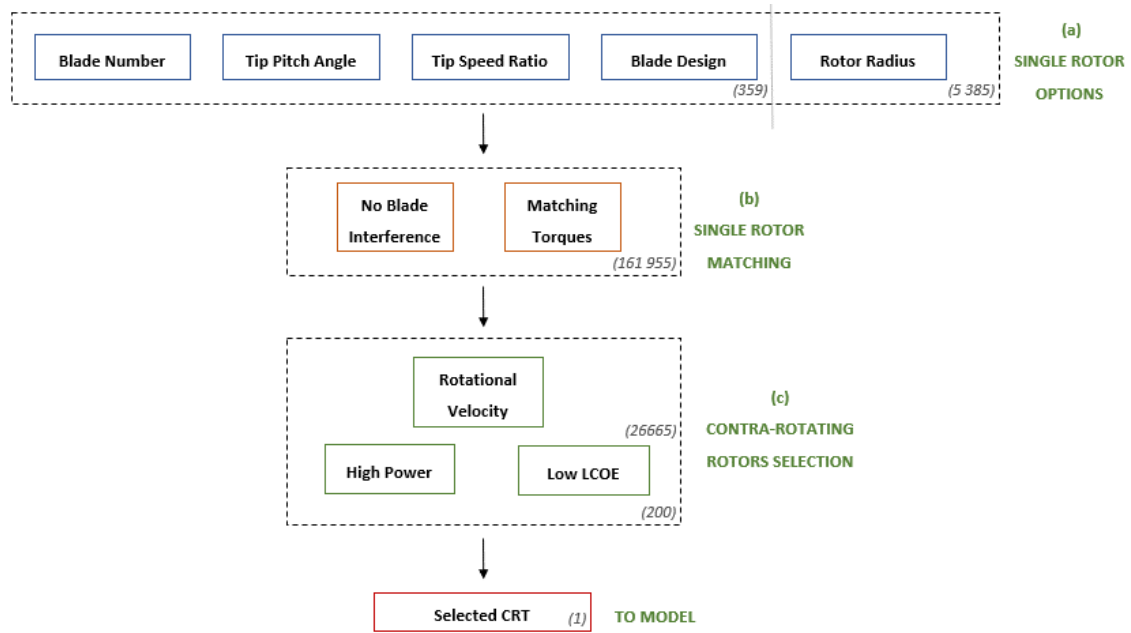


Figure 5.5: CRT Selection Process

Figure 5.5 summarises the procedure used to select the CRT configuration to model in CFD. Each rectangle refers to the rotors characteristics considered, and the numbers in brackets refer to the available possibilities after each step of the process.

The first block includes all the SRT modelled in Chapter 4, and the available rotors for matching when they are scaled to different radii (Section 5.3.1). The second step of the process (Section 5.3.2) refers to the possible matches between available single rotor geometries, limited by number of blades and torque values. The third step of the process refers to the model selection (Section 5.3.3) restricted by generator specifications, power output, and economic analysis. A CRT was selected based on economic feasibility, and modelled in CFD. Each of the steps are detailed next.

5.3.1 Single Rotor Options

Each of the simulations modelled (*rotor cases*) in Chapter 4 had one specific combination of blade design, number of blades, pitch angle, and tip speed ratio. They were all characterised with non-dimensionalised performance coefficients, which allowed a prediction of their performance to be made when scaling was done using the equations listed in Section 2.2.1. The specific non-dimensionalised characteristics for all the single *rotor cases* are shown in Appendix B.

To increase the pool of options for the contra-rotating configurations, the absolute power

output, torque, axial force (thrust), and rotational speed were predicted for all *rotor cases* with radii of 0.5 m, 1 m, 1.5 m, 2 m, 2.5 m, 3 m, 3.5 m, 4 m, 4.5 m, 5 m (reference *rotor case*), 5.5 m, 6 m, 6.5 m, 7 m, and 7.5 m. The 15 m maximum diameter was based on the extreme circumstances of Costa Rican depth (Brito e Melo 2013), as described in Section 1.2.2. By considering these 15 rotor sizes, the characterised *rotor cases* increased from 359 to 5 385.

5.3.2 Single Rotor Matching

Dual rotor contra-rotating configurations were created by combining *rotor cases* that had matching torques. Blade eclipsing was avoided minimising stall and dynamic blade interactions by not having the two contra-rotating rotors with: (a) equal number of blades, (b) or number of blades that are multiple of each other (Clarke et al. 2007b). Thus, only the combinations listed in Table 5.1 were considered as technically feasible.

Table 5.1: Possible CRT Blade Number Configurations

$N_{B,FR}$	$N_{B,BR}$
2	3 or 5
3	2 or 4 or 5
4	3 or 5
5	2 or 3 or 4

The torque output was limited by setting it to be *equal* from both rotors, as explained in Section 5.2.4. To account for the flow downstream changes when two single rotor turbines are rotating in close proximity, a torque difference $\leq 5\%$ was considered.

The possible CRT configurations, *contra-rotating cases*, that agreed with these two constraints were 161 955. A selection process to find one that could be optimised was proposed.

5.3.3 CRT Selection

To select one configuration from all the *contra-rotating cases* the total rotational velocity was limited based on the generator's capabilities. Then a comparison between power output, and economic feasibility was made.

For contra-rotating turbines in tidal stream technology generators have been designed for each specific case. Barbarelli et al. (2014a) proposed a generator configuration that would adapt to their open centre rotor. Due to the geometric differences with the CRT HATT analysed

in this thesis, their generator is not considered for reference.

Kanemoto et al. (2000) proposed a contra-rotating generator, located behind the turbine's rotors (Figure 5.6), that was adapted for tidal range (Kanemoto et al. 2010b), wind (Kubo et al. 2008), and tidal stream energy extraction (Kawashima et al. 2017). Kawashima et al. (2017) increased the efficiency of the 3-phases 4 poles permanent magnet synchronous AC contra-rotating generator with double rotating armatures, previously designed for wind energy turbines (Kanemoto et al. 2010a), by adding a heat pipe with an extremely high heat coefficient that helped cooling the whole unit with sea water.

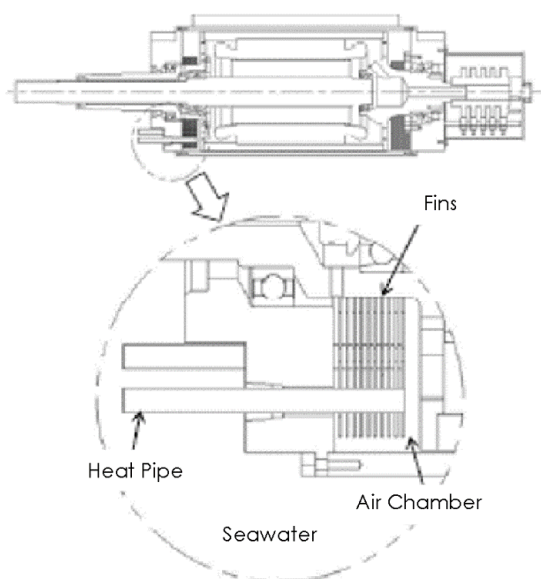


Figure 5.6: Kyushu's CRT Generator Diagram.
Source: Adapted from Kawashima et al. (2017)

Likewise, Clarke et al. (2010) designed a 3-phase axial flux direct drive generator, which would be located between the turbine's rotors (Figure 5.7). One of the turbine rotors drove the generator 'rotor' in one direction, and the second turbine rotor drove the 'stator' in the opposite direction. This contra-rotation increased the magnetic field's velocity, which reduced the unit's size. The lab made generator had 12 poles in each rotor, with a stator located in between. Slip rings collected the electrical output, which was converted to DC and then transmitted underwater using a two core cable. To protect it from marine conditions the whole device was coated, and experimental testing proved: (a) ease of construction, (b) generator/nacelle casing leaks were non-issues, (c) cooling was naturally provided, (d) no complex sealing requirements, and (e) no large diameter shaft seal section (Clarke et al. 2010). Further testing of a 500 kW scaled design proved successful operation of the direct drive contra-rotating generator (DD-CRG), where

cost and weight of the PTO were reduced with a simple design that copes with the marine environment. The device was modified to operate in sea water with the required waterproofing and corrosion management, and requires less maintenance increasing its availability (Porter et al. 1986).

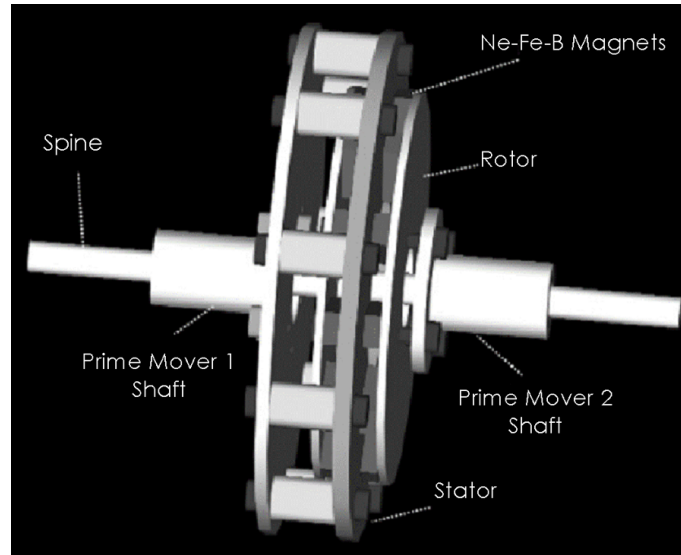


Figure 5.7: CoRMaT's CRT Generator Diagram.
Source: Adapted from Clarke et al. (2010)

Kawashima et al. (2017) proved that a generator previously designed for wind energy extraction could be adapted to operate in tidal stream conditions. Consequently, an off-the-shelf low velocities synchronous PMDDG, designed for wind turbines, was considered as a reference to set the rotational speed boundaries of the CRT. This decision was based on feasibility, where designing a generator was outside of the research's scope.

ABB's low speed permanent magnet generator's rotational velocity was selected as the guiding parameter to reduce the number of contra-rotating combinations. Their technical specifications, as provided by ABB (2012) were:-

- Powers up to 3 MW.
- Rated speed between 14 rpm and 30 rpm.
- Voltages from 690 V to 3300 V.

Equation (5.11) was defined to reduce the number of *contra-rotating cases*. With the lower boundary of the generator's rotational speed set to determine the CRTs with the highest total rotational velocity, 26 665 CRT combinations were found. This limit was set to reduce the torque

in the generator, and consequently the required electromagnetic material (Porter et al. 1986), the main cost component of the generator which also influences the LCOE.

$$\omega_{tot} \geq 14 \text{ rpm} \quad (5.11)$$

The final selection was made based on an economic feasibility study, where power output was compared against the reference LCOE (LCOE_{Ref}) value for each of the *contra-rotating cases*. The LCOE_{Ref} was calculated using the method detailed in Section 6.4.5, where the generator adaptation cost was not considered. The 200 CRT combinations with the highest power-lowest LCOE_{Ref} ratio (Figure 6.10) were selected, as described in Section 6.4.5. From the 200 possibilities, predicted power output could vary up to 18% with a LCOE_{Ref} variability up to 4%. The aim of this study was to determine if a device is economically (and technically) feasible to operate in low speed conditions, hence the low LCOE_{Ref} was considered the main selection parameter.

It was found that all 10 configurations with the lowest LCOE_{Ref} were 3 – 2 CRT, and they differed in the expected power output and cost by a maximum of 0.6% between them. The selected CRT combination to model with CFD (highlighted in Figure 6.10) had the averaged expected LCOE_{Ref} from the final 10 *contra-rotating cases*, £ 158.3 / MWh with a standard deviation $\sigma = \text{£ } 0.14 / \text{MWh}$, and an expected power output of 82 kW. The predicted performance characteristics and geometry specifications of this 3 – 2 CRT are detailed in Table 5.2.

Table 5.2: Contra-Rotating Turbine Theoretical Specifications

Variable	Front Rotor	Back Rotor	Total
Number of Blades	3	2	-
Blade	c	A	-
Radius (m)	6	6	6
Pitch Angle	5°	4°	-
ω (rad/s)	0.9	0.9	1.8
ω (rpm)	8.6	8.6	17.2
λ	4.5	4.5	9
Torque Coefficient	0.10	0.091	-
Torque (kN·m)	46.42	44.47	1.95
Power Coefficient	0.43	0.41	-
Power (kW)	41.8	40.02	81.8
Thrust Coefficient	0.87	0.81	-
Thrust (kN)	70.7	65.9	136.6
LCOE_{Ref} (£/ MWh)	-	-	158

To validate the predicted results with the selection process, a CFD simulation of the final model

was made as it is explained next.

5.4 Contra-Rotating CFD Model

The CFD set-up for the contra-rotating models was similar to the method explained in [Section 3.5](#). The initial geometry was made adapting two SRT to match the technical specifications listed in [Table 5.2](#), and locating them in two Multiple Frames of Reference that simulated the rotors' contra-rotation. The CRT models were analysed in steady state, and transient mode to account for the effect of the fluid behaviour in between rotors.

5.4.1 Contra-Rotating Geometry

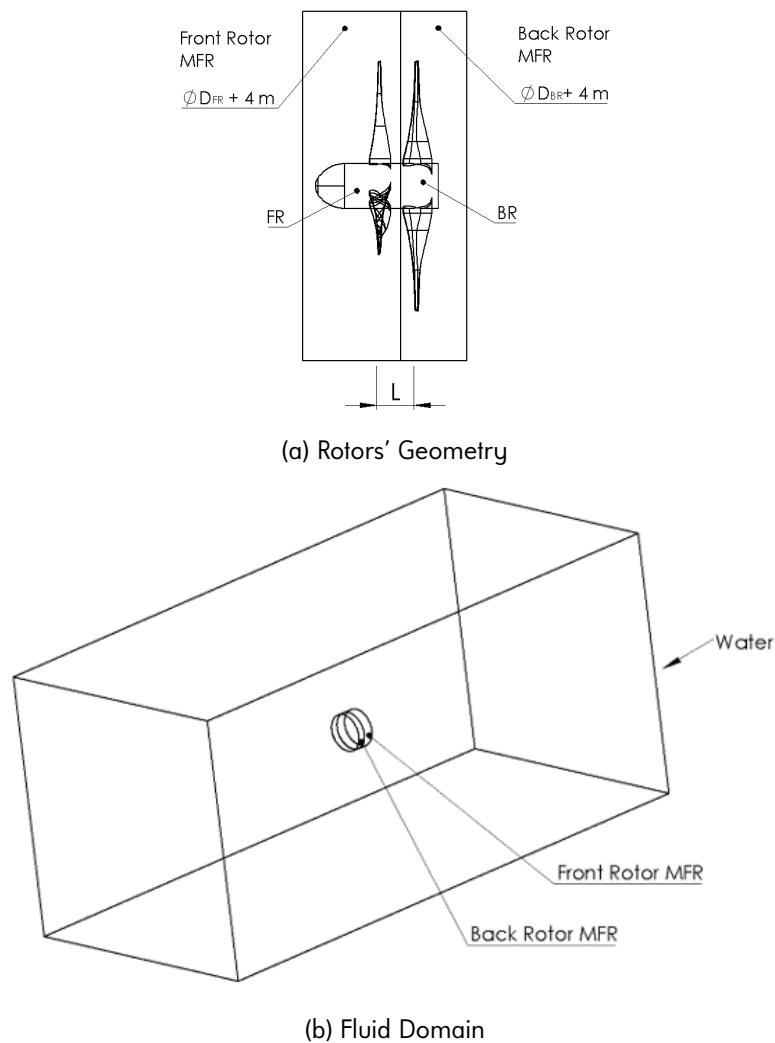


Figure 5.8: Contra-Rotating Models' Diagram

The FR's geometry was the same as its single rotor turbine. The BR was created using a

hub without nozzle, and the blades' leading edge facing the FR's opposite direction (mirrored from the original design). [Figure 5.8a](#) details the geometry parameters considered: the Front and Back Rotors' diameter, D_{FR} and D_{BR} , and their blades with respective pitch angles. The values used for each of these parameters are listed in [Table 5.2](#).

To obtain the maximum power output (Clarke et al. [2007b](#); Kubo et al. [2008](#)) the distance between rotors L measured from the blades' pin location was kept at $0.125D = 1.5$ m, the closest proximity possible when creating the geometry. The distance from blades to front and back of the hub was kept constant, matching those from the SRT configurations.

The Sea Domain-b shown in [Figure 5.8b](#) was used to model the 3 – 2 CRT. Two cylinder shapes matched each rotor's rotating boundary, and the rotors were directly connected to each other, leaving space between blades and the MFRs' boundaries to capture the fluid behaviour in that region. The MFRs radii was the same for both rotors, 2 m larger than their radii. The CRT domain was created adapting the one previously used for the SRT CFD models, shown in [Figure 3.3b](#). Unlike the SRT domain, where only one cylinder was used to fit the turbine's MFR, the CRT's domain had two cylinders made that matched the front and back rotors' MFR dimensions as pointed in [Figure 5.8](#).

5.4.2 Contra-Rotating Mesh

The front and back rotors were meshed separately, and then merged to the domain adapted to locate two rotors instead of one. The mesh procedure followed for the contra-rotating devices was similar to the one explained in [Section 3.4](#). The sea domain was meshed using Hexa shaped elements, whereas the rotors were meshed using Tet volumes with 5 prism layers over the turbine's surface to capture the flow boundary layer. [Figure 5.9](#) shows the mesh around the CRT.

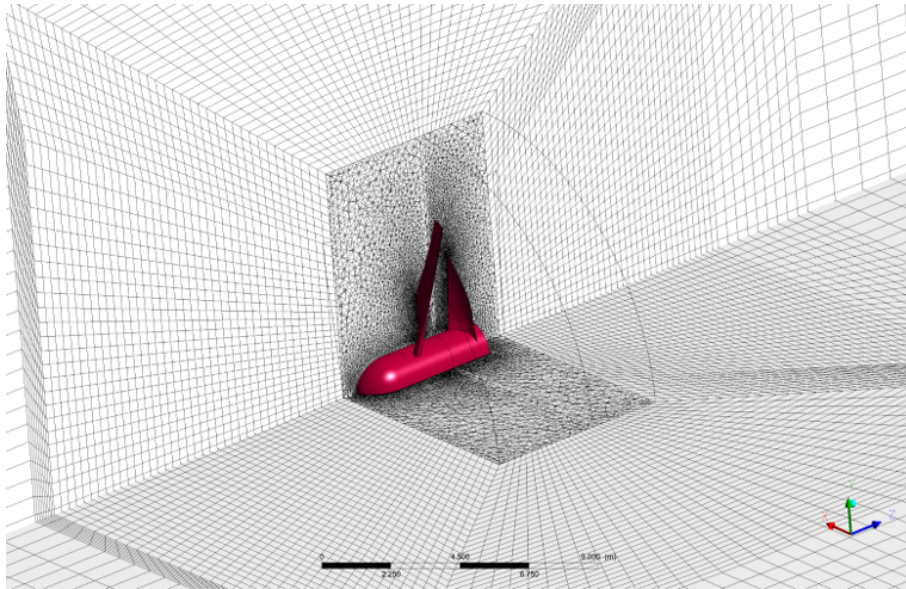


Figure 5.9: Contra-Rotating Models' Mesh

5.4.3 Contra-Rotating Model Set-up

The CRT model was analysed in steady state mode to use these results as initial conditions for transient models. The starting rotor configuration is shown in [Figure 5.10](#). The BR is rotated 20° off the FR's initial position to reduce blockage from the FR's blades in the steady state simulations.

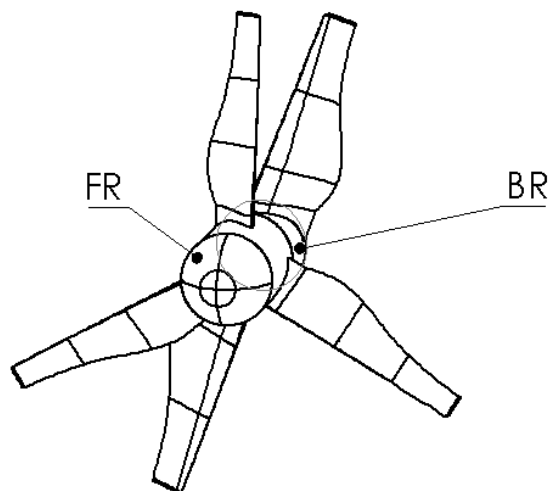


Figure 5.10: Contra-Rotating Models' Steady State Geometry

Once the steady state results were obtained, the transient simulations were run to model eleven rotations for the turbine to reach stability based on the blades' torque and thrust loads. Once the values oscillation was consistent, the simulations were considered converged. More details on the CFD set-up for the steady state and transient models is found in [Section 3.5](#).

5.5 Contra-Rotating Model Results

The 3 – 2 *CRT* geometry created was selected with the assumption that front and back rotors have a constant inflow velocity as if they were on stand alone mode (SRT configuration). The CFD results shown in this section describe the rotors' performance once they were modelled in tandem (CRT configuration). The performance characteristics were obtained using the equations described in [Section 5.2](#).

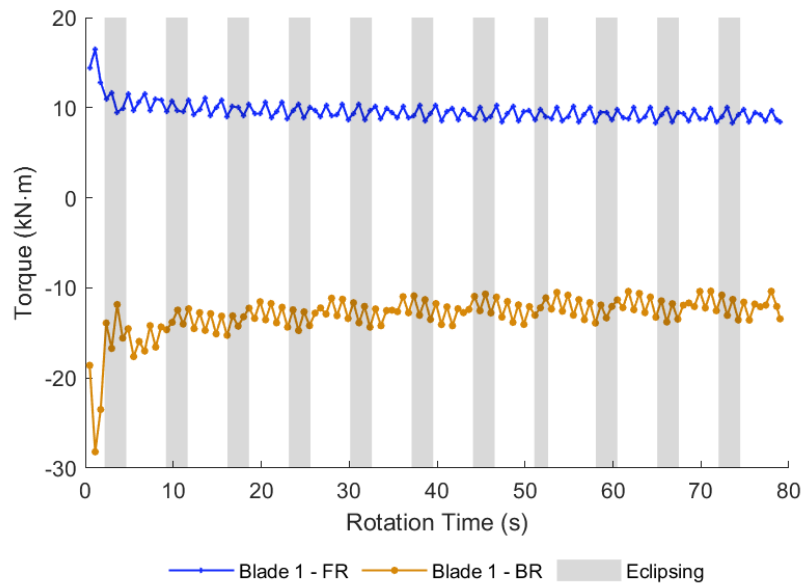
Table 5.3: Selected CRT Model Steady State Results

Variable	Front Rotor		Back Rotor		Total	
Torque Coefficient	0.045		0.028		0.054	
Torque (kN· m)	21.82	(-53%)	13.50	(-70%)	8.32	(+327%)
Thrust Coefficient	0.52		0.50		1.01	
Thrust (kN)	42.03	(-41%)	40.31	(-39%)	82.34	(-40%)
Power Coefficient	0.20		0.13		0.33	
Power (kW)	19.64	(-53%)	12.15	(-70%)	31.79	(-61%)

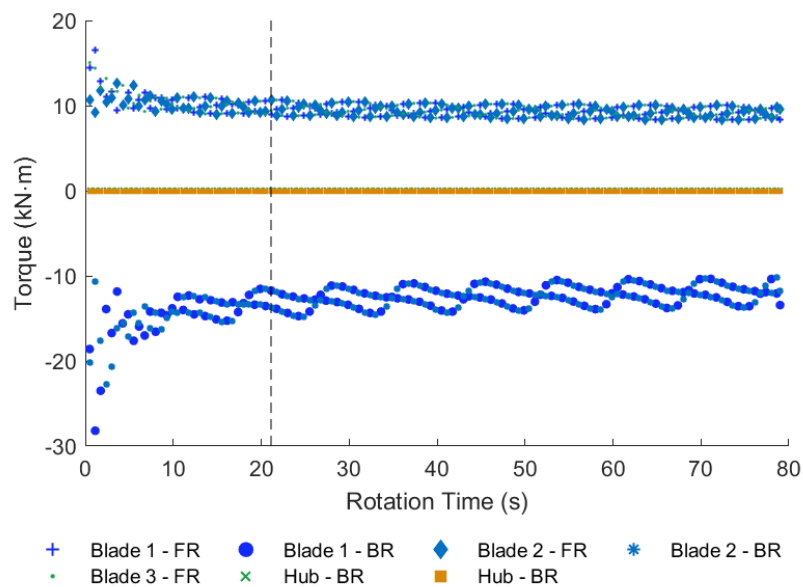
To determine the CRT's performance characteristics, the selected configuration rotors were modelled as steady state to obtain initial values, and then in transient conditions to capture the fluid interaction between front and back rotors. The results obtained from the steady state simulation are shown in [Table 5.3](#), with the percentages in brackets showing the results difference with the predicted values from [Table 5.2](#) in page 112. The torque and power outputs differed by more 50% on the FR's performance, whereas the BR's differ by 70% with respect to the predicted theoretical values. Total torque was more than three times the expected result with a difference of 40% between the two rotors, power was less than 60% from the initial matching forecast, and thrust was reduced in total and each of the rotors by about 40%.

These results are only valid for the specific position at which the CRT was modelled. To determine the performance characteristics which consider the two rotors' interaction, the transient simulation's results were analysed.

[Figure 5.11](#) shows the CRT's transient torque results for eleven rotations (79 s). Using the data from one blade belonging to front and back rotors as reference, Blade 1 - FR and Blade 1 - BR respectively, the torque's behaviour during the simulated time is illustrated in [Figure 5.11a](#). The FR's blade torque oscillated around a constant value (~ 10 kN·m), whereas the BR's torque oscillation pattern varied periodically during each rotation as the blades were affected by the FR's eclipsing. This phenomenon occurs when the FR and BR blades position in the XY plane



(a) Front and Back Rotors' Blade 1



(b) Front and Back Rotors' Blades and Hubs

Figure 5.11: Transient Torque Variation

matches, blocking the incoming flow to the BR and affecting its torque output.

To illustrate the eclipsing behaviour the grey sections in [Figure 5.11a](#) display the time at which the position of the BR's Blade 1 leading edge matches the position of the FR's blades leading edge in the XY plane as they rotate in the opposite direction. The eclipsing sections, per rotation, begin at the moment when the BR Blade 1's leading edge matched the FR Blade 1's leading edge

and end when the BR Blade 1's leading edge matched the FR Blade 3's leading edge. These results showed how when the turbine started rotating the BR's torque was highest when the fluid was not interrupted by the FR blades before reaching the BR. However, as the turbine kept rotating and the eclipsing happened periodically the torque transient behaviour was kept but the eclipsing effect was not seen immediately after.

The transient torque variation was found in all components from front and back rotors, as it is shown in Figure 5.11b. The first 22 s of simulation represent the turbine's torque variation from still (steady state) to constant rotation, where the interaction between front and back rotor was captured by the CFD transient model. Based on this the device's performance characteristics were then measured during the 'stable' rotation time, from 22 s to 79 s. Due to computational capabilities, these 57 s were considered representative of the CRT's constant rotation after start-up.

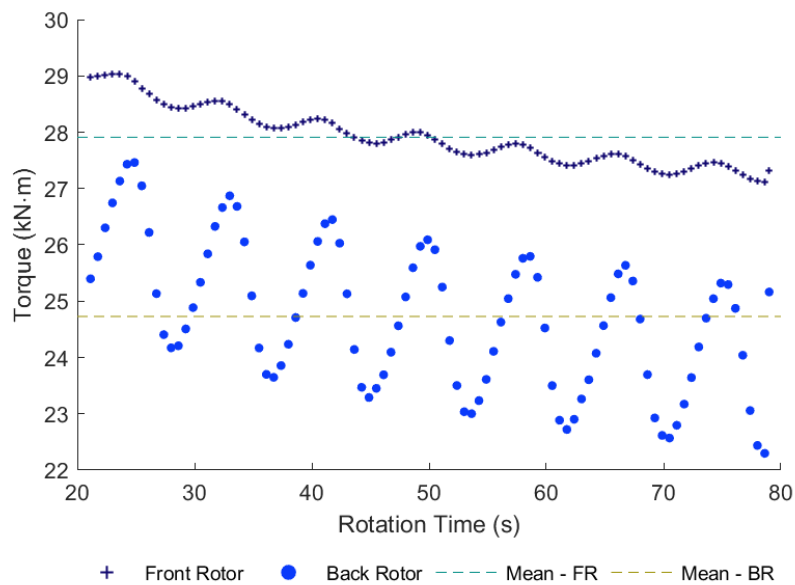


Figure 5.12: Contra-Rotating Rotors Transient Absolute Total Torque Variation

Total torque and thrust variations for each rotor, during these 57 s, are shown in Figure 5.12 and Figure 5.13, with absolute values displayed for reference. Mean values of torque and thrust were used to calculate the performance characteristics summarised in Table 5.5. They are shown with dotted lines in the figures, and their standard deviations are listed in Table 5.4.

The final transient results of the CRT simulation are shown in Table 5.5, with the percentage difference from the expected performance characteristics in brackets. The results proved that

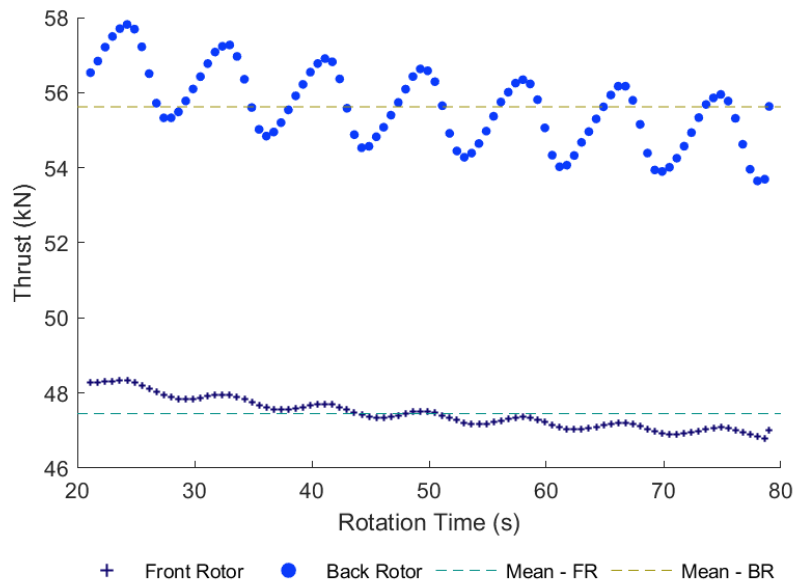


Figure 5.13: Contra-Rotating Rotors Transient Total Thrust Variation

Table 5.4: CRT Model Torque and Thrust Standard Deviations

Variable	Front Rotor	Back Rotor
Torque (kN· m)	0.51	1.28
Thrust (kN)	0.41	1.02

when characterising a CRT using CFD, transient simulations are needed to capture the rotors' interaction. Data showed that steady state results under predicts the turbines' output, and that the output varies depending on the rotors' blades' location with respect to each rotor.

Table 5.5: CRT Model Transient Results

Variable	Front Rotor	Back Rotor	Total
Torque Coefficient	0.057	0.051	0.069
Torque (kN· m)	27.91 (-40%)	24.73 (-44%)	3.18 (+63%)
Thrust Coefficient	0.59	0.69	1.27
Thrust (kN)	47.49 (-33%)	55.62 (-16%)	103.07 (-25%)
Power Coefficient	0.27	0.23	0.50
Power (kW)	26.24 (-40%)	22.26 (-44%)	48.49 (-41%)
LCOE _{Ref} (£ / MWh)	-	-	214 (+35%)

The transient data showed that the predicted performance for each single rotor was not the same when they were put together in tandem. The power output from each rotor (and in total)

was reduced by $\sim 40\%$ from the matching prediction, but the $C_p=0.5$ was higher than any of the SRT analysed in [Chapter 4](#).

The power output per rotor depends on the torque obtained from the simulation results, which is affected by the interaction between front and back rotors with the fluid during the turbine's rotation. For the modelled CRT, each rotor's torque output was reduced by $\sim 40\%$ from the expected value. When predicting the torque output based on the performance characteristics equations described in [Section 2.2.1](#), open flow conditions before and after the HATT were assumed (i.e. single disc blockage). Hence, when analysing each of the rotors in the CRT configuration individually with these set of equations, the effect of fluid interaction between rotors in the pressure differential required for power extraction was not considered. This effect was captured during the CFD simulations, where the FR's torque reduction was caused by the BR's blockage created immediately downstream the FR. Similarly, the BR's torque output decreased with the FR's rotation affecting the BR's upstream flow profile, and causing blade eclipsing as explained above.

The averaged total torque increased by 63% from what it was predicted when the CRT was selected, meaning that a difference between rotors torque of 11% was measured. The torque difference between rotors also varied throughout the CRT rotation, as shown in [Figure 5.14](#). During the simulation time, this difference changed from 1.5 kN·m to 5 kN·m ($\leq 80\%$ than the SRT on their own), achieving the near-zero torque reaction with this configuration. Even though this is higher than the 5% restriction when matching the rotors, a reduction of 90% in net torque was achieved when compared to a SRT. This translates to simpler supporting structures for the device installation reducing capital and operational costs of a tidal stream power plant.

The effect of fluid interaction between the CRT rotors was also found on the net thrust measured. The loads on each rotor were less than those predicted during the CRT selection process. Though the thrust coefficient was lower for each rotor when compared with their SRT equivalent, the modelled CRT had a thrust coefficient above one. These results could translate to higher capital costs for the supporting structure required by the CRT when compared to a SRT due to the loads it must withstand. Nonetheless, the effect of these costs on the total cost for power plant must be compared the other benefits of using a CRT over a SRT: (i) simpler structure, (ii) smaller rotor, (iii) higher rotational velocities that would eliminate the need for a gearbox, and (iv) near-zero torque reaction.

Using the scales created by Ocean Energy Systems et al. (2015), the predicted reference

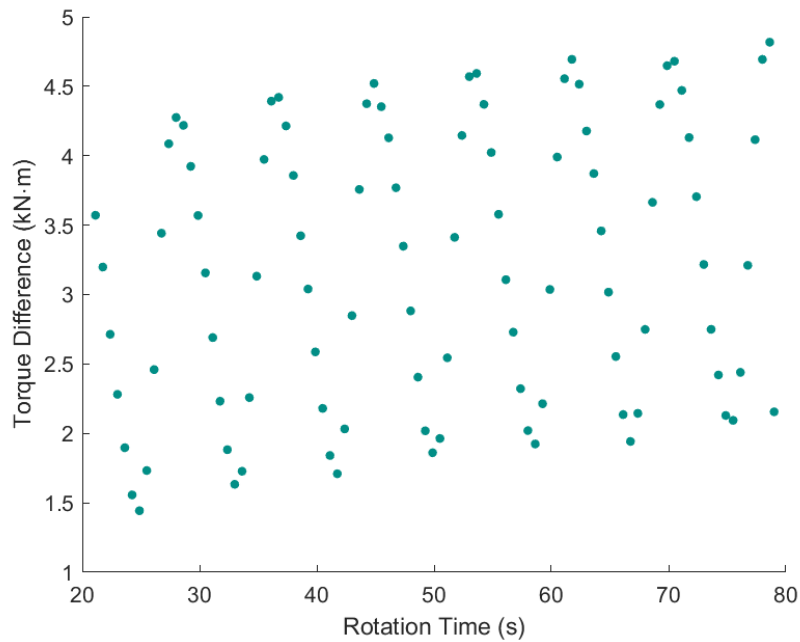


Figure 5.14: Contra-Rotating Rotors Total Torque Difference

LCOE of £ 158/MWh would locate the CRT within the range of commercial scale technologies (£ 88/MWh - £ 188/MWh), but with the results from the transient simulation this reference LCOE incremented to £ 214/MWh categorising the device within the second array stage (£ 88/MWh - £ 188/MWh). Using this value as a benchmark, it is possible to determine how the costs could be reduced in order to make a tidal stream power plant that uses the proposed CRT competitive when operating in low velocity conditions.

This chapter proved that it was technically feasible for CRT to operate in 1.2 m/s tidal velocities. The following chapter expands the results of the economic feasibility of the geometries studied in [Chapter 4](#) and [Chapter 5](#), and provides a more detailed LCOE calculation for the CRT if it was to be installed in a tidal stream power plant in the UK to determine cost reduction opportunities, and its applicability to Costa Rica.

Chapter 6

Economic Feasibility

To determine the economic feasibility of the rotor geometries modelled in [Chapter 4](#) and [Chapter 5](#), a levelised cost of energy (LCOE) was calculated for the SRT and CRT if they were to be used in a hypothetical tidal stream energy project based in the UK. Results obtained in [Section 6.4.4](#) were used in [Section 4.6](#) to analyse the SRT's economic feasibility. Likewise, results obtained in [Section 6.4.5](#) were used in [Section 5.3.3](#) and [Section 5.5](#) to select a CRT, and analyse its economic feasibility respectively.

This chapter describes how this economic tool has been used for tidal energy power plants, and gives a background of the theory used in this analysis. Then the LCOE calculation method used for reference in previous chapters and its results are presented. Using the reference data as a benchmark, the economic feasibility analysis was expanded for the CRT with a more detailed LCOE calculation that provided cost reduction opportunities which would make the proposed configuration commercially ready. The results were then used for reference to determine feasibility of a similar project based in Costa Rica.

6.1 Economic Feasibility Background for TSTs

Tidal stream energy extraction is not yet used in full size commercial scale power plants, but research has been done to determine its economic feasibility once the technology is ready. Early studies by Y. Li et al. (2011) suggested that tidal generation predictability was not enough for costs to break even when included in the electricity matrix, and it represented low-capacity credit investments. Since then, further operational experience, planning strategies, supply chain reliability, and economic assessment have been encouraged to reduce installation and operation costs (A.S Bahaj 2011).

The LCOE has been widely used by researchers such as Ioannou et al. (2017), Myhr et al. (2014), Segura et al. (2017), López et al. (2020), Barbarelli et al. (2018), Gifford et al. (2013) and Neary et al. (2014a); governmental organisations like DBEIS (2016), Instituto Costarricense de

Electricidad (2017) and U.S. Energy Information Administration (2019); and international agencies (Danish Energy Agency 2018; Carbon Trust et al. 2006; Ocean Energy Systems et al. 2015; ORE Catapult 2018b; SI Ocean 2013) to predict, analyse, and compare electricity generation costs. For tidal stream energy technologies costs data are limited, due to the lack of commercial projects (Uihlein et al. 2016), leading research to predict them with the available information and knowledge exchange from other technologies such as offshore wind turbines (Magagna et al. 2015). Therefore, when using the LCOE metric it is important to account for the weaknesses it inherently includes, as suggested by Aldersey-Williams et al. (2019), and to understand the assumptions taken when following a specific model (Foster et al. 2014).

Within the tidal stream technology sector, Y. Li et al. (2011) created an integrated LCOE model (using estimated costs) that would consider the total power output of a tidal farm depending on the hydrodynamic performance, the operation and maintenance costs that would change depending on the farm size. Allan et al. (2011) used the method proposed by Carbon Trust et al. (2006) to estimate the LCOE for wave and tidal stream devices, and compared it with 10 other technologies in the UK, showing large variability for the marine energy calculations that were caused by uncertainty in costs assumptions. To account for the uncertainties created with the use of LCOE, Dalton et al. (2015) provided a guide for an economic assessment of wave and tidal energy projects from the public and private perspective, and described how qualitative and quantitative risk analyses can be made with data based on assumptions that help understand the results' limitations.

Another LCOE calculation method was proposed by Vazquez et al. (2016b), where a levelised capital expense that accounts for turbine size, distance to shore, site's depth, and power output was defined. The set of equations was combined with a bathymetry numerical model, and hydrodynamic performance prediction, to select locations for tidal stream power plants development (Vazquez et al. 2016a). Vazquez et al. (2017) included the calculation of operational expenditures to the LCOE equations based on data from Ernst & Young (2010), and considered other uses a specific marine energy site could have to narrow locations where the tidal farm would be placed. In further research Astariz et al. (2015) analysed how the LCOE was affected by externalities -*positive or negative consequence of an economic activity that is experienced by unrelated third parties*-, and by comparing the results to other sources they determined that governments should support marine energy with subsidies for it to be competitive within the electricity generation sector. This LCOE calculation approach was used in the present research

to obtain reference LCOE values, as discussed in [section 6.4](#).

Dalton et al. (2015) noted that the LCOE results are useful for the private sector to help them determine if a project provides an acceptable return, based on the risk they are taking. Hence, new tidal turbine designs' feasibility are not limited to their technical specifications, their commercial application depends on economic benefit if they were to be deployed. Following that reasoning, Johnstone et al. (2013) analysed how second generation designs could reduce the capital and operational costs for tidal energy production. Similarly, Zupone et al. (2017) studied the case for their SintEnergy turbine design to calculate its pre commercial stage LCOE, and Barbarelli et al. (2018) extended the calculation for an array configuration. López et al. (2020) also proposed a tool that predicted the LCOE for second generation devices using the single rotor GISMEY design as a reference. Their method considered a conceptual array configuration; obtained the components costs with data from Fingersh et al. (2006) and The Crown Estate (2010) and commercial values when possible; and the operation costs were based on their own model which included reliability data for the main components of the power plant, window periods to service the devices, and simplifying the mete-oceanic model.

Various LCOE methods that combine tidal turbine arrays have also been published. Neary et al. (2014a) created an open source methodology that considered design, manufacturing and deployment, operations and maintenance strategy, and environmental compliance. All these modules were linked to the LCOE calculation, which could be made for a 10 - 100 units tidal farm. The effect of device interaction on LCOE has been analysed by Vazquez et al. (2015), where a cost variation of more than 20% due to hydrodynamic effects were found. It was determined that a cost reduction could be made if the farm was modified based on longitudinal spacing, array shape, size, and individual positioning of the turbines to maximise the power output, as shown by Vazquez et al. (2016c). To design a tidal farm, research by Culley et al. (2016) proposed an open source automated array design for tidal turbines that maximises the farm's power output and then includes cable cost prediction to optimise the farm distribution.

As a reference for wave, tidal, ocean, and river technologies Neary et al. (2014a) created models that can be used as a guide to different designs that have matching characteristics to the ones they proposed. Using a similar procedure on the level of details considered and the reporting style proposed by LaBonte et al. (2013), Neary et al. (2014a) described how to predict the costs for a marine energy project based on the information available for each case's device design, maintenance plans, and environmental compliance. Their assumptions

were based on previous research done for wind energy (Fingersh et al. 2006; Malcolm et al. 2006, 2003), environmental siting and permitting requirements for the devices in study (Neary et al. 2014b; Copping et al. 2011, 2013), vendor estimates, and cost data estimated by RE Vision Consulting LLC. These reference models were used in the present research to obtain a more detailed cost prediction for the CRT configuration proposed in Chapter 5, and the adaptation made is explained in Section 6.5.

LCOE results can be used to compare technologies with respect to each other and how costs change depending on when it was computed (or how they are projected). In the public sector, DBEIS (2016) and Logan et al. (2017) reported the LCOE values (and their calculation assumptions) for different energy sources, which can be used for policy, planning, and decision making. Ernst & Young (2010) calculated the costs for developing marine energy in the UK, and their results have been used to analyse new turbine designs and propose tidal stream farms. Carbon Trust et al. (2006) proposed a LCOE estimation methodology for marine energy and, a few years later when more data was available from developers, analysed how the costs could be reduced (Carbon Trust Marine Energy Accelerator 2011). More opportunities on how to decrease the predicted LCOE by modifying the devices, structures, foundations, power take off, control, connection, installation, operations and maintenance were also given by SI Ocean (2013).

This economic tool is also used for specific locations to understand how the market is changing in each country. ORE Catapult (2018a) showed how the LCOE for tidal and wave energy could decrease in the following years in the UK. Marine Energy Research and Innovation Center (2018) analysed Chile's supply chain readiness, and predicted LCOE for three different technologies that could be suitable for the country's marine resources. The World Energy Council (2016a) analysed the global situation for wave, tidal, OTEC, and offshore renewable energies, and used the LCOE as parameter to compare marine energy costs with other electricity sources. These reports are also useful to countries like Costa Rica, where their electricity generation plans (Instituto Costarricense de Electricidad 2017) can be made by comparing their reality to the new technologies' commercial stages and costs.

In 2015 OES presented a report Ocean Energy Systems et al. (2015) that gave an accepted (World Energy Council 2016a) general reference of ocean energy technologies LCOE values. The obtained results for tidal stream technology are summarised in Figure 6.1, with the numbers given in U.S. Dollars from 2014, and data obtained given by developers to the authors. The dark mid-range area shown in the graph represents an uncertainty of $\pm 30\%$ in the values, whereas

the dotted lines represent the maximum and minimum values provided by the developers. The results are listed in [table 6.1](#), with details of project capacity and costs variations. For consistency in the values presented in this chapter, the costs were exchanged to 2014 British pounds using an exchange rate of £ 1 = \$ 1.65 (X-Rates 2019), and then updated to 2019 British pounds using a rate of £₂₀₁₉ 1 = £₂₀₁₄ 1.11 (Official Data Foundation 2020).

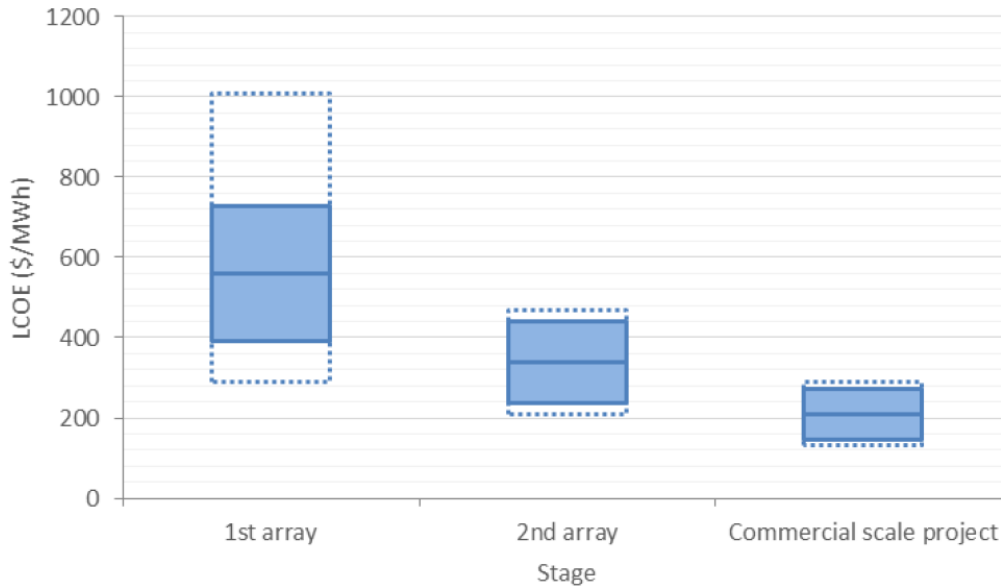


Figure 6.1: LCOE for Tidal Stream Turbines based on Technology's Deployment Stage. Source: Ocean Energy Systems et al. (2015)

Table 6.1: LCOE Costs per MW h. Source: Adapted from Ocean Energy Systems et al. (2015)

Deployment Stage	Capacity	Minimum	Average	Maximum
First Array	0.3 MW - 10 MW	£ 188	£ 310	£ 673
Second Array	0.5 MW - 28 MW	£ 141	£ 229	£ 316
Commercial Scale	3 MW - 90 MW	£ 88	£ 141	£ 188

A more recent study published by ORE Catapult (2018b) estimated that the cost of electricity in the UK when produced with tidal stream turbines, could be reduced to £ 150/MW h once 100 MW power plants are installed, which could then be further reduce to £ 90/MW h and £ 80/MW h when 1GW and 2 GW are installed, respectively. Based on their cost of electricity generation, an economic feasibility analysis was made for the turbines considered in this thesis to determine their commercial readiness according to these estimations. This chapter first shows the calculation of a reference LCOE for the Single Rotor Turbine (SRT) proposed in [Chapter 4](#) and to select the Contra-Rotating Rotors Turbine (CRT) that was modelled in [Chapter 5](#). Then a more detailed LCOE calculation, made for the modelled CRT using the CFD simulation's results

as the device characteristics, is described. With the final cost the CRT's economic feasibility was determined for the UK, and its possible application in Costa Rica was considered.

6.2 Economic Feasibility Theory

An economic feasibility study is done to determine if the economic advantages are greater than the costs (Cambridge University Press 2019) for a technically viable project. From the perspective of a private investor the study must determine if the project provides an acceptable return at an acceptable risk (Dalton et al. 2015).

For renewable energy projects, such as tidal stream energy extraction, economic tools help dictate the financial feasibility of a new technology. For the purpose of this research, the most commonly used tools (expected cash flow, net present value and internal rate of return (Segura et al. 2017)) are described to understand the calculation of LCOE, which was obtained for comparison of the previously proposed rotor geometries when operating in low speed conditions. A brief description of the weighted average capital cost (WACC) and progress ratio terms are given, but other alternative metrics, such as the undiscounted cost of energy (UCOE), the discounted costs cost of energy (DCCOE), and the total cost of energy (TCOE) are not considered for this study because of their limitations and lack of use in the sector (Aldersey-Williams et al. 2019).

6.2.1 Expected Cash Flow

Cash Flow is a finance statement that it is used to predict how much money will be moved in and out of a project (Cambridge University Press 2019), and it shows the amount of 'cash' that will be available throughout the expected lifetime of said project. All the projected income and expenses, which should be based on real projections and assumptions, are registered in the statement.

The calculation is made on a time period basis. When used in a project's feasibility study a future prediction is made, generally yearly, starting at year 0 where the initial investment is made. The Cash Flow is the starting point to obtain other financial parameters required to make the economic feasibility analysis of a project.

In Figure 6.2 a basic cash flow diagram for a renewable energy project is shown. The investment made in year 0 accounts for the initial capital expenses, and for years 1 to n the incomes are from energy sales, whereas expenses account for maintenance and operational

costs to keep a power plant functioning.

	Year 0	Year 1 to Year n
Cash Inflows	—————	Energy Sales
< Cash Outflows >	< Initial Capital Expenses >	< Operational Expenses >
<u>Available Cash</u>	Investment	Earnings

Figure 6.2: Cash Flow Diagram

6.2.2 Net Present Value

The Net Present Value (NPV) is defined as the value of an investment's future net cash flow after the cost of the original investment has been subtracted (Cambridge University Press 2019). It is a tool that enables stakeholders to know how much profit (or losses) will be made at the end of a project's expected lifetime. The NPV formula is shown in equation (6.1).

$$NPV = \sum_{n=0}^{LT} \frac{C_n}{(1+r)^n} \quad (6.1)$$

The number of years the project is expected to last is represented by LT , r is the discount rate at which the cash's value will be depreciated and C_n is the capital expense or profit made on year n . The cash flow created for the project, as illustrated in Figure 6.2, is used to obtain the data needed per year.

6.2.3 Internal Rate of Return

The Internal Rate of Return (IRR) indicates the efficiency of a project depending on the amount of money earned each year from a particular investment without considering things such as interest rates or inflation (Cambridge University Press 2019). The value is given in a rate quantity which can then be compared to other investment options. To obtain the IRR of a project equation (6.1) is equalled to 0 and the discount rate r that makes this happen is considered the Internal Rate of Return. Equation (6.2) describes the IRR formula.

$$NPV = \sum_{n=0}^{LT} \frac{C_n}{(1 + IRR)^n} = 0 \quad (6.2)$$

Developers have a minimum IRR (*cost of capital*) expected from a project before they agree to invest on it. For the investors to make a final decision they compare the project's IRR with their NPV and other factors affecting the project itself, such as LCOE. In Figure 6.3 the NPV and IRR's effect on the decision making process is shown. When a high IRR and a positive NPV (quadrant I) are predicted a project is considered economically feasible, and when the IRR is low and the NPV is negative (quadrant III) a project is considered uneconomically viable. Quadrant III projects should be halted because they have financial losses, and an alternative should be considered.

When the conditions land in any of the other quadrants (II - IV), the relevance, benefits and risks of the project should be considered. A 'low' IRR with a positive NPV (quadrant IV) project could be more attractive when the risks of the investment are lower than a ground-breaking project where the outcome is not yet clear. Emergency related projects tend to be on the opposite end (quadrant II), where there will be no earnings and the benefit is not monetary but the project must be completed regardless. Other examples of situations where qualitative factors may outweigh the financial analysis in the decision making process are (Saylor Academy 2012): (i) investing in new production facilities to maintain the leadership in innovation qualification, and (ii) investing in pollution control devices for social benefits.

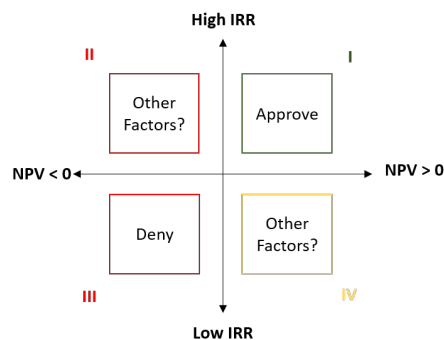


Figure 6.3: NPV - IRR Decision Making Process. Source: Adapted from Bishop (2012)

6.2.4 Weighted Average Capital Cost

Cost of capital is defined as the amount of money that a company must pay out in dividends to its shareholders, and in interest on bonds and other loans (Cambridge University Press 2019). The

Weighted Average Capital Cost (WACC) can be based on the hurdle rate (DBEIS 2016) definition: *the minimum project return that a plant owner would require over a project's lifetime on a pre-tax real basis and is set to reflect different financing costs for different technologies* (Aldersey-Williams et al. 2019). The WACC represents the real discount rate (Neary et al. 2014a), the appropriate rate, to be used by a firm to assess the perceived risk of the investment project (Allan et al. 2011).

6.2.5 Progress Ratio

The progress ratio is *the value of the learning rate subtracted from one*, where the learning rate is *the percentage that the cost of production falls with each doubling of the total number of units produced*. These two metrics try to account for reductions in costs that arise with economies of scale and technology improvements (Allan et al. 2011).

Progress ratio estimates are useful due to the lack of data for current and future costs of ocean energy (Uihlein et al. 2016), however caution must be taken when using them, particularly in emerging technologies (Dalton et al. 2015). The main concerns (Dalton et al. 2015) about using these rates are: (i) progress ratios are not always transferable between sectors, (ii) data provided to obtain progress ratios can be uncertain, (iii) the cumulative installed capacity at which the cost reduction occurs is unclear, (iv) progress ratios are time varying, and (v) it may be possible that the expected cost reductions have already happened if the ocean renewable sector relies on know-how developed by a different sector.

More detailed study on learning rates in the marine energy sector found that to achieve the required cost-reduction the level of deployment must increase enabling accelerated learning effects from experience and market size. This can be done with innovation and disruptive technologies that can create step changes in the cost of energy (MacGillivray et al. 2014), which can then provide more data to predict more accurate learning rate factors.

6.2.6 Levelised Cost of Energy

Depending on who is calculating the variable (e.g. researchers, governmental bodies, consultancy organisations, developers, etc.), the levelised cost of energy (LCOE) definition varies slightly, and so does the method to obtain a result (Foster et al. 2014). For the purpose of this research the definition of LCOE, where energy refers to electricity generation, is the discounted life time cost of ownership and use of a generation asset, converted into an equivalent unit of

cost in £/MWh (DBEIS 2016). To calculate the LCOE the costs incurred during the project's lifetime are brought to the present, and then related to the present value of the projected electricity that will be generated during this time period (equation (6.3)).

$$NPV = \frac{NPV \text{ of Total Costs}}{NPV \text{ of Electricity Generation}} \quad (6.3)$$

The numerator of equation (6.3) is obtained by substituting C_n of equation (6.1) with the capital and operations costs involved in a power plant project. The denominator is obtained by substituting C_n of equation (6.1) with the electricity generated in the power plant's lifetime. Then, the LCOE equation can be rewritten as equation (6.4).

$$LCOE = \frac{\sum_{n=0}^{LT} \frac{CAPEX+OPEX}{(1+r)^n}}{\sum_{n=1}^N \frac{E_n}{(1+r)^n}} \quad (6.4)$$

In the numerator of equation (6.4) *CAPEX* refers to Capital Expenditures that translates to I_n , the Investment in equation (6.5), and *OPEX* refers to the Operational Expenditures that translates to M_n and F_n , Operations and Maintenance, and Fuel Expenditures, respectively in equation (6.5). All these expenses are made in year n . As in the NPV and IRR (equations (6.1) and (6.2)), the expenditures are discounted from year 0, when the first capital expense occurs, but included in the formula as they occur (i.e. operational expenses are included from year 1 onwards). In the denominator, E_n represents the Electricity generated (and sold at constant price during the lifetime of the project) (Segura et al. 2017) in the year n starting from year 1, when the power is generated. The discount rate used to obtain the present value of the different components is labelled by r , and is considered constant during the project's lifetime (Segura et al. 2017).

$$LCOE = \frac{\sum_{n=0}^{LT} \frac{I_n+M_n+F_n}{(1+r)^n}}{\sum_{n=1}^N \frac{E_n}{(1+r)^n}} \quad (6.5)$$

The LCOE definition allows users to adapt the measurement to their needs making it flexible to use, but when used to compare LCOE values for different technologies and/or scenarios the circumstances and assumptions used for the calculation must be detailed.

6.2.6.1 LCOE Parameters

When calculating the LCOE for a specific project, the level of detail for the costs that are accounted depends on the method followed, such as those described in [Section 6.1](#). The main factors to consider when obtaining the LCOE are (Carbon Trust et al. 2006; Dalton et al. 2015; Hardisty 2009):-

(1) **Discount Rate:** The value of the discount rate should be selected from referenced sources, such as the ones used by government bodies (DBEIS 2016; Logan et al. 2017) and international agencies (SI Ocean 2013; Ocean Energy Systems et al. 2015). Depending on the project's location, the investors' options and how the LCOE calculation is going to be used, the discount rate differs. The LCOE result can vary significantly depending on the discount rate value and a sensitivity analysis would show the fluctuation, using the investor's WACC as the starting point.

(2) **Location:** The location for where the LCOE is calculated affects the result, because the costs related to installation, maintenance and operations depend on the place where the power plant is located: access, required infrastructure, regulations, and personnel availability, are some of the aspects that are influenced by the location. Also, the existing energy matrix affects directly the operation time of the power plant.

Once a location is selected the variables that are involved in the LCOE for a specific project can be determined (i.e. the technology selection, the discount rate used for comparison with other projects, and the conditions under which it will be operating).

(3) **Technology:** The technology selection for a specific project is based on the resource characteristics and the availability and adaptability of the options offered by the market. The selection of one device over another might affect the LCOE result.

(4) **Costs Included:** The LCOE must include the costs incurred in installation, maintenance and operations, and decommissioning. The level of detail used to obtain these values vary from case to case depending on the device type and its supporting structure, who is making the analysis and for whom it is made (e.g. technology or energy sector).

(5) **Moment of Calculation:** When calculating the LCOE, the time when the construction is made must be clear since different years of calculation can affect the result. A country's

planning strategies differ based on their current situation, and decisions like the Paris Agreement may affect the final investment cost. If a calculation is made for a specific moment and there is a regulation change before starting the project, an analysis should be made to determine how much the original LCOE is affected. Furthermore, to find the resilience of LCOE costings the initial calculation could include some sensitivity to certain changes. This is discussed below.

6.2.7 Sensitivity Analysis

A Sensitivity Analysis is a study that shows how a result changes when the variables involved in its calculation vary, measuring the uncertainty given by the assumptions taken (Dalton et al. 2015). There are two approaches which could be used for the LCOE (DBEIS 2016):-

- (i) Changing the same LCOE variables, with a specific increase and decrease percentage, for each technology/source that is being compared. It is common to divide the components in Fuel and CAPEX related costs, which allows a direct comparison between renewable and other electricity production methods.
- (ii) Changing each of the variables of the LCOE by a specific percentage whilst keeping the rest constant. This method is used to determine how much the LCOE is influenced by each component for specific projects. The percentage used varies on who is making the calculation; per example, DBEIS (2016) used $\pm 10\%$ variation in their study to compare how uncertainties affect the LCOE of different energy sources, whereas Allan et al. (2011) and Vazquez et al. (2016c) analysed their results with a $\pm 70\%$ and $\pm 20\%$ variation, respectively. The former to determine how construction costs affected the LCOE for various electricity generation technologies, and the latter to understand how the parameters involved in their calculation affected the LCOE result.

In marine energy, the sensitivity analysis is used to compare the different designs available to extract energy with more reliable sources, such as wind, solar or thermal energy; or when a new design is proposed to determine its economic feasibility. For the purpose of this research, a sensitivity analysis was made to the LCOE calculation when comparing the geometries proposed for low velocities conditions. The second approach described above was followed and results are summarised either with a Tornado Chart; or with line charts that show how the rate at which

the LCOE changes as each variable is modified by a certain percentage, previously used by Allan et al. (2011).

6.3 Economic Analysis Procedure

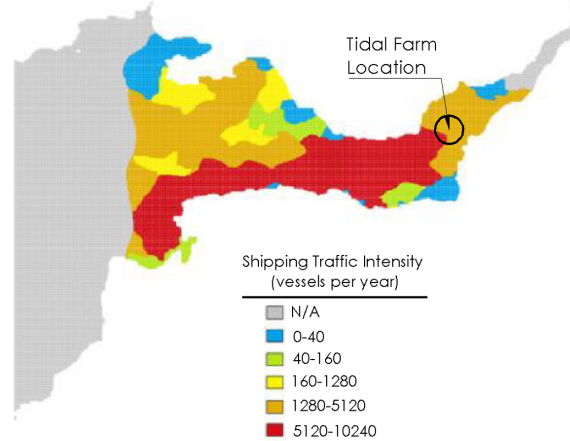
Research calculating the LCOE for Tidal Stream Energy Projects (TSEP) has been done using predictions with the limited commercial data available, and assumptions based on knowledge from other sectors. The models made to predict the LCOE for TSEP are used to compare initial results with other sources to show the cost reductions and what needs to be done for the technology to be competitive in the renewable energy market (De Andres et al. 2014). The aim of the economic feasibility study presented in this chapter aligns with work done by ORE Catapult (2018a, 2019), SI Ocean (2013) and Carbon Trust Marine Energy Accelerator (2011), where opportunities to make tidal energy technology a commercial industry were given. The research described in this thesis specifically analysed if it is economically feasible for a contra-rotating turbine, adapted from existing blade design previously used by CMERG (Mason-Jones et al. 2012; Morris et al. 2015; Frost et al. 2015) to operate in low velocity conditions, to be implemented in a tidal stream power plant. Suggestions are then made on how to reduce the proposed configuration's LCOE. The cost estimations presented in this chapter relate only to the rotors presented in Chapter 4 and Chapter 5.

The UK's leading position in the world (O'Rourke et al. 2010) with regards to marine energy research provides a good reference for countries where this resource has not yet been explored. For this reason the techno-economic analysis made in this thesis was based on the characteristics of a hypothetical tidal stream power plant, in the UK, that would use TSTs with the technical specifications of the geometries previously modelled. Using the country's detailed resource characterisation, the Severn Estuary was selected because it has matching conditions to those of the CFD models (tide velocities between 1 m/s - 2 m/s). As a reference Figure 6.4a, and Figure 6.4b show the tidal stream farm site in the map.

The procedure followed in this thesis was based on the method proposed by Carbon Trust et al. (2006), where a baseline LCOE calculation is compared with pessimistic and optimistic assumptions. The adapted version for this research includes a *Reference LCOE* calculation made with approximations used in the device selection process (pessimistic case), a more *Detailed LCOE* analysis for the final contra-rotating configuration (baseline case), and cost reduction



(a) Location in Map. Source: Esri (2018)



(b) Site Resource Characteristics.
Source: Adapted from Vazquez et al. (2017)

Figure 6.4: Tidal Stream Farm in the United Kingdom

suggestions for the device to be commercially competitive (optimistic case).

The process is illustrated in Figure 6.5, where it is shown that the reference LCOE results obtained in this chapter were previously used to: (i) justify in Chapter 4 why a CRT was a possible solution for tidal conditions with low velocity flows, and (ii) select a CRT turbine to model with CFD in Chapter 5. The CRT's simulation results were then used to expand in detail the CRT's LCOE analysis using them as the input technical specifications for the proposed power plant, to finally propose cost reduction alternatives for this low velocity technology. The boxes with text in bold represent CFD modelling, and the others calculations made using the simulations'

results. The process was divided by chapters, and the boxes with a star refer to the mention of LCOE results in previous chapters.

The second row from top to bottom of [Figure 6.5](#) refers to the reference LCOE ($LCOE_{Ref}$) calculations, which are shown in [section 6.4](#). They were obtained for all the rotor configurations analysed in this thesis using the equations proposed by Vazquez et al. (2018) to determine the capital and operational expenditures for a tidal stream power plant in the UK. The fourth row from top to bottom of [Figure 6.5](#) refers to the detailed LCOE ($LCOE_{Det}$) presented in [section 6.4](#). This calculation was based on the tidal stream and ocean currents reference models created by Neary et al. (2014a), adapting their costs and assumptions for the CRT selected in [Chapter 5](#). A comparison of both methods is made in [Section 6.5.5](#).

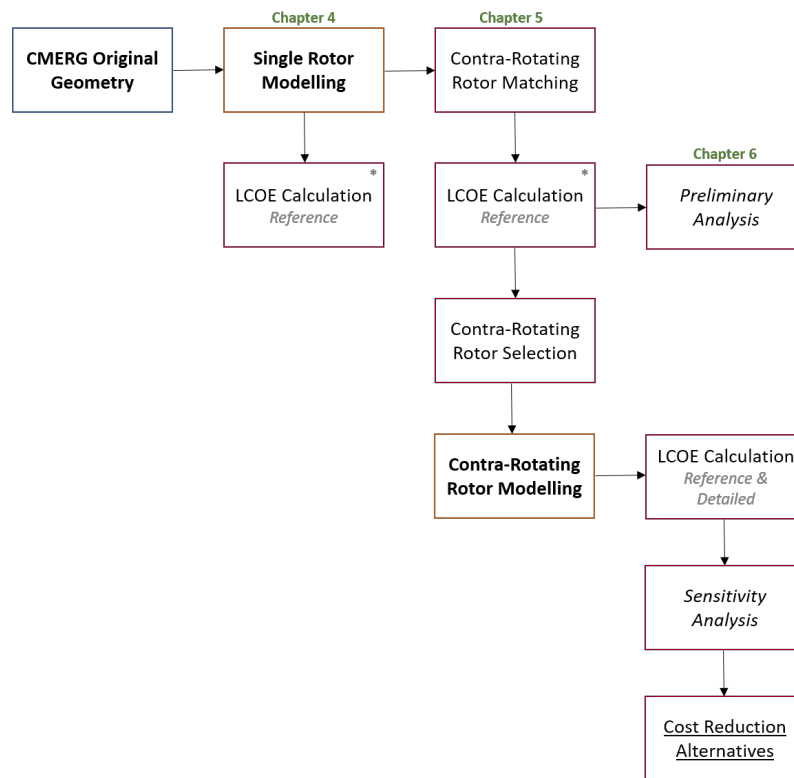


Figure 6.5: LCOE Calculation Process

Though the methods differ on how much information is considered to get a LCOE value, some assumptions were taken for both as listed below and summarised in [Table 6.2](#):-

- (1) The LCOE was calculated based on the definition given by DBEIS (2016), and described in [section 6.2.6](#).
- (2) No fuel consumption was considered because of the renewable nature of the source.

- (3) In agreement with previous research (Neary et al. 2014a; Vazquez et al. 2016b; Ocean Energy Systems et al. 2015), a project lifetime of $T = 20$ years was assumed.
- (4) Due to the uncertainty caused by progress ratios (Dalton et al. 2015), no learning rates were used.
- (5) The discount rate used was a constant $r = 10\%$ to maintain a conservative approach because TSEP involve high capital costs and they are associated with greater technological risks when compared to conventional power plants (Vazquez et al. 2015). This value was consistent with the study made by Ocean Energy Systems et al. (2015).
- (6) A constant depth of $depth = 30$ m was considered, based on the initial results of the conditions available in the Gulf of Nicoya in Costa Rica (Brito e Melo 2013) and within the range of depths for the Bristol Channel where the modelled velocity conditions are found (Vazquez et al. 2018).
- (7) The power plant would be located at a $dist = 5000$ m from shore, as shown in Figure 6.4. This assumption was based on the shortest distance to the coast from the turbines' array location.
- (8) The water was considered to have a density of $\rho = 997$ kg/m³, consistent to the temperature of $T = 25$ °C that was used to validate the numerical models.
- (9) The tidal inflow velocity $v = 1.2$ m/s was used for power prediction.

Table 6.2: LCOE Assumptions Summary

Variable	Symbol	Value
Lifetime	T	20 years
Discount rate	r	10%
Depth	d	30 m
Distance to Shore	$dist$	5000 m
Water Density	ρ	997 kg/ m ³
Inflow Velocity	v	1.2 m/s

6.4 Reference LCOE Calculation

The $LCOE_{Ref}$ calculation provided an approximate LCOE value that led to a selection of the most feasible HATT configuration to operate in low velocity conditions. The value was computed for

all SRT and CRT configurations modelled in this thesis considering the main LCOE variables: Capital Cost, Operational Cost, and the Annual Energy Production.

As described previously, the method followed was the one created by Vazquez et al. (2018), where the broad categories associated with CAPEX were considered using the percentage distribution shown in Figure 6.6, and OPEX were determined by the power production (Vazquez et al. 2016b, 2017). The equations used to calculate the $LCOE_{Ref}$ are explained next, and the general considerations taken for this particular approach are listed below:-

- (1) The power plant was considered to be commercially ready to compete in the renewable energy market.
- (2) The power plant assumed an ideal operation time of $h = 14$ h per day and $days = 365$ per year.
- (3) The power plant was assumed to be installed in the UK.
- (4) The tidal stream farm consisted of an array with $N_D = 45$ turbines.

6.4.1 Capital Expenditures (CAPEX)

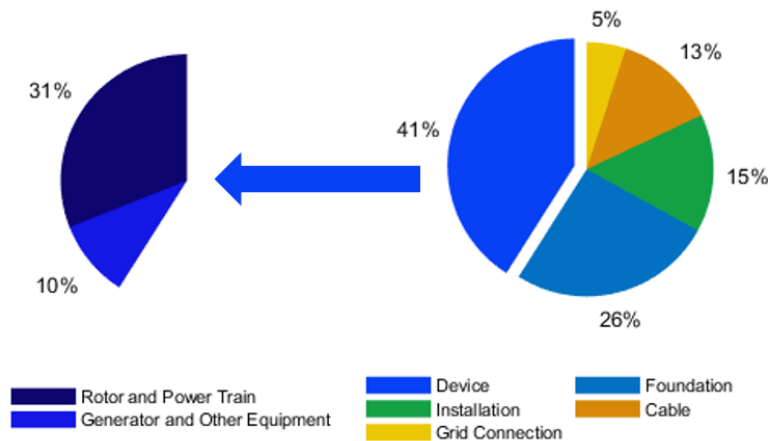


Figure 6.6: Breakdown of Capital Costs. Source: Adapted from Vazquez et al. (2016b)

The first component of equation (6.4) is the capital cost, which for the $LCOE_{Ref}$ considered the four main turbine components: rotor, cables, foundation, and installation. The rotor cost, C_R ,

includes the generator and drive train costs; and it was obtained using equation (6.6) where the diameter D , and the number of devices N_D were the variables needed. The equation was built using the function proposed by Bryden et al. (1998), and the constants were determined by Vazquez et al. (2016b) with data obtained in a previous feasibility study made for the Orkney and Shetland islands (Bryden et al. 1995).

$$C_R = N_D \cdot 80.388 \cdot D^{2.687} \quad (6.6)$$

The cable cost, C_C , was calculated using the closest distance to shore, $dist$, in metres as the input to obtain the value. Equation (6.6) shows the relationship between $dist$ and C_C , created by Vazquez et al. (2016b) based on the data from Bryden et al. (1998, 1995). These costs were calculated on the basis of a one-off hypothetical 4-bladed turbine, installed in a monopile, with a shaft connected to a 2-stage epicyclic 150:1 gearbox, and a standard marine-quality type generator (Bryden et al. 1995). The values were predicted for 10 m, 15 m, and 20 m diameter turbines; with cable distances from 200 m to 1000 m (Bryden et al. 1998). It was assumed that a single large cable would connect the turbines cluster to the distribution centre on shore.

$$C_C = 169.79 \cdot dist \quad (6.7)$$

The foundation cost, C_F , depended on the power plant's location's $depth$ in metres. According to Vazquez et al. (2016b) the cost varies with the depth range as presented in equation (6.8), which is based on a study made by Serrano-González et al. (2011) for offshore wind turbine installations. The function is based on the assumption that monopile or gravity foundations are commonly used for shallow waters ($0 \text{ m} \leq depth \leq 30 \text{ m}$); intermediate water depths ($30 \text{ m} \leq depth \leq 60 \text{ m}$) use tripods, jackets and trusses; and floating options are the best option for deep water ($depth > 60 \text{ m}$) installations.

Vazquez et al. (2017) converted (Serrano-González et al. 2011)'s equations from 2010 Euros to 2010 British pounds using an exchange rate of $\pounds_{2010} 1 = \text{€}_{2010} 1.25$ to create equation (6.8). For the purpose of this analysis the equation for shallow waters was used because it gives the lowest cost for a 30 m depth location, which is expected for a second generation technology device as the one proposed in this research.

$$C_F = \begin{cases} (0.1875 + 1.5 \times 10^{-5} \cdot depth^3) \times 10^6, & \text{if } 0 \text{ m} \leq depth \leq 30 \text{ m} \\ (0.4375 + 5 \times 10^{-5} \cdot depth^3) \times 10^6, & \text{if } 30 \text{ m} < depth \leq 60 \text{ m} \\ (0.1875 + 0.02 \cdot depth) \times 10^6, & \text{if } depth > 60 \text{ m} \end{cases} \quad (6.8)$$

To account for installation and grid connection costs are included in the CAPEX proposed by Vazquez et al. (2016b) using $\lambda_{(C_R+C_C+C_F)}$. The variable represents the rotor, cable and foundation percentage contribution to the total capital cost. For this analysis $\lambda_{(C_R+C_C+C_F)} = 70\%$, based on the cost distribution shown in Figure 6.6, adding the grid connection and installation costs to the final CAPEX calculation with equation (6.9) (Vazquez et al. 2016a).

$$CAPEX = (C_R + C_C + C_F) \cdot \frac{1}{\lambda_{(C_R+C_C+C_F)}} \quad (6.9)$$

6.4.2 Operational Expenditures (OPEX)

Following equation (6.4) the operational expenses OPEX were obtained next. Equation (6.11), proposed by Vazquez et al. (2016a), relates the operational costs to the project's total power output, $TotPow$, where the unit power P is taken from the CFD models' torque results. The function is based on the report made by Ernst & Young (2010), where OPEX include operation and maintenance (O&M), insurance, de-commissioning and other costs (including Crown Estate rent, Transmission Network Use of System and national grid charges).

$$TotPow = P \cdot N_D \quad (6.10)$$

$$OPEX = \frac{310000 \cdot TotPow}{1 \times 10^3} \quad (6.11)$$

The results from equations (6.6), (6.7), and (6.11) were given in 2010 British pounds, therefore a rate of $\pounds_{2010} 1 = \pounds_{2019} 1.27$ (Official Data Foundation 2020) was used to present them in the equivalent cost for 2019 British pounds.

6.4.3 Energy Produced

The last variable considered from equation (6.4) was the Annual Energy Production (AEP) predicted for the power plant, which depends on the turbine's design and efficiency of the

whole assembly (rotor, generator, and transmission). Using $TotPow$ it was possible to calculate the expected AEP with equation (6.12).

$$AEP = TotPow \cdot h \cdot days \quad (6.12)$$

6.4.4 SRT Reference LCOE Results

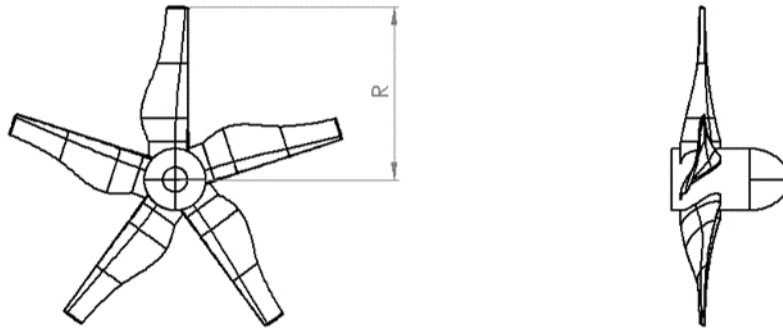


Figure 6.7: Single Rotor Diagram for $LCOE_{Ref}$.

In this section the results of the $LCOE_{Ref}$ for single rotor geometries that would operate in low velocity conditions are shown. The method described in Section 6.3 was followed using power output results from the CFD models run in Chapter 4. The $LCOE_{Ref}$ obtained for each rotor was then used as a reference to relate the analysed configuration technology to LCOE values obtained in industry.

To find the 'optimum' (high power-low cost) single rotor turbine configuration, from the geometries analysed, the LCOE was calculated for each of the models created in the solidity analysis (Chapter 4). The $LCOE_{Ref}$ was calculated using the depth, distance to shore, discount rate, number of units, life, and operation data provided above. Then using the power coefficient from each CFD model and varying the device's radius, R , by 0.5 m from 0.5 m to 7.5 m, the power output P (equation (6.13)) and $LCOE_{Ref}$ were computed for all cases.

$$P = C_P \cdot \frac{T \cdot \omega}{1/2 \cdot \rho \cdot \pi \cdot R^2 \cdot u^3} \quad (6.13)$$

In Figure 6.8 the $LCOE_{Ref}$ results are shown for the 200 SRT configurations with the lowest $LCOE_{Ref}$ to power ratio. To illustrate how the ratio varied from highest and lowest a gradient was used, as labelled in the sidebar, and the SRT configuration with the lowest $LCOE_{Ref}$ to power ratio is highlighted. This device was selected as the optimum SRT, and its characteristics are

listed in [Table 6.3](#).

From this analysis it was found that a 9% difference in cost between the turbine with highest power and lowest LCOE ratio led to a 14% difference in power output, with a cost variation from £ 164/MW h to £ 179/MW h and a power output fluctuation from 61 kW to 70 kW.

It was also found that most of the SRT configurations displayed in the plot have a 7.5 m radius, except for those located in the bottom left corner which have a 7 m radius. These results showed that according to the method proposed by Vazquez et al. (2016a) a compromise in power output would keep the same LCOE of the selected turbine, but could make installation and maintenance logistics simpler with the handling of a smaller rotor.

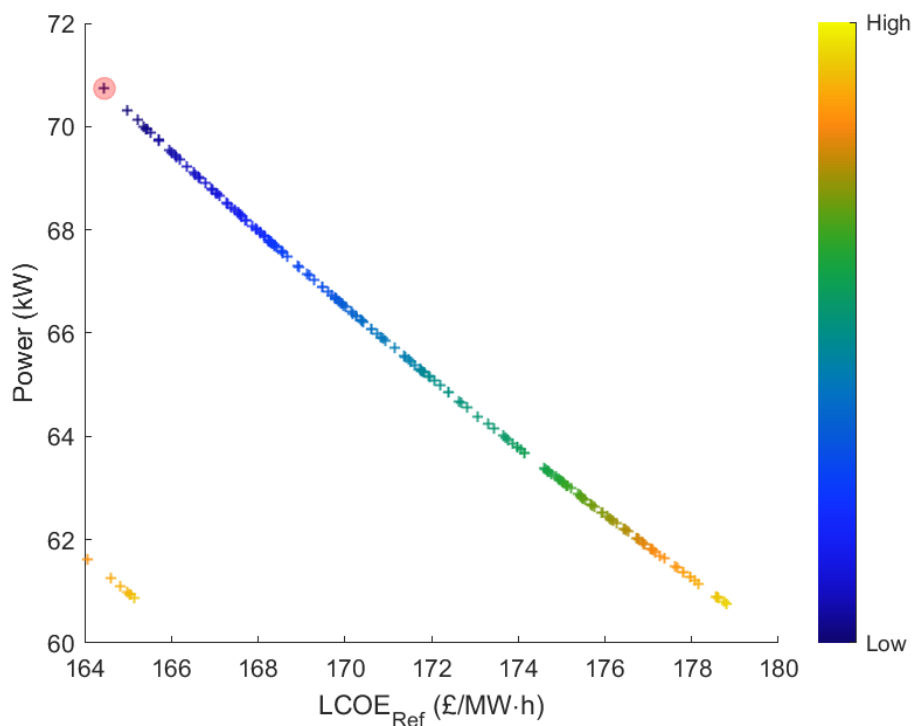


Figure 6.8: Power v LCOE_{Ref} for SRT Selection

Comparing the LCOE_{Ref} result for the SRT with the expected values previously shown in [Figure 6.1](#), it was found that the SRT's LCOE_{Ref} was within the range of expected LCOE for tidal turbines in a commercial power plant. However, Johnstone et al. (2013) and Jung et al. (2019) showed that HATT CRT configurations could be more cost effective when operating in a power plant. Therefore, to address the need to reduce costs even further in order for tidal stream technology to be competitive with all energy sources a CRT configuration was considered as an alternative for low velocity conditions, as explained in [Section 4.6](#) (page 95). The reference LCOE results for the CRT selection process are shown next.

Table 6.3: Optimum Single Rotor Turbine Specifications

Variable	Symbol	Value
Radius	R	7.5 m
Number of Blades	N_B	5
Blade	-	A
Tip Pitch Angle	β	11°
Rotational Speed	ω	0.496 rad/s
Power Coefficient	C_P	0.47
<hr/>		
Power	P	70.8 kW
Levelised Cost of Energy	$LCOE_{Ref}$	£ 164/MW h

6.4.5 CRT Reference LCOE Results

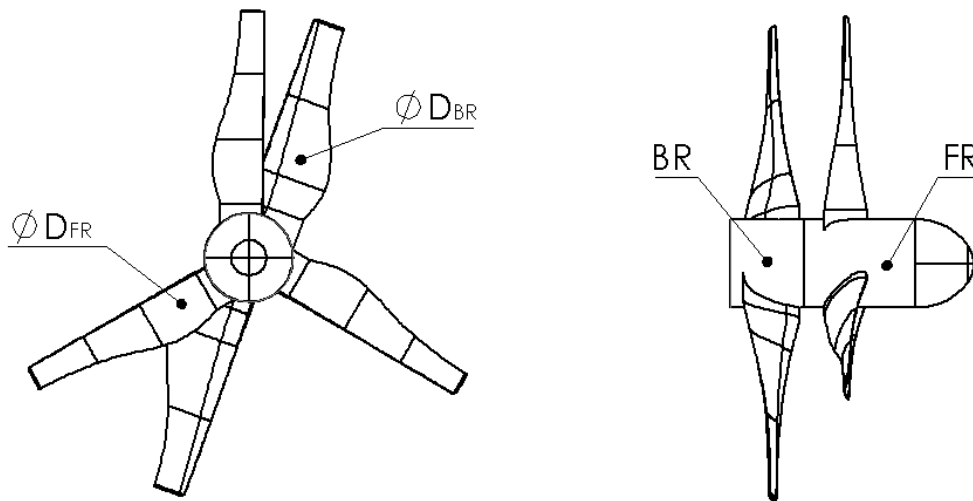


Figure 6.9: Contra-Rotating Rotor Diagram for LCOE

As described in [Figure 6.5](#) the $LCOE_{Ref}$ was calculated twice during the selection process for the CRT: (i) to determine which contra-rotating turbine should be modelled with CFD; and (ii) to obtain a final value for the selected contra-rotating turbine using CFD results, which then was compared to a more detailed LCOE calculation.

The $LCOE_{Ref}$ calculation was made following the equations described in [Section 6.4.1](#) and [Section 6.4.2](#) but using equation (6.14) instead of equation (6.6) to account the CRT's two rotors. For the purpose of this initial analysis, there was no consideration on how the drive-train configuration for a CRT would affect the cost calculation. The diameters D_{FR} and D_{BR} refer to front (FR) and back rotor (BR) respectively, and the CRT's total power output was the sum of each rotor's power output, P_{FR} and P_{BR} . A diagram of the CRT geometries is shown in

Figure 6.9 for reference.

$$C_R = N \cdot 80.388 \cdot (D_1^{2.687} + D_2^{2.687}) \quad (6.14)$$

The aim of finding an 'optimum' CRT was to maximise the power generated with the turbine when located in low velocity conditions so to reduce the LCOE when compared to the SRT. From over twenty five thousand contra-rotating configurations that matched the technical specifications detailed in Section 5.3, the 200 options with highest power output were plotted against their $LCOE_{Ref}$ in Figure 6.10 with a colour bar representing $LCOE_{Ref}$ to power ratio. To select the contra-rotating arrangement to model with CFD, the 10 CRT possibilities with the lowest ratio were considered because, as seen in Figure 6.10, the points overlap within the low $LCOE_{Ref}$ to power ratio area. The mean $LCOE_{Ref}$ of those 10 arrangements was £ 158/MWh with a standard deviation of £ 0.14/MWh, and the configuration with the resulting cost was selected and modelled with CFD as explained in Section 5.5. Using the simulation's data the $LCOE_{Ref}$ was calculated again for comparison, and the results are summarised in Table 6.4.

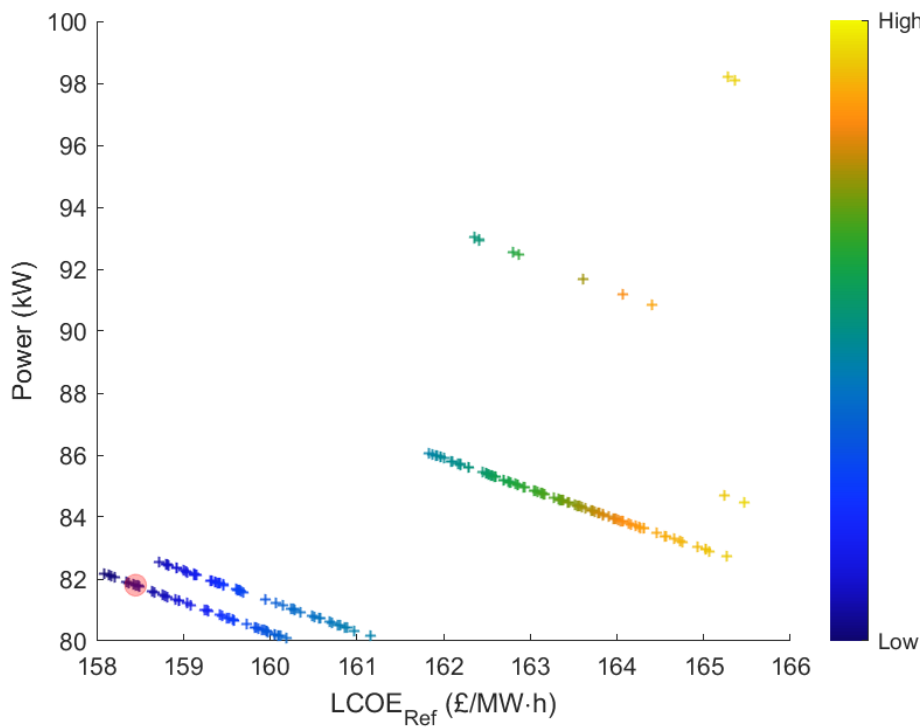


Figure 6.10: Power v $LCOE_{Ref}$ for CRT Selection

When modelling the selected geometry, the CRT power output decreased from the predicted total due to the interaction between front and back rotors, as explained in Section 5.5. The total

Table 6.4: Contra-Rotating Rotor Turbine $LCOE_{Ref}$ Results

Variable	Symbol	Prediction	Simulation
Front Rotor			
Radius	R_{FR}	6 m	6 m
Number of Blades	$N_{B,FR}$	3	3
Blade	-	c	c
Tip Pitch Angle	β_{FR}	5°	5°
Rotational Speed	ω_{FR}	0.9 rad/s	0.9 rad/s
Power	P_{FR}	41.8 kW	26.2 kW
Power Coefficient	$C_{P,FR}$	0.43	0.27
Back Rotor			
Radius	R_{BR}	6 m	6 m
Number of Blades	$N_{B,BR}$	2	2
Blade	-	A	A
Tip Pitch Angle	β_{BR}	4°	4°
Rotational Speed	ω_{BR}	0.9 rad/s	0.9 rad/s
Power	P_{BR}	40.02 kW	22.3 kW
Power Coefficient	$C_{P,BR}$	0.41	0.23
Total Power	$TotPow$	81.8 kW	48.5 kW
Levelised Cost of Energy	$LCOE$	£ 158/MWh	£ 214/MWh

power output of the CRT is 15% higher than the SRT's, but the $LCOE_{Ref}$ increased by 35% due to the addition of a second rotor in equation (6.14). These results showed that at this stage, the technology would not be within the commercial stage cost category from Ocean Energy Systems et al. (2015), but within the second array scale of a power plant. The following sections provide more detail on what should be done for this configuration to be competitive with other tidal stream devices at the commercial scale.

A comparison on how the variables involved in the $LCOE_{Ref}$ equations affected the CRT and SRT's cost results is described in Section 6.4.6.

6.4.6 Reference LCOE Sensitivity Analysis

In this section a study of how the $LCOE_{Ref}$ fluctuates when the variables involved in the calculation change is presented. A sensitivity analysis showed how the variation of one cost component, whilst keeping the others constant, affected the final result for the 'optimum' SRT and CRT. The variables considered in the sensitivity analysis were:-

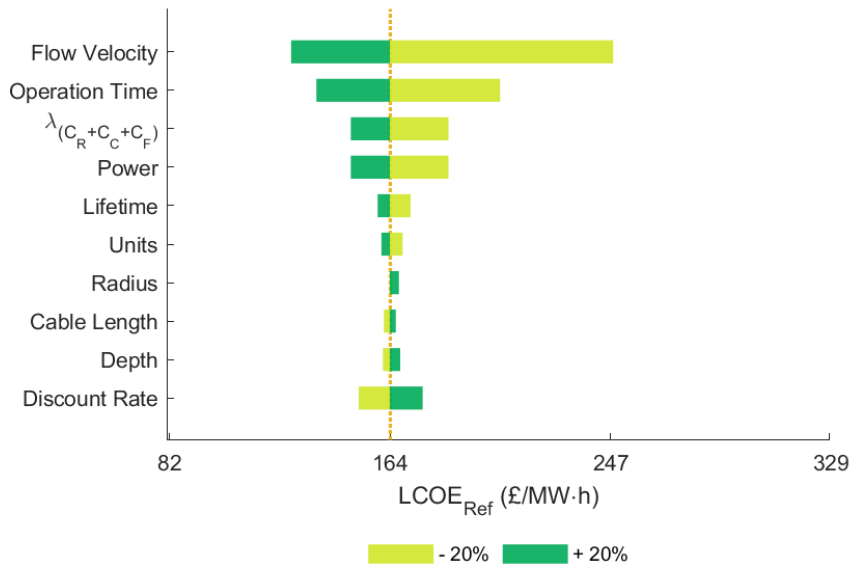
- (i) Power output.

- (ii) Rotors' radii.
- (iii) Percentage of CAPEX associated to rotor, cable and foundation costs.
- (iv) Depth of the selected site for the power plant installation.
- (v) Distance to shore (cable length).
- (vi) Expected lifetime.
- (vii) Operation time.
- (viii) Inlet velocity.
- (ix) Number of units.
- (x) Discount rate.

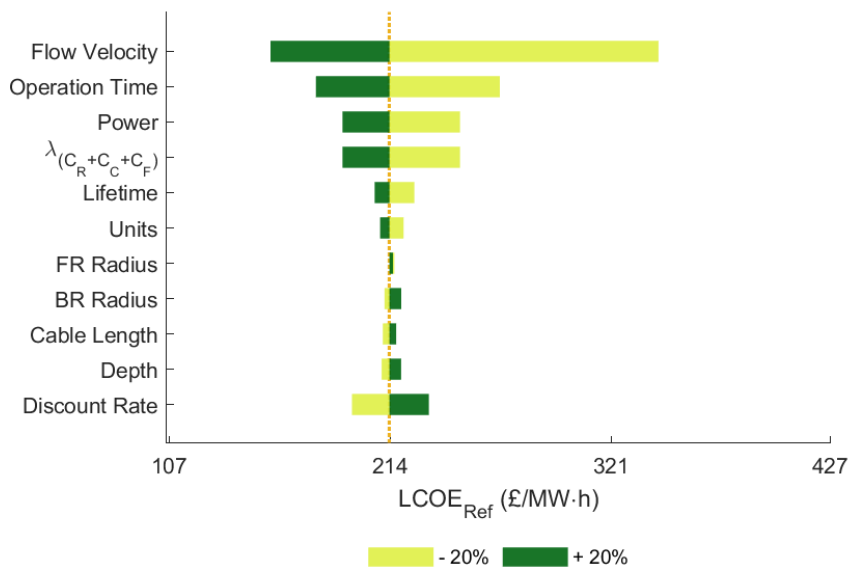
The charts in [Figure 6.11](#) summarise the $LCOE_{Ref}$ sensitivity analyses, where a $\pm 20\%$ variation on the initial parameters was considered. The biggest effect on the $LCOE_{Ref}$ for both CRT and SRT was the flow velocity, its cubic effect in the power output could decrease the LCOE by $\sim 25\%$ or increase it up to $\sim 61\%$ with a $\pm 20\%$ fluctuation. The operation time was the variable with second highest impact on the $LCOE_{Ref}$, able to increase the cost up to $\sim 25\%$ and reduce it $\sim 17\%$. Power, and $\lambda_{(C_R+C_C+C_F)}$ from equation (6.9) had a similar effect on the $LCOE_{Ref}$ regardless of rotor configuration. For these variables, the variation could increase the $LCOE_{Ref}$ up to $\sim 16\%$ or decrease it $\sim 10\%$ from the initial calculation. The results also showed that lifetime, cable length, depth, and a number of units variation affected the $LCOE_{Ref} \pm 20\%$ value in less than 6%.

For both configurations, a decrease in the discount rate would reduce the $LCOE_{Ref}$ result within $\sim \pm 9\%$, and a 20% augment of the variable would have a similar impact on the $LCOE_{Ref}$ in the opposite direction. This data reaffirms the need to make a comparison of results based on the discount rate variation, the correct value will provide a more reliable result. Results also confirmed that the optimum configurations were selected in this study: whether the rotor size was increased or reduced, in both SRT or CRT, the $LCOE_{Ref}$ value increased.

Though helpful to provide a reference on how the various components of the $LCOE_{Ref}$ affect the final value, data shown in [Figure 6.11a](#) illustrate the limitations of the tool made by Vazquez et al. (2016b) for the CRT application. The equations did not account for the benefits of using a moored CRT with regards to installation, maintenance, and operation when compared to a



(a) Single Rotor Turbine



(b) Contra-Rotating Rotors Turbine

Figure 6.11: LCOE_{Ref} Sensitivity Analysis for Selected Rotors

gravity based SRT in a tidal stream power plant. The difference in rotors' swept area was not included in the analysis either (SRT's radius is 25% larger than the CRT's), disregarding the added complications created by having a larger device towed and installed.

Figure 6.12 compares the capital and operational costs of the SRT optimum turbine to the CRT selected turbine. The CRT costs were obtained using the predicted performance characteristics

from the matching process (predicted), and the CFD simulation results (modelled). The costs were levelised with each turbine's *AEP*, and plotted in Figure 6.13.

As expected, the levelised operational costs were equal for all devices because OPEX depends solely on power production. The lowest levelised capital costs were found for the predicted CRT, because the AEP was expected to be the highest. CFD results proved that when two rotors act in tandem the total power output reduced by $\sim 40\%$ to what they would produce as two single turbines, and the modelled CRT had a power output $\sim 31\%$ lower than the optimum SRT on its own. The modelled CRT had the lowest AEP and the highest levelised CAPEX from all configurations, which could be attributed to the general C_R and C_F assumptions made in this model that did not account for each device's specific design and operation characteristics.

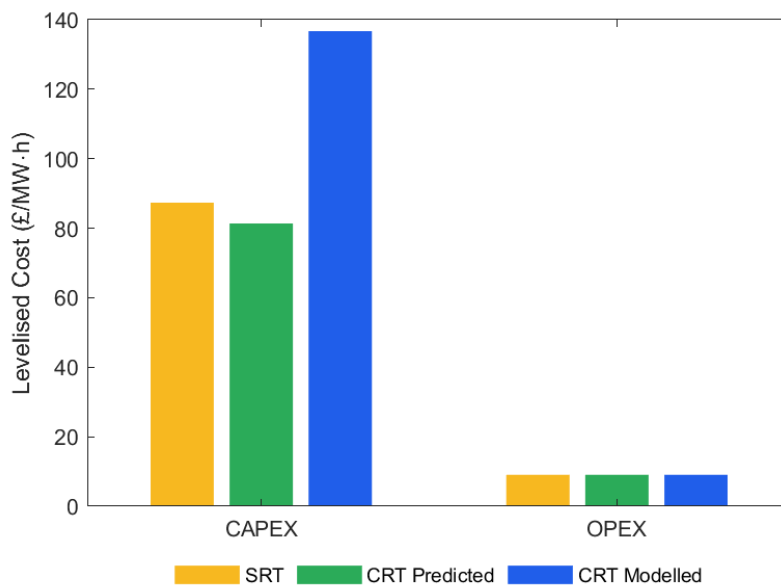
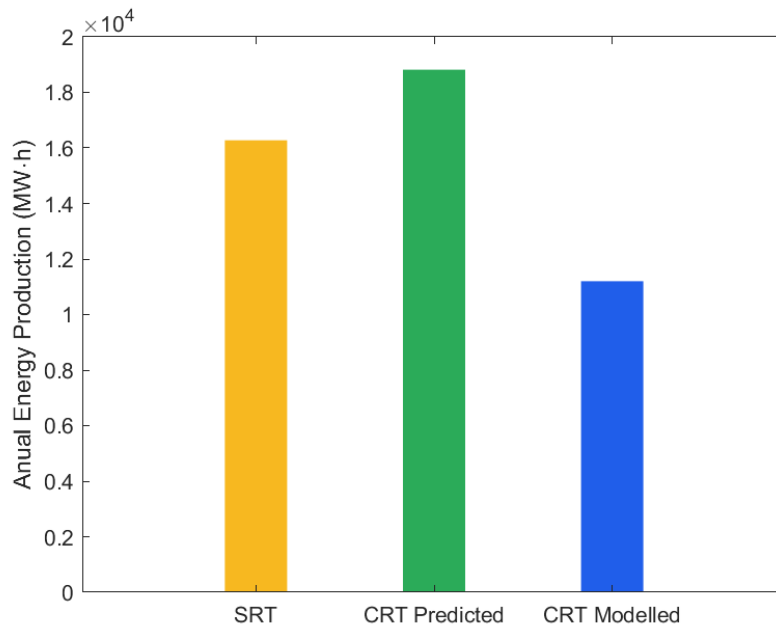


Figure 6.12: LCOE_{Ref} Costs Comparison

The net LCOE_{Ref} values for the SRT and CRT showed that for low speed velocities, the proposed turbines were within the 2nd array and commercially ready tidal stream technologies projected by Ocean Energy Systems et al. (2015). However, the assumptions in the equations developed by Vazquez et al. (2016b) limit the possibilities to refine the results for a specific case, such as the CRT device proposed in this thesis, and though the economic advantages of using a contra-rotating device (i.e. transportation and operation logistics based on device's size, simpler foundations, and no gearbox in the drive train) were not captured with this reference calculation, the direct approach was useful in the selection process of a contra-rotating turbine to simulate.

Figure 6.13: $LCOE_{Ref}$ Annual Production Comparison

It related the main turbines' geometry parameters with the economic aspects of a tidal stream power plant, creating an even comparison between options and reducing the computational time a more complex LCOE method would have required.

According to the $LCOE_{Ref}$ results, the proposed changes to CMERG's turbine, when operating in low velocity conditions, could make the device en par with other similar technologies. The selected CRT predicted a lower $LCOE_{Ref}$ with higher power output than the SRT, but when modelled the results showed a variation from the expected values. Chapter 5 described how the CRT's LCOE could be reduced with a device's design optimisation aimed at increasing the annual energy production. From the sensitivity analysis presented above, it was determined that an increase in flow velocity would have the biggest impact on economic feasibility. Therefore, for low velocity resource areas, accelerating the flow (e.g. with tidal fences, venturi effect devices, etc.) could make extracting energy from those conditions more viable if the increase in power output outweighs the economic implication of using such devices.

Other factors to address in TSEP, that could make this technology economically feasible, can also be determined with a more accurate cost calculation that considers the specific Power Take Off (PTO) configuration for the turbine, number of rotors, support structure, and installation and maintenance logistics required for contra-rotating HATTs. In the next section a more detailed LCOE is calculated for the modelled CRT to expand on what is required for low velocity CRTs in

TSEP to be commercially ready. Following the process described in Figure 6.5, recommendations on how to reduce the cost for CRT in low velocity conditions are then given.

6.5 Detailed LCOE Calculation

Due to the limited description given by the $LCOE_{Ref}$ model on how much a CRT power plant would cost, a more in depth cost calculation was made. This section describes the method, assumptions, and results of the $LCOE_{Det}$ obtained for the CRT modelled in Section 5.4.

The detailed LCOE model was based on the *Reference Models* LCOE calculation made by Neary et al. (2014a), who estimated the costs for hypothetical power plants using their example of technologies for tidal, hydrokinetic, wave, and marine current devices (Figure 6.14). For the $LCOE_{Det}$ computation of the CRT presented in this research, the reference models used for tidal and marine current technologies, RM1 and RM4 respectively, were taken as guideline.

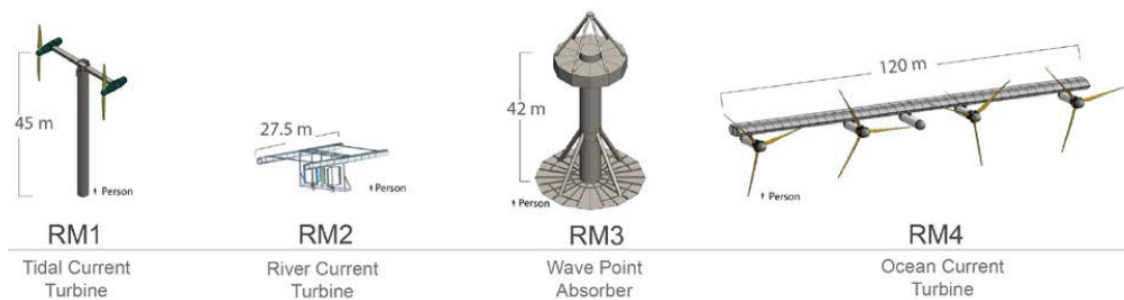


Figure 6.14: Marine Energy Conversion Reference Models. Source: Neary et al. (2014a)

The RM1 consists of a 20 m diameter dual-rotor HATT (550 kW each) located on a cross-arm assembly mounted on a monopile foundation, whereas the RM4 is a 33 m diameter moored glider with four horizontal axis ocean current turbines (1 MW each). The proposed CRT configuration consists of a single unit moored HATT with the technical characteristics given in Table 6.4, therefore the $LCOE_{Det}$ adopted the suitable similarities from each case, and merged them to have a final result. Similar to the method published by LaBonte et al. (2013), the analysis was made by organising the costs with a hierarchical system that covers capital and operational expenditures in different levels (from 0 to 4 in some cases), being Level 0 the main project from which all other costs stem (Neary et al. 2014a). Level 1 refers to CAPEX and OPEX totals, and each subsequent level refers to how specific the quoted activity/component is.

This hierarchical system allowed a better understanding of how each component of a CRT TSEP affect the LCOE prediction, and from the results determine how to reduce costs increasing

the commercial feasibility of the technology. The general assumptions from this model are described in the following section, and the specifics on how each of the costs listed above were obtained are described in [Section 6.5.2](#) and [Section 6.5.3](#). A summary of the Level 3 costs is given on tables within this chapter, and more detailed cost calculations are provided in [Appendix C](#) when required.

The summarised costs are presented with predictions for one, ten, and fifty units power plants. Following the definition and approach made by Neary et al. (2014a), the single unit case represented a pilot power plant project (prototype stage), 10 units was considered as a small commercial power plant, and 50 units represented a fully commercial power plant. The comparison was made to relate how the economies of scale reduce the influence of one component in the overall cost, which is shown as a percentage of the total CAPEX for each component in every scenario.

6.5.1 General Assumptions

- (1) It was recognised by Neary et al. (2014a) that some of their cost estimates may be overly optimistic, representing a mature industry. Considering that the CRT is smaller in size and power output (and loading) than RM1 and RM4's devices, it was assumed that the optimistic effect was counterbalanced by using their same cost estimation.
- (2) The $LCOE_{Det}$ only accounted for plant-level production costs (International Energy Agency and Nuclear Energy Agency 2015). Transmission costs were not considered.
- (3) Neary et al. (2014a)'s report was an outcome of interdisciplinary collaboration, with data taken from previous studies and adapted for the *Reference Models*. Following their experience, some calculations made in the $LCOE_{Det}$ analysis were done using their references.
- (4) For the $LCOE_{Det}$ calculation, it was assumed that the CRT was connected to an adapted direct drive contra-rotating generator similar to the ones proposed by Clarke et al. (2010) and Kawashima et al. (2017). This arrangement replaced the power train with gearbox configuration commonly used.
- (5) The estimated cost relied heavily on land base wind power plants (Neary et al. 2014a).
- (6) A turbine/array yearly availability of 95% was assumed (Neary et al. 2014a).
- (7) To account for heat loss, a 98% transmission efficiency was assumed (Neary et al. 2014a).

- (8) Weather windows were not considered in the OPEX estimations.
- (9) No OPEX mitigation costs for environmental damage were included in the estimation.
- (10) Array hydrodynamic models were not considered as part of the analysis, hence the power output per device was considered to be constant regardless of the units installed in the TSEP.
- (11) Unless stated otherwise, the components and materials were assumed to be the same from Neary et al. (2014a)'s RM1 or RM4.
- (12) Decommissioning costs were not included because their discounted value after 20 years was expected to be negligible in the $LCOE_{Det}$ calculation (Neary et al. 2014a).
- (13) Contingency costs were expected to be 10% of the total CAPEX (Neary et al. 2014a).
- (14) All yearly costs were assumed to be constant during the power plant's lifetime (i.e. 20 years).
- (15) The costs presented in the tables below and in Appendix C were given in 2019 British Pounds. Unless stated otherwise, an exchange rate of $\text{£}_{2011} 1 = \text{\$}_{2011} 1.61$ (X-Rates 2019) was used, and then updated to 2019 British pounds using the rate of $\text{£}_{2011} 1 = \text{£}_{2019} 1.21$ (Official Data Foundation 2020).
- (16) Percentages included in the following tables with costs were rounded to one significant digit.
- (17) The analysis did not include a profit within the calculation.

6.5.2 Capital Expenses

This section details the specific assumptions for the CAPEX considered in the $LCOE_{Det}$ calculation. The Level 2 capital expenses considered in the calculation were: (i) development, (ii) infrastructure, (iii) mooring, (iv) device structural components, (v) power take off system, (vi) installation, and (vii) other costs. They are summarised in the following subsections, and each of the components considered in the subsequent levels are described.

6.5.2.1 Development

The development costs considered for the CRT were obtained using the same approach as Neary et al. (2014a), where three Level 3 components were considered: (i) permitting and environmental compliance; (ii) site assessment; and (iii) project design, engineering, and management.

The **Permitting and Environmental Compliance** cost estimation was based on the study presented by Copping et al. (2011, 2013). With the technical specifications of the *Reference Models*, an approximation was made for how much would the studies and regulatory processes cost to site and permit the marine hydrokinetic devices (Copping et al. 2011). Their approach grouped the requirements in: (i) siting and scoping; (ii) pre-installation studies; (iii) post-installation studies; and (iv) permitting and process. The cost components included in each of those requirements are detailed in Section C.1.1. Due to the similarity in project characteristics the costs from RM1 were replicated for most components. Exceptions are mentioned as required.

Siting and scoping costs included the studies required to determine the site's feasibility based on the resource characteristics, preliminary environmental issues of concern, community involvement to understand all stakeholders' perspectives, and the regulatory requirements for that specific location (Copping et al. 2011). The values used in the $LCOE_{Det}$ are given in Table C.1.

Pre-Installation Studies refer to the baseline assessment of environmental impacts (on marine mammals, fish and invertebrates, seabirds, water quality, and habitat), potential conflicts with other users (cultural resources, navigation, and recreation), and a more detailed resource characterisation (detailed resource assessment; hydrodynamic modelling; and seabed survey, mapping and bottom composition) (Copping et al. 2011). Due to the lack of clear requirements for TSEP, the costs included were based on the concerns that would likely need to be addressed during this stage of a power plant project. The costs assumed are listed in Table C.2.

Post-Installation Studies were meant to be an extension on pre-installation analysis. For pilot projects the concerns should be aimed at the device's nearfield to understand how animals interact when the device is in operation, and their long term effect to the ecosystem (Copping et al. 2011). Costs for these studies are listed in Table C.3.

The mooring characteristics of the CRT analysed are similar to the proposed RM4, therefore the following studies done for the TSEP were replicated from this model instead:-

- The navigation pre-installation studies because the CRT was submerged but located closer to the surface (15 m below sea level), similar to the RM4.
- The marine mammals and fish post-installation monitoring. The mooring system has a different effect on them than the monopile foundation, including more likelihood to entanglement.
- The effects on seabirds ecosystems. RM4 accounted for these due to the device's depth location, which could affect these animals when feeding.

During both pre and post-installation sample collection and analysis, data analysis and interpretation, quality assurance and control, and documentation for regulatory purposes (*Permitting and Process*) have to be completed (Copping et al. 2011). These costs were accounted for according to the U.S. National Environmental Policy Act (NEPA) requirements, and the values used are detailed in Table C.4.

The **Site Assessment** estimation was based on a survey that includes geotechnical studies for the cable landing, the subsea cable route, and the moorings. These studies included a bathymetric and geophysical survey with sub-bottom profiling, magnetometer, grab samples, and underwater video (Neary et al. 2014a). Specifics for each of the analyses were not available in the date provided by Neary et al. (2014a), therefore the value was directly replicated from the RM1 to the CRT application.

To account for the **Project Design, Engineering, and Management** costs a percentage of the total CAPEX was used (5%, 3%, or 2%) depending on the quantity of units installed in the power plant (1, 10, or 50 respectively) (Neary et al. 2014a). This computation was made once all CAPEX were obtained, and it is summarised in Table 6.5 with all previously described development costs. The percentage included next to each cost represents its proportion to the total CAPEX.

Table 6.5: Development Costs for CRT

Component	1 Unit		10 Units		50 Units	
	Cost	%	Cost	%	Cost	%
Permitting and Environmental Compliance	£ 2 781 685	32%	£ 3 975 902	17%	£ 4 876 638	6%
Site Assessment	£ 145 773	2%	£ 221 002	1%	£ 221 002	0.3%
Project Design, Engineering, and Management	£ 186 618	2%	£ 510 472	2%	£ 1 396 074	2%
Total Development Costs	£ 3 114 076	36%	£ 4 707 377	20%	£ 6 494 715	8%

6.5.2.2 Infrastructure

Infrastructure costs were linked to the transmission cables (including fibre optic lines for communication) from shore to the turbines' array, riser cables to interconnect devices, their termination and connectors, and dockside improvements. These expenses covered material only, installation costs are described in Section 6.5.2.6. The **Subsea Cables** cost estimations were based on

the distance between turbines taking the RM1 prediction as reference, and the RM4 array shape to account for the riser cable required for the interconnection between devices. The distances were modified to fit the CRT characteristics as follows:-

- (i) The CRT was located 5 km from the seashore, instead of the 30 km assumed for the RM4 site.
- (ii) The CRT was assumed to be installed in a site with a 30 m depth location, contrary to the 800 m depth for the RM4 Ocean Current Turbine.
- (iii) The longitudinal distance between devices was the equivalent to 2.5 diameters (30 m), and the space between rows equalled to 20 diameters (240 m). The array distance was not optimised to account for hydrodynamic effects in the turbines' performance.

Figure 6.15 illustrates the turbines' distribution in the array, where the yellow circles represent one CRT. Depending on how many units were installed the number of rows varied and so did the number of trunk cables required (each can support up to 25 units). The total trunk cable length required, summarised in Table C.5, accounted for the distance between shore and the array (5 km), the directional drilling distance (5000 m), and a 20% contingency.

The trunk cable costs per metre (Table C.7), estimated by Neary et al. (2014a), increased with the number of units, and were based on the cables' capacity, diameter, and weight. It was assumed that the 3-phase AC cable specifications, shown in Table C.6, matched the requirements for the presented CRT.

The **Riser Cable** was used to transmit electricity via a riser cable to a junction box, and a trunk cable connected each junction box. They were connected to the turbines in the array as shown in Figure 6.16, where the yellow circle represents the CRT. Estimations made by Neary et al. (2014a) were also used to obtain the cost of this component, and they were included in the infrastructure section following their recommendations. The riser cable length for the TSEP is summarised in Table C.8, where the distance between devices and rows (30 m and 240 m), the water depth (30 m), and contingency (20%) variables were considered for every unit. Similar to the trunk cables, the cost per metre varied depending on the array size.

The cables' **Termination and Connectors** were assumed to be 10% of the total cable cost, and the dockside improvements required for the project's functionality were included in the overall project contingency. The resulted infrastructure costs' are shown in Table 6.6. The percentage included next to each cost represents its proportion to the total CAPEX.

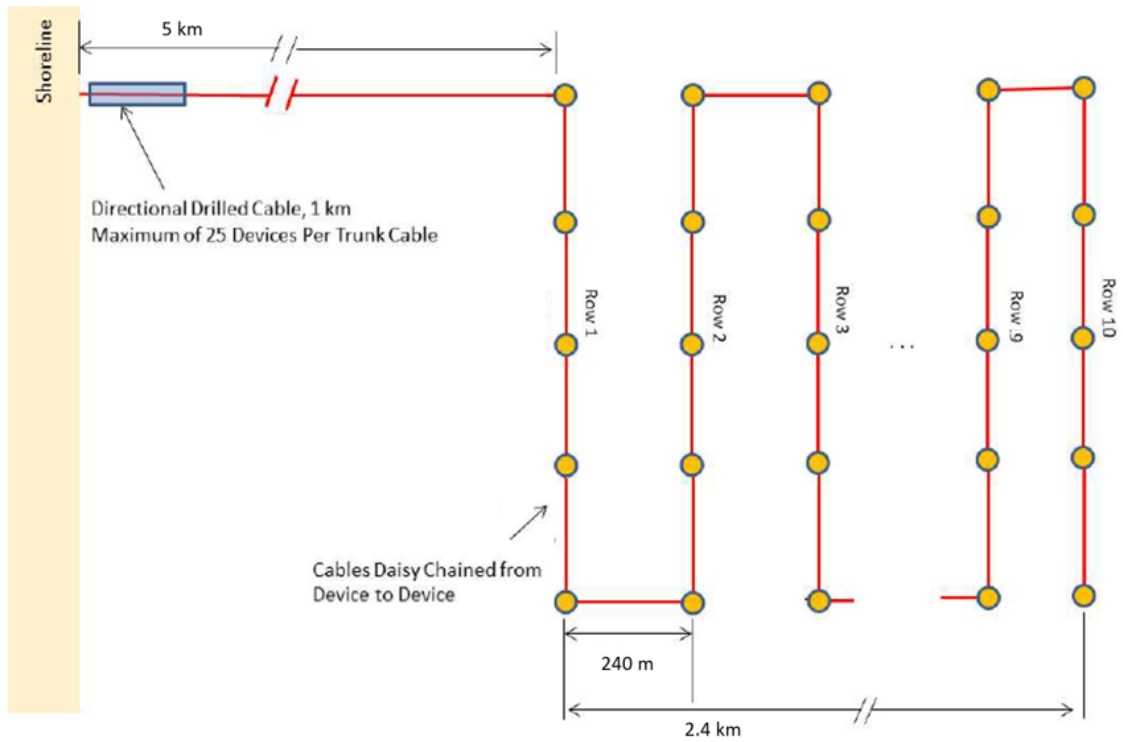


Figure 6.15: CRT Array Configuration. Source: Adapted from Neary et al. (2014a)

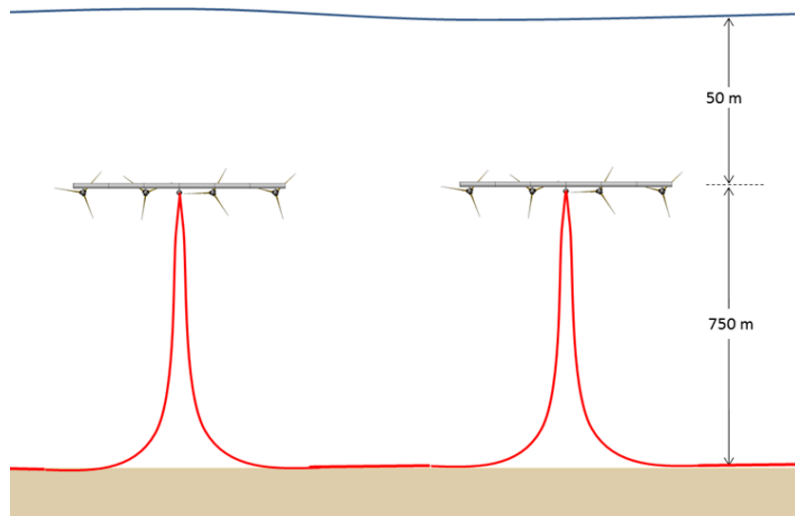


Figure 6.16: Riser Cable Diagram. Source: Adapted from Neary et al. (2014a)

Table 6.6: Infrastructure Costs for CRT

Component	1 Unit		10 Units		50 Units	
	Cost	%	Cost	%	Cost	%
Subsea Cables	£ 631 304	7%	£ 791 761	3%	£ 1 919 165	2%
Riser Cables	£ 18 671	0.2%	£ 186 707	1%	£ 933 536	1%
Terminations and Connectors	£ 63 130	1%	£ 79 176	0.3%	£ 191 917	0.2%
Total Infrastructure Costs	£ 713 106	8%	£ 1 057 644	4%	£ 3 044 618	4%

6.5.2.3 Moorings

The CRT device was designed to have near zero reaction torque to reduce foundation costs using mooring lines instead of monopile structures, similar to the RM4 design. To estimate the costs from these components their parameters were used as reference.

The system consisted of two mooring lines: tension (buoyancy) and thrust. The former was secured to the sea floor with a suction pile, and the latter used a drag embedment anchor with a weight clamp attached to a studlink chain to insure protection from near seabed abrasion. [Figure 6.17](#) shows a diagram of the mooring with the yellow circle representing the CRT. The depth (30 m) was taken from the site's characteristics for the CRT, the thrust mooring distance and chain length were scaled down based on that value, and the line from turbine to the buoyancy point was scaled down from 100 m to 36 m based on the turbines' diameter.

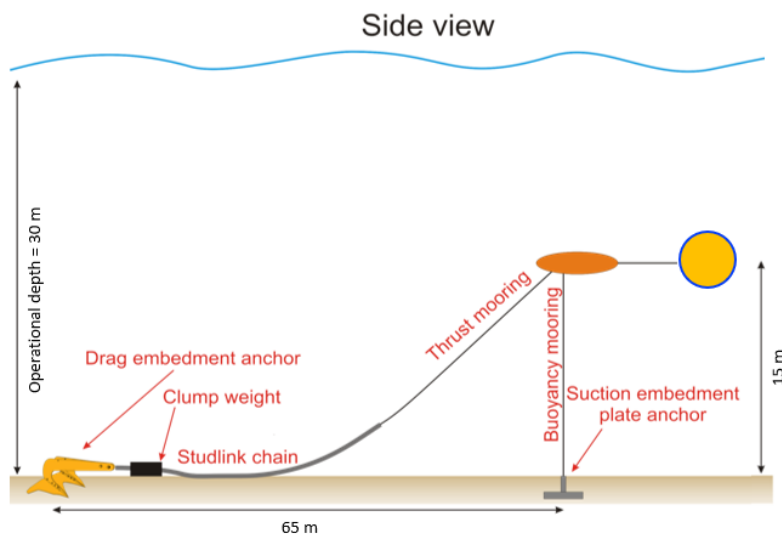


Figure 6.17: CRT Mooring System. Source: Adapted from Neary et al. (2014a)

All mooring lines were made of polyester because the material is lightweight, has an extensive record in offshore industry, and was relatively inexpensive (Neary et al. 2014a). Polyester lines were considered to cost £ 17.3/m, whereas the certified chain was assumed to cost £ 1 150/m. The summary of this **Mooring Lines/Chain** cost calculation is given in [Table C.10](#).

The selected **Anchors** were a rough selection of what could be used for the RM4 circumstances. Their estimation applied for the CRT was used based on their cost per kW assuming a constant load regardless of the power output. This assumption gave a safety factor because the hydrodynamic loads for the CRT would be less than those of the RM4 devices.

The **Connecting Hardware** required to complete the mooring system was assumed to be 10% of the cost, based on previous experience by Neary et al. (2014a). They represent miscellaneous

items such as shakes, certifications, etc. All mooring costs are summarised in [Table C.11](#). The percentage included next to each cost represents its proportion to the total CAPEX.

Table 6.7: Moorings Costs for CRT

Component	1 Unit		10 Units		50 Units	
	Cost	%	Cost	%	Cost	%
Moorings Lines/Chain	£ 6 187	0.07%	£ 46 501	0.2%	£ 232 503	0.3%
Anchors	£ 6 930	0.08%	£ 20 005	0.1%	£ 84 608.3	0.1%
Connecting Hardware	£ 1 312	0.02%	£ 6 651	0.03%	£ 31 711	0.04%
Total Moorings Costs	£ 14 429	0.2%	£ 73 156	0.3%	£ 348 822	0.4%

6.5.2.4 Power Take Off

To account for the PTO costs the following components were considered: (i) generator, (ii) hydraulic system, (iii) assembly and testing, (iv) PTO mounting, (v) frequency converter, (vi) step-up transformer, (vii) control system, (viii) rotors, (ix) seals, (x) bearings and linear guides, and (xi) others. There was no gearbox included because a Direct Drive Permanent Magnet Generator (DDPMG) was used. This configuration was selected to: (i) reduce maintenance costs (Carroll et al. 2017) by removing the gearbox (Smolders et al. 2010), (ii) reduce transmission losses (Polinder et al. 2006), and (iii) achieve a higher yield energy to cost ratio (H. Li et al. 2008). A description on each component's cost estimation is given next, and the values used are summarised in [Table 6.8](#).

Both the RM1 and RM4 proposed bespoke cost estimations for their PTO systems, which were not compatible with the CRT design. There is limited data on CRT DDPMG drivetrains: previous CRT proposals (Clarke et al. 2008a; Huang et al. 2016a) have created a specific power train that would suit their requirements; and after consultation via private communication, industry representatives from DNV (C. Bittencourt on 31 October 2019), ORE Catapult (A. Gray on 11 November 2019), NREL (S. Jenne on 7 November 2019; R. Murray on 27 December 2019), IRENA (A. Salgado on 29 November 2019), OES (R. Silva-Casarin on 31 Oct 2019), and MERIC (D. Mediavilla on 18 Nov 2019) recommended to estimate the cost for a PTO system that would fit the CRT specifications based on available wind energy data because commercial information would be difficult to obtain. Designing a PTO was out of this work's scope, hence a cost approximation for the CRT's PTO was made following guidance from DDPMG WindPACT drive

train design proposed by Poore et al. (2003). Due to the lack of available data, the bespoke CRT generator cost was estimated following the guidelines given by Poore et al. (2003) for a rotor/stator configuration.

Similarly to the studies by Neary et al. (2014a) and Copping et al. (2011), the WindPACT project provided information for wind turbine's rotor design (Malcolm et al. 2006, 2003), drivetrain design (Poore et al. 2003; Bywaters et al. 2004), and scaling studies (Griffin 2001; Smith 2001; Bortolotti et al. 2019) that can be replicated. For the purpose of this analysis, the design method provided by Poore et al. (2003) was used to estimate the PTO system costs, and (Griffin 2001)'s report to predict the rotors' costs.

Poore et al. (2003) detailed how wind turbine drivetrains could be designed based on their configuration, and provided a cost estimation tool for each of them. The report included preliminary/conceptual studies for Baseline, Integrated, Single Permanent Magnet, Multi-Permanent Magnet, Direct Drive, Multi-Induction, Klatt, Heller-de Julio, and Henderson drivetrains. For the purpose of this research the DDPMG concept, that had 94.4% efficiency, was used as reference to fit the proposed CRT. All costs were given in U.S dollars from 2000, hence a rate of $\$_{2000} 1 = \$_{2011} 1.31$ (Coin News Media Group LLC 2020) was applied in addition to the values mentioned in Section 6.5.1.

The **Generator** cost was found using the methodology proposed by Poore et al. (2003). Based on the stator radius, mainshaft rotational velocity, and the desired power output, the design tool uses a set of 67 equations that provided the cost of a generator that accounts for material and manufacturing costs using the device's specifications. The CRT mechanical power output was expected to be 48.5 kW, the rotational velocity used was 16.6 rpm, and a 2 m stator radius was assumed for being the most cost efficient diameter (Poore et al. 2003). The device specifications given by the design tool are shown in table Table C.16 for reference.

The final cost results per generator, presented in Table C.12, were divided in: (i) active magnetics and the generator jacket; (ii) mainshaft; (iii) brake system; and (iv) extra components represented in an extra 10% that accounts for rotor iron, bearings, stator cold plate ring, and housing (Poore et al. 2003).

The PTO's **Hydraulic System's** cost depended on the heat load based on the generator efficiency (Poore et al. 2003), as it is shown in equation (6.15). The heat load in kW is represented by P_{cooler} , and P_{loss} refers to the percentage of power loss in the generator (5.6% for the CRT design). The heat load expected for the present drivetrain was then 2.72 kW. Using mass

prediction curves from vendor catalogues, and assuming a cost of £ 20/kg, equation (6.16) was created by Poore et al. (2003) to estimate the generator's cooling system cost. The final cost shown in Table 6.8 was determined by adding £ 541 for the cooling line plumbing's large radius.

$$P_{cooler} = P \cdot P_{loss} \quad (6.15)$$

$$Cost_{cooler} = -0.6698 \cdot P_{cooler}^2 + 101.98 \cdot P_{cooler} - 246.19 \quad (6.16)$$

The drivetrain **Assembly and Testing** cost was obtained with the design tool model described above. Poore et al. (2003)'s cost approximation related the generator's specifications with the required working hours to: (i) assemble the main structure (42.3 h), (ii) assemble generator to system (22.3 h), (iii) assemble cooling (19.7 h), and (iv) test and paint (23.3 h). The number of hours (107.7 h in total) were predicted based on the generator specifications with an assumed labour rate of £ 64/h, as part of the tool outputs.

The **PTO Mounting** was the nacelle structure that directly supports the drivetrain, and its cost was also estimated as part of the outputs given by the design tool proposed by Poore et al. (2003) tool described above. The final value shown in Table 6.8 accounted for the manufacturing costs of: (i) main housing, (ii) gudgeon shaft, (iii) rotating spider, (iv) outside ring support, and (v) mainshaft retainer. Details of each component's cost are given in Table C.13. They were based on each part's weight, and the technical specifications given by the drivetrain design tool.

The PTO's **Frequency Converter** and **Step-Up Transformer** were used to convert the produced electricity to an output that can be fed into the grid (Neary et al. 2014a). Using the data from Poore et al. (2003) as guideline, the cost for the converter was £ 34/kW, and for the transformer £ 17/kW. A **Control System** to manage generator's torque, rotor speed, and volt-ampere output was considered as part of each turbine's PTO with an estimated cost of £ 7.6/kW.

Rotor cost estimates were done by calculating costs for the CRT required master blades and mold sets, blades tooling and production, and hub manufacturing. Blade structural analysis and manufacturing logistics was out of this thesis' scope, hence an approximation was made based on personal communication with R. Murray from NREL (on 27 December 2019) and WindPACT's guidelines (Griffin 2001). The master blades and mold costs ($Blade_{mold}$) were obtained following equation (6.17), where S refers to the blade's surface area in m^2 . For the CRT, two mold sets per blade design (suction and pressure sides) needed to be created, giving a total of four because

the front and back rotors have different designs. The tooling $Blade_{tool}$ was calculated using equation (6.18) that accounted for reinforcement requirements based on the surface size and area. Regardless of the units in the power plant, tooling and mold costs were accounted just once (R. Murray, personal communication on 27 December 2019).

$$Blade_{mold} = 1880 \cdot S \quad (6.17)$$

$$Blade_{tool} = 4300 \cdot \left(\frac{R}{35}\right)^{0.5} \cdot S \quad (6.18)$$

It was assumed that the CRT's five 3 m blades were made of fibreglass epoxy composite materials with a weight average of 30 kg/m (R. Murray, personal communication on 27 December 2019). The production costs per blade were estimated to be £ 41.2/kg when 1 to 20 units were built, and £ 15.4/kg if more than 20 units were made (Griffin 2001). Finally, the hub cost was approximated to be the same of one more blade by averaging the total cost of the CRT's 7 blades (R. Murray, personal communication on 27 December 2019). The rotors' summary cost, shown in Table C.15, was given in 2001 U.S dollars, hence an inflation rate of $\$_{2001} 1 = \$_{2011} 1.2$ (Coin Nawa Media Group LLC 2020) was applied in addition to the rate mentioned above.

Seals and Bearings and Linear Guides costs were estimated based on the RM4 model designed by Neary et al. (2014a). The seals needed in the PTO system to keep the enclosure water-sealed were estimated to be 8.5% of the total PTO cost, and the bearings that transfer loads from the rotor shaft to the nacelle were assumed to cost 17% of the total PTO cost.

Other components listed in Table 6.8 accounted for: (i) switchgear, (ii) cable for the electrical systems, and (iii) other subsystems. The cost assumptions for each of the components were based on their price per kW: £ 7/kW, £ 11/kW, and £ 16/kW respectively. The final values are shown in Table C.14. The percentage included next to each cost represents its proportion to the total CAPEX.

Table 6.8: Power Take Off Costs for CRT

Component	1 Unit		10 Units		50 Units	
	Cost	%	Cost	%	Cost	%
Generator	£ 51 851	1%	£ 518 514	3%	£ 2 592 568	4%
Hydraulic System	£ 568	0.01%	£ 5 681	0.03%	£ 28 404	0.03%
Assembly	£ 7 067	0.1%	£ 70 665	0.3%	£ 353 325	0.4%
PTO Mounting	£ 10 648	0.1%	£ 106 484	0.5%	£ 532 422	1%
Frequency Converter	£ 1 679	0.02%	£ 16 785	0.1%	£ 83 927	0.1%
Step-Up Transformer	£ 827	0.01%	£ 8 273	0.04%	£ 41 364	0.05%
Control System	£ 369	0.004%	£ 3 693	0.02%	£ 18 464	0.02%
Rotors	£ 130 362	2%	£ 197 968	1%	£ 425 316	1%
Seals	£ 23 862	0.3%	£ 120 675	1%	£ 543 156	1%
Bearings	£ 47 724	1%	£ 241 351	1%	£ 1 086 313	1%
Other	£ 1 647	0.02%	£ 16 474	0.1%	£ 82 368	0.1%
Total PTO Costs	£ 276 605	4%	£ 1 306 563	5%	£ 5 787 628	7%

6.5.2.5 Device Structural Components

The device structural components for the RM4 included wing, nacelle, fairing, device access, and buoyancy tank designed to accommodate their four rotors. The CRT adaptation of these costs included only nacelle, and device access because the other components were not required as part of the proposed configuration.

The CRT's **Nacelle** cost was estimated with the generator design tool proposed by Poore et al. (2003) explained above. The approximation considered the required material and labour work for the nacelle manufacturing based on the DDPMG's design parameters given in Table C.16: (i) airgap diameter, (ii) outside diameter, (iii) mainshaft rear bearing diameter, and (iv) pole stack length.

The **Device Access** costs (e.g. railings, and ladders) were assumed to be 10% of the device structural parts' total cost (i.e. the nacelle). All costs are presented in Table 6.9. The percentage included next to each cost represents its proportion to the total CAPEX.

Table 6.9: Device Structural Components Costs for CRT

Component	1 Unit		10 Units		50 Units	
	Cost	%	Cost	%	Cost	%
Nacelle	£ 11 099	0.1%	£ 110 990	1%	£ 554 949	1%
Device Access	£ 1 110	0.01%	£ 11 099	0.1%	£ 55 495	0.1%
Total Device Structural Components Costs	£ 12 209	0.1%	£ 122 089	1%	£ 610 444	1%

6.5.2.6 Installation

Installation costs included for the $LCOE_{Det}$ calculation were: (i) cable shore landing, (ii) mooring installation, (iii) subsea cables, (iv) device installation, and (v) device commissioning. Using RM1 from Neary et al. (2014a) as reference, it was assumed that the device was already on site, therefore no transport to the staging site was considered. Likewise, the transportation time from shore to the array site was taken from RM1 due to the CRT location characteristics (i.e. 5 km from shore). All other installation logistics and costs were replicated from RM4, based on the model's similarity to the CRT floating system.

Cable Shore Landing installation costs refer to the required horizontal drilling for 1 km, as shown in Figure 6.15, where a conduit connected the cable to the first row of devices, reducing installation and maintenance costs (Neary et al. 2014a). Assumed values are shown in Table 6.10.

Mooring System installation required four different vessels to complete the process: (i) a crane barge with a lift capacity to handle all mooring components, (ii) an anchor handling vessel, (iii) a dynamic position (DP) vessel for marine operations, and (iv) a crew boat. The required tasks are then divided in five main categories: (i) at dock tasks including loading and unloading the vessels with the required equipment, (ii) transit/anchoring, (iii) mooring and anchors installation, (iv) mobilisation charges, and (v) standby contingency that included weather windows assumed to be 15% of the mooring system installation time. Duration and cost details for each category are given in Table C.17.

Subsea Cables installation costs and times are listed in Table C.18 and Table C.19, where trunk cable and riser cable operations are summarised. Trunk cable installation was done using a dynamic positioning (DP) vessel equipped for this function, and it was assumed that the seabed is adequate for burial without major obstructions on the route (Neary et al. 2014a). The task categories required to complete the operations are: (i) at dock tasks including loading

and unloading the vessels; (ii) loading cable; (iii) installation operations for shore end cable, trunk cable, first connection to device, cable between device, end for end interconnect, and next device connection; (iv) mobilisation charges, and (v) standby contingency that included weather windows assumed to be 25% of the trunk cable installation time.

Riser cable installation costs and days required varied depending on the number of units deployed in the array. The installation process was divided in the following categories: (i) transit, (ii) installation of cable between two devices, (iii) installation of splice cables, and (iv) operational contingency that included weather windows assumed to be 15% of the riser cable installation time.

Device installation was made with a dynamic positioning vessel that tows the CRT to the site attaching mooring lines, and installing the riser cable system (Neary et al. 2014a). To account for the costs, summarised in Table C.20, the operations were categorised in: (i) barge-in device, (ii) unload and ready device, (iii) tow-out and install device, (iv) commission device, and (v) operational contingency that included weather windows assumed to be 25% of the device installation time.

The complete list of the CRT installation costs included in the $LCOE_{Det}$ is shown in Table 6.10. The percentage included next to each cost represents its proportion to the total CAPEX.

Table 6.10: Installation Costs for CRT

Component	1 Unit		10 Units		50 Units	
	Cost	%	Cost	%	Cost	%
Cable Shore Landing	£ 501 286	6%	£ 576 591	3%	£ 1 152 882	1%
Mooring System	£ 1 843 373	21%	£ 7 799 849	36%	£ 34 004 705	41%
Subsea Cables	£ 1 224 756	14%	£ 2 421 404	11%	£ 6 636 912	8%
Device	£ 351 558	4%	£ 3 515 576	16%	£ 17 577 880	21%
Total Installation Costs	£ 3 920 972	45%	£ 14 313 421	66%	£ 59 372 380	71%

6.5.2.7 Other Costs

The final capital expenses to consider were the subsystem integration, and contingency costs. **Subsystem Integration** refers to grid connection which was assumed to be 10% of the machine cost (PTO and Device Structure) regardless of the number units. **Contingency** costs, estimated to be 10% of the total CAPEX, were included in the study as a buffer to account for items not well understood, or not sufficiently detailed. The values used for **Other Costs** are shown in

Table 6.11. The percentage included next to each cost represents its proportion to the total CAPEX.

Table 6.11: Other Capital Costs for CRT

Component	1 Unit		10 Units		50 Units	
	Cost	%	Cost	%	Cost	%
Subsystem Integration	£ 28 881	0.3%	£ 142 865	0.6%	£ 639 807	1%
Contingency	£ 496 620	6%	£ 1 701 574	7%	£ 6 980 370	8%
Total Other Costs	£ 525 502	6%	£ 1 844 439	8%	£ 7 620 177	9%

To summarise the previously detailed cost assumptions, [Table 6.12](#) shows all capital expenses considered in the $LCOE_{Det}$ calculation for the proposed 3 – 2 CRT. The percentage included next to each cost represents its proportion to the total CAPEX.

Table 6.12: Capital Expenses Summary for CRT

Component	1 Unit		10 Units		50 Units	
	Cost	%	Cost	%	Cost	%
Development	£ 3 114 076	36%	£ 4 707 377	20%	£ 6 493 715	8%
Infrastructure	£ 713 106	8%	£ 1 057 644	4%	£ 3 044 618	3.6%
Moorings	£ 14 429	0.2%	£ 73 156	0.3%	£ 348 822	0.4%
PTO System	£ 276 605	4%	£ 1 057 644	6%	£ 3 044 618	8%
Device Structural Components	£ 12 209	0.1%	£ 122 089	1%	£ 610 444	1%
Installation	£ 3 920 972	45%	£ 14 313 421	61%	£ 59 372 380	71%
Other Costs	£ 496 620	6%	£ 1 701 574	8%	£ 6 980 370	8%
Total CAPEX	£ 8 576 898	100%	£ 23 424 689	100%	£ 83 277 784	100%

6.5.3 Operational Expenses

This section details the specific assumptions for the OPEX considered in the $LCOE_{Det}$ calculation. The Level 2 operational expenses accounted in the $LCOE_{Det}$ were: (i) insurance, (ii) environmental monitoring and regulatory compliance, (iii) marine operations, (iv) shoreside operations, and (v) replacement parts. Consumables were not included in the OPEX because they were negligible ($\sim 0.1\%$) in relation with the other components. The costs accounted for OPEX were considered to be yearly, and they were assumed to be constant during the power plant's lifetime (i.e. 20 years) unless stated otherwise.

Insurance costs were directly related to the perceived risk of a project (Neary et al. 2014a). The CRT insurance estimates were based on a percentage of the total CAPEX (without the contingency estimation), and the number of units deployed in the array: (i) 2% for one unit, (ii) 2% for ten units, and (iii) 1% for fifty units. The yearly costs depending on project size are given in Table 6.13.

The operation costs for **Environmental Monitoring and Regulatory Compliance** were based on the studies made by Neary et al. (2014a) and Copping et al. (2011). The yearly costs accounted in the calculation were the same as the ones described in Section 6.5.2.1, and listed in Table C.3 for post-installation studies.

The report by Neary et al. (2014a) describes a cost profile that was applied assuming costs would gradually decrease during the first two years of the plant's operation. They would then stay constant for near-field monitoring of animals thought to be at risk, with periodic increases that accounted for special studies that could evaluate far-field effects or validate trends from the first years, and to address new concerns that may arise (Copping et al. 2011). This profile was created with information from developers, researchers, and consultants involved in facilitating deployment of marine energy devices in the United States, and it was not provided in the publication from Copping et al. (2011). Therefore, RM1 values were replicated for this $LCOE_{Det}$ component assuming they were constant during the plant's lifetime. The yearly costs are shown in Table 6.13.

Marine Operations costs were based on the number of interventions needed for each device per year. The prediction was based on wind energy failure rates experience, where an addition of redundancies were added to the PTO system to reduce the number of interventions needed (Neary et al. 2014a). With this assumption, it was predicted that each device had to be intervened 1.97 times per year, for annual maintenance and for one yearly (expected) system failure. Regular maintenance accounted for: filter elements replacement, refurbishments, cleaning biofouling, and spot-repainting. The cost approximation, summarised in Table 6.13, included a 24 h crew, fuel and consumables required per intervention.

Shoreside Operations costs were replicated from RM4, which accounted for salaries of the personnel needed: site manager (1), administrative assistants (2), senior technicians (1-4), and junior technicians (4-9). The number of technicians required would vary during the operation life years and the number of units (Neary et al. 2014a). The assumed values for this component of OPEX are detailed in Table C.22.

The **Replacement Parts** were the last component to consider as part of the OPEX. The cost assumptions were based on RM4, where percentages of previously calculated costs represent the required value for yearly replacement parts: (i) 0.94% of the PTO active parts cost, (ii) 10% of mooring system capital and installation costs, and (iii) 10% of the riser cable capital cost. [Table C.23](#) shows details of the used values in the $LCOE_{Det}$ computation.

The summary of all annual operational expenses estimated for the CRT is given in [Table 6.13](#). These values were used with the CAPEX totals from [Section 6.5.2](#), and the annual energy production estimation described in next section, to obtain the detailed LCOE value for the proposed CRT. The percentage included next to each cost represents its proportion to the total OPEX.

Table 6.13: Annual Operational Expenses Summary for CRT

Component	1 Unit		10 Units		50 Units	
	Cost	%	Cost	%	Cost	%
Insurance	£ 74 647	7%	£ 255 765	11%	£ 524 612	8%
Environmental Monitoring and Regulatory Compliance	£ 503 540	49%	£ 738 589	31%	£ 738 589	11%
Marine Operations	£ 33 159	3%	£ 331 594	14%	£ 1 657 970	24%
Shoreside Operations	£ 234 581	23%	£ 234 581	10%	£ 280 466	4%
Replacement Parts	£ 189 801	18%	£ 817 305	34%	£ 3 578 339	53%
Total OPEX	£ 1 035 729	100%	£ 2 377 834	100%	£ 6 779 975	100%

6.5.4 Annual Energy Production

The AEP estimation for the $LCOE_{Det}$ did not differ much from the obtained values for the $LCOE_{Ref}$. The AEP value for the detailed LCOE calculation, AEP_{Det} accounted for the following variables: (i) CRT (total) power output, $TotPow$, from CFD results that varies with the power plant's number of units N_D (equation (6.10)); (ii) PTO efficiency η_{Gen} , 94.4% from the generator design tool; (iii) turbine's availability Av , assumed to be 95% (Neary et al. 2014a); (iv) transmission efficiency η_T , assumed to be 98% (Neary et al. 2014a); and (v) CRT's capacity factor CF , estimated to be an optimistic 50% (ORE Catapult 2019). The final AEP per unit, given in MWh was then obtained using equation (6.19), and the results for the different power plant sizes are summarised in [Table 6.14](#). Each power plant's rated capacity is also included for reference.

$$AEP_{Det} = \frac{TotPow \cdot \eta_{Gen} \cdot Av \cdot \eta_T \cdot CF}{1 \times 10^3} \quad (6.19)$$

Table 6.14: Annual Energy Production for CRT

Devices	Rated Capacity	AEP
1 Unit	49 kW	238 MW h
10 Units	487 kW	2384 MW h
50 Units	2436 kW	11 918 MW h

6.5.5 CRT Detailed LCOE Results

The $LCOE_{Det}$ was also computed using equation (6.4). The AEP calculated in Section 6.5.4 was used as E_n in the equation, the CAPEX and OPEX results from previous sections were included in the numerator of the equation. The calculation results are shown in Table 6.15 introducing the economic feasibility study detailed in this section. For the purpose of this thesis to determine the feasibility of a power plant using the proposed CRT, the costs were compared to those (average) projected by Ocean Energy Systems et al. (2015) and shown in Table 6.1. The first array was related to the 1 unit TSP, the second array to the 10 units TSP, and the commercial scale project to the 50 units TSP analysed in this chapter.

Table 6.15: Contra-Rotating Turbine $LCOE_{Det}$ Summary

	1 Unit	10 Units	50 Units
CAPEX	£ 8 576 898	£ 23 424 689	£ 83 277 784
OPEX	£ 1 035 729	£ 2 377 834	£ 6 779 975
AEP	238 MW	2384 MW	11 918 MW

LCOE	£ 8572 /MWh	£ 2152 /MWh	£ 1390 /MWh

The $LCOE_{Det}$ results displayed in Table 6.15 proved that a project using the CRT proposed in this thesis would not be economically feasible when operating in 1.2 m/s tide velocity conditions, disproving the prediction made by the $LCOE_{Ref}$. The demonstration scale cost was 27 times higher than the predicted value by Ocean Energy Systems et al. (2015), whereas the second array and the commercial scale projects costs were more than 8 times the projected cost. Nonetheless, due to the detail of the calculation, it was possible to determine what factors affect the cost most allowing to understand how the costs could be reduced for this type of project to be commercially competitive as it was expected with more mature technologies.

The power plant's size cost comparison demonstrated that economies of scale will have an effect in the development of TSP. Figure 6.18 illustrates how the final $LCOE_{Det}$ decreased when the

of units increased. Following the approach suggested by Bryden et al. (1998), and implemented by Vazquez et al. (2016b), a power curve was fitted to the points showing how the costs vary with the number of units installed in a power plant. The total $LCOE_{Det}$ was reduced 299% when the TSP size varied from 1 to 10 units, and a further reduction of 54% was found from 10 to 50 units. The slope displayed in the $LCOE_{Det}$ power curve suggests that the cost could be reduced even further with a higher number of units installed in a power plant. This possibility is discussed to a greater extent in Section 6.6.

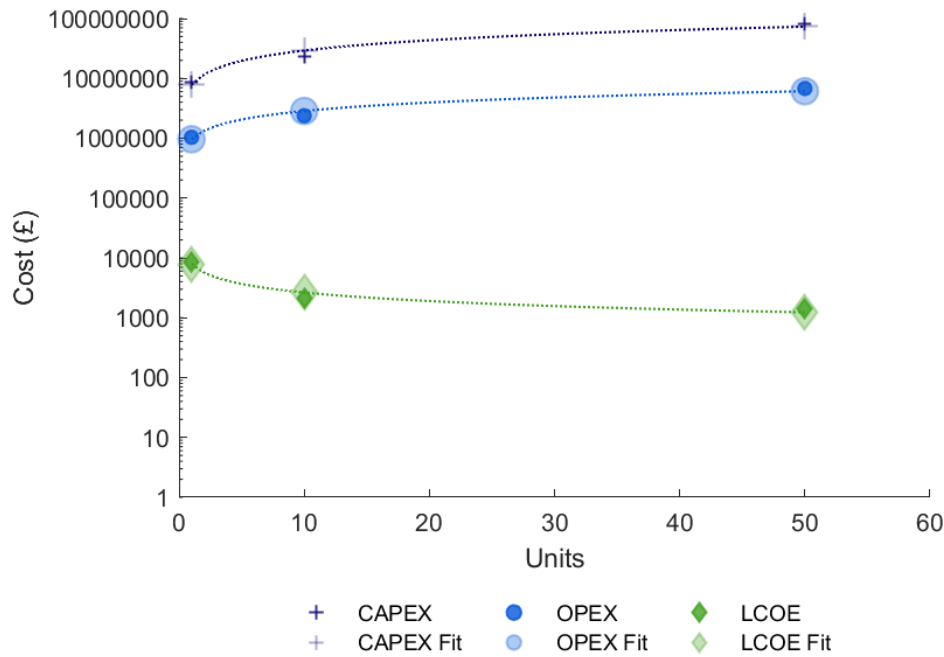
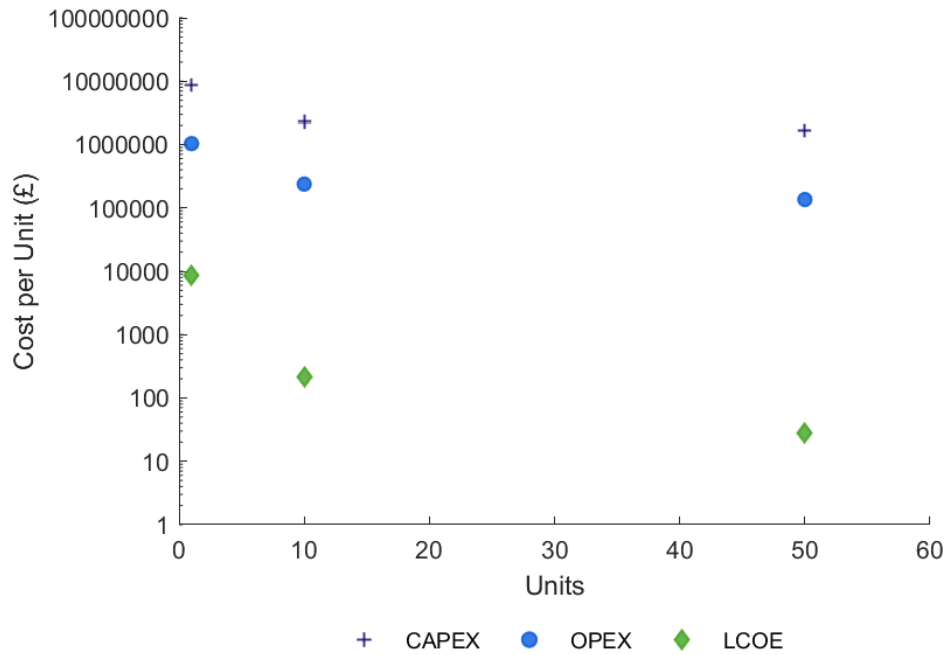


Figure 6.18: $LCOE_{Det}$ Costs

Capital and operational expenses inherently increased with the number of devices, but the cost per unit was reduced with the augment in number of units. This behaviour can be seen in Figure 6.19, where an overall increase of 272% in CAPEX led to a decrease of 73% in the capital cost per unit from 1 to 10 units, and a further increase of 257% in the CAPEX from 10 to 50 units led to a decrease of 27% in the cost per unit. Similarly, the total OPEX increased with the number of units (129% more from 1 to 10 units, and 185% from 10 to 50 units) but this ratio caused a decrease in the OPEX per unit (77% less from 1 to 10 units, and 43% less from 10 to 50 units).

The same trend was also observed when analysing the $LCOE_{Det}$ per unit as the size of the power plant increased. The $LCOE_{Det}$ per unit for a 10 units power plant was 40 times lower than

Figure 6.19: LCOE_{Det} Costs per Unit

the LCOE_{Det} for a 1 unit power plant, and when increasing the size to 50 units the LCOE_{Det} per unit was 7 times lower than that. The main contributor for this reduction was the OPEX input in the final value as the number of units increased.

The effects of each component listed in the previous sections on the total CAPEX and OPEX changed with the power plant's size, as it is shown in Figure 6.20 and Figure 6.21. All Level 2 components of the LCOE_{Det} are included in those charts to account for the 100% of capital and operational expenses.

In Figure 6.20 it is seen how the installation represented the largest percentage of total capital costs as the power plant size increased from 1 unit (demonstration size with 45% of CAPEX) to 50 units (commercial project with 71% of CAPEX), because the required vessel and labour time increased with the number of units. The capital development costs input in a power plant did not vary significantly with the power plant size (they duplicated), as the TSP got bigger they represented less of an expense in relation to the other components. The infrastructure required had a bigger impact on the total initial expense when there was one unit installed, but as the number of devices increased the percentage was reduced by half. The moorings' effect on CAPEX stayed relatively constant regardless of the power plant size, as it did the contingency fund and the subsystem integration because their input to the cost was directly related to

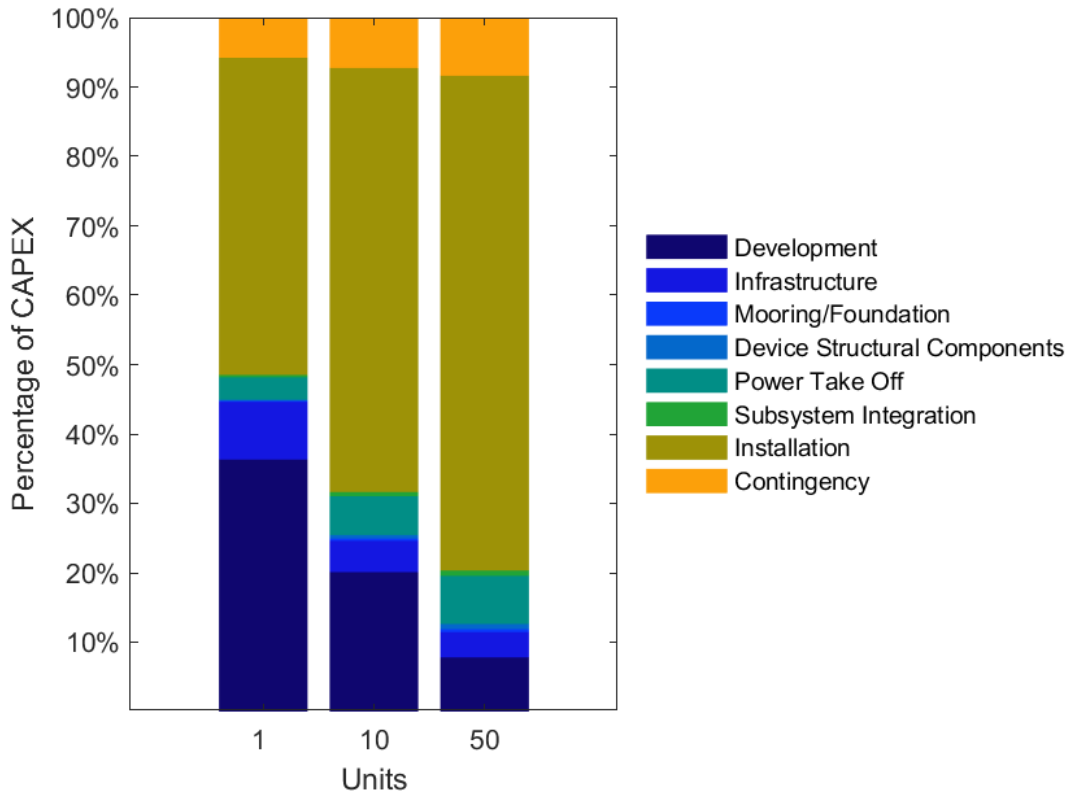


Figure 6.20: LCOE_{Det} Capital Expenses Breakdown

the power plants rated capacity. The PTO system’s effect on CAPEX doubled from 4% in the demonstration TSP to 8% in the commercial project. From these results it was concluded that the main factor to address when aiming to reduce the LCOE for a TSP that intends to use a CRT in a low velocity conditions site was the installation cost, since it was the main contributor to the capital expenses and its impact on the cost increased with the project size.

The OPEX components breakdown is displayed in Figure 6.21. The insurance’s input to the annual OPEX was relatively constant (as expected) with the increment in power plant size from 7% in a demonstration project to 8% in a commercial TSP. Similar to the CAPEX breakdown, the environmental monitoring cost represented less of an input to the OPEX as the project got larger, being the main component when 1 unit was installed with 59% of the total annual OPEX to 11% for a 50 units deployment because the requirements are relatively similar regardless of the project’s size. The shoreside operations percentage in the annual operation costs decreased with the number of units (from 23% in demonstration stage to 4% at commercial size) as the required labour to manage a site can handle several units at once reducing the effect on cost per device management. On the contrary, the marine operations and replacement parts costs

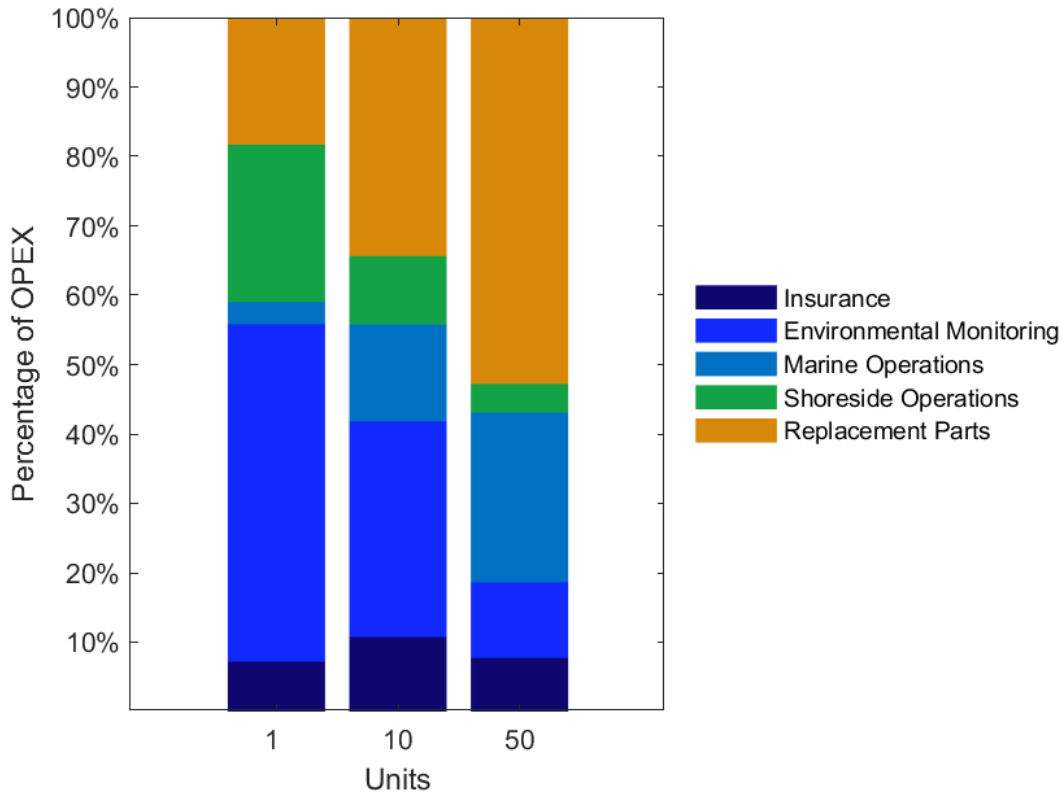


Figure 6.21: LCOE_{Det} Annual Operational Expenses Breakdown

percentage in the annual OPEX increased with the number of devices deployed. The former represented only 3% of OPEX when 1 unit was installed and increased to 24% when 50 units are in place, with the main drivers to these costs similar to those required for the installation, therefore as the plant size increases so does these expenses. As most of the OPEX components decreased the replacement parts became the largest contributor to the annual costs increasing from 18% in the demonstration stage to 53% in a commercial project.

From the LCOE_{Det}'s results it was found that as the TSP got larger the on-site work in the sea for maintenance and installation represented a significant percentage of the overall costs, suggesting that a reduction on these expenses would reduce the LCOE to a value that would make the CRT more competitive with other technologies. Likewise, if the manufacturing cost for the device itself and its replacement parts could be reduced, the overall plant's costs could decrease helping to achieve the required economic feasibility for the CRT to be deployed.

The following section expands on how the main cost components in the LCOE calculation could be reduced to be en par with the predicted costs from Ocean Energy Systems et al. (2015). The LCOE_{Det}'s final value for a 50 units power plant also showed that the LCOE_{Ref}

computed in [Section 6.4](#) for a commercial size power plant was 5.5 times lower, proving that the method created by Vazquez et al. (2018) underestimated the costs involved in a TSP. The main variables affecting the $LCOE_{Det}$, installation and operation costs, were largely generalised by Vazquez et al. (2018) making that method unreliable when estimating the real LCOE for a TSP.

Due to the limitation on the information provided by the $LCOE_{Ref}$ approach, the cost reduction opportunities proposed in the following section were based in the data provided by the $LCOE_{Det}$, which will be referred to as LCOE from here onwards.

6.6 Cost Reduction Opportunities

From the results obtained for the LCOE, an extended analysis was made to determine how the costs could be reduced in order to make the CRT device proposed in this thesis economically feasible when operating in tide velocities of 1.2 m/s. This section expands on the findings mentioned above with a sensitivity analysis for the commercial size power plants, and a forecast on the size of a power plant to achieve competitive costs if the current costs were kept. Then a list of suggestions on how the LCOE calculation (and assumptions) could be improved for future research is given.

6.6.1 Sensitivity Analysis

This section provides a study made to understand how the variation of the components involved in the LCOE calculation would affect the final result, and how much they would need to change in order to achieve the expected average values projected by Ocean Energy Systems et al. (2015): £ 310/MWh for a 1 unit TSP, £ 229/MWh for a 10 units TSP, and £ 141/MWh for a 50 units TSP. The charts shown in this section refer to the results for the commercial size power plant (50 units); the same charts are included in [Appendix D](#) along with their version for the 1 unit and 10 units power plants. These plots display the sensitivity analysis made to the LCOE results in a way that: (i) the x-axes represent a $\pm 20\%$ variation of each component considered in the chart, with 0% being the value used in the original LCOE calculation, and (ii) the y-axes show the LCOE fluctuation when each component considered is varied $\pm 20\%$ and all the other variables involved in the LCOE calculation remained constant.

On [Figure 6.22](#) the Level 0 variables were analysed. A variation of $\pm 20\%$ was made to

the CAPEX, OPEX, AEP, and discount rate to understand their effect on the LCOE results whilst all other variables were kept constant. It was found that said change would not make the technology commercially ready: a – 20% variation on the discount rate would only reduce the LCOE to £ 1 288/MWh, and for the LCOE to reach £ 141/MWh the CAPEX and OPEX alone would have to decrease 152% and 221% respectively, and the AEP would need to increase 891%. The cost variation may be difficult to achieve, but the AEP could be increased if the factors involved in its calculation were to be modified.

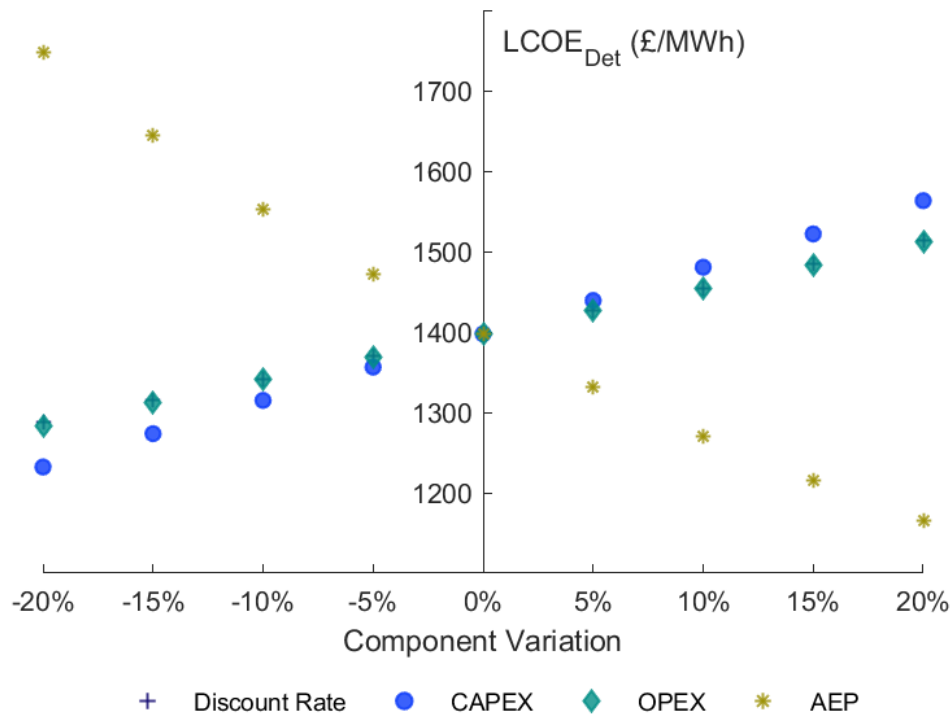


Figure 6.22: LCOE_{Det} Sensitivity Analysis for a 50 Units TSP

The main value affecting the annual energy production would be the power output. With the help of Figure 6.23 the effect on the LCOE was studied by considering the device's power, the fluid velocity, and the power plant's capacity factor. Similar to the analysis made for the LCOE_{Ref}, it was found that the variation in the velocity had the most significant impact on the LCOE result due to its cubic effect in the theoretical equation used to determine the available power in a specific location, visible in the figure below. Though an improvement of 20% would not achieve the desired competitive cost of £ 141/MWh, if there was a way to increase the velocity up to 2.9 m/s a power plant in this CRT would reach that LCOE. The device's power

output and the plant's capacity factor had the same sensitivity curve which showed that a 20% increase would not suffice to make the CRT economically viable. In order for that to happen, a power increase of over 1200% (to 659 MW) or a capacity factor increase of 900% would be required. The former can be achieved by adding more devices in the power plant, but the latter is not physically possible.

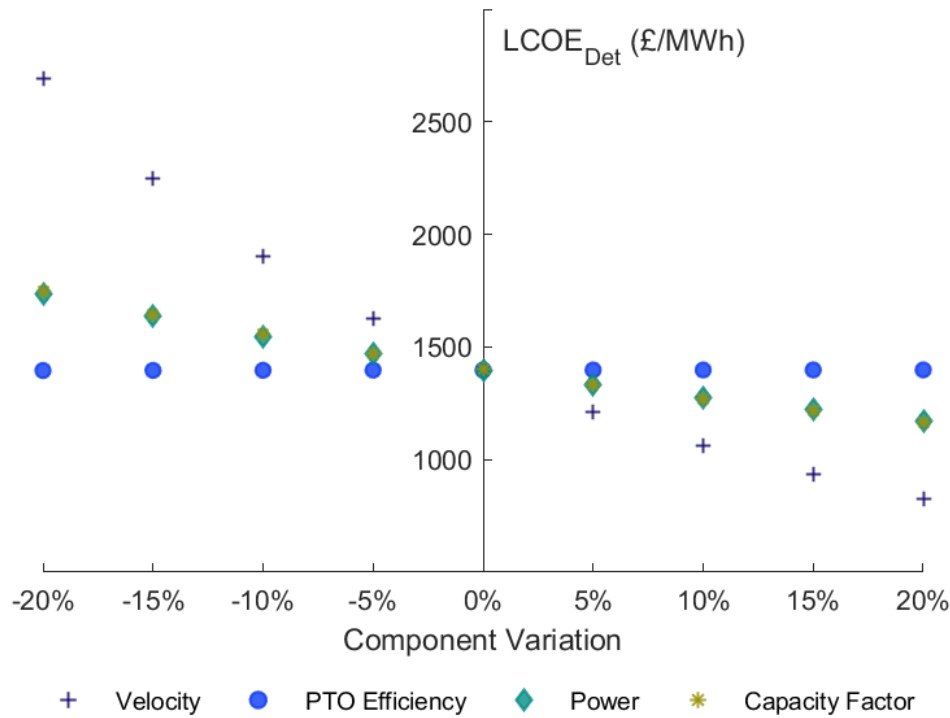


Figure 6.23: LCOE_{Det} Power Related Sensitivity Analysis for a 50 Units TSP

As mentioned before, modifying the CAPEX and OPEX on their own without changing any other component will not bring the cost down enough for the CRT to be economically feasible as it is. However, it was found from [Section 6.5.5](#) that the main factors affecting the cost in both operational and capital expenses are related to marine operations and installations. To expand on how they affect the LCOE when each of them were modified on their own, [Figure 6.24](#) was made. In [Appendix D](#), the results are divided in OPEX and CAPEX components for more detail. In the CAPEX charts, development and generator costs were added because of their relevance at different project stages. Development costs represented a large portion of CAPEX in a 1 Unit power plant, whereas the PTO, with the generator as its main contributor ([Table 6.8](#)), increased its percentage of the cost in the commercial size deployment. The sensitivity analysis showed

that their $\pm 20\%$ variation in a commercial power plant's LCOE was less than $\pm 1\%$, thus they were removed from this study. For the same reason, OPEX environmental compliance and shoreside operations costs were removed from this analysis.

It was found that the main costs affecting the LCOE with the presented method were the installation costs, followed by the replacement parts, and marine operations. The slopes indicate that a $\pm 20\%$ variation in the installation costs would influence the LCOE value by $\mp 10\%$. The same variation on the replacement parts and marine operations costs would change the LCOE by $\mp 4\%$ and $\mp 2\%$, respectively.

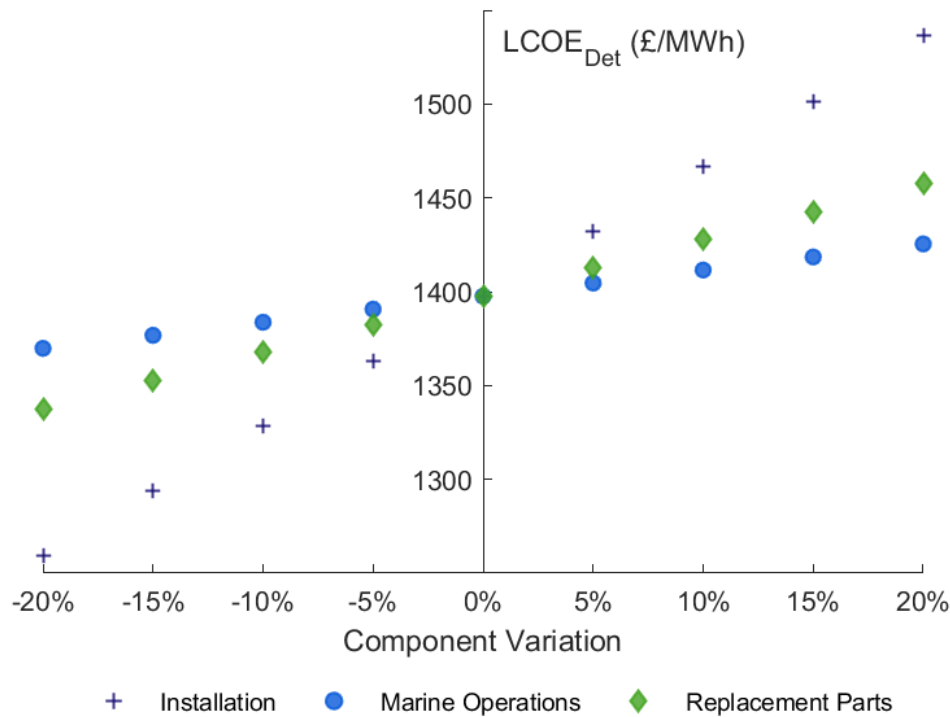


Figure 6.24: LCOE_{Det} CAPEX and OPEX Main Components Sensitivity Analysis for a 50 Units TSP

Installation costs could be reduced with improved logistics, planning, and weather forecasting to reduce the operation time per unit. With the development of marine energy dedicated vessels the daily cost could also decrease reducing the final LCOE. By having more experience and better planning the contingency days required for installation could also decrease. The installation procedure presented in this thesis was replicated from Neary et al. (2014a), where the assumptions were made by experience and for the RM4 device concept intended to be deployed in Gulf Stream off the southeast coast of Florida, in the United States. Future work

could be aimed at creating a specific installation cost estimation for the CRT in the location that was intended to be used (i.e. the Severn Estuary). It was also assumed that a dedicated vessel, proposed by Neary et al. (2014a), was available for operation during installation and maintenance. The daily rate was estimated with this hypothetical vehicle, bringing uncertainty to the final LCOE number.

Though the initial capital costs for the device did not represent a major effect in the LCOE, their replacement during maintenance did. Following the method provided by Neary et al. (2014a), the rate at which each part would fail was estimated assuming a fixed percentage value. This data could be narrowed down with more in detail analysis on how the CRT would operate, and how often parts would require replacement during the device's lifetime. Their individual cost was assumed to be constant with the initial expense, but with economy of scale and the industry's development, each part could cost less than the initial estimated cost.

Marine operations were also significant in the LCOE calculation. Their cost could also be reduced when planning, more experience, and maintenance predictions improve as industry develops. A more in detail study that applies directly to the proposed CRT and power plant could determine more accurate costs for the LCOE calculation. Neary et al. (2014a) based their predictions from wind industry learning assuming redundancy in the turbine design, that would reduce the maintenance per device. An opportunity to decrease the LCOE would be proposing a manufacturing design process for the CRT that would implement the redundancies to determine the real costs for the turbine, and the specific maintenance required. This data along with improved planning and lower vessel daily costs, could create an opportunity for the CRT to be competitive with other tidal stream technologies.

Using the computed LCOE as benchmark, it was found that for the CRT to reach a cost of £ 141/MWh the predicted OPEX and CAPEX (in combination) must be 10 times lower than their current values. The above analysis has proven that there is a long way to go for tidal turbines to be economical in velocity conditions down to 1.2 m/s; the industry must grow to reduce the uncertainty (and costs) in marine operations for installation and maintenance, and for capital costs to decrease. These can be achieved with the development of smaller projects to learn the know-how and reduce the uncertainty by having successful deployments.

At the current stage of technology it could be useful to start deployment of turbines in locations where the need for electricity from renewable sources with access to the source out is larger than the need to make profit from the power plants. These projects would be categorised

in quadrant II from [Figure 6.3](#), where the monetary gain is not the main factor to determine their implementation.

6.6.2 LCOE Forecast

In [Section 6.5.5](#) it was found that the costs involved in the calculation of the LCOE varied with the number of units following a power curve. Expanding on those results this section analyses how this data could be used to forecast the LCOE based on the number units installed in a power plant. The curves included in this section were verified with 1, 10, and 50 unit points to confirm their accuracy. Differences of $\sim 8\%$, $\sim 20\%$, and $\sim 11\%$ were found for the CAPEX, OPEX, and LCOE curves, respectively.

In the previous section opportunities on how to reduce the cost for various components of the LCOE were presented. However, if a reduction on all those items was not achievable, the curves from [Figure 6.25](#) show that by increasing the number of units the LCOE would reach the aimed value of £ 141/MWh. Using the power law equations fitted to the data for 1, 10, and 50 units it was estimated that a power plant with 4824 CRT devices would make the project commercially competitive. A power plant this size would have a rated power of 235 MW, which differs from the 659 MW estimated required power by the sensitivity analysis. The difference lies on how the LCOE is predicted between the methods: the sensitivity analysis predicts the value using the equations included in the detailed LCOE calculation that relate the power output with the costs involved in the power plant, whereas the forecast is based on the trend created by several points in a chart based on units and final costs.

This prediction was made assuming that costs would behave following the trend found between 1, 10, and 50 units, and the $LCOE_{Forecast}$ is estimated applying the power law equation for the LCOE curve. Equations (6.20) to (6.22) describe the fitted curves from [Figure 6.25](#), including CAPEX ($CAPEX_{Forecast}$) and OPEX ($OPEX_{Forecast}$) curve equations. By applying these, it was found that the cost per CAPEX and OPEX per unit would decrease 88% and 15% from the current value, respectively, if 4824 units were to be installed.

$$LCOE_{Forecast} = 7877 \cdot N_D^{-0.474} \quad (6.20)$$

$$CAPEX_{Forecast} = 7.8 \times 10^6 \cdot N_D^{0.5711} \quad (6.21)$$

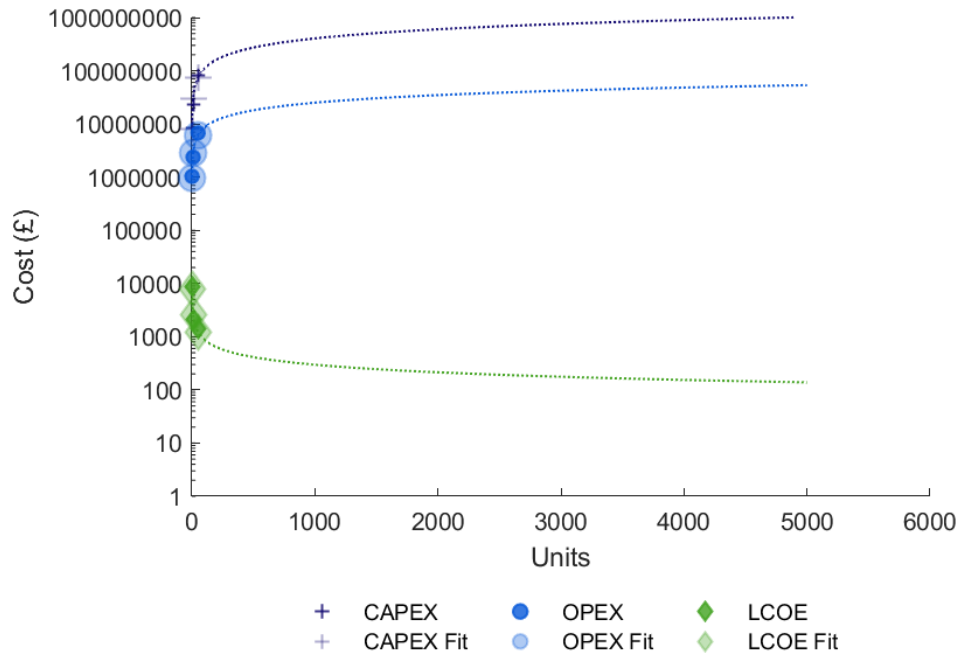


Figure 6.25: Forecast $LCOE_{Det}$ Costs

$$OPEX_{Forecast} = 9.6 \times 10^5 \cdot N_D^{0.4721} \quad (6.22)$$

From the cost reduction opportunities study it was found that a combination factors would make the device economically feasible and commercially ready to be in a power plant: number of units deployed, and reduction in installation, maintenance, and replacement parts costs. The device's bespoke mechanical design, manufacturing process, mooring system, PTO, installation process, maintenance plan, and environmental requirements would allow to confirm the LCOE prediction. From the experience of this analysis, a list of suggestions on how to improve the accuracy of the LCOE computation is given in the following section.

6.6.3 LCOE Improvement Suggestions

- (i) The environmental and development costs were based on the regulations stipulated for the United States. Each country has their own procedures, and fees which could affect the LCOE.
- (ii) Environmental characteristics, and available databases also vary depending on the location. When calculating the LCOE the information required for environmental impact as-

assessment could differ from the estimated value presented above.

- (iii) The site assessment costs were replicated from Copping et al. (2011). Based on the available data of the power plant site, this assumption could make the LCOE vary.
- (iv) Hydrodynamic effects of the array configuration (and distance) were not taken in consideration when calculating the LCOE. Further research on the interaction between devices could allow for a more accurate cost prediction.
- (v) The cable costs per metre were assumed to be the same from Neary et al. (2014a). To determine a more accurate LCOE cable design and cost should be made considering the required electric specifications for the proposed CRT.
- (vi) The mooring costs were assumed using the same lines and chains used by Neary et al. (2014a) for the RM4, but relating the costs to the power output. A bespoke design, based on the turbine's loads for the CRT, would provide a more accurate value for this component.
- (vii) Anchor design was based on cost per kW. A detailed LCOE should consider selected anchors based on the device's loads.
- (viii) The PTO cost was obtained assuming a regular stator-rotor generator using the specs from Poore et al. (2003). A bespoke contra-rotating generator for the CRT would provide a more realistic cost.
- (ix) The vessels' used for installation and maintenance were assumed to be the same as those for the reference models. Using more accurate values for the device's physical specifications (i.e. size and weight), other (smaller) vessels could be considered.
- (x) Manufacturing costs could change based on real salary, reduced time, and experience of the companies that would fabricate the real CRT. These costs could be obtained by providing a full mechanical design of how the CRT should be built.
- (xi) Depending on who's using the LCOE results, a profit margin might be required to be included in the LCOE calculation.
- (xii) Mooring landing costs were based on a project that required to moor a device in a site with 700 m depth. The daily costs may vary for a shallower installation, where a different vessel could be used.

- (xiii) OPEX costs were considered to be constant during the device's lifetime. This uncertainty could be reduced by projecting costs for the LCOE calculation.
- (xiv) The capacity factor was assumed to be an optimistic 60%. This value could be changed based upon the site's characteristics.
- (xv) The insurance cost could decrease when there's less risk and uncertainty with marine energy projects.
- (xvi) Economy of scale was not considered in all cost predictions. With the availability of commercial data as the industry develops this factor could be included in the LCOE calculation.

The LCOE data was obtained based on parameters that applied to the United States, and then adapted for the United Kingdom. To determine how these results would be expected if the devices were to be installed in Costa Rica, the CRT application for such project is analysed next in [Section 6.7](#).

6.7 Applications to Costa Rica

Costa Rica produced more than 99% of its electricity from renewable energy in 2019 (Presidencia de Costa Rica 2019), but a reduced number of renewable source power plants planned for the following years could lead to the use of fossil fuels as an alternative to deal with the predicted demand increase (Instituto Costarricense de Electricidad 2017). Though marine energy is not considered for commercial scale in Costa Rica, this new technology could be an option if its technical and economic characteristics suit the country's needs.

This section provides context on how a tidal stream power plant would be if a proposal was made for Costa Rica. Using data from initial studies (Brito e Melo 2013) a hypothetical power plant is proposed in Gulf of Nicoya, the highlighted region in [Figure 6.26](#). The expected velocities in that area can be up to 1.2 m/s, and the points in the map show existing transmission stations which would facilitate the power plant connection to the grid.

If the turbines proposed in this thesis were to be used, the LCOE values for Costa Rica would differ to results for the UK. Due to the lack of data for marine energy extraction to produce electricity in Costa Rica, a comparison was made using wind technology from 2016 as reference, when both the UK and Costa Rican governments provided data on costs per energy for the power plants used in each country.

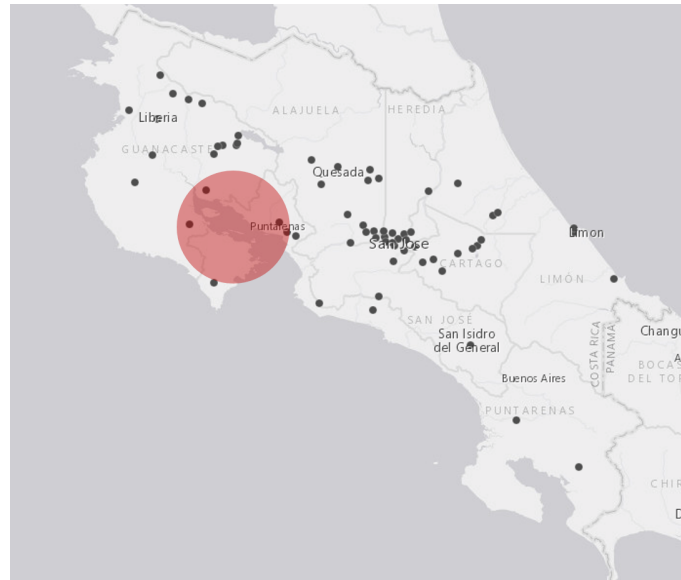


Figure 6.26: Tidal Stream Farm Location in Costa Rica.
Source: Esri (2018)

Using an exchange rate of £ 1 = \$ 1.24 (November 2016 (X-Rates 2019)), it cost £ 64/MWh to produce electricity in the UK from wind farms (DBEIS 2016). In Costa Rica, it cost £ 103/MWh to produce electricity using the same energy source (Instituto Costarricense de Electricidad 2017). Applying the same ratio to the CRT LCOE_{Def}'s results, it would cost £ 2 244/MWh to generate power in Costa Rica if the devices were to be deployed there. The cost varies because of each country's reality: Costa Rica must import devices from abroad increasing capital costs, and each system has different policies that may or may not support the development of renewable energy power plants.

These results are not competitive with the electricity market in Costa Rica, where the highest LCOE of £ 224/MWh is found for a geothermal power plant, *El Encanto* (Instituto Costarricense de Electricidad 2017). As mentioned in the previous sections, the capital and operation costs must decrease before tidal energy can be considered to produce electricity as part of the country's electricity matrix. A resource characterisation campaign should also be made to find the real velocity tidal values, and with that data determine the real economically feasibility in the country. It is also recommended to obtain costs based on quotations, and planning that would apply directly to the installation of the specific technology in Gulf of Nicoya. Other areas could also be considered based on the resource availability.

When making a more in depth economic feasibility study all the aspects that are involved in a project must be considered, including planning, design and environmental impacts. Depending

on regulations, the permits required may represent a significant cost, from the time needed to complete all the procedures, to the studies that are made and the direct cost for the deployment licence application (Dalton et al. 2015). If the turbine was technically and economically feasible to operate in Costa Rica, a stream power plant proposal would be limited by the planning procedure. Currently, it is not possible to develop a project of this kind because there is no regulation plan that includes marine energy extraction (Hernandez-Madrigal et al. 2016), as explained in Section 2.3.2.3.2. Taking UK's expertise for reference, a comparison between procedures was made to determine how marine energy in Costa Rica could eventually be incorporated in the electricity matrix:-

- (a) **Centralised System:** The UK has a more centralised system with clear procedures for developers to follow depending on the marine energy project's size. Costa Rica's bureaucracy requires the developer to contact different entities and determine on their own what is required for each specific case. When it comes to marine energy projects, it would be useful to have one organisation in charge of giving the guidelines for a project of its kind. The UK created National Significant Infrastructure Projects (NSIP) that makes the developer to deal mainly with one entity avoiding repetition of documents. Costa Rica could implement an approach similar to the UK's, where developers can find information they need on-line with clear links to the other parties involved, procedures and contact information.
- (b) **Marine Licence Procedure:** The UK has very clear divisions and types of permits required depending on the size of an offshore (and onshore) energy project. Costa Rica could use a guideline for projects of this type to be ready for when the technology is feasible to be used in the country. Previous plans made for ports, marines or water concessions can be used as reference. A marine lease method must also be established with construction, maintenance, operation and closing requirement procedures well specified. The Safety Zone Scheme used by the UK can be used as a guidelines for other users that will be affected by the project. Organisations and users involved in the resource's use could create a data base to determine what areas would be allowed for marine energy extraction.
- (c) **Environmental Impact Assessment (EIA):** Even though the methods in both countries are different the final outcomes are similar, with Costa Rican legislation providing more detailed requirements on the information that the EIA must include. The main difference between countries is the procedures duration, the deadlines given by SETENA in Costa Rica are not

always followed, therefore the process must be improved. SETENA should also provide details of the different stages of a marine power plant to be included in the EIA, and the Marine Licence procedure could be included in the same process. Requirements should adapt to different technologies since wave, tidal, offshore wind, and OTEC have different impacts.

- (d) **Electricity companies:** Legislation in the UK allows for private developers to propose new renewable energy projects. Costa Rica's law limits the private sector involvement and leaves one organisation (Costa Rican Electricity Institute, ICE) to make all the decisions related to project development. A change in legislation might allow the creating of smaller projects and diversify the electricity matrix management.
- (e) **Public Involvement:** In Costa Rica public interaction is decided by the developer, which depends on how much they intend to engage with the community, which are considered once the EIA is finished. In the UK for a marine energy project, the company must engage with the community from early stages and their opinions are considered for the approval and analysis of all the documents presented by the developer. Costa Rica could implement this system, where all documents, including communication between organisations, are available to the public on-line and in physical form if requested. This method makes the process more efficient because if there are technical studies suggested by interested parties that can delay/stop a project, they would be considered at an earlier stage and not when the EIA has been approved.
- (f) **Tariffs:** In Costa Rica a public company produces and manages the electric system, therefore the financial gain from projects are not required to be as high those for a private company. In the UK a project might not be developed if the tariffs are not beneficial for the end user and economically feasible for the developer. A balance must be found between both systems and, for marine energy specifically, the technology costs must decrease to be competitive with other renewable sources and fossil fuels.
- (g) **Tendering:** In Costa Rica tendering is offered only for generation projects limited to 50 MW if ICE proposes the project, or 20 MW if it is proposed by a private company. Transmission and distribution is managed by public companies that vary depending on the location, whereas the UK's system allows private companies to participate and manage the different stages of the electricity production (generation, transmission, and distribution). A larger

involvement of the private sector could be beneficial for Costa Rica in terms of competitiveness and options for the consumer.

The findings presented in this thesis concluded that though it might not be currently feasible to use the proposed CRT configuration in 1.2 m/s velocity conditions, further development in the marine energy sector might allow similar devices to be part of the electricity matrix in the future.

Chapter 7

Conclusions and Recommendations

This chapter presents a summary of the findings made in this thesis. The work presented analysed how CMERG's HATT performed in low velocity conditions when its well characterised geometry was modified, and modelled with ANSYS CFX following the methods described in [Chapter 3](#). Modifications were made to the single rotor turbine (SRT) based on its solidity characteristics in [Chapter 4](#), and a contra-rotating rotors turbine (CRT) was proposed in [Chapter 5](#). To determine their economic feasibility the levelised cost of energy (LCOE) was calculated for both configurations in [Chapter 6](#).

The conclusions are presented for each rotor configuration, and are followed by the economic feasibility outcome. Specific observations are given, and recommendations for future research are suggested based on these results.

7.1 Conclusions

7.1.1 Single Rotor Turbines

The single rotor HATT's performance was analysed for rotors that were modified from the original geometry using three cases: (i) constant chord length, (ii) constant solidity, and (iii) constant number of blades.

As explained in [Section 4.3.1](#), three rotor geometries were modelled per case. The optimum SRT geometry at which the maximum power output was obtained was found for each case. Their respective pitch angle, rotational speed, and performance coefficients were calculated. The optimum configurations that have this condition are listed in [Table 4.2](#).

The effects of solidity on a HATT's performance when operating in low velocity conditions can be predicted with the tools proposed in [Section 4.5](#). Performance equations were proposed for the single rotor turbines studied. The tip speed ratio, power, thrust, and torque coefficients for the maximum power configurations can be found based on the rotor's solidity for case (i) and case (iii). For case (ii) the prediction can be made based on the number of blades. The

graphs shown in [Figure 4.19](#), [Figure 4.20](#), and [Figure 4.21](#) have third degree polynomials fitted curves, with their respective equations listed in [Section 4.5](#).

7.1.1.1 Specific Observations on Single Rotor Turbines

At peak C_p for each rotor, it was found that a variation of up to 9° in the pitch angle could reduce the power output by 22%, and at the same time decrease the thrust by 37%. This reduction in loads could allow a compromise in power when designing the support structure for a SRT. This performance in variation allows to predict the turbine's behaviour in a variable pitch angle design.

All rotors, regardless of their geometry changes, operated in the same range of power and thrust coefficients. Turbine d was the exception, where a significant reduction on the loads was found whilst keeping the same power output. In general, it was found that solidity did not have a major impact on these performance characteristics.

The torque coefficient showed a different trend: it stayed relatively stable during all the modelled pitch angles, but the value itself was different for each rotor, with the highest C_θ obtained by Turbine A (i.e. 0.18). The torque variation at different pitch angles was not higher than $\sim 5\%$. This behaviour eases the selection of a generator that matches the rotor's torque for a variable pitch angle turbine.

For each analysed rotor, the tip speed ratio at which the maximum C_p was constant irrespective of the tip pitch angle. This characteristic could be advantageous when designing a variable pitch turbine, where the maximum power rotational speed would not vary.

The tip pitch angles at which Turbine B and Turbine C matched previous studies where the turbine was modelled at higher velocities. As shown in [Table 4.2](#), the tip pitch angle for case (ii) rotors match the value from Turbine A because they have the same solidity. The optimum lift coefficient and angle of attack should be the same under those conditions, as described in [equation \(4.9\)](#) and [equation \(4.11\)](#).

The highest net power output obtained from Turbine D was 3% higher than Turbine A's estimated power, 31 kW. The lowest power output was predicted by Turbine B, 28 kW, 8.5% lower than Turbine A's.

7.1.2 Contra-Rotating Rotors Turbine

A contra-rotating matching rotors process was proposed to determine a technically feasible CRT configuration to model with CFD using the SRT geometries from [Chapter 4](#). The process, explained in [Section 5.3](#), was divided in three steps: (a) single rotor possibilities, (b) rotor matching, and (c) rotor selection.

The single rotor options were dependant on: number of blades, tip pitch angle, tip speed ratio, blade shape, and radius. The combinations that had rotors with matching net torque outputs, and did not have blade interference with each other were found. To reduce the number of configurations, their total rotational speed was restricted by the specifications of an off-the-shelf direct drive permanent magnet generator to select those options with the highest speed, and the 200 combinations with highest power output were compared to their LCOE.

The average LCOE of the 10 configurations with lowest value was obtained, and the combination that had this cost predicted was modelled with CFD. The geometry specifications, and expected performance characteristics are shown in [Table 5.2](#).

The CRT selection process was proved to be effective for a technically suitable CRT. As expected, the CFD steady state model results differed from the predicted turbine's performance because the interaction between rotors during rotation was not captured by the performance coefficients equations. The transient model results did not match the predicted turbine performance, but they were aligned with the initial contra-rotating requirements, and the overall power coefficient was higher than all SRTs.

7.1.2.1 Specific Observations on Contra-Rotating Rotors Turbines

The final transient results of the selected CRT showed a 11% torque difference between the front and back rotors, and the power coefficient increased from 0.47 with the optimum SRT to 0.50. The total CRT trust also decreased from the predicted value by 25%, but the overall thrust coefficient was higher than 1. The results showed that when a bespoke power plant is proposed for the CRT, the benefits of using a CRT configuration must be compared with the costs of using a supporting structure that withstands the loads.

The CRT power output was 49 kW, 41% less than the 82 kW predicted result with the theoretical selection process. This reduction in power increased the LCOE by 35%, categorising the device as ready to be part of a second array stage power plant instead of the commercially ready stage, as initially predicted.

7.1.3 Levelised Cost of Energy for SRT and CRT

An economic feasibility approach based on LCOE was proposed for the SRT and CRT modelled. A reference LCOE ($LCOE_{Ref}$) was calculated for the SRT to determine its economic feasibility, and based on the results a CRT was considered to reduce costs even further. The reference LCOE calculation was adapted to account for both rotors of the CRT, with predictions showing that the cost could be reduced with the use of a said configuration in a power plant. The simulation results of the CRT configuration showed an increase in cost, hence a detailed LCOE ($LCOE_{Det}$) that would allow to determine possible cost reductions was computed. The calculations were made considering previous site studies on the Severn Estuary in the UK.

The $LCOE_{Ref}$ was calculated for 15 SRT rotor diameters of each rotor condition analysed. The configuration with highest power to LCOE ratio was found to be a 7.5 m radius, 5 bladed Turbine D configuration with an expected power output of 71 kW, and a predicted £ 164/MWh. This result showed that the configuration was technically capable to operate in low velocity conditions and if located in a power plant, it would have a cost within the expected range for commercial power plants. It was also found that if a compromise in power was made when selecting the optimum SRT, the LCOE could be kept constant using a smaller rotor that could make installation and maintenance logistics simpler.

The $LCOE_{Ref}$ results for CRT were used as a variable to select a technologically feasible CRT combination to model. The predicted $LCOE_{Ref}$ for the 6 m 3–2 CRT was £ 158/MWh. Simulation results showed that the net power output was 41% less than predicted by the selection process, and the $LCOE_{Ref}$ increased to £ 214/MWh. The calculated cost showed that the technology was not in the commercial stage category, but within the second array scale of a power plant.

Due to the limited information given by the $LCOE_{Ref}$ on how to reduce TSP costs, the $LCOE_{Det}$ was obtained using cost predictions and assumptions from tidal stream and ocean current references models which provided values that were adapted for the CRT proposed configuration. It was calculated for three cases: 1, 10, and 50 units power plants that would represent the different stages of technology development (prototype, small commercial power plant, and fully commercial power plant). To account for all the costs involved in a tidal stream power plant the capital and operational expenses were divided into components, which were then divided once again to capture all the parameters involved in the $LCOE_{Det}$ calculation. The capital expenses included: (i) development, (ii) infrastructure, (iii) mooring, (iv) device structural components, (v) power take off system, (vi) installation, and (vii) other costs; and the operational expenses

considered: (i) insurance, (ii) environmental monitoring and regulatory compliance, (iii) marine operations, (iv) shoreside operations, and (v) replacement parts costs. All the values used in the cost calculation were summarised in tables within [Chapter 6](#) and more detail of the assumptions are given in [Appendix C](#) for the cases when it was needed.

It was demonstrated that economy of scale have an effect in the development of tidal stream power plants. Capital and operational expenses increased with the number of units, but the cost per unit decreased as the power plant size augmented. Due to the required vessel and labour time needed per unit, installation costs represented the largest component in the capital expenses as the power plant's size increased. For operational expenses, marine operations and replacements parts represented the main component of the cost with the increase in number of units. These results indicated that a reduction in costs for on-site work in the sea and device parts manufacturing could help to make the CRT economically feasible to be deployed in a commercial size power plant.

Finally, an analysis was made to determine the applicability of this technology in Costa Rica. Due to the lack of development in marine energy in Costa Rica, a comparison was made relating current costs for wind energy devices in the UK and Costa Rica. The linear comparison showed an increase in the LCOE to £ 2 244/MWh for the CRT were they to be installed in the Gulf of Nicoya. These results made the technology not feasible to compete in the Costa Rican renewable energy market until there is a significant reduction in capital and operation costs. Nonetheless, even if a device was technologically and economically feasible to operate in conditions like the ones found in Costa Rica, the current legislation would not allow the proposal for a power plant to use the tidal stream resources. There is no marine licence procedure, nor regulation to give the required permits for a marine energy development. In [Section 6.4](#) a comparison was made with the planning process used in the UK.

7.1.3.1 Specific Observations on Levelised Cost of Energy for SRT and CRT

A sensitivity analysis was made for the $LCOE_{Ref}$ in [Section 6.4.6](#) for the proposed CRT and SRT. The flow velocity had the biggest effect on the $LCOE_{Ref}$ due to its cubic presence in the power equation (equation (2.3)). The capital and operational costs were compared for the SRT, the selected CRT, and the modelled CRT. Simulation results showed that since the power output was lower than predicted for the selected CRT, the capital expenses increased making the SRT configuration the most economically feasible turbine from the proposed devices according to

the $LCOE_{Ref}$. This calculation was found effective to provide a reference on the parameters involved in the LCOE calculation and helpful to relate the turbine geometry characteristics with economic factors, allowing to select a CRT to simulate based on the $LCOE_{Ref}$ results. However, this tool was not able to capture the benefits of using a moored CRT when compared to a monopile foundation with a SRT in terms of logistics, transportation, and maintenance. Because this study lacked the possibility to determine what needs to be done for the modelled CRT to be commercially ready, the $LCOE_{Det}$ was calculated.

The $LCOE_{Det}$ results for 1, 10, and 50 units power plants that would use the modelled 3–2 CRT were £ 8 572/MWh, £ 2 152/MWh, and £ 1 390/MWh, respectively. These values disproved the prediction made by $LCOE_{Ref}$ showing that the proposed CRT would not be economically feasible when operating in 1.2 m/s tide velocity conditions. However, given the detail of the calculation it was possible to determine how costs could be reduced in order for the device to be commercially competitive with more mature technologies.

A sensitivity analysis was also made for the $LCOE_{Det}$ (LCOE from here onwards) to further understand how the cost components used in the calculation affected the final results, and how much they would need to vary in order for the CRT to be en par with other commercially ready tidal stream technologies. Plots were made to assess the effect of: (i) the variables used in the LCOE equation (equation (6.4)), (ii) the factors affecting the annual energy production, and (iii) the main components of OPEX and CAPEX described above, in the LCOE using a $\pm 20\%$ variation from the values used in the initial calculation whilst keeping all other costs constant. These charts were displayed in Section 6.6.1 for the 50 units power plant, and with more detail in Appendix D for the 1, 10, and 50 units power plants. It was found that for the CRT to be economically feasible CAPEX and OPEX would need to decrease by 152% and 221% respectively if all other variables were kept constant. The annual energy production could decrease the LCOE to commercially ready values if the tide velocity increased to 2.9 m/s.

The $\pm 20\%$ variation in installation, marine operations, and replacement parts costs showed their effect on the LCOE calculation. Bespoke logistics for the CRT proposed power plant, along with a reduction in manufacturing costs that come with learning and experience in the tidal stream technology development could reduce the final LCOE value. The industry must grow to reduce uncertainty in the cost prediction and for capital costs to decrease.

To describe the cost predictions behaviour found in this research, it was noticed that a power law curve could describe it if the trend used in the LCOE calculation remained constant. The

effect of economy of scale, found with the results for different power plant sizes, was used to estimate the number of units required in a power plant for the CRT costs to be within the expected range for commercially ready technologies: 4824 turbines. These data combined with the sensitivity analysis made showed that a combination of factors are needed for the proposed CRT to be economically feasible when deployed in a tidal stream power plant.

7.2 Recommendations and Further Work

- For the SRT rotors from case (ii), where the solidity was kept constant, a 4% difference was found with the angle of attack from Turbine A. A more refined mesh around the blades could capture the fluid interaction with the turbine for the results to match the expected values.
- The curves created for each case in [Chapter 4](#) allow to determine what performance is expected in peak power conditions. The solidity values are limited, and more points could be added to the curves with future studies.
- These SRT prediction curves are useful for the analysed CMERG's specific blade shape, and further studies could determine their applicability to different geometries.
- The selected CRT was modelled assuming a 3 bladed front rotor, and a 2 bladed back rotor. The selection criteria did not account the rotors' location hydrodynamics, hence further work could compare results if their relative location was swapped.
- The proposed CRT could be modelled following modifications suggested by previous studies, such as: (1) a 7° increase in the back rotor's pitch angle from its optimum SRT configuration by Huang et al. (2016b), or (2) a 9% difference between rotors' diameter by Wei et al. (2016). Both changes could increase the power output.
- Depending on computational capabilities, the fluid behaviour in between rotors of the CRT could be further characterised.
- The 20 rotors with highest power output had an estimated LCOE value with a variability of < 1%. Further studies could model the other 19 CRT configurations to expand on the proposed methodology's capability.
- The LCOE calculation followed assumptions made for projects that were based in the United States. A bespoke cost prediction analysis could provide more realistic results for the proposed

CRT.

- Due to the limitations and uncertainty given by the LCOE study, a list of recommendations to improve the calculation in future work was given in [Section 6.6.3](#).
- The HATT could be further studied within ducts to determine their real effect on economic feasibility. As shown in the sensitivity analysis, the flow velocity had a significant effect in the LCOE reduction. An additional structure that accelerates the flow could affect the LCOE.
- The LCOE comparison between the UK and its application in Costa Rica considered a linear implication between two different technologies. A more accurate LCOE prediction could be made considering the Costa Rica's supply chain, and costs incurred with the required logistics for deployment of a hypothetical marine energy power plant.
- The turbines analysed in this research were optimised based on maximum power output when they operated in low velocity conditions (i.e. 1.2 m/s). Given that power depends on torque and rotational velocity, further work could emphasise the rotor optimisation on rotational velocity increase to reduce the required torque. This approach might cause a decrease in cost with the need of a smaller generator that would require smaller transportation vessels during installation and maintenance of the devices.

Appendix A

Turbines' Geometry Details

A.1 Baseline Turbine Blade Chord Length Variation

Table A.1: Blade A Details - 5 m Radius Turbine. Source: Mason-Jones et al. (2012)

Distance to Last Plane mm	Radius mm	Local Pitch Angle °	Chord Length mm
-	1086.54	40.54	1597.86
130.90	1217.44	37.59	1600.85
130.90	1348.33	34.75	1604.63
130.90	1479.23	32.09	1606.45
130.90	1610.13	29.65	1603.52
130.90	1741.02	27.45	1593.04
130.90	1871.92	25.47	1573.18
130.90	2002.82	23.69	1543.48
130.90	2133.71	22.08	1504.44
130.90	2264.61	20.62	1457.06
130.90	2395.51	19.28	1402.61
130.90	2526.41	18.03	1342.53
130.90	2657.30	16.87	1278.44
130.90	2788.20	15.77	1212.07
130.90	2919.10	14.71	1145.25
130.90	3049.99	13.70	1079.85
130.90	3180.99	13.28	1017.83
130.90	3311.79	12.29	961.01
130.90	3442.68	11.37	913.98
130.90	3573.58	10.54	873.86
130.90	3704.48	9.75	837.19
130.90	3835.38	9.02	803.87
130.90	3966.27	8.36	773.81
130.90	4097.17	7.76	746.89
130.90	4228.07	7.25	723.04
130.90	4358.96	6.82	702.17
130.90	4489.86	6.48	684.21
130.90	4620.76	6.23	669.11
130.90	4751.65	6.08	656.79
130.90	4882.55	6.00	647.22
77.72	4960.27	6.00	642.81
39.73	5000.00	2.48	550.24

Table A.2: Blade A Details - 6 m Radius Turbine

Distance to Last Plane mm	Radius mm	Local Pitch Angle °	Chord Length mm
192.31	1086.54	40.54	1597.86
164.34	1250.88	37.59	1600.85
164.34	1415.23	34.75	1604.63
164.34	1579.57	32.09	1606.45
164.34	1743.92	29.65	1603.52
164.34	1908.26	27.45	1593.04
164.34	2072.61	25.47	1573.18
164.34	2236.95	23.69	1543.48
164.34	2401.30	22.08	1504.44
164.34	2565.64	20.62	1457.06
164.34	2729.99	19.28	1402.61
164.34	2894.33	18.03	1342.53
164.34	3058.68	16.87	1278.44
164.34	3223.02	15.77	1212.07
164.34	3387.37	14.71	1145.25
164.34	3551.71	13.70	1079.85
164.34	3716.06	13.28	1017.83
164.34	3880.40	12.29	961.01
164.34	4044.75	11.37	913.98
164.34	4209.09	10.54	873.86
164.34	4373.44	9.75	837.19
164.34	4537.78	9.02	803.87
164.34	4702.13	8.36	773.81
164.34	4866.47	7.76	746.89
164.34	5030.82	7.25	723.04
164.34	5195.16	6.82	702.17
164.34	5359.51	6.48	684.22
164.34	5523.85	6.23	669.11
164.34	5688.20	6.08	656.79
164.34	5852.54	6.00	647.22
97.57	5950.11	6.00	642.81
49.89	6000.00	2.48	550.24

A.2 Modified Blades Details

A.2.1 Chord Length Calculations

A.2.1.1 Blade b Equations

$$\sigma_b = \sigma_A = 21\% \quad (\text{A.1a})$$

$$\frac{N_{B,b} c_{b,i}}{\pi R} = \frac{N_{B,A} c_{A,i}}{\pi R} \quad (\text{A.1b})$$

$$c_{b,i} = \frac{N_{B,A} c_{A,i}}{N_{B,b}} \quad (\text{A.1c})$$

$$N_{B,b} = 2 \quad (\text{A.1d})$$

$$c_{b,i} = \frac{3c_{A,i}}{2} \quad (\text{A.1e})$$

$$c_b = \frac{3c_A}{2} = 1.661 \text{ m} \quad (\text{A.1f})$$

A.2.1.2 Blade c Equations

$$\sigma_c = \sigma_A = 21\% \quad (\text{A.2a})$$

$$\frac{N_{B,c} c_{c,i}}{\pi R} = \frac{N_{B,A} c_{A,i}}{\pi R} \quad (\text{A.2b})$$

$$c_{c,i} = \frac{N_{B,A} c_{A,i}}{N_{B,c}} \quad (\text{A.2c})$$

$$N_{B,c} = 4 \quad (\text{A.2d})$$

$$c_{c,i} = \frac{3c_{A,i}}{4} \quad (\text{A.2e})$$

$$c_c = \frac{3c_A}{4} = 0.830 \text{ m} \quad (\text{A.2f})$$

A.2.1.3 Blade d Equations

$$\sigma_d = \sigma_A = 21\% \quad (\text{A.3a})$$

$$\frac{N_{B,d} c_{d,i}}{\pi R} = \frac{N_{B,A} c_{A,i}}{\pi R} \quad (\text{A.3b})$$

$$c_{d,i} = \frac{N_{B,A} c_{A,i}}{N_{B,d}} \quad (\text{A.3c})$$

$$N_{B,d} = 5 \quad (\text{A.3d})$$

$$c_{d,i} = \frac{3c_{A,i}}{5} \quad (\text{A.3e})$$

$$c_d = \frac{3c_A}{5} = 0.664 \text{ m} \quad (\text{A.3f})$$

A.2.2 Modified Blades Chord Length Variation

A.2.2.1 Blade b Chord Length Details

Table A.3: Blade b Details - 5 m Radius Turbine

Distance to Last Plane mm	Radius mm	Local Pitch Angle °	Chord Length mm
-	1086.539	40.54	2396.78
130.90	1217.436	37.59	2401.28
130.90	1348.333	34.75	2406.95
130.90	1479.230	32.09	2409.68
130.90	1610.127	29.65	2405.27
130.90	1741.024	27.45	2389.56
130.90	1871.921	25.47	2359.77
130.90	2002.818	23.69	2315.22
130.90	2133.715	22.08	2256.65
130.90	2264.612	20.62	2185.60
130.90	2395.509	19.28	2103.92
130.90	2526.406	18.03	2013.80
130.90	2657.303	16.87	1917.66
130.90	2788.200	15.77	1818.11
130.90	2919.097	14.71	1717.88
130.90	3049.994	13.70	1619.77
130.90	3180.891	13.28	1526.75
130.90	3311.788	12.29	1441.52
130.90	3442.685	11.37	1370.97
130.90	3573.582	10.54	1310.78
130.90	3704.479	9.75	1255.79
130.90	3835.376	9.02	1205.81
130.90	3966.273	8.36	1160.71
130.90	4097.170	7.76	1120.34
130.90	4228.067	7.25	1084.56
130.90	4358.964	6.82	1053.26
130.90	4489.861	6.48	1026.33
130.90	4620.758	6.23	1003.67
130.90	4751.655	6.08	985.19
130.90	4882.552	6.00	970.83
77.72	4960.267	6.00	964.22
39.73	5000.000	2.48	825.37

A.2.2.2 Blade c Chord Length Details

Table A.4: Blade c Details - 5 m Radius Turbine

Distance to Last Plane mm	Radius mm	Local Pitch Angle °	Chord Length mm
-	1086.54	40.54	1198.39
130.90	1217.44	37.59	1200.64
130.90	1348.33	34.75	1203.47
130.90	1479.23	32.09	1204.84
130.90	1610.13	29.65	1202.64
130.90	1741.02	27.45	1194.78
130.90	1871.92	25.47	1179.89
130.90	2002.82	23.69	1157.61
130.90	2133.71	22.08	1128.33
130.90	2264.61	20.62	1092.80
130.90	2395.51	19.28	1051.96
130.90	2526.41	18.03	1006.90
130.90	2657.30	16.87	958.83
130.90	2788.20	15.77	909.05
130.90	2919.10	14.71	858.94
130.90	3049.99	13.70	809.89
130.90	3180.89	13.28	763.37
130.90	3311.79	12.29	720.76
130.90	3442.68	11.37	685.49
130.90	3573.58	10.54	655.39
130.90	3704.48	9.75	627.89
130.90	3835.38	9.02	602.91
130.90	3966.27	8.36	580.35
130.90	4097.17	7.76	560.17
130.90	4228.07	7.25	542.28
130.90	4358.96	6.82	526.63
130.90	4489.86	6.48	513.16
130.90	4620.76	6.23	501.83
130.90	4751.65	6.08	492.60
130.90	4882.55	6.00	485.42
77.72	4960.27	6.00	482.11
39.73	5000.00	2.48	412.68

Table A.5: Blade c Details - 6 m Radius Turbine

Distance to Last Plane mm	Radius mm	Local Pitch Angle °	Chord Length mm
-	1086.54	40.54	1198.39
164.34	1250.88	37.59	1200.64
164.34	1415.23	34.75	1203.47
164.34	1579.57	32.09	1204.84
164.34	1743.92	29.65	1202.64
164.34	1908.26	27.45	1194.78
164.34	2072.61	25.47	1179.89
164.34	2236.95	23.69	1157.61
164.34	2401.30	22.08	1128.33
164.34	2565.64	20.62	1092.80
164.34	2729.99	19.28	1051.96
164.34	2894.33	18.03	1006.90
164.34	3058.68	16.87	958.83
164.34	3223.02	15.77	909.05
164.34	3387.37	14.71	858.94
164.34	3551.71	13.70	809.89
164.34	3716.06	13.28	763.37
164.34	3880.40	12.29	720.76
164.34	4044.75	11.37	685.49
164.34	4209.09	10.54	655.39
164.34	4373.44	9.75	627.89
164.34	4537.78	9.02	602.91
164.34	4702.13	8.36	580.35
164.34	4866.47	7.76	560.17
164.34	5030.82	7.25	542.28
164.34	5195.16	6.82	526.63
164.34	5359.51	6.48	513.16
164.34	5523.85	6.23	501.83
164.34	5688.20	6.08	492.60
164.34	5852.54	6.00	485.42
97.57	5950.11	6.00	482.11
49.89	6000.00	2.48	412.68

A.2.2.3 Blade d Chord Length Details

Table A.6: Blade d Details - 5 m Radius Turbine

Distance to Last Plane mm	Radius mm	Local Pitch Angle °	Chord Length mm
-	1086.54	40.54	958.71
130.90	1217.44	37.59	960.51
130.90	1348.33	34.75	962.78
130.90	1479.23	32.09	963.87
130.90	1610.13	29.65	962.11
130.90	1741.02	27.45	955.83
130.90	1871.92	25.47	943.91
130.90	2002.82	23.69	926.09
130.90	2133.71	22.08	902.66
130.90	2264.61	20.62	874.24
130.90	2395.51	19.28	841.57
130.90	2526.41	18.03	805.52
130.90	2657.30	16.87	767.06
130.90	2788.20	15.77	727.24
130.90	2919.10	14.71	687.15
130.90	3049.99	13.70	647.91
130.90	3180.89	13.28	610.70
130.90	3311.79	12.29	576.61
130.90	3442.68	11.37	548.39
130.90	3573.58	10.54	524.31
130.90	3704.48	9.75	502.31
130.90	3835.38	9.02	482.32
130.90	3966.27	8.36	464.28
130.90	4097.17	7.76	448.13
130.90	4228.07	7.25	433.82
130.90	4358.96	6.82	421.30
130.90	4489.86	6.48	410.53
130.90	4620.76	6.23	401.47
130.90	4751.65	6.08	394.08
130.90	4882.55	6.00	388.33
77.72	4960.27	6.00	385.69
39.73	5000.00	2.48	330.15

Appendix B

Single Rotor Turbines Performance Curves

B.1 Case (i) Turbines

B.1.1 Turbine B Performance Curves

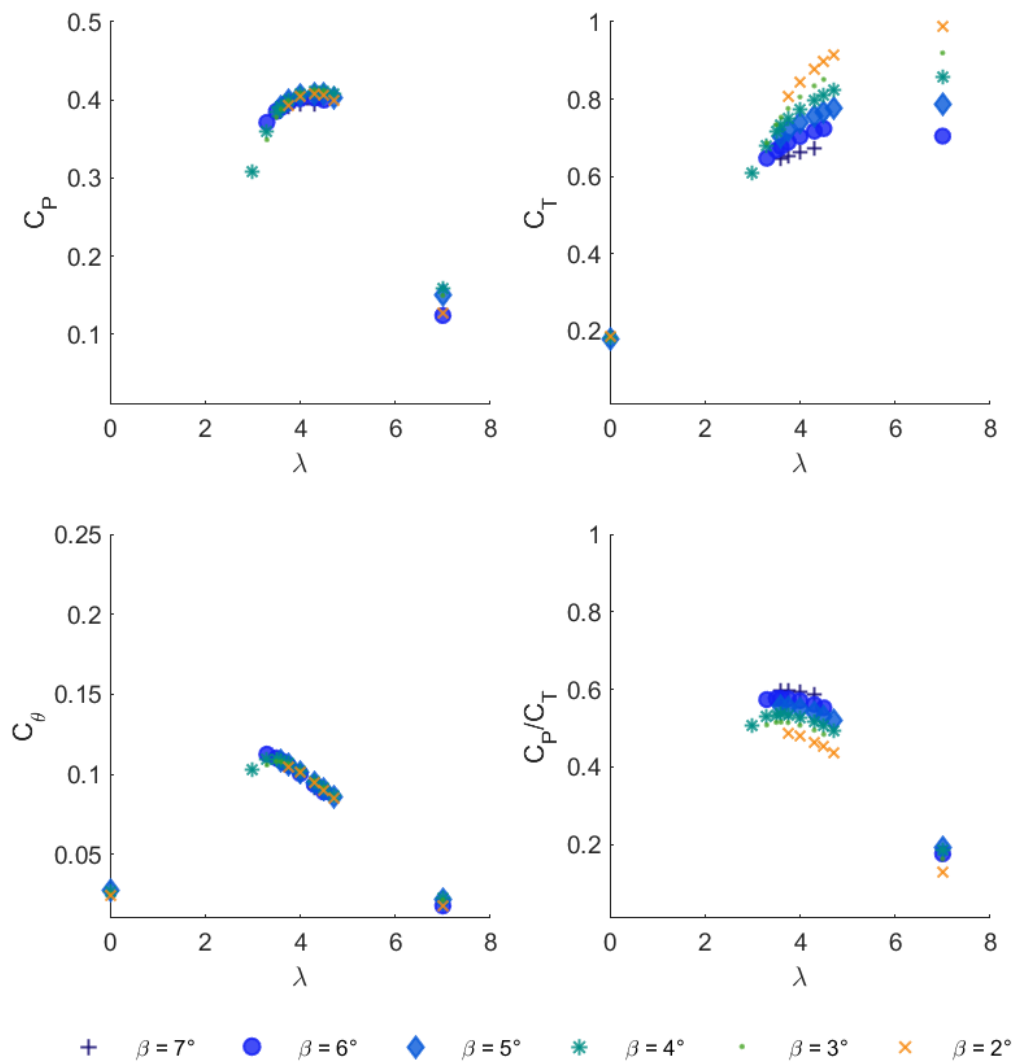


Figure B.1: Turbine B's Performance Coefficients

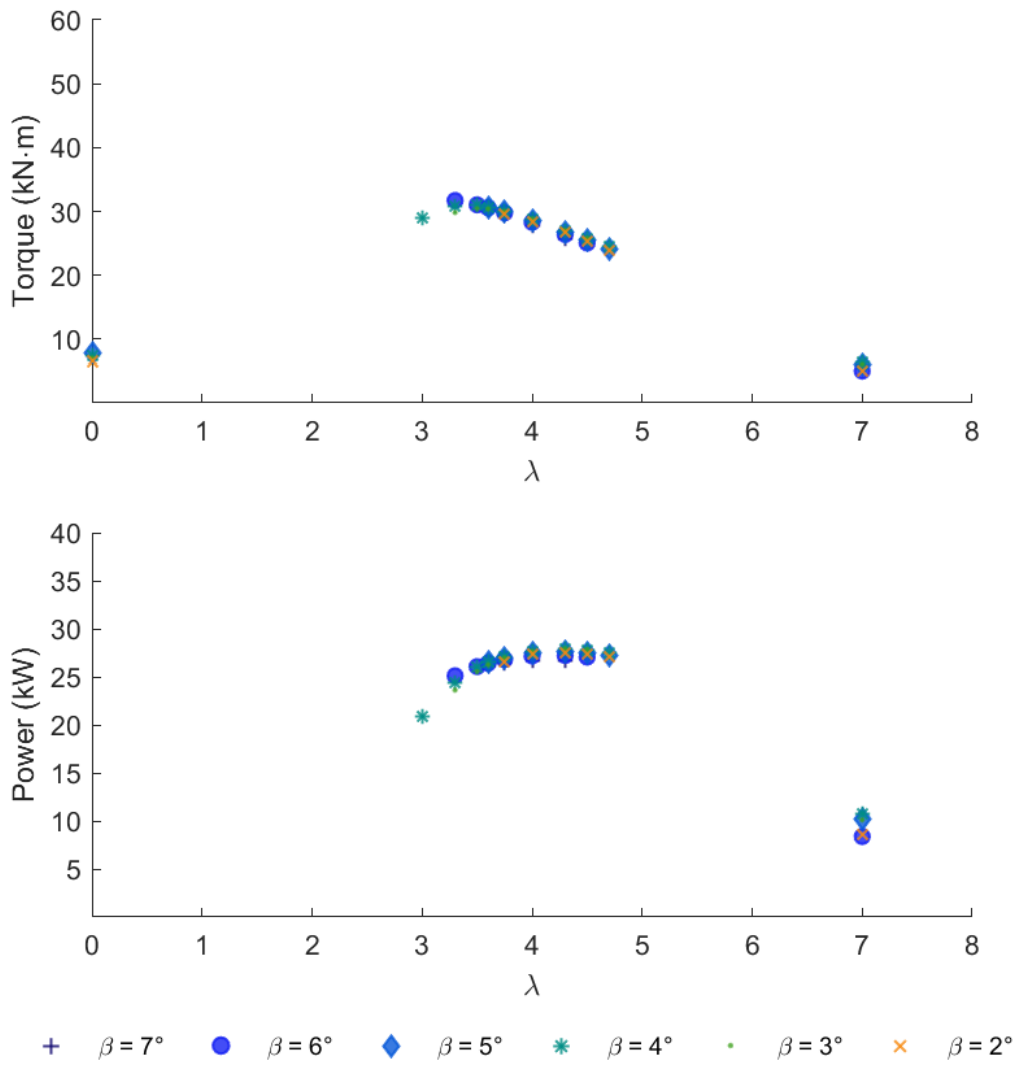


Figure B.2: Turbine B's Torque and Power Output

B.1.2 Turbine C Performance Curves

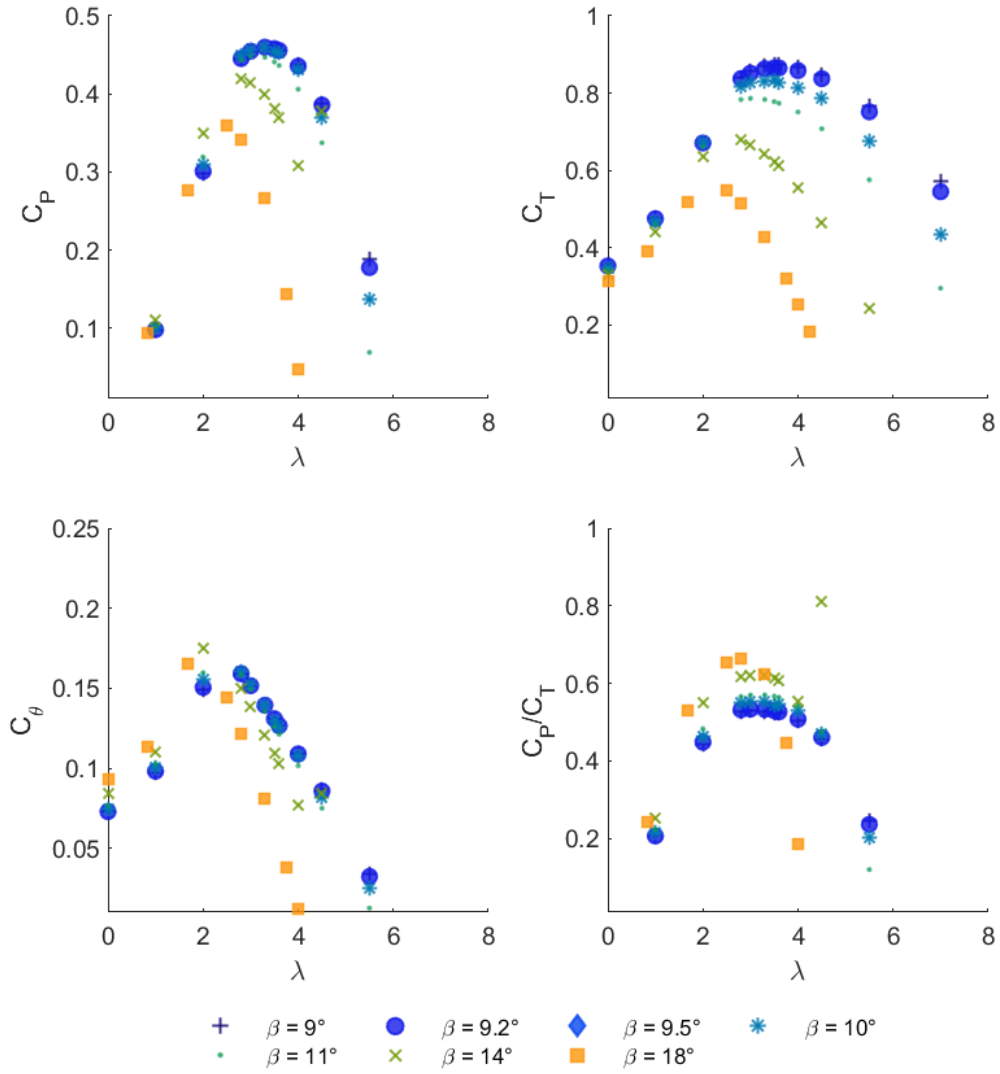


Figure B.3: Turbine C's Performance Coefficients

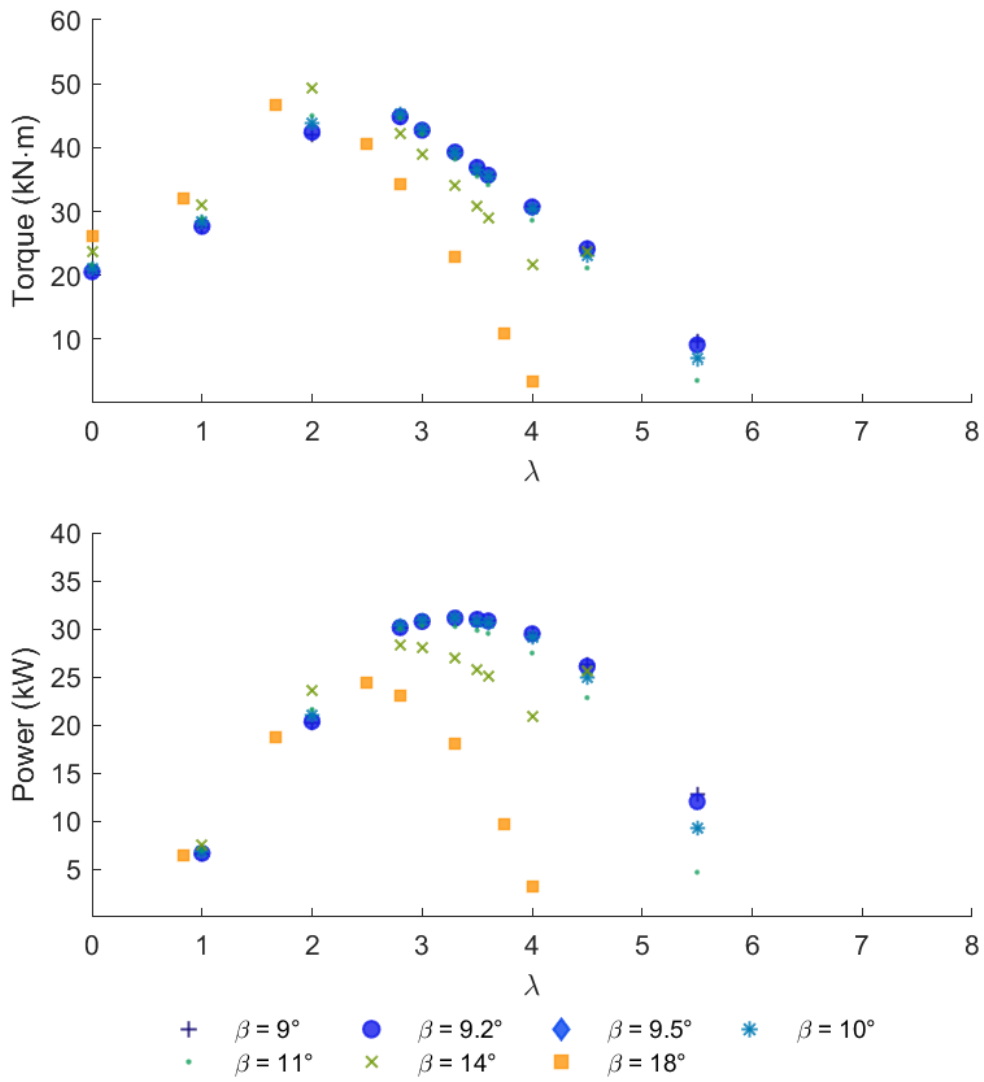


Figure B.4: Turbine C's Torque and Power Output

B.1.3 Turbine D Performance Curves

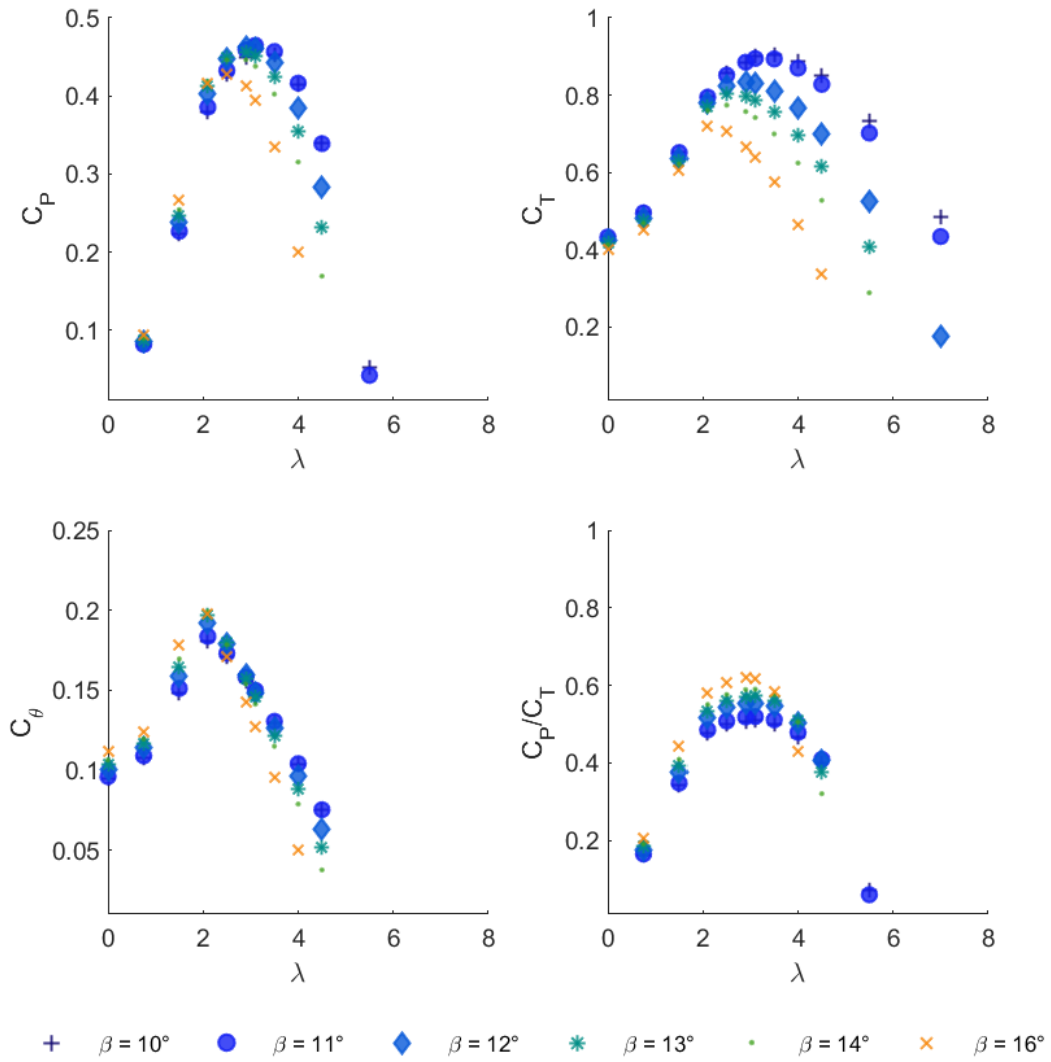


Figure B.5: Turbine D's Performance Coefficients

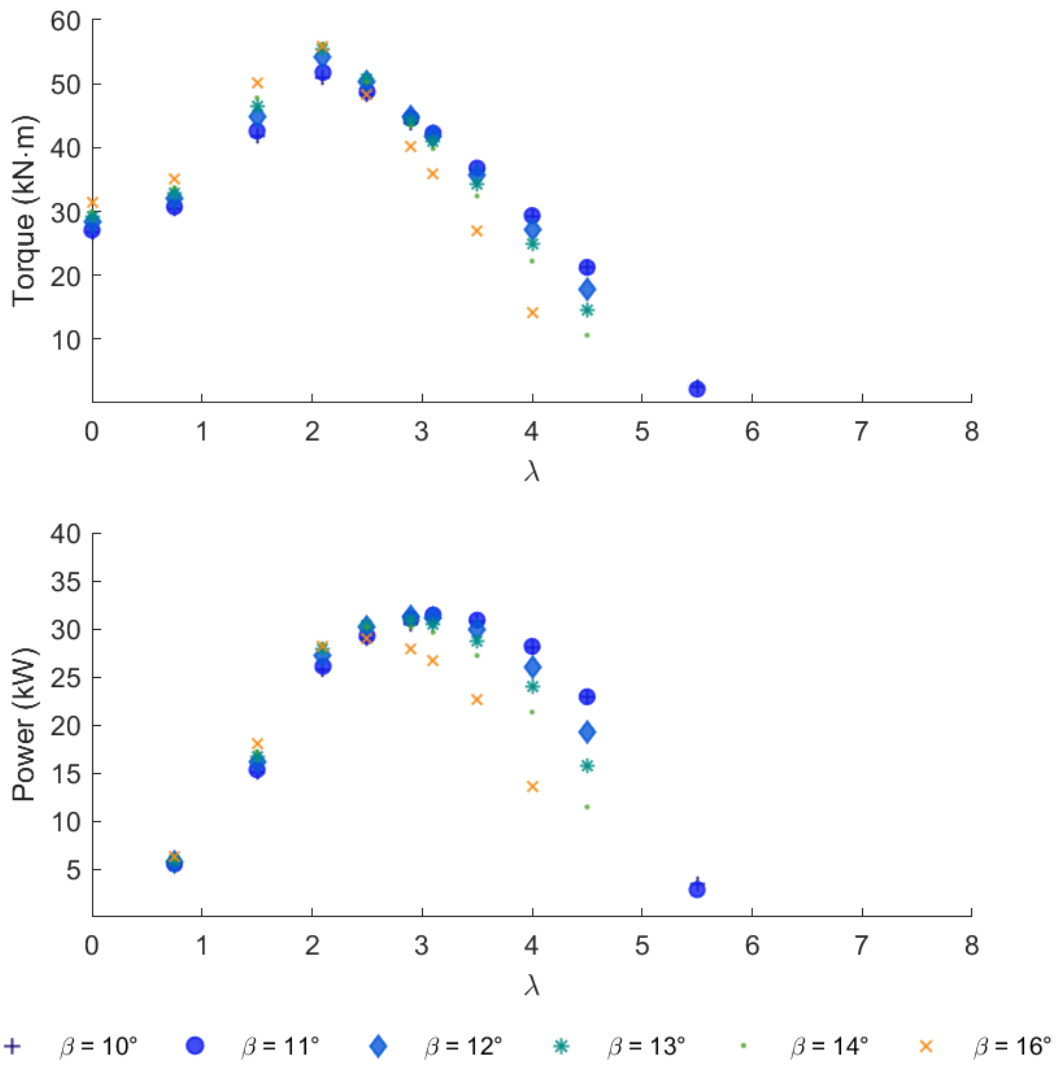


Figure B.6: Turbine D's Torque and Power Output

B.2 Case (ii) Turbines

B.2.1 Turbine b Performance Curves

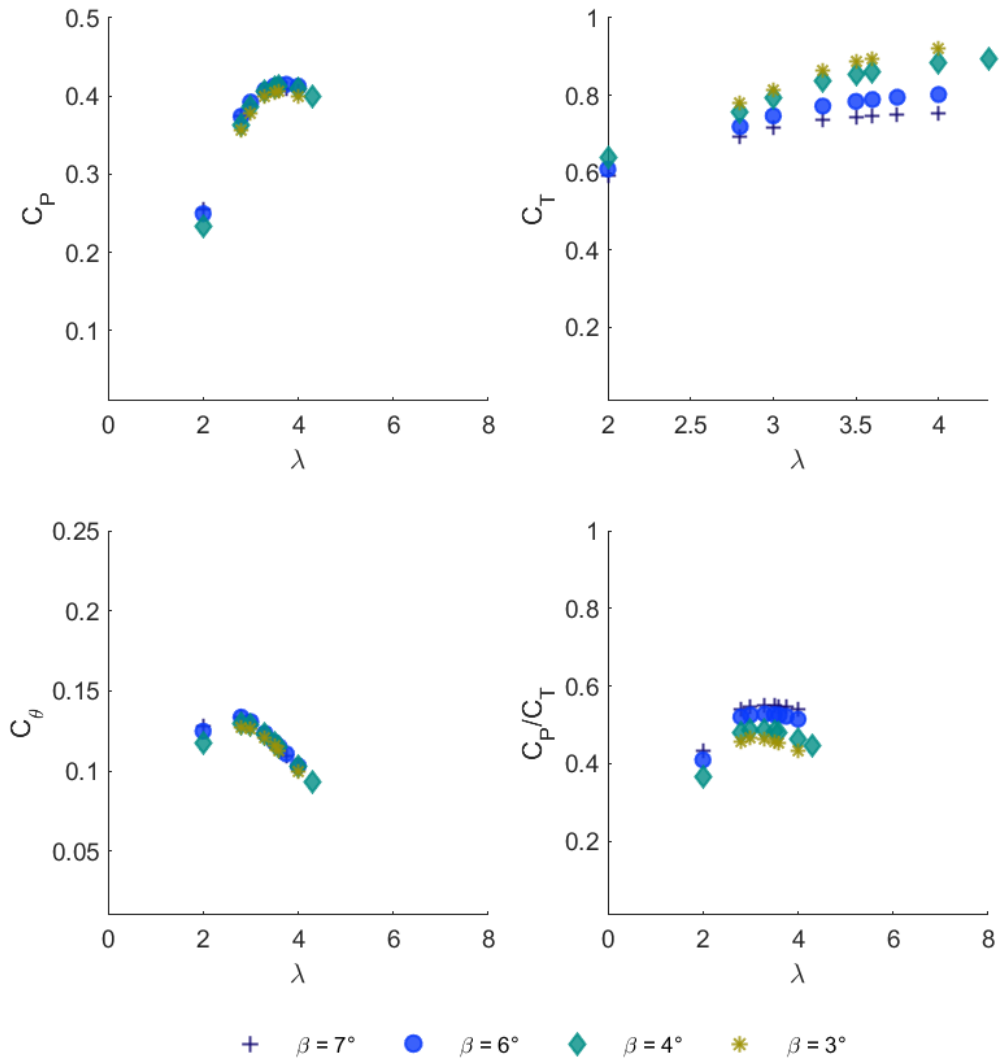


Figure B.7: Turbine b's Performance Coefficients

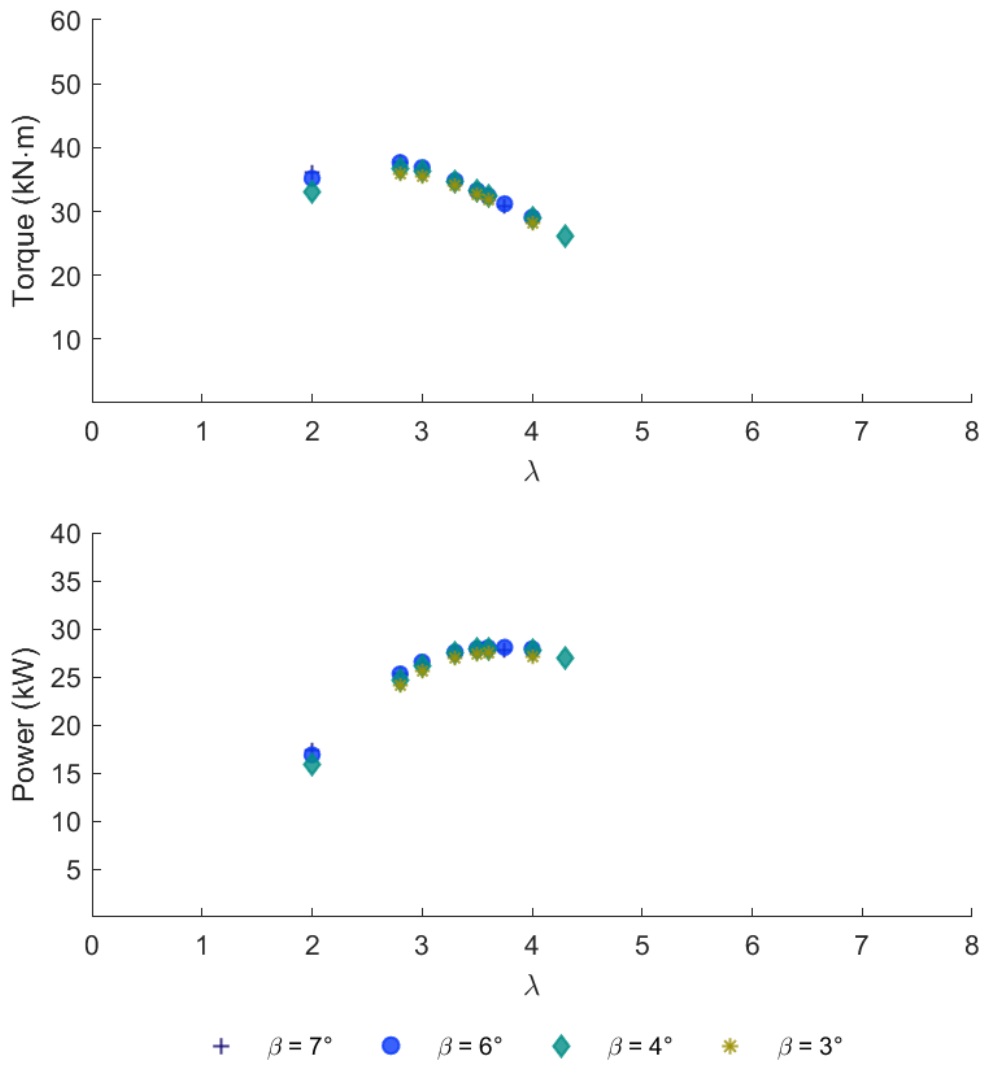


Figure B.8: Turbine b's Torque and Power Output

B.2.2 Turbine c Performance Curves

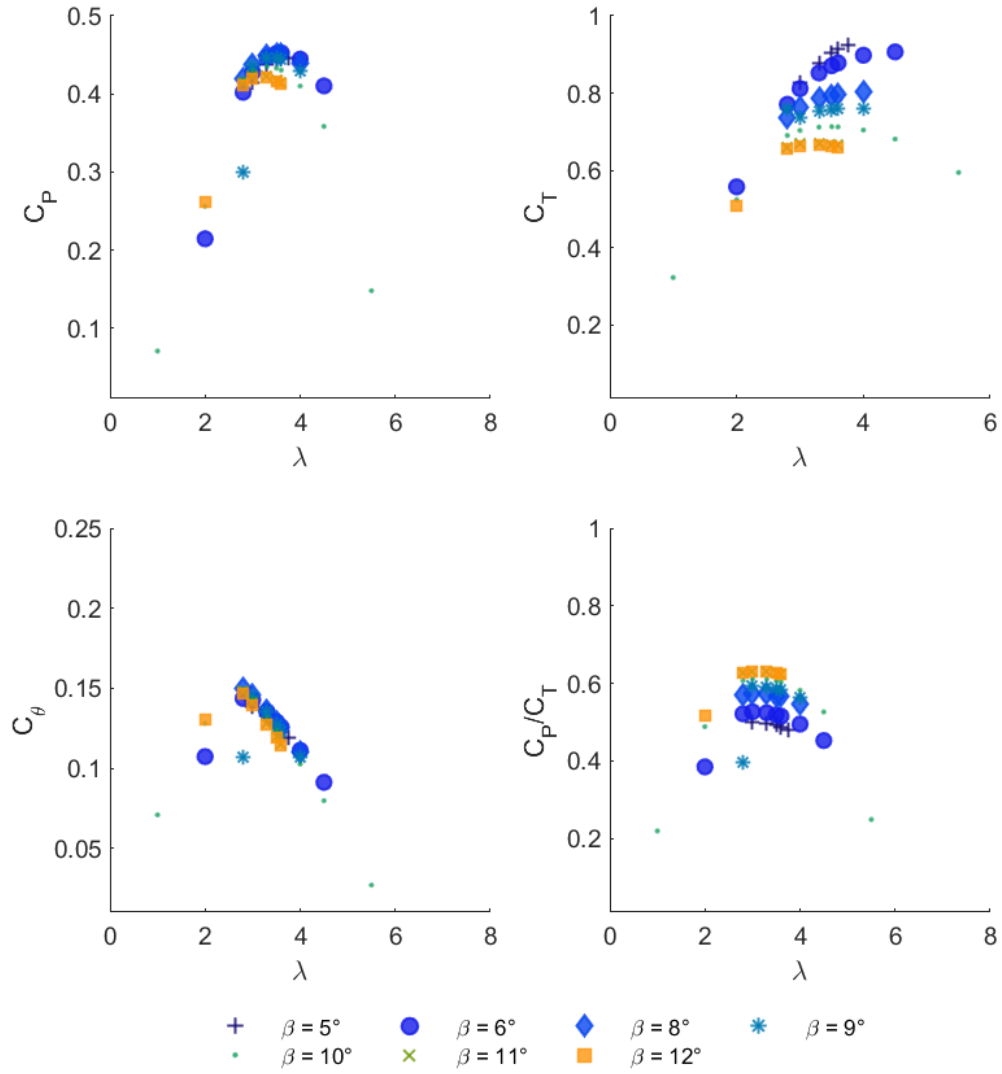


Figure B.9: Turbine c's Performance Coefficients

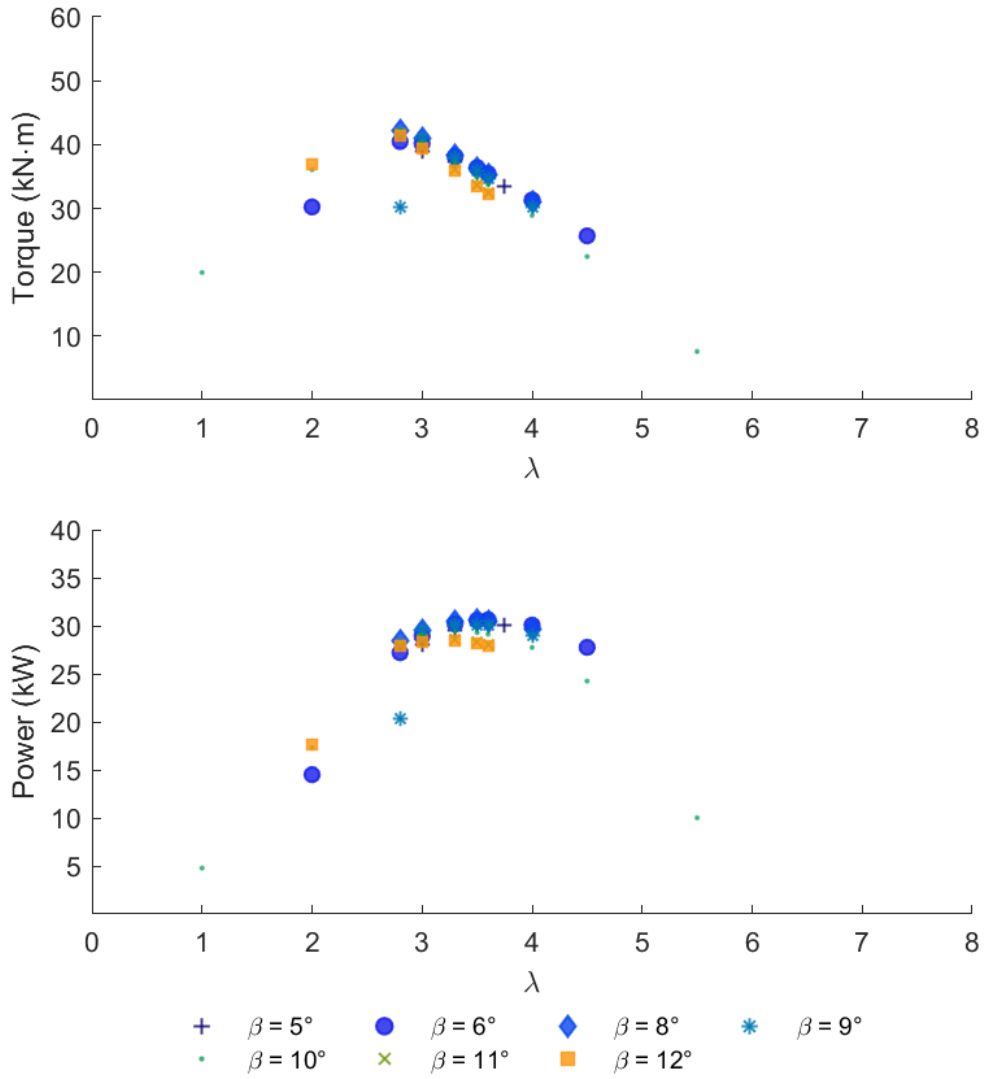


Figure B.10: Turbine c's Torque and Power Output

B.2.3 Turbine d Performance Curves

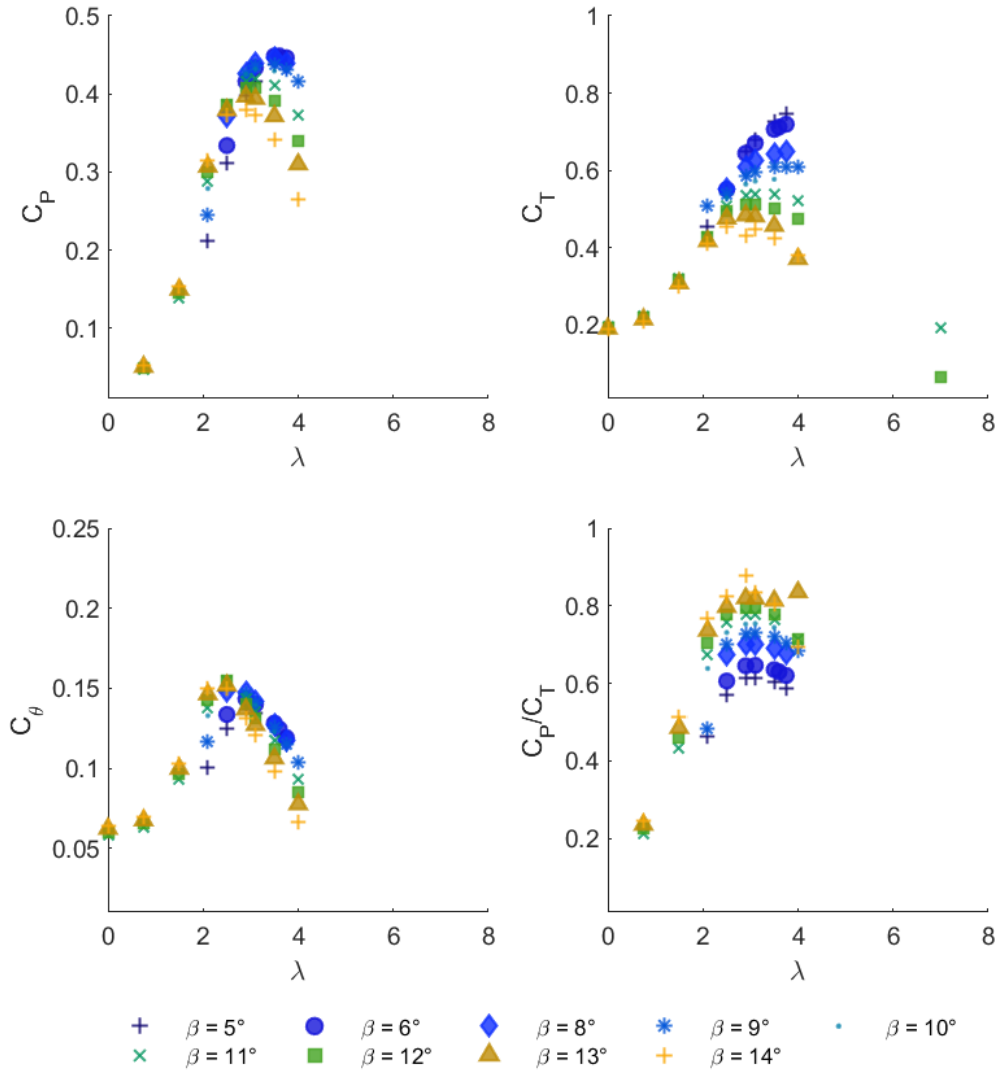


Figure B.11: Turbine d's Performance Coefficients

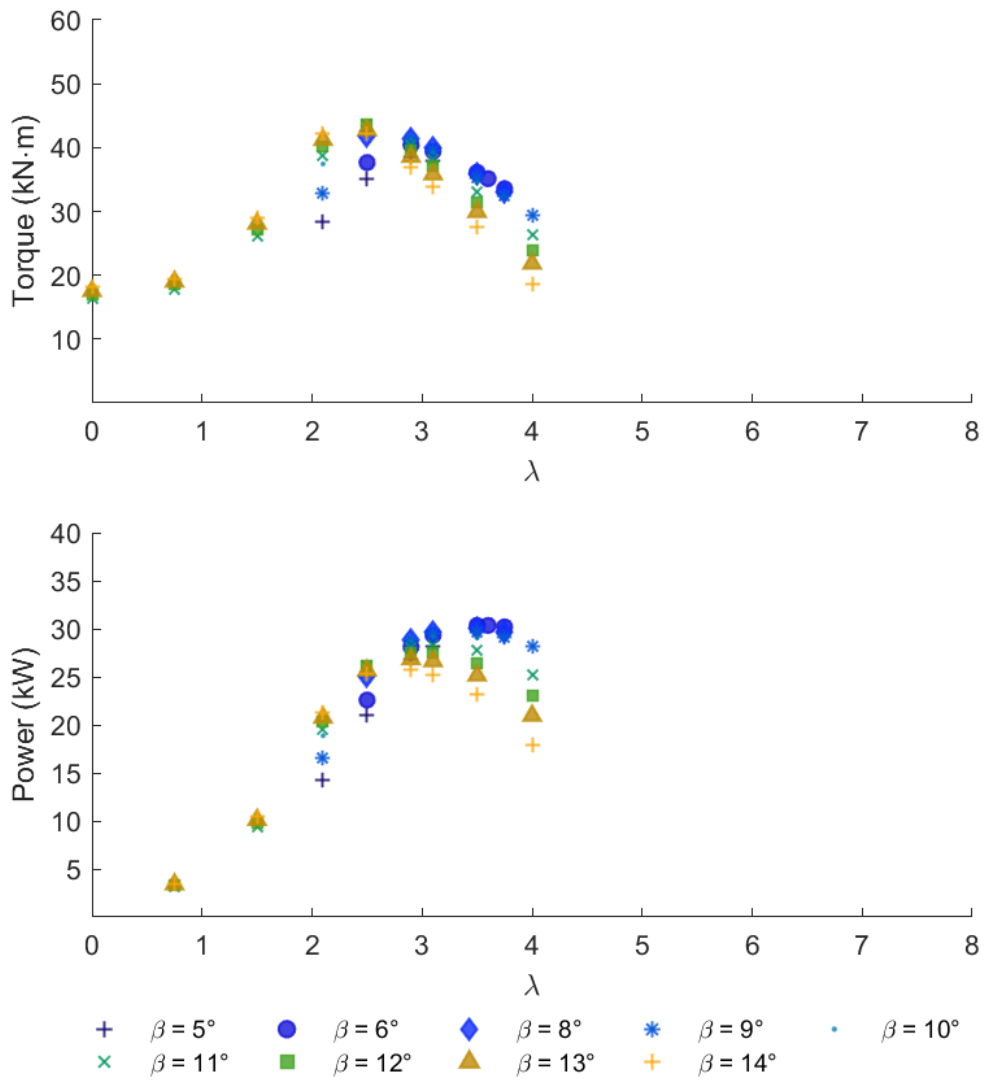


Figure B.12: Turbine d's Torque and Power Output

B.3 Case (iii) Turbines

B.3.1 Turbine A_b Performance Curves

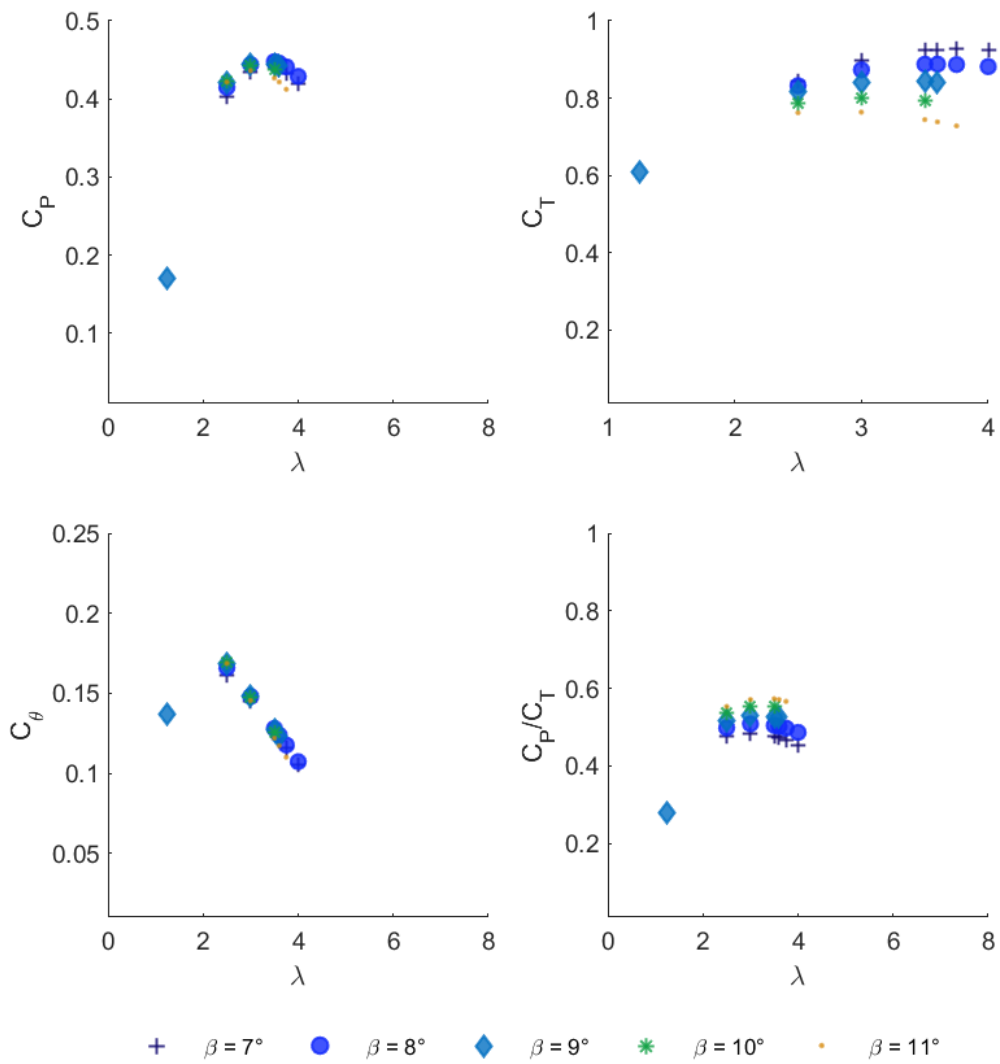


Figure B.13: Turbine A_b's Performance Coefficients

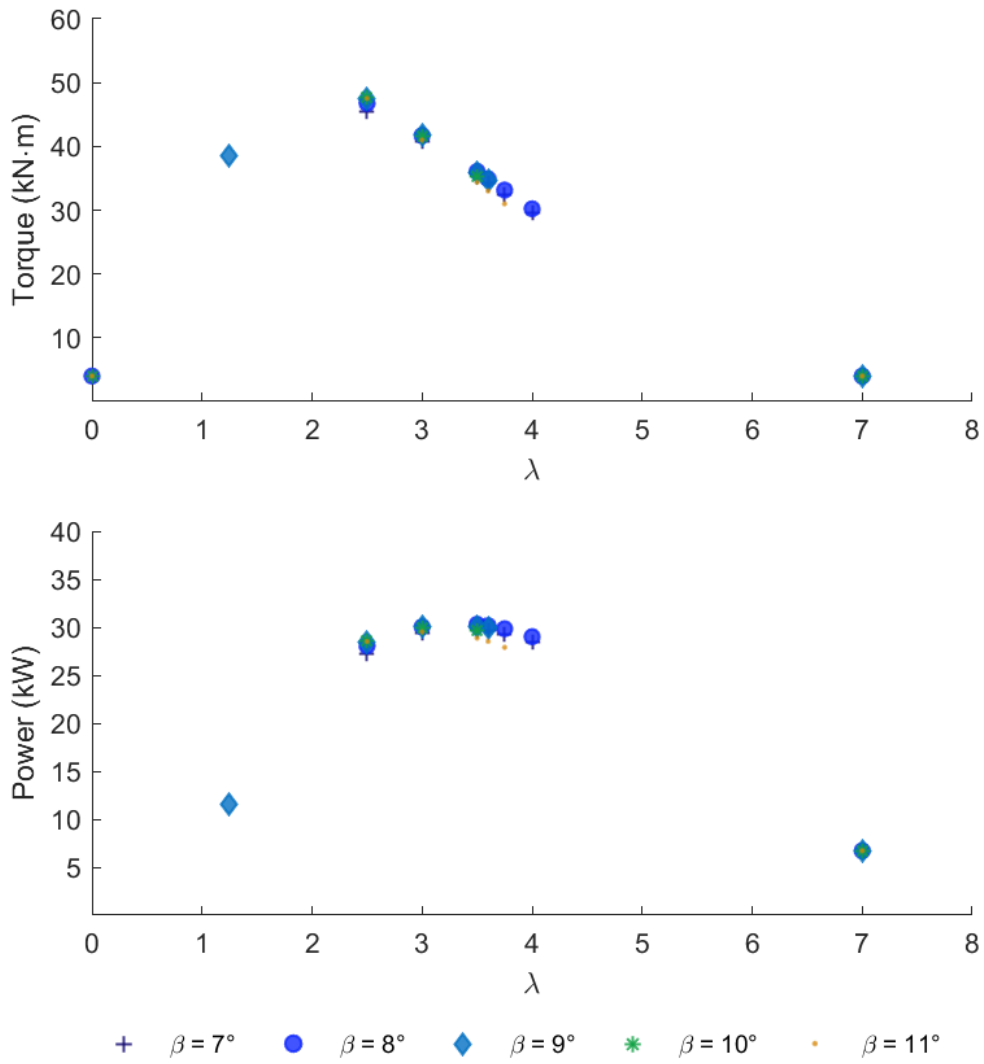


Figure B.14: Turbine A_b's Torque and Power Output

B.3.2 Turbine A_c Performance Curves

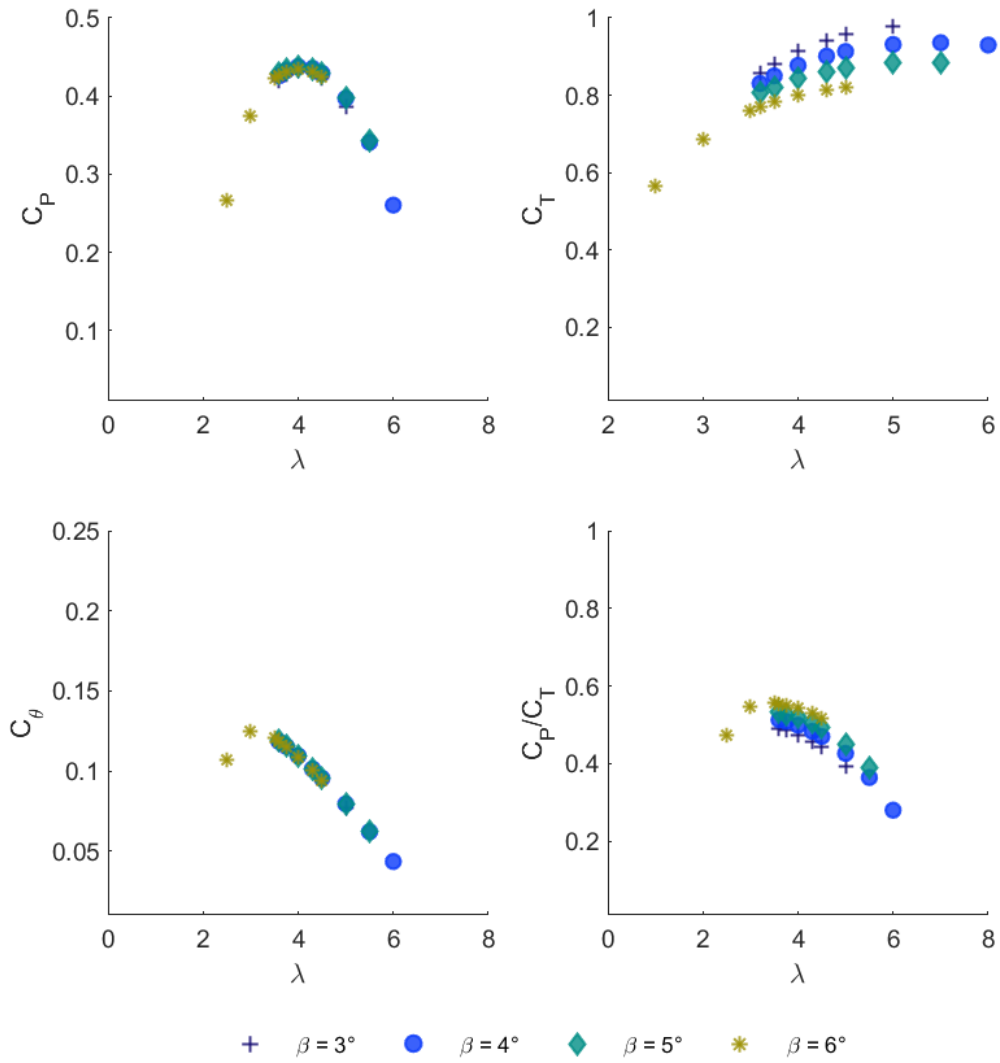


Figure B.15: Turbine A_c's Performance Coefficients

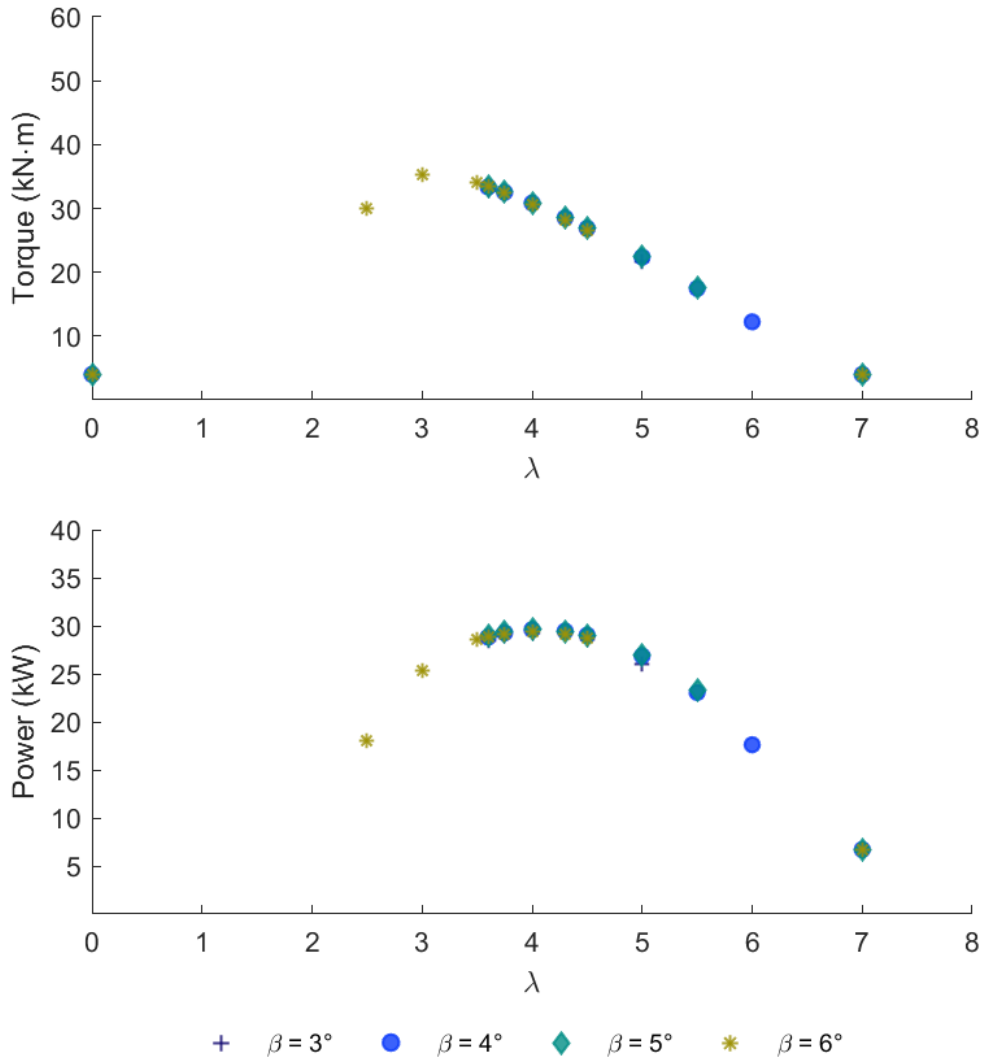


Figure B.16: Turbine A_c's Torque and Power Output

B.3.3 Turbine A_d Performance Curves

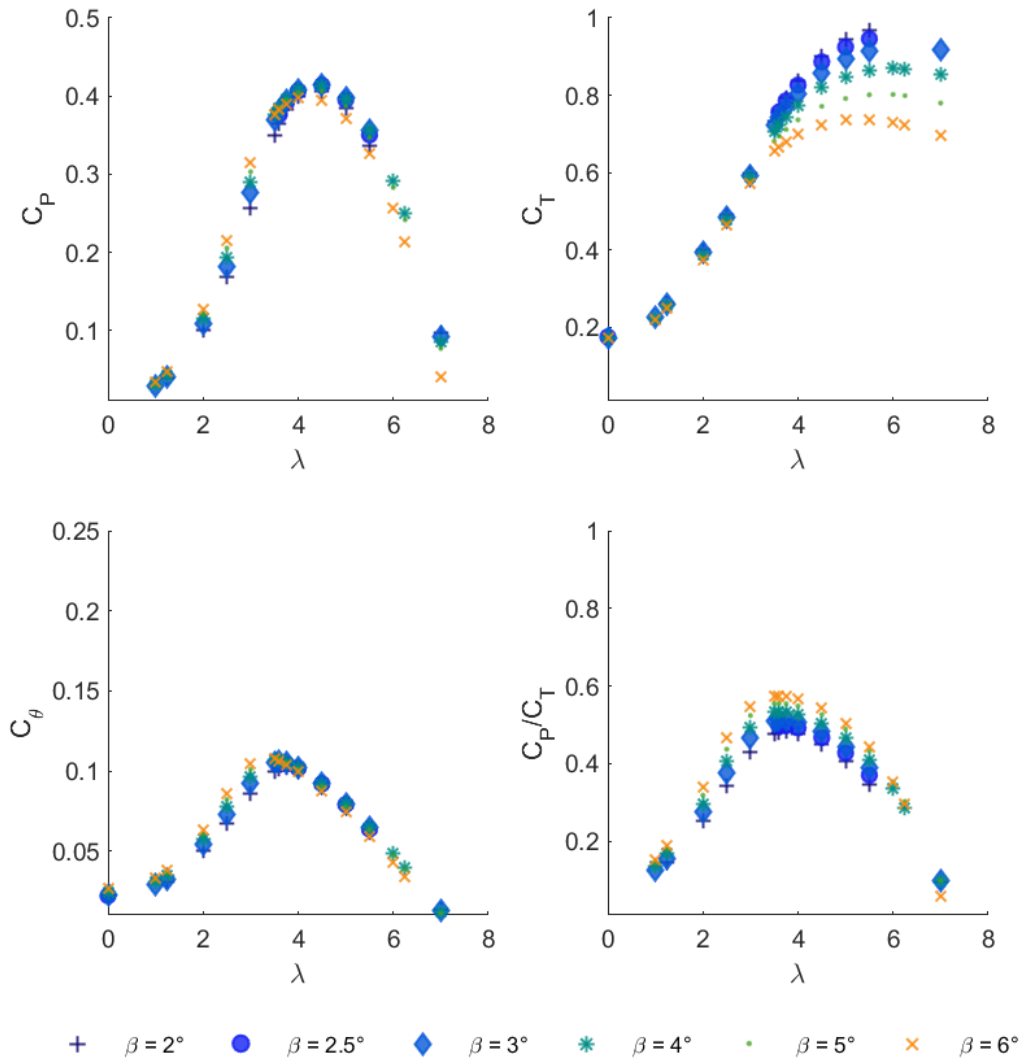


Figure B.17: Turbine A_d's Performance Coefficients

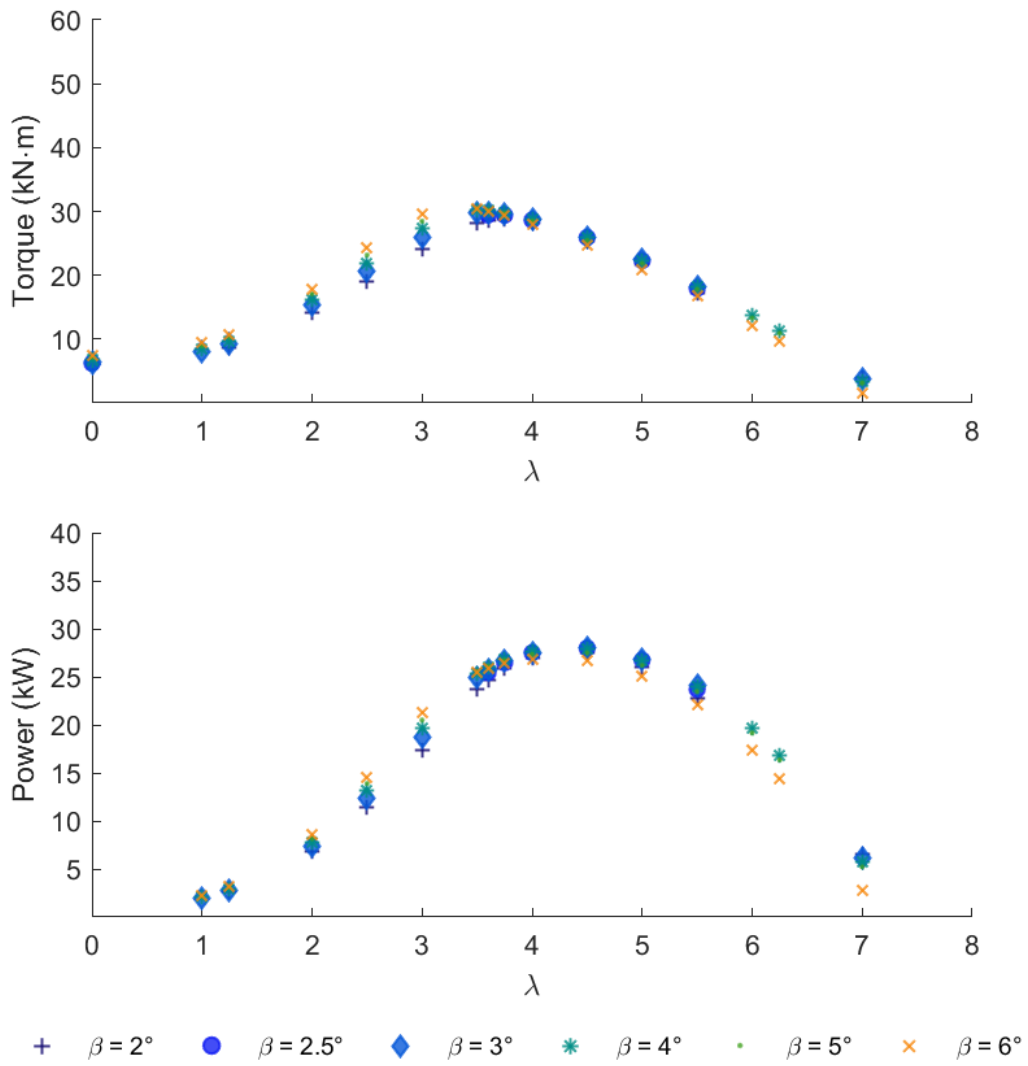


Figure B.18: Turbine A_d's Torque and Power Output

Appendix C

Detailed LCOE Calculation Tables

All costs included in this Appendix are presented in 2019 British Pounds.

C.1 Capital Expenses

C.1.1 Development Costs

Table C.1: Siting and Scoping Costs for CRT

Component	1 Unit Cost	10 Units Cost	10-100 Units Cost
Preliminary Resource Assessment	£ 33 820	£ 33 820	£ 33 820
Environmental Scoping	£ 28 183	£ 35 699	£ 35 699
Community Outreach	£ 48 851	£ 97 702	£ 108 975
Regulatory Outreach	£ 41 335	£ 52 609	£ 52 609
Total	£ 152 189	£ 219 829	£ 231 102

Table C.2: Pre-Installation Studies Costs for CRT

Component	1 Unit Cost	10 Units Cost	10-100 Units Cost
Detailed Resource Assessment	£ 187 888	£ 234 860	£ 263 043
Hydrodynamic Modelling	-	£ 105 217	£ 105 217
Seabed Survey, Mapping and Bottom Composition	£ 150 311	£ 150 311	£ 206 677
Marine Mammals	£ 289 348	£ 338 199	£ 338 199
Fish and Invertebrates	£ 343 835	£ 392 686	£ 392 686
Seabirds	£ 18 789	£ 75 155	£ 75 155
Water Quality	£ 116 491	£ 116 491	£ 139 037
Habitat	£ 16 910	£ 37 578	£ 187 888
Cultural Resources	£ 78 913	£ 90 186	£ 95 823
Navigation	£ 15 031	£ 15 031	£ 34 571
Recreation	£ 31 941	£ 219 829	£ 219 829
Total	£ 1 249 457	£ 1 775 543	£ 2 058 127

Table C.3: Post-Installation Capital Costs for CRT

Component	1 Unit Cost	10 Units Cost	10-100 Units Cost
Marine Mammals	£ 415 233	£ 588 654	£ 722 924
Fish	£ 232 042	£ 292 730	£ 539 803
Benthos	£ 60 124	£ 108 975	£ 108 975
Turbine Monitoring	£ 54 488	-	£ -
Acoustic Characterization Monitoring	£ 31 941	£ 35 699	£ 35 699
Ecosystem Effects Marine Mammals	-	£ 150 311	£ 150 311
Ecosystem Effects Fish	-	£ 150 311	£ 150 311
Total	£ 793 828	£ 1 326 679	£ 1 708 092

Table C.4: Documentation and Process Costs for CRT

Component	1 Unit Cost	10 Units Cost	10-100 Units Cost
Document Preparation	£ 526 087	£ 536 665	£ 751 553
Monitoring and Study Plans	£ 60 124	£ 90 186	£ 127 764
Total	£ 586 211	£ 653 851	£ 879 317

C.1.2 Infrastructure

Table C.5: Trunk Cable Length

Component	Length
Site Distance to Shore	5000 m
Directional Drilling Distance	1000 m
Contingency (20%)	1000 m
Total Length	7000 m

Table C.6: Trunk Cable Specifications Assumed for CRT

Component	Units	1 Unit	10 Units	50 Units
Voltage Level	kV	30	45	110
Ampacity	A	245	530	530
Capacity	MVA	13	41	101
Conductor Size	mm ²	70	300	300
Cable Outer Diameter	mm	100.6	130	157
Cable Weight	kg	120	150.5	182.4

Table C.7: Trunk Cable Costs for CRT

Component	Units	1 Unit	10 Units	50 Units
Number of Parallel Trunk Cables		1	1	2
Total Cable Length	m	7000	7000	14000
Cost	£/m	90.2	113.1	137.1
Total		£ 631 304	£ 791 761	£ 1 919 165

Table C.8: Riser Cable Length

Component	Length
Device Centerline Spacing	240 m
Water Depth	30 m
Contingency (20%)	60 m
Total Length	360 m

Table C.9: Riser Cable Costs for CRT

Component	Units	1 Unit	10 Units	50 Units
Total Cable Length	m	360	3 600	18 000
Cost	£/m	113	113	113
Total		£ 18 671	£ 186 707	£ 933 536

C.1.3 Mooring

Table C.10: Mooring Lines and Chain Costs for CRT

Component	Distance	1 Unit Cost	10 Units Cost	50 Units Cost
Thrust Mooring Line	65 m	£ 1 122	£ 11 219	£ 56 095
Turbine Connection Mooring Line	36 m	£ 2 706	£ 27 056	£ 135 280
Tension Mooring Line	15 m	£ 259	£ 2 589	£ 12 945
Studlink Chain	1 m	£ 564	£ 5 637	£ 28 183
Total		£ 4 650	£ 46 501	£ 232 503

Table C.11: Anchors Costs for CRT

Component	1 Unit Cost	10 Units Cost	50 Units Cost
Embedment Anchor	£ 1 429	£ 10 661	£ 50 342
SEA Anchor	£ 3 203	£ 4 512	£ 10 553
Concrete Clump	£ 577	£ 4 832	£ 23 714
Total	£ 5 208	£ 20 005	£ 84 608

C.1.4 Power Take Off

Table C.12: Generator Costs for CRT

Component	1 Unit Cost	10 Units Cost	50 Units Cost
Active Magnetics	£ 35 842	£ 358 419	£ 1 792 095
Mainshaft	£ 194	£ 1 941	£ 9 702
Brake System	£ 11 095	£ 110 947	£ 554 735
Extra Components	£ 4 721	£ 47 207	£ 236 026
Total	£ 51 851	£ 518 514	£ 2 592 568

Table C.13: Power Take Off Mounting Costs for CRT

Component	<u>1 Unit</u> Cost	<u>10 Units</u> Cost	<u>50 Units</u> Cost
Main Housing	£ 546	£ 5 456	£ 27 278
Gudgen Shaft	£ 150	£ 1 498	£ 7 490
Rotating Spider	£ 2 014	£ 20 137	£ 100 686
Outside Ring Support	£ 7 927	£ 79 273	£ 396 365
Mainshaft Retainer	£ 12	£ 121	£ 603
Total	£ 10 649	£ 106 484	£ 532 422

Table C.14: Other Power Take Off Costs for CRT

Component	<u>1 Unit</u> Cost	<u>10 Units</u> Cost	<u>50 Units</u> Cost
Cable	£ 513	£ 5 132	£ 25 658
Switchgear	£ 335	£ 3 348	£ 16 738
Other Subsystems	£ 799	£ 7 995	£ 39 973
Total	£ 1 647	£ 16 474	£ 82 368

Table C.15: Rotor Costs for CRT

Component		1 Unit Cost	10 Units Cost	50 Units Cost
<i>CRT Blades' Molds</i>				
	<i>Surface Area</i>			
Front Rotor Blade - Pressure Side	4.52 m ²	£ 8 372	£ 8 372	£ 8 372
Front Rotor Blade - Suction Side	4.73 m ²	£ 8 763	£ 8 763	£ 8 763
Back Rotor Blade - Pressure Side	7.27 m ²	£ 13 454	£ 13 454	£ 13 454
Back Rotor Blade - Suction Side	7.61 m ²	£ 14 089	£ 14 089	£ 14 089
<i>CRT Blades' Tooling</i>				
Front Rotor Blade - Pressure Side	4.52 m ²	£ 5 606	£ 5 606	£ 5 606
Front Rotor Blade - Suction Side	4.73 m ²	£ 5 868	£ 5 868	£ 5 868
Back Rotor Blade - Pressure Side	7.27 m ²	£ 9 010	£ 9 010	£ 9 010
Back Rotor Blade - Suction Side	7.61 m ²	£ 9 435	£ 9 435	£ 9 435
<i>CRT Blades' Production</i>				
	<i>Weight</i>			
Front Rotor Blades	90 kg	£ 11 111	£ 41 681	£ 208 406
Back Rotor Blades	90 kg	£ 7 408	£ 74 076	£ 138 937
Hub Cost		£ 37 246	£ 7 614	£ 3 376
Total		£ 130 362	£ 197 968	£ 425 316

Table C.16: Permanent Magnet Generator for CRT Specifications

Component	Units	Value
<i>CRT Design Drivetrain Input Variables</i>		
Mechanical Design Load	kW	49
Mainshaft Rotational Velocity	rpm	16.6
Stator Radius	m	2
<i>Concept Drivetrain Constants</i>		
Generator Efficiency	%	94
Electrical Load	kW	46
Jacket Thickness	mm	30
Housing Wall Thickness	mm	35
Magnet and Pole Cap	mm	35
Stator Pole Height	mm	80
Stator Pole Pitch	mm	120.054
Stator Back Iron	mm	20
Airgap	mm	5
Rotor Back Iron	mm	25
Generator Jacket Thickness	mm	32
Number of Brake Calipers	mm	5
<i>System Design Output Specifications</i>		
Nominal Airgap Diameter	mm	3.7
Poles per Generator		96
Frequency at Rated Speed	Hz	96
Power per Pole	kW	0.96
Frequency at Medium Speed	Hz	0.17
Power per Pole at Reference Speed		0.018
Intermediate Impedance	Ω	0.244
<i>Generator Design Output Specifications</i>		
Actual Airgap Diameter	m	3.669
Pole Stack Length	mm	60.49
Active Area	m ²	0.6971
Generator Outside Diameter	mm	3958.57
Electrical Torque	N m	28 020.24
Shear Stress	mPa	0.0219
<i>Variable Dimensions</i>		
Mainshaft Front Bearing Diameter	mm	419.87
Mainshaft Back Bearing Diameter	mm	322.98
Attachment Diameter to Nacelle	mm	4 038.57
Rotating Spider Diameter	mm	2 934.86
Armature Rotor Diameter	mm	3 588.57
Rotating Iron Diameter	mm	3 538.57
Mean Inner Rim Diameter	mm	3 527.92
Brake Disc Pitch Diameter	m	3.278

C.1.5 Installation

Table C.17: Mooring Installation Costs for CRT

Component	£/day	1 Units		10 Units		50 Units	
		Days	Cost	Days	Cost	Days	Cost
At Dock (Mob/Demob)	93 362	10	£ 933 616	28	£ 2 614 126	108	£ 10 083 058
Transit/Anchoring	87 932	2.5	£ 219 829	7	£ 615 522	27	£ 2 374 155
Mooring Installation	106 382	2.7	£ 289 005	32.2	£ 3 421 964	160.8	£ 17 109 820
Standby	95 902	2.3	£ 218 896	10.1	£ 966 212	44.4	£ 4 255 647
Mobilisation Charges			£ 182 026		£ 182 026		£ 182 026
Total		17.5	£ 1 843 373	77.2	£ 7 799 849	340.2	£ 34 004 705

Table C.18: Trunk Cable Installation Costs for CRT

Component	£/day	1 Units		10 Units		50 Units	
		Days	Cost	Days	Cost	Days	Cost
At Dock (Mob/Demob)	51 662	2	£ 103 325	2	£ 103 325	2	£ 103 325
Loading Cable	60 816	1.7	£ 103 895	3.3	£ 197 653	4.8	£ 291 412
Installation Operations	60 895	6	£ 363 676	7.7	£ 470 241	9.5	£ 576 807
Standby	58 129	2.4	£ 140 680	3.2	£ 188 515	4.1	£ 263 350
Mobilisation Charges			£ 407 793		£ 407 793		£ 407 793
Total		12.1	£ 1 119 368	16.2	£ 1 367 527	20.3	£ 1 615 687

Table C.19: Riser Cable Installation Costs for CRT

Component	£/day	Days per Unit	1 Units Cost	10 Units Cost	50 Units Cost
Transit	60 895	0.4	£ 27 064	£ 270 643	£ 1 353 213
Cable between Devices Installation	60 895	0.1	£ 4 229	£ 42 288	£ 211 440
Splice Cables Installation	60 895	1	£ 60 895	£ 608 946	£ 3 044 729
Operational Contingency	58 129	0.2	£ 13 200	£ 132 001	£ 660 005
Total		1.7	£ 105 388	£ 1 053 877	£ 5 269 385

Table C.20: Device Installation Costs for CRT

Component	£/day	Days per Unit	1 Units Cost	10 Units Cost	50 Units Cost
Barge-in Device	20 089	5	£ 100 445	£ 1 004 450	£ 5 022 252
Unload and Ready Device	20 089	5	£ 100 445	£ 1 004 450	£ 5 022 252
Tow-Out and Install Device	20 089	2	£ 40 178	£ 401 780	£ 2 008 901
Commission Device	20 089	2	£ 40 178	£ 401 780	£ 2 008 901
Contingency	20 089	3.5	£ 70 312	£ 703 115	£ 3 515 576
Total		17.5	£ 351 558	£ 3 515 576	£ 17 577 880

C.2 Operational Expenses

Table C.21: Marine Operations Costs for CRT

Component	1 Units Cost	10 Units Cost	50 Units Cost
Maintenance Operations per Year	2	20	98
Operational Cost per Intervention	£ 16 854	£ 16 854	£ 16 854
Total	£ 33 159	£ 331 594	£ 1 657 970

Table C.22: Shoreside Operations Costs for CRT

Component	1 Units Cost	10 Units Cost	50 Units Cost
Site Manager Salary	£ 96 158	£ 96 158	£ 96 158
Administrative Assistant Salary	£ 39 595	£ 39 595	£ 39 595
Senior Technician Salary	£ 42 355	£ 42 355	£ 52 944
Junior Technician Salary	£ 56 473	£ 56 473	£ 91 769
Total	£ 234 581	£ 234 581	£ 280 466

Table C.23: Replacement Parts Costs for CRT

Component	% of Cost	1 Units Cost	10 Units Cost	50 Units Cost
Powertrain	0.94	£ 2 512	£ 11 334	£ 49 632
Mooring	10	£ 185 422	£ 787 301	£ 3 435 353
Riser Cable	10	£ 1 867	£ 18 671	£ 93 354
Total		£ 189 801	£ 817 305	£ 3 578 339

Appendix D

Detailed LCOE Sensitivity Analysis Charts

The sensitivity analysis charts included in this appendix refer to the Detailed LCOE components described in [Section 6.5.5](#).

D.1 Detailed LCOE Sensitivity Analysis Results for 1 Unit TSP

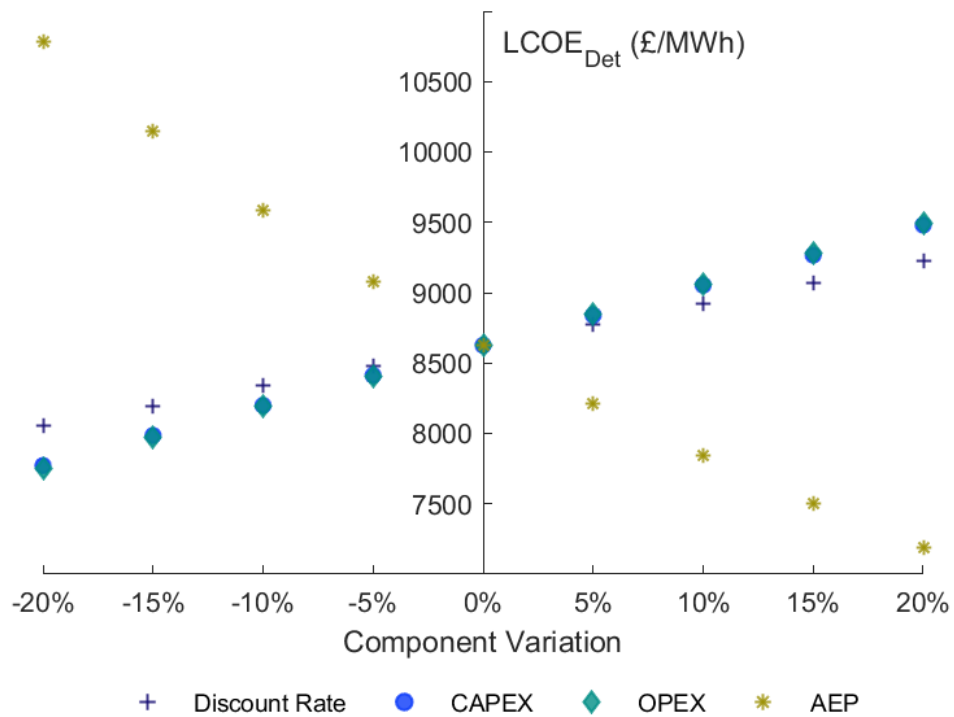


Figure D.1: LCOE_{Det} Sensitivity Analysis for a 1 Unit TSP

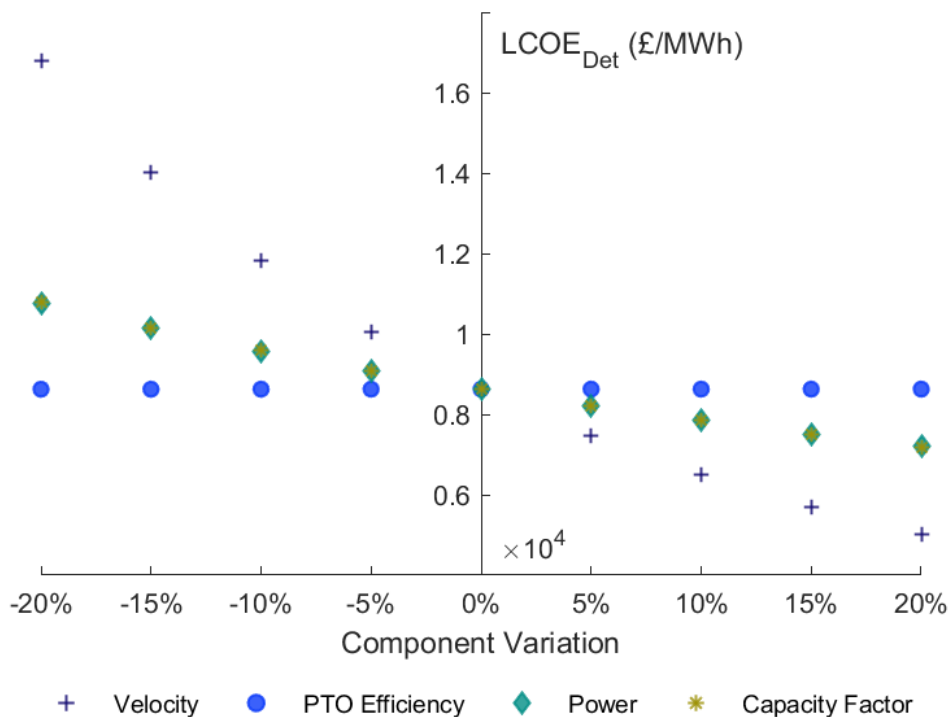


Figure D.2: $LCOE_{Det}$ Power Related Sensitivity Analysis for a 1 Unit TSP

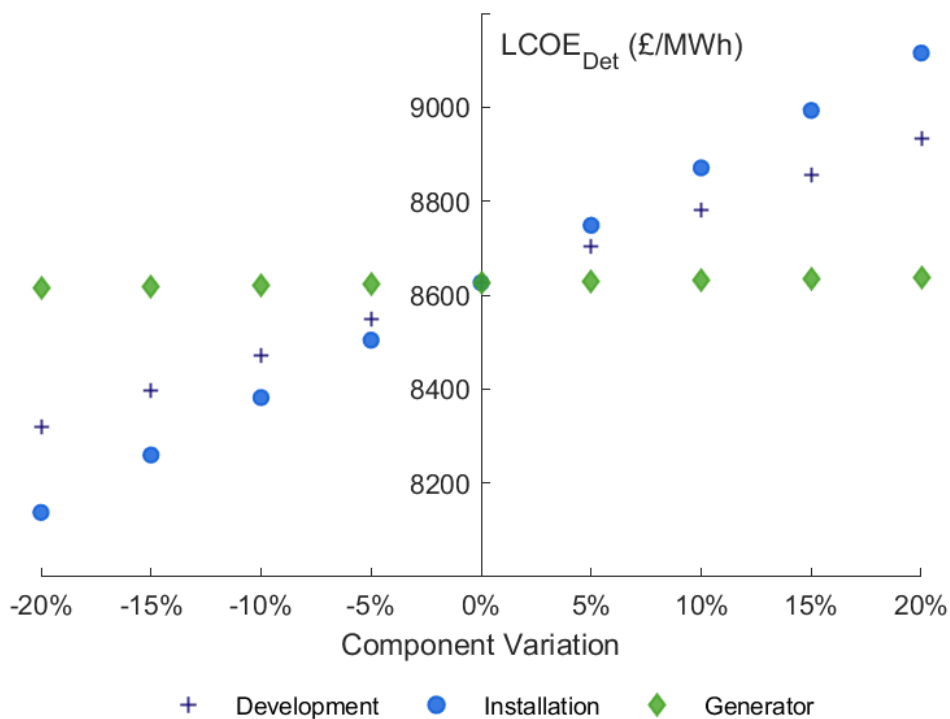


Figure D.3: $LCOE_{Det}$ CAPEX Components Sensitivity Analysis for a 1 Unit TSP

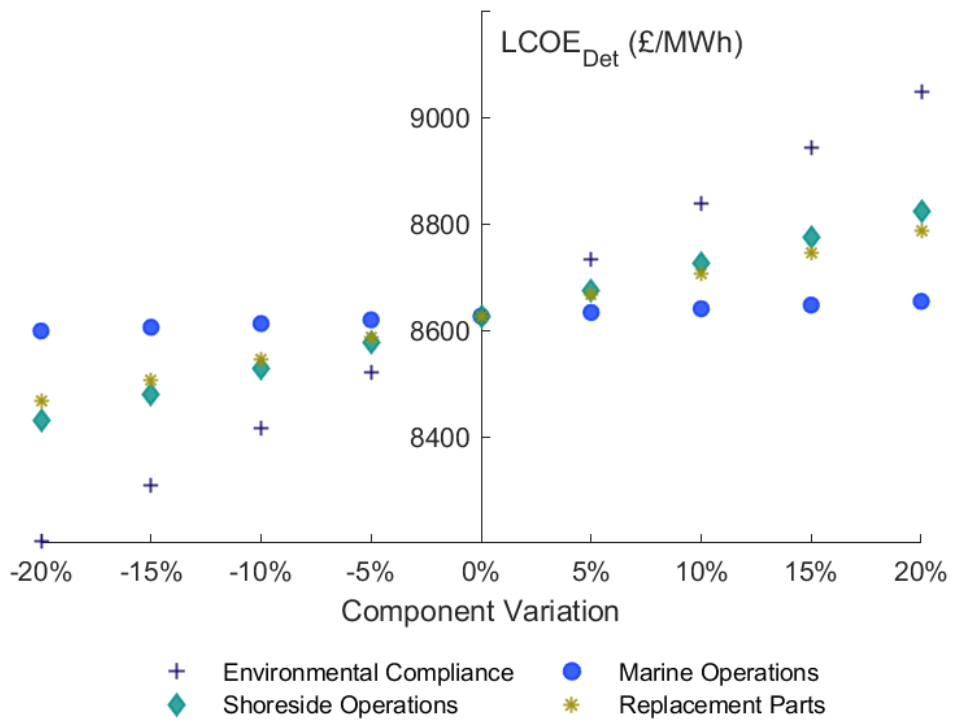


Figure D.4: LCOE_{Det} OPEX Components Sensitivity Analysis for a 1 Unit TSP

D.2 Detailed LCOE Sensitivity Analysis Results for 10 Units TSP

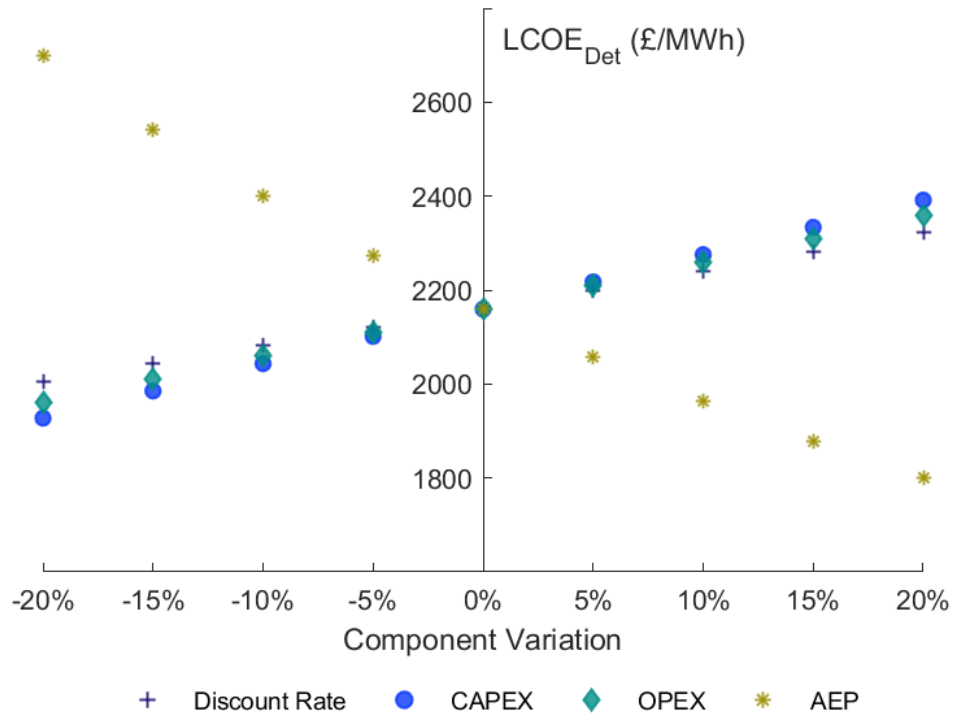


Figure D.5: LCOE_{Det} Sensitivity Analysis for a 10 Units TSP

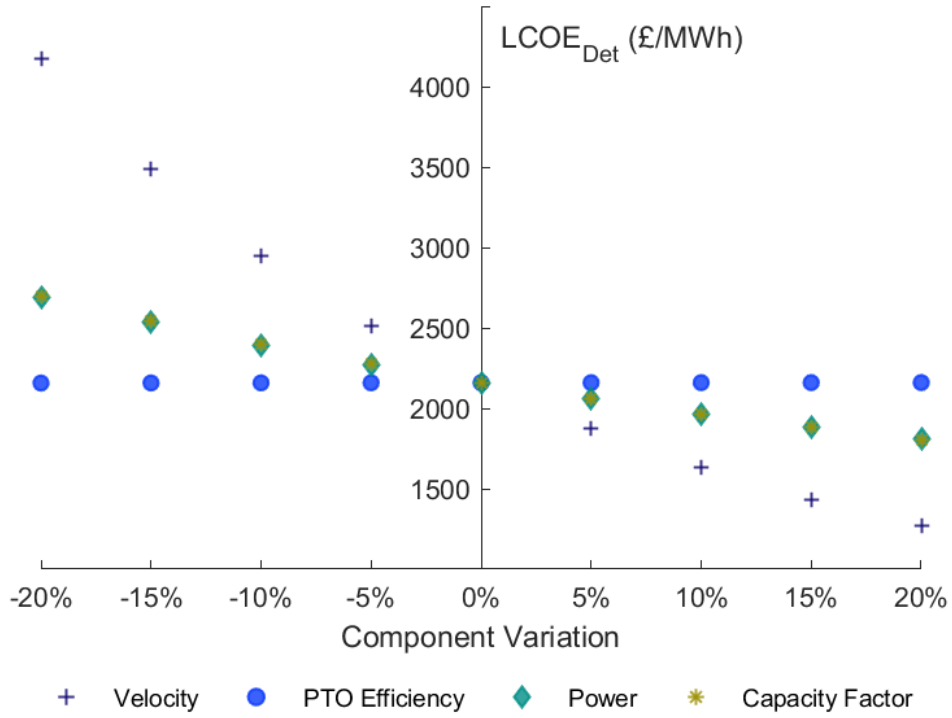


Figure D.6: $LCOE_{Det}$ Power Related Sensitivity Analysis for a 10 Units TSP

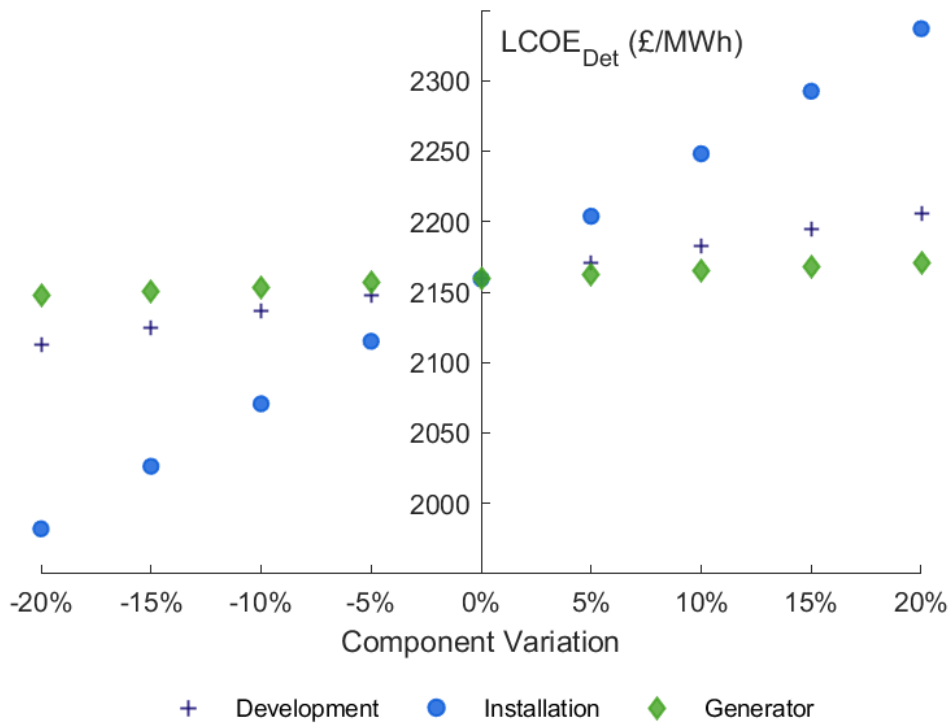


Figure D.7: $LCOE_{Det}$ CAPEX Components Sensitivity Analysis for a 10 Units TSP

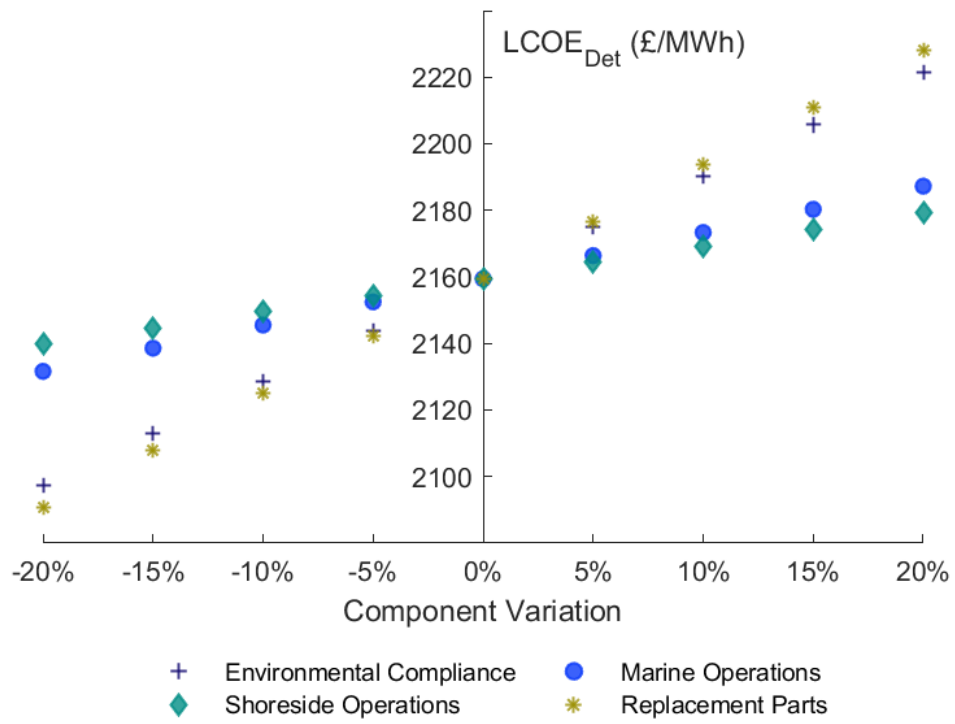


Figure D.8: LCOE_{Det} OPEX Components Sensitivity Analysis for a 10 Units TSP

D.3 Detailed LCOE Sensitivity Analysis Results for 50 Units TSP

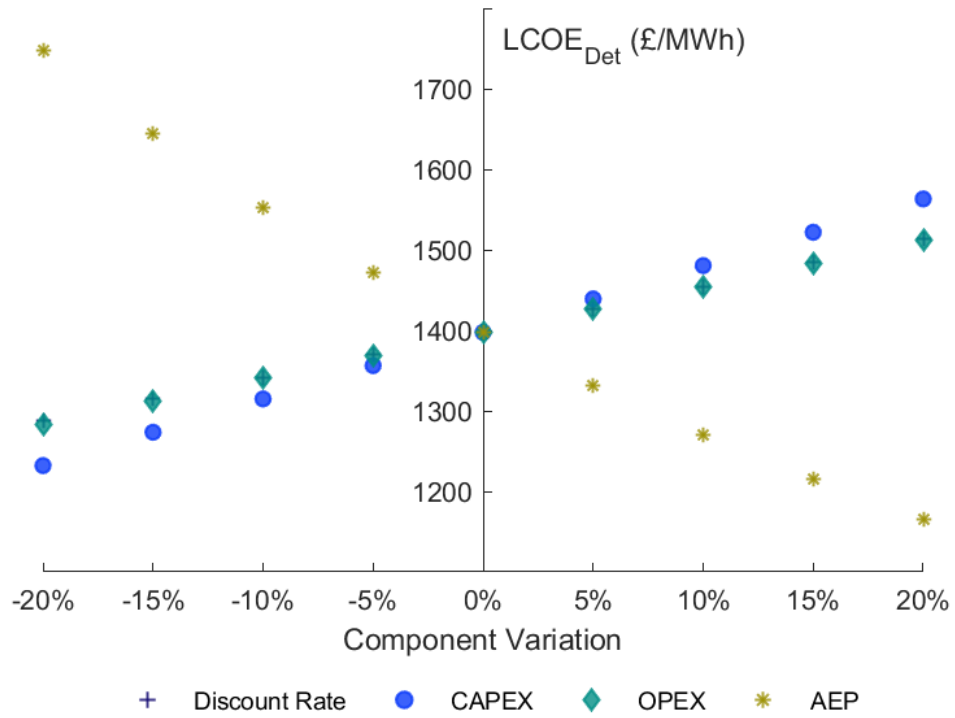


Figure D.9: LCOE_{Det} Sensitivity Analysis for a 50 Units TSP

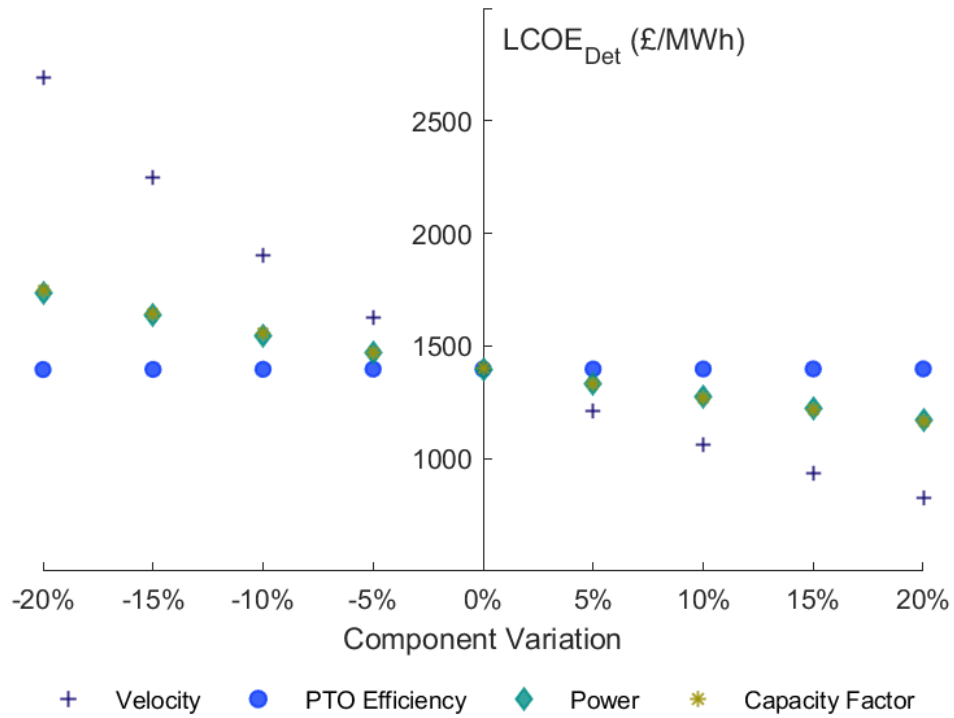


Figure D.10: LCOE_{Det} Power Related Sensitivity Analysis for a 50 Units TSP

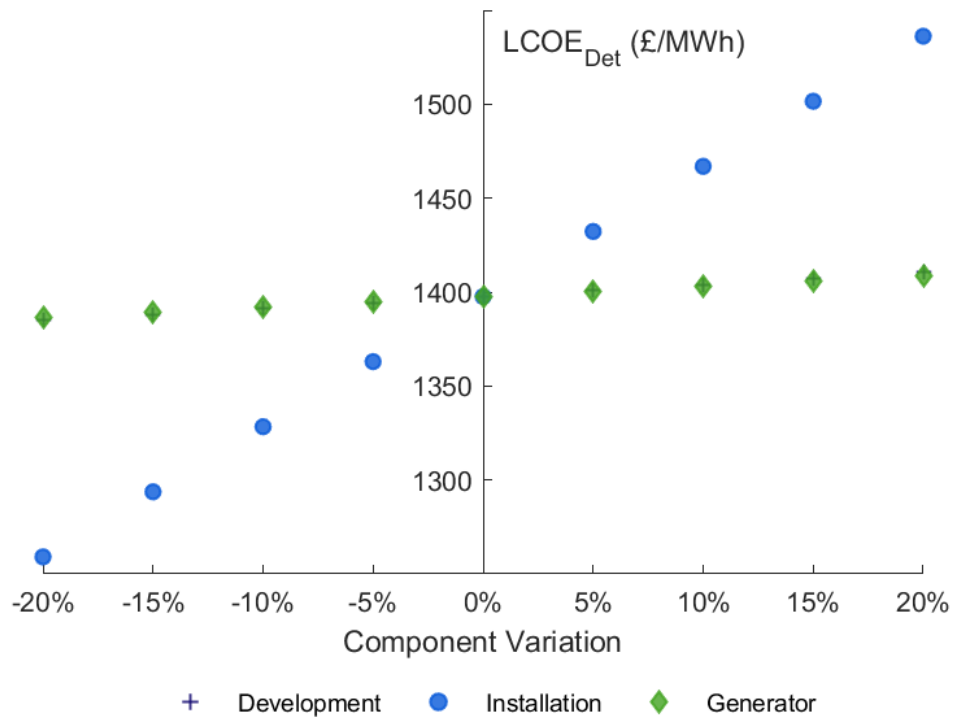


Figure D.11: LCOE_{Det} CAPEX Components Sensitivity Analysis for a 50 Units TSP

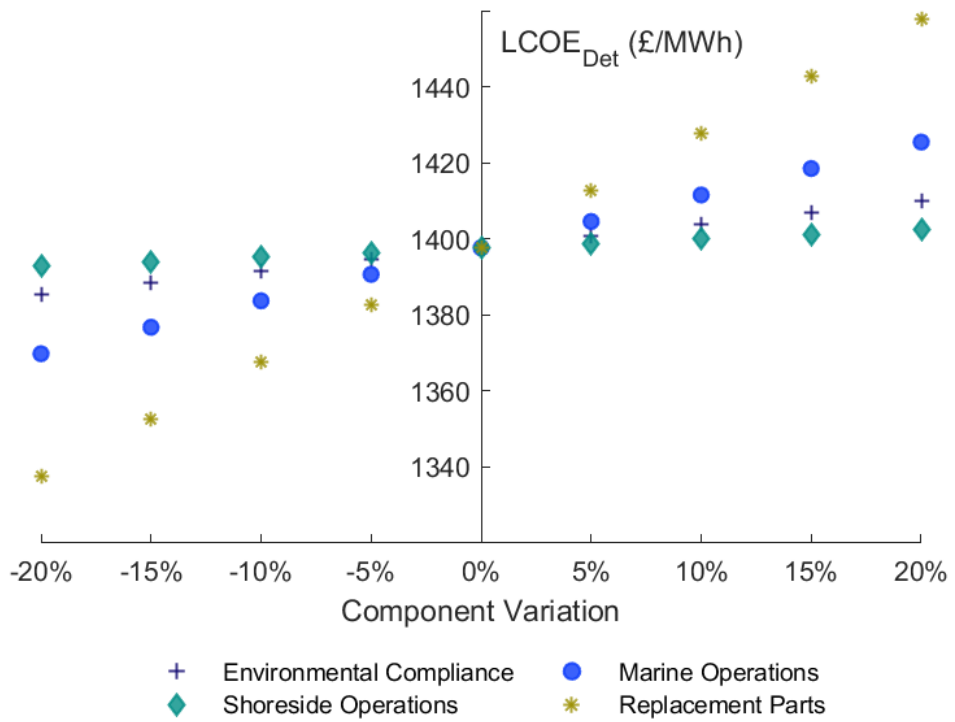


Figure D.12: LCOE_{Det} OPEX Components Sensitivity Analysis for a 50 Units TSP

Appendix E

Matlab Codes

E.1 Contra-Rotating Rotors Matching Script

This code organises all the possible CRT configurations, from the SRT geometries modelled in [Chapter 4](#). It includes the single condition to avoid blade interference between front and back rotors' number of blades. The code was applied specifically for the process described in [Section 5.3.2](#).

```
function ARRANGEMENTS = matching_rotors (folder, error)
%% Obtain data
clc
% Open Folder an Get SRT Data
currentfold = pwd;
fold = folder;
err = error; % Torque Difference between Rotors
addpath('D:/Geometry variations/')
data = extract_data(fold); % Get Single Rotor Turbines Performance Data
cd(currentfold)
% Creating torque matrices with different rotor sizes
Radius = [0.5 1 1.5 2 2.5 3 3.5 4 4.5 5 5.5 6 6.5 7 7.5];
vel = 1.2; % Inlet velocity in m/s
counter = 0; % Combinations Counter
%% FINDING ALL MATCHING ROTORS
% Case (i) and Case (ii) Matching Rotors
for N = 2 : 5 % Number of Blades from Front Rotor
for M = 2 : 5 % Number of Blades from Back Rotor
if (N == 2 && M == 3) || ( N == 2 && M == 5) || ( N == 4 && M == 3)...
|| ( N == 4 && M == 5) || ( N == 5 && M == 3)
for s = 1 : 2
% Declaring Rotors from Case (i)
if s == 1 && (N~=3 && M~=3)
```

Appendix E Matlab Codes

```
% Matching Two Rotors from Case (i)
COMB = [];
for A = 1 : length(data.(sprintf('DIFFSOL_%dblades',N)).Angles)
    anga = data.(sprintf('DIFFSOL_%dblades',N)).Angles(A);
    a = strrep(num2str(ang), '.', 'p');
    for B = 1 : length(data.(sprintf('DIFFSOL_%dblades',M)).Angles)
        angb = data.(sprintf('DIFFSOL_%dblades',M)).Angles(B);
        b = strrep(num2str(angb), '.', 'p');
        for ROW = 1 : size(data.(sprintf('DIFFSOL_%dblades',N))....
            (sprintf('DIFFSOL_%dblades_%sdeg', N, a))....
            (sprintf('DIFFSOL_%dblades_%sdeg_Torque_DiffRadius', N, a)),1)
            for RN = 1 : length(Radius)
                TORQUE_DS1 = data.(sprintf('DIFFSOL_%dblades',N))....
                    (sprintf('DIFFSOL_%dblades_%sdeg', N, a))....
                    (sprintf('DIFFSOL_%dblades_%sdeg_Torque_DiffRadius', N, a))(ROW, RN + 2);
                ROT_DS1 = data.(sprintf('DIFFSOL_%dblades',N))....
                    (sprintf('DIFFSOL_%dblades_%sdeg', N, a))....
                    (sprintf('DIFFSOL_%dblades_%sdeg_Torque_DiffRadius', N, a))(ROW, 2) * vel / Radius(RN);
                POW_DS1 = TORQUE_DS1 * ROT_DS1;
                RPM_DS1 = ROT_DS1 / (2 * pi()) * 60;
                TORQUE_DS2 = data.(sprintf('DIFFSOL_%dblades',M))....
                    (sprintf('DIFFSOL_%dblades_%sdeg', M, b))....
                    (sprintf('DIFFSOL_%dblades_%sdeg_Torque_DiffRadius', M, b));
                TORQUE_DS2_2 = TORQUE_DS2(:, 4:end);
                [rows, col] = find( abs((TORQUE_DS2_2 - TORQUE_DS1)/TORQUE_DS1) < err );
                MATRIX = [ rows, col ];
                if isempty(MATRIX) == 0
                    for mat = 1 : size(MATRIX,1)
                        torque_DS2 = TORQUE_DS2_2( MATRIX(mat,1), MATRIX(mat,2));
                        ROT_DS2 = TORQUE_DS2( MATRIX(mat), 3) / ;
                        POW_DS2 = torque_DS2 * ROT_DS2;
                        RPM_DS2 = ROT_DS2 / (2 * pi()) * 60;
                        Radius_DS2 = Radius( MATRIX(mat,2));
                        COMB(mat, 1:16) = [ 1 N anga Radius(RN) ROT_DS1 RPM_DS1 TORQUE_DS1/1000 ...
                            POW_DS1/1000 1 M angb Radius_DS2 ROT_DS2 RPM_DS2 torque_DS2/1000 ...
                            POW_DS2/1000 ];
                    end
                counter = counter + 1;
                COUNTER.(sprintf('DIFFSOL_%db_DIFFSOL_%db_%d_comb', N, M, counter)) = COMB;
```

```

end

MATRIX = [];
COMB = [];
end end end end

% Matching Rotors from Case (i) with Rotors from Case (ii)
for A = 1 : length(data.(sprintf('DIFFSOL_%dblades',N)).Angles)
    anga = data.(sprintf('DIFFSOL_%dblades',N)).Angles(A);
    a = strrep(num2str(ang), '.', 'p');
    for B = 1 : length(data.(sprintf('SAMESOL_%dblades',M)).Angles)
        angb = data.(sprintf('SAMESOL_%dblades',M)).Angles(B);
        b = strrep(num2str(angb), '.', 'p');
        for ROW = 1 : size(data.(sprintf('DIFFSOL_%dblades',N))....
            (sprintf('DIFFSOL_%dblades_%sdeg', N, a))....
            (sprintf('DIFFSOL_%dblades_%sdeg_Torque_DiffRadius', N, a)),1)
            for RN = 1 : length(Radius)
                TORQUE_DS3 = data.(sprintf('DIFFSOL_%dblades',N))....
                    (sprintf('DIFFSOL_%dblades_%sdeg', N, a))....
                    (sprintf('DIFFSOL_%dblades_%sdeg_Torque_DiffRadius', N, a))(ROW, RN + 3);
                ROT_DS3 = data.(sprintf('DIFFSOL_%dblades',N))....
                    (sprintf('DIFFSOL_%dblades_%sdeg', N, a))....
                    (sprintf('DIFFSOL_%dblades_%sdeg_Torque_DiffRadius', N, a))(ROW, 2);
                POW_DS3 = TORQUE_DS3 * ROT_DS3;
                RPM_DS3 = ROT_DS3 / (2 * pi()) * 60;
                TORQUE_SS1 = data.(sprintf('SAMESOL_%dblades',M))....
                    (sprintf('SAMESOL_%dblades_%sdeg', M, b))....
                    (sprintf('SAMESOL_%dblades_%sdeg_Torque_DiffRadius', M, b));
                TORQUE_SS1_2 = TORQUE_SS1(:, 4:end);
                [rows, col] = find( abs((TORQUE_SS1_2 - TORQUE_DS3)/TORQUE_DS3) < err );
                MATRIX = [ rows, col ];
                if isempty(MATRIX) == 0
                    for mat = 1 : size(MATRIX,1)
                        torque_SS1 = TORQUE_SS1_2( MATRIX(mat,1), MATRIX(mat,2));
                        ROT_SS1 = TORQUE_SS1( MATRIX(mat), 2);
                        POW_SS1 = torque_SS1 * ROT_SS1;
                        RPM_SS1 = ROT_SS1 / (2 * pi()) * 60;
                        Radius_SS1 = Radius(MATRIX(mat,2));
                        COMB(mat, 1:16) = [ 1 N anga Radius(RN) ROT_DS3 RPM_DS3 TORQUE_DS3/1000 ...
                            POW_DS3/1000 2 M angb Radius_SS1 ROT_SS1 RPM_SS1 torque_SS1/1000 ...
                            POW_SS1/1000 ];
                    end
                end
            end
        end
    end
end

```

Appendix E Matlab Codes

```
end

counter = counter + 1;
COUNTER.(sprintf('DIFFSOL_%db_SAMESOL_%db_%d_comb', N, M, counter)) = COMB;
end
MATRIX = [];
COMB = [];
end end end end end

% Matching Rotors from Case (i) and Turbine A
if s == 1 && (M == 3)
COMB=[];
for A = 1 : length(data.(sprintf('DIFFSOL_%dblades',N)).Angles)
anga = data.(sprintf('DIFFSOL_%dblades',N)).Angles(A);
a = strrep(num2str(anga), '.', 'p');
for ROW = 1 : size(data.(sprintf('DIFFSOL_%dblades',N))....
    (sprintf('DIFFSOL_%dblades_%sdeg', N, a))....
    (sprintf('DIFFSOL_%dblades_%sdeg_Torque_DiffRadius', N, a)),1)
for RN = 1 : length(Radius)
TORQUE_DS4 = data.(sprintf('DIFFSOL_%dblades',N))....
    (sprintf('DIFFSOL_%dblades_%sdeg', N, a))....
    (sprintf('DIFFSOL_%dblades_%sdeg_Torque_DiffRadius', N, a))(ROW, RN + 3);
ROT_DS4 = data.(sprintf('DIFFSOL_%dblades',N))....
    (sprintf('DIFFSOL_%dblades_%sdeg', N, a))....
    (sprintf('DIFFSOL_%dblades_%sdeg_Torque_DiffRadius', N, a))(ROW, 2);
POW_DS4 = TORQUE_DS4 * ROT_DS4;
RPM_DS4 = ROT_DS4 / (2 * pi()) * 60;
TORQUE_ORIG1 = data.(sprintf('ORIGINAL_%dblades',M))....
    (sprintf('Box_220m')).(sprintf('Torque'));
TORQUE_ORIG1_2 = TORQUE_ORIG1(:, 3);
[rows, col] = find( abs((TORQUE_ORIG1_2 - TORQUE_DS4)/TORQUE_DS4) < err );
MATRIX = [ rows, col ];
if isempty(MATRIX) == 0
for mat = 1 : size(MATRIX,1)
torque_ORIG1 = TORQUE_ORIG1_2( MATRIX(mat,1), MATRIX(mat,2));
ROT_ORIG1 = TORQUE_ORIG1( MATRIX(mat), 1);
POW_ORIG1 = torque_ORIG1 * ROT_ORIG1;
RPM_ORIG1 = ROT_ORIG1 / (2 * pi()) * 60;
Radius_ORIG1 = Radius(MATRIX(mat,2));
COMB(mat, 1:16) = [ 2 N anga Radius(RN) ROT_DS4 RPM_DS4 TORQUE_DS4/1000 ...
    POW_DS4/1000 0 3 6 Radius_ORIG1 ROT_ORIG1 RPM_ORIG1 ...
```

```

torque_ORIG1/1000 POW_ORIG1/1000 ];
end
counter = counter + 1;
COUNTER.(sprintf('DIFFSOL_%db_ORIGINAL_%d_comb', N, counter)) = COMB;
end
MATRIX = [];
COMB = [];
end end end end
% Declaring Rotors from Case (ii)
if s == 2 && (N~=3 && M~=3)
% Matching Two Rotors from Case (ii)
for A = 1 : length(data.(sprintf('SAMESOL_%dblades',N)).Angles)
anga = data.(sprintf('SAMESOL_%dblades',N)).Angles(A);
a = strrep(num2str(anga), '.', 'p');
for B = 1 : length(data.(sprintf('SAMESOL_%dblades',M)).Angles)
angb = data.(sprintf('SAMESOL_%dblades',M)).Angles(B);
b = strrep(num2str(angb), '.', 'p');
for ROW = 1 : size(data.(sprintf('SAMESOL_%dblades',N))....
(sprintf('SAMESOL_%dblades_%sdeg', N, a))....
(sprintf('SAMESOL_%dblades_%sdeg_Torque_DiffRadius', N, a)),1)
for RN = 1 : length(Radius)
TORQUE_SS2 = data.(sprintf('SAMESOL_%dblades',N))....
(sprintf('SAMESOL_%dblades_%sdeg', N, a))....
(sprintf('SAMESOL_%dblades_%sdeg_Torque_DiffRadius', N, a))(ROW, RN + 3);
ROT_SS2 = data.(sprintf('SAMESOL_%dblades',N))....
(sprintf('SAMESOL_%dblades_%sdeg', N, a))....
(sprintf('SAMESOL_%dblades_%sdeg_Torque_DiffRadius', N, a))(ROW, 2);
POW_SS2 = TORQUE_SS2 * ROT_SS2;
RPM_SS2 = ROT_SS2 / (2 * pi()) * 60;
TORQUE_SS3 = data.(sprintf('SAMESOL_%dblades',M))....
(sprintf('SAMESOL_%dblades_%sdeg', M, b))....
(sprintf('SAMESOL_%dblades_%sdeg_Torque_DiffRadius', M, b));
TORQUE_SS3_2 = TORQUE_SS3(:, 4:end);
[rows, col] = find( abs((TORQUE_SS3_2 - TORQUE_SS2)/TORQUE_SS2) < err );
MATRIX = [ rows, col ];
if isempty(MATRIX) == 0
for mat = 1 : size(MATRIX,1)
torque_SS3 = TORQUE_SS3_2( MATRIX(mat,1), MATRIX(mat,2));
ROT_SS3 = TORQUE_SS3( MATRIX(mat), 2);

```

Appendix E Matlab Codes

```

POW_SS3 = torque_SS3 * ROT_SS3;
RPM_SS3 = ROT_SS3 / (2 * pi()) * 60;
Radius_SS3 = Radius(MATRIX(mat,2));
COMB(mat, 1:16) = [ 2 N anga Radius(RN) ROT_SS2 RPM_SS2 TORQUE_SS2/1000 ...
    POW_SS2/1000 2 M angb Radius_SS3 ROT_SS3 RPM_SS3 torque_SS3/1000 POW_SS3/1000 ];
end
counter = counter + 1;
COUNTER.(sprintf('SAMESOL_%db_SAMESOL_%db_%d_comb', N, M, counter)) = COMB;
end
MATRIX = [];
COMB = [];
end end end end
%% Matching Rotors from Case (ii) and Turbine A
if s == 2 && (M==3)
for A = 1 : length(data.(sprintf('SAMESOL_%dblades',N)).Angles)
anga = data.(sprintf('SAMESOL_%dblades',N)).Angles(A);
a = strrep(num2str(angas), '.', 'p');
for ROW = 1 : size(data.(sprintf('SAMESOL_%dblades',N))....
    (sprintf('SAMESOL_%dblades_%sdeg', N, a))....
    (sprintf('SAMESOL_%dblades_%sdeg_Torque_DiffRadius', N, a)),1)

for RN = 1 : length(Radius)
TORQUE_SS4 = data.(sprintf('SAMESOL_%dblades',N))....
    (sprintf('SAMESOL_%dblades_%sdeg', N, a))....
    (sprintf('SAMESOL_%dblades_%sdeg_Torque_DiffRadius', N, a))(ROW, RN + 3);
ROT_SS4 = data.(sprintf('SAMESOL_%dblades',N))....
    (sprintf('SAMESOL_%dblades_%sdeg', N, a))....
    (sprintf('SAMESOL_%dblades_%sdeg_Torque_DiffRadius', N, a))(ROW, 2);
POW_SS4 = TORQUE_SS4 * ROT_SS4;
RPM_SS4 = ROT_SS4 / (2 * pi()) * 60;
TORQUE_ORIG2 = data.(sprintf('ORIGINAL_%dblades',M))....
    (sprintf('Box_220m')).(sprintf('Torque'));
TORQUE_ORIG2_2 = TORQUE_ORIG2(:, 3);
[rows, col] = find( abs((TORQUE_ORIG2_2 - TORQUE_SS4)/TORQUE_SS4) < err );
MATRIX = [ rows, col ];
if isempty(MATRIX) == 0
for mat = 1 : size(MATRIX,1)
torque_ORIG2 = TORQUE_ORIG2_2( MATRIX(mat,1), MATRIX(mat,2));
ROT_ORIG2 = TORQUE_ORIG2( MATRIX(mat), 1);

```

```

POW_ORIG2 = torque_ORIG2 * ROT_ORIG2;
RPM_ORIG2 = ROT_ORIG2 / (2 * pi()) * 60;
Radius_ORIG2 = Radius(MATRIX(mat,2));
COMB(mat, 1:16) = [ 2 N anga Radius(RN) ROT_SS4 RPM_SS4 TORQUE_SS4/1000 ...
    POW_SS4/1000 0 3 6 Radius_ORIG2 ROT_ORIG2 RPM_ORIG2 torque_ORIG2/1000 POW_ORIG2/1000 ];
end
counter = counter + 1;
COUNTER.(sprintf('SAMESOL_%db_ORIGINAL_%d_comb', N, counter)) = COMB;
end
MATRIX = [];
COMB = [];
end end end end end end end end
% Case (iii) Matching Rotors
for N = 2 : 5 % Number of Blades from Front Rotor
for M = 2 : 5 % Number of Blades from Back Rotor
% Declaring Rotors from Case (iii)
if (N ~= 3 && M ~= 3) %&& s == 3
% Matching Rotors from Case (iii) with Rotors from Case (i)
for A = 1 : length(data.(sprintf('SSa3b_%dbCHORD_3b',N)).Angles)
anga = data.(sprintf('SSa3b_%dbCHORD_3b',N)).Angles(A);
a = strrep(num2str(ang), '.', 'p');
for B = 1 : length(data.(sprintf('DIFFSOL_%dblades',M)).Angles)
angb = data.(sprintf('DIFFSOL_%dblades',M)).Angles(B);
b = strrep(num2str(angb), '.', 'p');
for ROW = 1 : size(data.(sprintf('SSa3b_%dbCHORD_3b',N))....
    (sprintf('SSa3b_%dbCHORD_3b_%sdeg', N, a))....
    (sprintf('SSa3b_%dbCHORD_3b_%sdeg_Torque_DiffRadius', N, a)),1)
for RN = 1 : length(Radius)
TORQUE_CH1 = data.(sprintf('SSa3b_%dbCHORD_3b',N))....
    (sprintf('SSa3b_%dbCHORD_3b_%sdeg', N, a))....
    (sprintf('SSa3b_%dbCHORD_3b_%sdeg_Torque_DiffRadius', N, a))(ROW, RN + 3);
ROT_CH1 = data.(sprintf('SSa3b_%dbCHORD_3b',N))....
    (sprintf('SSa3b_%dbCHORD_3b_%sdeg', N, a))....
    (sprintf('SSa3b_%dbCHORD_3b_%sdeg_Torque_DiffRadius', N, a))(ROW, 2);
POW_CH1 = TORQUE_CH1 * ROT_CH1;
RPM_CH1 = ROT_CH1 / (2 * pi()) * 60;
TORQUE_DS5 = data.(sprintf('DIFFSOL_%dblades',M))....
    (sprintf('DIFFSOL_%dblades_%sdeg', M, b))....
    (sprintf('DIFFSOL_%dblades_%sdeg_Torque_DiffRadius', M, b));

```

Appendix E Matlab Codes

```
TORQUE_DS5_2 = TORQUE_DS5(:, 4:end);
[rows, col] = find( abs((TORQUE_DS5_2 - TORQUE_CH1)/TORQUE_CH1) < err );
MATRIX = [ rows, col ];
if isempty(MATRIX) == 0
for mat = 1 : size(MATRIX,1)
torque_DS5 = TORQUE_DS5_2( MATRIX(mat,1), MATRIX(mat,2));
ROT_DS5 = TORQUE_DS5( MATRIX(mat), 2);
POW_DS5 = torque_DS5 * ROT_DS5;
RPM_DS5 = ROT_DS5 / (2 * pi()) * 60;
Radius_DS5 = Radius(MATRIX(mat,2));
COMB(mat, 1:16) = [ 3+(N/10) 3 anga Radius(RN) ROT_CH1 RPM_CH1 TORQUE_CH1/1000...
    POW_CH1/1000 1 M angb Radius_DS5 ROT_DS5 RPM_DS5 torque_DS5/1000 POW_DS5/1000 ];
end
counter = counter + 1;
COUNTER.(sprintf('SSa3b_%dbCHORD_DIFFSOL_%db_%d_comb', N, M, counter)) = COMB;
end
MATRIX = [];
COMB = [];
end end end end
% Matching Rotors from Case (iii) with Rotors from Case (ii)
for A = 1 : length(data.(sprintf('SSa3b_%dbCHORD_3b',N)).Angles)
anga = data.(sprintf('SSa3b_%dbCHORD_3b',N)).Angles(A);
a = strrep(num2str(angas), '.', 'p');
for B = 1 : length(data.(sprintf('SAMESOL_%dblades',M)).Angles)
angb = data.(sprintf('SAMESOL_%dblades',M)).Angles(B);
b = strrep(num2str(angb), '.', 'p');
for ROW = 1 : size(data.(sprintf('SSa3b_%dbCHORD_3b',N))....
    (sprintf('SSa3b_%dbCHORD_3b_%sdeg', N, a))....
    (sprintf('SSa3b_%dbCHORD_3b_%sdeg_Torque_DiffRadius', N, a)),1)
for RN = 1 : length(Radius)
TORQUE_CH2 = data.(sprintf('SSa3b_%dbCHORD_3b',N))....
    (sprintf('SSa3b_%dbCHORD_3b_%sdeg', N, a))....
    (sprintf('SSa3b_%dbCHORD_3b_%sdeg_Torque_DiffRadius', N, a))(ROW, RN + 3);
ROT_CH2 = data.(sprintf('SSa3b_%dbCHORD_3b',N))....
    (sprintf('SSa3b_%dbCHORD_3b_%sdeg', N, a))....
    (sprintf('SSa3b_%dbCHORD_3b_%sdeg_Torque_DiffRadius', N, a))(ROW, 2);
POW_CH2 = TORQUE_CH2 * ROT_CH2;
RPM_CH2 = ROT_CH2 / (2 * pi()) * 60;
TORQUE_SS5 = data.(sprintf('SAMESOL_%dblades',M))....
```

```

    (sprintf('SAMESOL_%dblades_%sdeg', M, b))....
    (sprintf('SAMESOL_%dblades_%sdeg_Torque_DiffRadius', M, b));
TORQUE_SS5_2 = TORQUE_SS5(:, 4:end);
[rows, col] = find( abs((TORQUE_SS5_2 - TORQUE_CH2)/TORQUE_CH2) < err );
MATRIX = [ rows, col ];
if isempty(MATRIX) == 0
for mat = 1 : size(MATRIX,1)
torque_SS5 = TORQUE_SS5_2( MATRIX(mat,1), MATRIX(mat,2));
ROT_SS5 = TORQUE_SS5( MATRIX(mat), 2);
POW_SS5 = torque_SS5 * ROT_SS5;
RPM_SS5 = ROT_SS5 / (2 * pi()) * 60;
Radius_SS5 = Radius(MATRIX(mat,2));
COMB(mat, 1:16) = [ 3+(N/10) 3 anga Radius(RN) ROT_CH2 RPM_CH2 TORQUE_CH2/1000...
    POW_CH2/1000 2 M angb Radius_SS5 ROT_SS5 RPM_SS5 torque_SS5/1000 POW_SS5/1000 ];
end
counter = counter + 1;
COUNTER.(sprintf('SSa3b_%dbCHORD_SAMESOL_%db_%d_comb', N, M, counter)) = COMB;
end
MATRIX = [];
COMB = [];
end end end end end end end
vars1 = { 'a' 'A' 'anga' 'angb' 'b' 'B' 'col' 'COMB' 'M' 'mat' 'MATRIX' 'N' ...
    'Radius_DS2' 'Radius_DS5' 'Radius_ORIG1' 'Radius_ORIG2' 'Radius_SS1' ...
    'Radius_SS3' 'Radius_SS5' 'RN' 'ROT_CH1' 'ROT_CH2' 'ROT_DS1' 'ROT_DS2' ...
    'ROT_DS3' 'ROT_DS4' 'ROT_DS5' 'ROT_ORIG1' 'ROT_ORIG2' 'ROT_SS1' 'ROT_SS2'...
    'ROT_SS3' 'ROT_SS4' 'ROT_SS5' 'ROW' 'rows' 's' 'TORQUE_CH1' 'TORQUE_CH2' ...
    'TORQUE_DS1' 'torque_DS2' 'TORQUE_DS2' 'TORQUE_DS2_2' 'TORQUE_DS3' ...
    'TORQUE_DS4' 'TORQUE_DS5' 'TORQUE_DS5_2' 'torque_DS5' 'TORQUE_ORIG1' ...
    'torque_ORIG1' 'TORQUE_ORIG1_2' 'TORQUE_ORIG2' 'torque_ORIG2' 'TORQUE_ORIG2_2' ...
    'torque_SS1' 'TORQUE_SS1' 'TORQUE_SS1_2' 'TORQUE_SS2' 'TORQUE_SS3' ...
    'torque_SS3' 'TORQUE_SS3_2' 'TORQUE_SS4' ...
    'TORQUE_SS5' 'TORQUE_SS5_2' 'torque_SS5' };
% Deleting Dummy Variables
clear(vars1{:});

%% ORGANISING MATCHING ROTORS BY SOLIDITY, NUMBER OF BLADES,
%% PITCH ANGLE (AND RADIUS) OF EACH ROTOR.
% Declaring Dummy Variables
fields = fieldnames(COUNTER);

```

Appendix E Matlab Codes

```
arrangements = 0;
rep = 0;
REF_nblades1 = 0;
REF_nblades2 = 0;
REF_ang1 = 0;
REF_ang2 = 0;
REF_rad1 = 0;
REF_rad2 = 0;
check = 0;
% Create the Organised Structure with Arrangements Output
for n = 1 : counter;
rows = size(COUNTER.(fields{n}),1);
for i = rows
nblades1 = COUNTER.(fields{n})(i, 2);
nblades2 = COUNTER.(fields{n})(i, 10);
angle1 = COUNTER.(fields{n})(i, 3);
ang1 = strrep(num2str(angle1), '.', 'p');
angle2 = COUNTER.(fields{n})(i, 11);
ang2 = strrep(num2str(angle2), '.', 'p');
rad1 = COUNTER.(fields{n})(i, 4);
rad2 = COUNTER.(fields{n})(i, 13);
Sol1 = COUNTER.(fields{n})(i, 1);
Sol2 = COUNTER.(fields{n})(i, 9);
if rad1 ~= 0 && rad2 ~= 0
if nblades1 == REF_nblades1 && nblades2 == REF_nblades2 && ...
angle1 == REF_ang1 && angle2 == REF_ang2
rep = rep + 1;
else
rep = 1;
arrangements = arrangements + 1;
end
if Sol1 == 1 && Sol2 == 1
ARRANGEMENTS.(sprintf('DIFFSOL%db%sdeg_DIFFSOL%db%sdeg_comb%d', ...
nblades1, ang1, nblades2, ang2, arrangements))(rep,:) = ...
COUNTER.(fields{n})(i, :);
check = check + 1;
else
if Sol1 == 1 && Sol2 == 2
ARRANGEMENTS.(sprintf('DIFFSOL%db%sdeg_SAMESOL%db%sdeg_comb%d', ...
```

```

    nblades1, angl, nblades2, ang2, arrangements))(rep,:) = ...
    COUNTER.(fields{n})(i, :);
check = check + 1;
else
if Sol1 == 2 && Sol2 == 2
ARRANGEMENTS.(sprintf('SAMESOL%db%sdeg_SAMESOL%db%sfdeg_comb%d', ...
    nblades1, angl, nblades2, ang2, arrangements))(rep,:) = ...
    COUNTER.(fields{n})(i, :);
check = check + 1;
else
if Sol1 == 1 && Sol2 == 0
ARRANGEMENTS.(sprintf('DIFFSOL%db%sdeg_ORIGINAL%db%sdeg_comb%d', ...
    nblades1, angl, nblades2, ang2, arrangements))(rep,:) = ...
    COUNTER.(fields{n})(i, :);
check = check + 1;
else
if Sol1 == 2 && Sol2 == 0
ARRANGEMENTS.(sprintf('SAMESOL%db%sdeg_ORIGINAL%db%sdeg_comb%d', ...
    nblades1, angl, nblades2, ang2, arrangements))(rep,:) = ...
    COUNTER.(fields{n})(i, :);
check = check + 1;
else
if Sol1 >= 3 && Sol2 == 1
ARRANGEMENTS.(sprintf('SSa3b_%dbCHORD%sdeg_DIFFSOL%db%sdeg_comb%d', ...
    nblades1, angl, nblades2, ang2, arrangements))(rep,:) = ...
    COUNTER.(fields{n})(i, :);
check = check + 1;
else
if Sol1 >= 3 && Sol2 == 2
ARRANGEMENTS.(sprintf('SSa3b_%dbCHORD%sdeg_SAMESOL%db%sdeg_comb%d', ...
    nblades1, angl, nblades2, ang2, arrangements))(rep,:) = ...
    COUNTER.(fields{n})(i, :);
check = check + 1;
end end end end end end end
REF_nblades1 = nblades1;
REF_nblades2 = nblades2;
REF_ang1 = angle1;
REF_ang2 = angle2;
REF_rad1 = rad1;

```

```
REF_rad2 = rad2;
end end end
vars2 = { 'ang1' 'ang2' 'angle1' 'angle2' 'n' 'nblades1' 'nblades2' 'rad1' ...
          'rad2' 'REF_ang1' 'REF_ang2' 'REF_nblades1' 'REF_nblades2' 'REF_rad1'...
          'REF_rad2' 'rep' 'Sol1' 'Sol2' };
% Deleting Dummy Variables
clear(vars2{:});
end % End of Function
```

E.2 Contra-Rotating Rotors Selection Script

This code selects the technically feasible CRT combinations, from the arrangements created by the previous function in [Section E.1](#). The conditions, and limitations included in this code are described in [Section 5.3.3](#).

```
% Preamble
clear all
clc
close all
currentfold = pwd;
folder = 'I:\Geometry Variations - Recovery - BackUp\Counter-rotating';
% Difference of Torque Values Between Rotors
error = 0.05; Rotors
% Get Arrangements from Matching Rotors Function
ARRANGEMENTS = matching_rotors_usinglambda(folder, error);
fields = fieldnames(ARRANGEMENTS);
%% Filters
% Total Rotational Velocity Must add to a Value between 14 rpm and 30 rpm
rpm_a = 16; % Min rpm
rpm_b = 28; % Max rpm
limpow = 80; % Minimum Total Power Output
dist = 5000; % Distance to Shore
% Dummy Variables
count = 1;
k = 0;
comb = 0;
s = 0;
```

```

% Headers for Output File
CONTRA_COMB = {'SOL_1' 'BLADES_1' 'PITCH_1' 'RADIUS_1' 'RAD/S_1' 'RPM_1' ...
              'TORQUE_1' 'POWER_1' 'SOL_2' 'BLADES_2' 'PITCH_2' 'RADIUS_2' 'RAD/S_2' ...
              'RPM_2' 'TORQUE_2' 'POWER_2' 'TOTRPM' 'SIZDIF' 'TORQDIF' 'TOTPOW' 'LCOE'};
fileID = fopen('CONTRA_COMBINATIONS.txt', 'w');
fprintf(fileID, '%s\t %s\t ...
              %s\t %s\t %s\t %s\t %s\t %s\t %s\t %s\t\t %s\r\n', CONTRA_COMB{1,:});
% Find LCOE and for Arrangements with Power Higher than Zero
for n = 1 : size (fields, 1)
rows = size (ARRANGEMENTS.(fields{n}),1);
for i = 1: rows
rot1 = ARRANGEMENTS.(fields{n})(i, 6);
rot2 = ARRANGEMENTS.(fields{n})(i, 14);
size1 = ARRANGEMENTS.(fields{n})(i, 4);
size2 = ARRANGEMENTS.(fields{n})(i, 12);
torque1 = ARRANGEMENTS.(fields{n})(i, 7);
torque2 = ARRANGEMENTS.(fields{n})(i, 15);
power1 = ARRANGEMENTS.(fields{n})(i, 8);
power2 = ARRANGEMENTS.(fields{n})(i, 16);
blade1 = ARRANGEMENTS.(fields{n})(i, 2);
blade2 = ARRANGEMENTS.(fields{n})(i, 10);
% Rotational Velocity Limitation to have Highest Rotational Velocities
if rpm_a <= (rot1 + rot2)
% Power Output Limitation
if power1 + power2 >= 0
k = k + 1;
Data = [ 2*size1 2*size2 20 dist 30 power1+power2 ];
% Create New Structure with LCOE Data for All Possible Combinations
FILTCONTRA.(fields{n})(k, 1:16) = ARRANGEMENTS.(fields{n})(i, 1:16);
FILTCONTRA.(fields{n})(k, 17) = rot1 + rot2;
FILTCONTRA.(fields{n})(k, 18) = abs((size1-size2)/max(size1, size2)) * 100;
FILTCONTRA.(fields{n})(k, 19) = abs((torque1-torque2)/torque1) * 100;
FILTCONTRA.(fields{n})(k, 20) = power1 + power2;
FILTCONTRA.(fields{n})(k, 21) = LCOE(Data);
if power1 + power2 >= limpow
comb = comb + 1;
POWER(comb,1) = power1 + power2;
ALLCOMB(comb,:) = FILTCONTRA.(fields{n})(k, :);
% Store in .txt File

```

```

comb_values = [num2cell(FILTCONTRA.(fields{n})(k, :))];
fprintf(fileID, '%2.1f\t\t\t %d\t\t %2.1f\t\t %2.1f\t\t %4.3f\t\t %5.3f\t ...
    %7.3f\t %6.3f\t\t %2.1f\t\t %d\t\t %2.1f\t\t %2.1f\t\t %4.3f\t\t ...
    %5.3f\t %7.3f\t %7.3f\t %5.3f\t %3.2f\t %3.2f\t\t %5.1f\t\t %5.1f\r\n', ...
    comb_values{1,:});
end end end end end
k = 0;
end
fclose(fileID);
%% Get Top 200 High Power - Low LCOE Configurations
SORT = sortrows(ALLCOMB, [21 -20] );
top200 = SORT((1 : 200), :);
fileID = fopen('TOP200_CONTRA_COMBINATIONS.txt', 'w');
fprintf(fileID, '%s\t %s\t ...
    %s\t %s\t %s\t %s\t %s\t %s\t %s\t %s\t\t %s\r\n', CONTRA_COMB{1,:});
for c = 1 : 200
top200_values = [num2cell(top200(c, :))];
fprintf(fileID, '%2.1f\t\t\t %d\t\t %2.1f\t\t %2.1f\t\t %4.3f\t\t %5.3f\t ...
    %7.3f\t %6.3f\t\t %2.1f\t\t %d\t\t %2.1f\t\t %2.1f\t\t %4.3f\t\t ...
    %5.3f\t %7.3f\t %7.3f\t %5.3f\t %3.2f\t %3.2f\t\t %5.1f\t\t %5.1f\r\n', ...
    top200_values{1,:});
end
fclose(fileID)

```

E.3 Single Rotor Turbines LCOE Calculation

This code calculates the $LCOE_{Ref}$ for 15 rotor diameters from the geometries modelled in [Chapter 4](#). The $LCOE_{Ref}$ variables used are detailed in [Section 6.4](#). The top 200 rotors with highest power are listed, and used in [Section 4.6](#) to select the most economically feasible SRT.

```

% Preamble
clear all
close all
clc
fold = 'I:\Geometry Variations - Recovery - BackUp\Geometry variations';
% Get Rotors' Performance Data
CleanData = csvread('DATA_clean.csv',1,0);

```

```

% Create Different Radii Rotors
Radius = [0.5 1 1.5 2 2.5 3 3.5 4 4.5 5 5.5 6 6.5 7 7.5];
Data = [10 10 20 5000 30]; % LCOE Variables
Time = Data(3); % Lifetime
Length = Data(4); % Distance from Shore in m
depth = Data(5); % Water Depth in m
PERC = 0.70; % Percentage of CAPEX from Rotor, Cable and Foundation - 70%
rate = 0.1; % Discount Rate
rho = 997; % Water density in kg/m^3
num = 45; % Number of rotors in array
vel = 1.2; % Water velocity in m/s
hours = 14; % Operation Hours
days = 365; % Days per year
k = 0;

% Text File Headers
SRT_DATA = {'#Blades' 'Blade' 'Solidity' 'Pitch' 'Radius' 'Lamda' ...
            'RotVel' 'Cp' 'Power' 'LCOE'};
fileID = fopen('SRT_LCOE.txt', 'w');
fprintf(fileID, '%s\t%s\t%s\t%s\t%s\t%s\t%s\t%s\t%s\t%s\t%s\r\n',...
        SRT_DATA{1,:});

% Allocating Matrices to Reduce Computational Time
SRTs = zeros(5146,6);
SRT_LCOE = zeros(5146,10);

% Calculating LCOE
for n = 1 : size(CleanData, 1)
for m = 1 : size(Radius, 2)
R = Radius(m);
omega = CleanData(n,6) * vel / R;
Pow = 0.5 * CleanData(n,7) * rho * R^2 * pi() * vel^3;
if Pow > 0
k = k + 1;
SRTs(k,:) = CleanData(n,[1:4 6 7]);
%% CAPEX Calculation
% Rotor
Cost_Rotor = 80.388 * (2*R)^(2.687) * num;
% Cable
Cost_Cable = 169.79 * Length;
% Foundation
Cost_Foundation = (0.1875 + 1.5e-5 * depth^3)*10^6;

```

```

end end

% Installation and Grid Connection
lambda = 1 / PERC; % 30 percent of the total cost of the CAPEX
CAPEX = (Cost_Rotor + Cost_Cable + Cost_Foundation) * lambda;
%% OPEX Calculation
TotPow = Pow * num;
OPEX = 310000 * TotPow / 1e6;
%% AEP Calculation
AEP = TotPow * hours * 365 / 1e6; % Annual Energy Production in MWh
%% LCOE Calculation
syms t
LCOE_top = CAPEX + double(symsum((OPEX) / (1 + rate)^t , t , 1 , Time));
LCOE_bottom = double(symsum( AEP / ((1 + rate)^t) , t , 1 , Time));
LCOE = LCOE_top / LCOE_bottom;
SRT_LCOE(k, :) = [SRTs(k, 1:4) R SRTs(k, 5) omega SRTs(k, 6) Pow/1000 LCOE];
comb_values = num2cell(SRT_LCOE(k, :));
fprintf(fileID, '%2.1f\t\t %2.1f\t %3.2f\t %2.1f\t\t %2.1f\t\t %3.2f\t\t ...
    %5.4f\t\t %5.4f\t\t %5.3f\t\t %7.4f\r\n', comb_values{1, :});
end end end

fclose(fileID);
%% Get Top 200 Hig Power - Low LCOE Configurations
SORT = sortrows(SRT_LCOE, [-9 10] );
top200 = SORT((1 : 200), :);
fileID = fopen('SRT_LCOE_Top200.txt', 'w');
fprintf(fileID, '%s\t %s\t %s\t %s\t %s\t %s\t %s\t %s\t %s\t %s\r\n', ...
    SRT_DATA{1, :});
for c = 1 : 200
comb_values = num2cell(top200(c, :));
fprintf(fileID, '%2.1f\t\t %2.1f\t %3.2f\t %2.1f\t\t %2.1f\t\t %3.2f\t\t ...
    %5.4f\t\t %5.4f\t\t %5.3f\t\t %7.4f\r\n', comb_values{1, :});
end
end

```

E.4 Contra-Rotating Rotors Turbines LCOE Calculation

This code calculates the $LCOE_{Ref}$ for all the technically feasible CRT combinations selected in [Section 5.3.3](#). The $LCOE_{Ref}$ variables used are detailed in [Section 6.4](#). The top 200 rotors with highest power are listed, and used in [Section 5.3.3](#) as a parameter to select the CRT to be modelled with CFD, as described in [Section 5.4](#).

```

function LCOE = LCOE(Data)
%% Variables
D1 = Data(1); % Rotor 1 Diameter in m
D2 = Data(2); % Rotor 2 Diameter in m
Time = Data(3); % Years of operation
Length = Data(4); % Distance from shore in m
depth = Data(5); % Water Depth in m
Pow = Data(6) * 1e3; % Power in MW
PERC = 0.70; % Percentage of CAPEX from Rotor, Cable and Foundation
rate = 0.1; % Discount Rate
rho = 997; % Water density in kg/m^3
num = 45; % Number of rotors in array
vel = 1.2; % Water Velocity in m/s
hours = 14; % Operation Hours
days = 365; % Days per year

%% CAPEX Calculation
% Rotors
Cost_Rotor1 = 80.388 * D1^(2.687);
Cost_Rotor2 = 80.388 * D2^(2.687);
Cost_Rotor = num * (Cost_Rotor1 + Cost_Rotor2); % Total Turbine Cost
% Cable
Cost_Cable = 169.79 * Length;
% Foundation
Cost_Foundation = (0.1875 + 1.5e-5 * depth^3)*10^6;
end end end

% Installation and Grid Connection
lambda = 1 / PERC; % 30 percent of the total cost of the CAPEX
CAPEX = (Cost_Rotor + Cost_Cable + Cost_Foundation) * lambda;

%% OPEX Calculation
TotPow = Pow * num;
OPEX = 310000 * TotPow / 1e6;

%% AEP Calculation
AEP = TotPow * hours * 365 / 1e6; % Annual Energy Production in MWh

%% LCOE Calculation
syms t
LCOE_top = CAPEX + double(symsum((OPEX) / (1 + rate)^t , t , 1 , Time));
LCOE_bottom = double(symsum( AEP / ((1 + rate)^t) , t , 1 , Time));
LCOE = LCOE_top / LCOE_bottom;
end

```


References

- ABB (2012). *ABB Brochure Generators for Wind Power*. Pamphlet. URL: <https://search-ext.abb.com/library/Download.aspx/?DocumentID=9AKK105649%5C&LanguageCode=en%5C&DocumentPartId=%5C&Action=Launch>.
- ACCIONA (2019). URL: <https://www.accionacom/climate-change/> (visited on 12/06/2019).
- Akimoto, H., K. Tanaka, J. C. Park and S. m. Jeong (2012). 'Conceptual Study of Tidal Stream and Ocean Current Turbine with Floating Axis Configuration'. In: *2012 Oceans - Yeosu*, pp. 1-4. DOI: [10.1109/OCEANS-Yeosu.2012.6263627](https://doi.org/10.1109/OCEANS-Yeosu.2012.6263627).
- Alcorn, R. and D. O'Sullivan (2013). *Electrical Design for Ocean Wave and Tidal Energy Systems*. The Institution of Engineering and Technology. ISBN: 1849195641.
- Aldersey-Williams, J. and T. Rubert (2019). 'Levelised Cost of Energy: A Theoretical Justification and Critical Assessment'. In: *Energy Policy* 124, pp. 169-179. ISSN: 0301-4215.
- Allan, G., M. Gilmartin, P. McGregor and K. Swales (2011). 'Levelised Costs of Wave and Tidal Energy in the UK: Cost Competitiveness and the Importance of "Banded" Renewables Obligation Certificates'. In: *Energy Policy* 39.1, pp. 23-39. ISSN: 0301-4215. DOI: <http://dx.doi.org/10.1016/j.enpol.2010.08.029>. URL: <http://www.sciencedirect.com/science/article/pii/S0301421510006440>.
- Amelio, M., S. Barbarelli, G. Florio, N.M. Scornaienchi, G. Minniti, A. Cutrupi and M. Sánchez-Blanco (2012). 'Innovative Tidal Turbine with Central Deflector for the Exploitation of River and Sea Currents in On-Shore Installations'. In: *Applied energy* 97, pp. 944-955. ISSN: 0306-2619.
- ANDRITZ HYDRO Hammerfest (2019). URL: www.andritzhydrohammerfest.co.uk (visited on 08/06/2019).
- ANSYS (2016a). *CFX Theory Guide*. Computer Program.
- (2016b). *ICEM CFD User Manual*. Computer Program.
- Aqua-RET Project (2012). URL: www.aquaret.com (visited on 12/06/2019).
- Aquaret Consortium (2008a). *A guide to Aquatic Renewable Energy Technologies - Offshore Wind*. Pamphlet.
- (2008b). *A guide to Aquatic Renewable Energy Technologies - Tidal Impoundment*. Pamphlet.
- (2008c). *A guide to Aquatic Renewable Energy Technologies - Wave*. Pamphlet.

- Argyll Tidal Ltd and Nautricity (Dec. 2013). *Environmental Appraisal for the Argyll Demonstrator Project*. Report.
- Astariz, S., A. Vazquez and G. Iglesias (2015). 'Evaluation and Comparison of the Levelized Cost of Tidal, Wave, and Offshore Wind Energy'. In: *Journal of Renewable and Sustainable Energy* 7.5, p. 053112. ISSN: 1941-7012.
- Bahaj, A.S (2011). 'Generating Electricity from the Oceans'. In: *Renewable and Sustainable Energy Reviews* 15.7, pp. 3399–3416. ISSN: 1364-0321.
- Bahaj, A.S., W.M.J. Batten and G. McCann (2007). 'Experimental Verifications of Numerical Predictions for the Hydrodynamic Performance of Horizontal Axis Marine Current Turbines'. In: *Renewable Energy* 32.15, pp. 2479–2490. ISSN: 0960-1481. DOI: <http://dx.doi.org/10.1016/j.renene.2007.10.001>. URL: <http://www.sciencedirect.com/science/article/pii/S0960148107002996>.
- Bakker, A. and ANSYS FLUENT (Mar. 2002). *Meshing*. Electronic Article.
- Barbarelli, S., M. Amelio, T. Castiglione, G. Florio, N.M. Scornaienchi, A. Cutrupi and G.L. Zupone (2014a). 'Analysis of the Equilibrium Conditions of a Double Rotor Turbine Prototype Designed for the Exploitation of the Tidal Currents'. In: *Energy conversion and management* 87, pp. 1124–1133. ISSN: 0196-8904.
- Barbarelli, S., M. Amelio, G. Florio, N. M. Scornaienchi, A. Cutrupi and G.L. Zupone (2014b). 'Transients Analysis of a Tidal Currents Self-Balancing Kinetic Turbine with On Shore Basement'. In: *Energy Procedia* 61, pp. 962–969. ISSN: 1876-6102.
- Barbarelli, S., T. Castiglione, G. Florio, N.M. Scornaienchi and G.L. Zupone (2016). 'Design and Numerical Analysis of a Double Rotor Turbine Prototype Operating in Tidal Currents'. In: *Energy Procedia* 101, pp. 1199–1206. ISSN: 1876-6102.
- Barbarelli, S., T. Castiglione, G.L. Zupone, S. Bova and J. Yan (2019). 'CFD Investigation of the Open Center on the Performance of a Tidal Current Turbine'. In: *Energy Procedia* 159, pp. 28–33. ISSN: 1876-6102.
- Barbarelli, S., G. Florio, M. Amelio, N.M. Scornaienchi, A. Cutrupi and G.L. Zupone (2014c). 'Design Procedure of an Innovative Turbine with Rotors Rotating in Opposite Directions For the Exploitation of the Tidal Currents'. In: *Energy* 77, pp. 254–264. ISSN: 0360-5442.
- Barbarelli, S., G. Florio, G.L. Zupone and N.M. Scornaienchi (2018). 'First Techno-Economic Evaluation of Array Configuration of Self-Balancing Tidal Kinetic Turbines'. In: *Renewable energy* 129, pp. 183–200. ISSN: 0960-1481.

- Batten, W.M.J., A.S. Bahaj, A.F. Molland and J.R. Chaplin (2006). 'Hydrodynamics of marine current turbines'. In: *Renewable Energy* 31.2, pp. 249–256. ISSN: 0960-1481. DOI: <http://dx.doi.org/10.1016/j.renene.2005.08.020>. URL: <http://www.sciencedirect.com/science/article/pii/S0960148105002314>.
- (2007). 'Experimentally Validated Numerical Method for the Hydrodynamic Design of Horizontal Axis Tidal Turbines'. In: *Ocean Engineering* 34.7, pp. 1013–1020. ISSN: 0029-8018. DOI: <http://dx.doi.org/10.1016/j.oceaneng.2006.04.008>. URL: <http://www.sciencedirect.com/science/article/pii/S0029801806001843>.
- (2008). 'The Prediction of the Hydrodynamic Performance of Marine Current Turbines'. In: *Renewable Energy* 33.5, pp. 1085–1096. ISSN: 0960-1481. DOI: <http://dx.doi.org/10.1016/j.renene.2007.05.043>. URL: <http://www.sciencedirect.com/science/article/pii/S0960148107002133>.
- Beam, M., B. Kline, B. Elbing, W. Straka, A. Fontaine, M. Lawson, Y. Li, R. Thresher and M. Previsic (2012). *Marine Hydrokinetic Turbine Power-Take-Off Design for Optimal Performance and Low Impact on Cost-of-Energy*. Report. National Renewable Energy Lab.(NREL), Golden, CO (United States).
- Belloni, C.S.K. (2013). 'Hydrodynamics of Ducted and Open-centre Tidal Turbines'. Thesis.
- Benelghali, S., M.E.H. Benbouzid and J.F. Charpentier (2012). 'Generator Systems for Marine Current Turbine Applications: A Comparative Study'. In: *IEEE Journal of Oceanic Engineering* 37.3, pp. 554–563. ISSN: 0364-9059.
- Bishop, J. (2012). *Project Selection Criteria*. URL: blog.thehigheredcio.com/project-selection-criteria (visited on 01/06/2019).
- Blue Energy Canada Inc (2019). URL: www.blueenergy.com (visited on 08/06/2019).
- Bluewater (2019). URL: <https://www.bluewater.com> (visited on 08/06/2019).
- Borthwick, A.G.L. (2016). 'Marine Renewable Energy Seascape'. In: *Engineering* 2.1, pp. 69–78. ISSN: 2095-8099.
- Bortolotti, P., D.S. Berry, R. Murray, E. Gaertner, D.S. Jenne, R.R. Damiani, G.E. Barter and K.L. Dykes (2019). *A Detailed Wind Turbine Blade Cost Model*. Report. National Renewable Energy Lab.(NREL), Golden, CO (United States).
- Brito e Melo, A. (Nov. 2013). *INFORME FINAL - Costa Rica - Determinación del Potencial de Energía Marina para Generación Eléctrica*. Report. WavEC.

- Bryden, I.G., C.R. Bullen, M.S. Baine and O. Paish (1995). 'An Assessment of Tidal Streams as Energy Sources in Orkney and Shetland'. In: *Underwater Technology-Journal of the Society for Underwater Technology* 21.2, pp. 21–29. ISSN: 0141-0814.
- Bryden, I.G., S. Naik, P. Fraenkel and C.R. Bullen (1998). 'Matching Tidal Current Plants to Local Flow Conditions'. In: *Energy* 23.9, pp. 699–709. ISSN: 0360-5442.
- Burton, T., N. Jenkins, D. Sharpe and E. Bossanyi (2011). 'Wind Energy Handbook'. In: DOI: [10.1002/9781119992714](https://doi.org/10.1002/9781119992714).
- Bywaters, G., V. John, J. Lynch, P. Mattila, G. Norton, J. Stowell, M. Salata, O. Labath, A. Chertok and D. Hablanian (2004). 'Northern Power Systems WindPACT Drive Train Alternative Design Study Report'. In: *NREL, Golden, Colorado, Report no. NREL/SR-500-35524*.
- CAELULUM and Aquatera (2017). *Wave & Tidal Energy: State of the Industry*. Report.
- Cambridge University Press (2019). *English Dictionary*. URL: <https://dictionary.cambridge.org/dictionary/english>.
- Carbon Trust and Entec (May 2006). *Cost Estimation Methodology*. Report. Carbon Trust.
- Carbon Trust Marine Energy Accelerator (July 2011). *Accelerating Marine Energy*. Report. Carbon Trust.
- Carroll, J., A. McDonald, I. Dinwoodie, D. McMillan, M. Revie and I. Lazakis (2017). 'Availability, Operation and Maintenance Costs of Offshore Wind Turbines with Different Drive Train Configurations'. In: *Wind Energy* 20.2, pp. 361–378. ISSN: 1095-4244.
- CFIA (2014). *Manual de Subclasificación de Proyectos de Construcción*. Government Document.
- Chen, F. (2010). 'Kuroshio Power Plant Development Plan'. In: *Renewable and Sustainable Energy Reviews* 14.9, pp. 2655–2668. ISSN: 1364-0321.
- (2013). *The Kuroshio Power Plant*. Vol. 225. Springer.
- Clarke, J.A., G. Connor, A. Grant, C. Johnstone and S.E. Ordonez-Sanchez (2008a). 'Contra-Rotating Marine Current Turbines: Performance in Field Trials and Power Train Developments'. In: *10th World Renewable Energy Congress*.
- (2009a). 'Contra-Rotating Marine Current Turbines: Single Point Tethered Floating System-Stability and Performance'. In: *8th European Wave and Tidal Energy Conference, EWTEC*.
- Clarke, J.A., G. Connor, A.D. Grant, C. Johnstone and S.E. Ordonez-Sanchez (2008b). 'A Contra-Rotating Marine Current Turbine on a Flexible Mooring: Development of a Scaled Prototype'. In: *Proceedings of the 2nd International Conference on Ocean Energy*. Vol. 15, p. 17.

- Clarke, J.A., G. Connor, A.D. Grant and C.M. Johnstone (2007a). 'Design and Testing of a Contra-Rotating Tidal Current Turbine'. In: *Proceedings of the Institution of Mechanical Engineers, Part A: Journal of Power and Energy* 221.2, pp. 171–179. ISSN: 0957-6509.
- Clarke, J.A., G. Connor, A.D. Grant, C.M. Johnstone and D. Mackenzie (2007b). 'Development of a Contra-Rotating Tidal Current Turbine and Analysis of Performance'. In: ISSN: 9899507938.
- Clarke, J.A., G. Connor, A.D. Grant, C.M. Johnstone and S. Ordonez-Sanchez (2010). 'Analysis of a Single point Tensioned Mooring System for Station keeping of a Contra-Rotating Marine Current Turbine'. In: *IET Renewable Power Generation* 4.6, pp. 473–487. ISSN: 1752-1424.
- Clarke, J.A., A. Grant, G. Connor and C. Johnstone (2009b). 'Development and In-Sea Performance Testing of a Single Point Mooring Supported Contra-Rotating Tidal Turbine'. In: *ASME 2009 28th International Conference on Ocean, Offshore and Arctic Engineering*. American Society of Mechanical Engineers, pp. 1065–1073.
- Coin Newa Media Group LLC (2020). URL: <https://www.usinflationcalculator.com/> (visited on 14/01/2020).
- Consul, C.A., R.H.J. Willden, E. Ferrer and M.D. McCulloch (2009). 'Influence of Solidity on the Performance of a Cross-Flow Turbine'. In: *Proceedings of the 8th European Wave and Tidal Energy Conference., Uppsala, Sweden*.
- Copping, A.E. and S.H. Geerlofs (2011). *The Contribution of Environmental Siting and Permitting Requirements to the Cost of Energy for Marine Hydrokinetic Devices; Reference Models #1, #2 and #3*. Report. Sandia National Lab.(SNL-NM).
- Copping, A.E., L.A. Hanna and S.H. Geerlofs (2013). *The Contribution of Environmental Siting and Permitting Requirements to the Cost of Energy for Marine Hydrokinetic Devices; Reference Models #4*. Report. Sandia National Lab.(SNL-NM).
- Costa Rica Limpia (2016). *Consulta Ciudadana sobre Energias Limpias*. Report.
- Cresswell, N.W., G.L. Ingram and R.G. Dominy (2015). 'The Impact of Diffuser Augmentation on a Tidal Stream Turbine'. In: *Ocean Engineering* 108, pp. 155–163. ISSN: 0029-8018.
- Culley, D.M., S.W. Funke, S.C. Kramer and M.D. Piggott (2016). 'Integration of Cost Modelling within the Micro-Siting Design Optimisation of Tidal Turbine Arrays'. In: *Renewable Energy* 85, pp. 215–227. ISSN: 0960-1481.
- Dalton, G., G. Allan, N. Beaumont, A. Georgakaki, N. Hacking, T. Hooper, S. Kerr, A.M. O'Hagan, K. Reilly and P. Ricci (2015). 'Economic and Socio-Economic Assessment Methods for Ocean

- Renewable Energy: Public and Private Perspectives'. In: *Renewable and Sustainable Energy Reviews* 45, pp. 850–878. ISSN: 1364-0321.
- Danish Energy Agency (May 2018). *The Danish Levelized Cost of Energy Calculator*. Report.
- DBEIS (2011). *Applying for Safety Zones Around Offshore Renewable Energy Installation - Guidance Notes*. Legal Rule or Regulation.
- (Nov. 2016). *Electricity Generation Costs*. Government Document.
 - (2018). *UK Energy in Brief*. Report.
- De Andres, A., A. MacGillivray, R. Cuanche and H. Jeffrey (2014). 'Factors Affecting LCOE of Ocean Energy Technologies: a Study of Technology and Deployment Attractiveness'. In: *Proceedings of the International Conference on Ocean Energy, Halifax, NS, Canada*, pp. 4–6.
- Draper, S. and T. Nishino (2014). 'Centred and Staggered Arrangements of Tidal Turbines'. In: *Journal of Fluid Mechanics* 739, pp. 72–93. ISSN: 0022-1120.
- Duquette, M.M., J. Swanson and K.D. Visser (2003). 'Solidity and Blade Number Effects on a Fixed Pitch, 50 W Horizontal Axis Wind Turbine'. In: *Wind Engineering* 27.4, pp. 299–316. ISSN: 0309-524X. DOI: [10.1260/030952403322665271](https://doi.org/10.1260/030952403322665271).
- Ebdon, T., D.M. O'Doherty, T. O'Doherty and A. Mason-Jones (2016). 'Simulating Marine Current Turbine Wakes Using Advanced Turbulence Models'. In: *Asian Wave and Tidal Energy Conference 2016*.
- (2017). 'Modelling the Effect of Turbulence Length Scale on Tidal Turbine Wakes Using Advanced Turbulence Models'. In: *European Wave and Tidal Energy Conference 2017*.
- Eboibi, O., L.A.M. Danao and R.J. Howell (2016). 'Experimental Investigation of the Influence of Solidity on the Performance and Flow Field Aerodynamics of Vertical Axis Wind Turbines at Low Reynolds Numbers'. In: *Renewable energy* 92, pp. 474–483. ISSN: 0960-1481.
- Edmunds, M., R. Malki, A.J. Williams, I. Masters and T.N. Croft (2014). 'Aspects of Tidal Stream Turbine Modelling in the Natural Environment Using a Coupled BEM–CFD Model'. In: *International Journal of Marine Energy* 7, pp. 20–42. ISSN: 2214-1669.
- Edmunds, M., A.J. Williams and I. Masters (2017a). 'Power Shedding from Stall and Pitch Controlled Tidal Stream Turbines'. In: *European Wave and Tidal Energy Conference 2017*.
- Edmunds, M., A.J. Williams, I. Masters and T.N. Croft (2017b). 'An Enhanced Disk Averaged CFD Model for the Simulation of Horizontal Axis Tidal Turbines'. In: *Renewable energy* 101, pp. 67–81. ISSN: 0960-1481.

- Edmunds, M., A.J. Williams, I. Masters, A. Vinod, A. Lawrence and A. Banerjee (2017c). 'Aspects of Small Scale Flume Correlation with a BEM-CFD Model'. In: *European Wave and Tidal Energy Conference 2017*.
- Egarr, D.A., T. O'Doherty, S. Morris and R.G. Ayre (2004). 'Feasibility Study Using Computational Fluid Dynamics for the Use of a Turbine for Extracting Energy from the Tide'. In: *15th Australasian Fluid Mechanics Conference, The University of Sydney, Sydney, Australia*.
- Egarr, D.A., T. O'Doherty, S. Morris, N. Syred and R.G. Ayre (2005). 'Computational Study of Tidal Turbines for Extracting Energy from the Tides'. In: *International Symposium on EcoTopia Science*.
- Elbatran, A.H., O. Yaakob, Y. Ahmed and F. Abdallah (2016). 'Augmented Diffuser for Horizontal Axis Marine Current Turbine'. In: *International Journal of Power Electronics and Drive Systems (IJPEDS) 7.1*. ISSN: 2088-8694.
- Eriksson, S., H. Bernhoff and M. Leijon (2008). 'Evaluation of Different Turbine Concepts for Wind Power'. In: *renewable and sustainable energy reviews 12.5*, pp. 1419–1434. ISSN: 1364-0321.
- Ernst & Young (Oct. 2010). *Cost of and Financial Support for Wave, Tidal Stream and Tidal Range Generation in the UK*. Report. Ernst & Young.
- ESMAP (2018). URL: <https://trackingsdg7.esmap.org> (visited on 12/06/2019).
- (2019). *Tracking SDG7: The Energy Progress Report 2019*. Report. World Bank.
- Esri (2018). *Datos de Transmisión 2018-Subestaciones 2018*. URL: https://www.arcgis.com/home/webmap/viewer.html?panel=gallery%5C&suggestField=true%5C&url=https%5C%3A%5C%2F%5C%2Fservices1.arcgis.com%5C%2FcW2Gf04rBCLoFwgj%5C%2Farcgis%5C%2Frest%5C%2Fservices%5C%2FDatos_Transmission_2018%5C%2FFeatureServer%5C%2F0.
- Fingersh, L., M. Hand and A. Laxson (2006). *Wind Turbine Design Cost and Scaling Model*. Report. National Renewable Energy Lab.(NREL).
- Fleming, C.F. and R.H.J. Willden (2016). 'Analysis of Bi-Directional Ducted Tidal Turbine Performance'. In: *International Journal of Marine Energy 16*, pp. 162–173. ISSN: 2214-1669. DOI: <http://dx.doi.org/10.1016/j.ijome.2016.07.003>. URL: <http://www.sciencedirect.com/science/article/pii/S2214166916300480>.
- Flumill (2014). *Flumill: Fra Sterke Maritime tradisjoner Via Olje og Gass til Ledende Fornybar Teknologi*. Pamphlet. URL: https://www.vaf.no/media/5242376/9_Flumill-fra-

sterke - maritime - tradisjoner - via - olje - og - gass - til - ledende - fornybar - teknologi .pdf.

- Foster, J., L. Wagner and A. Bratanova (2014). 'LCOE Models: A Comparison of the Theoretical Frameworks and Key Assumptions'. In:
- Fraenkel, P. (2014). 'Energy from Tidal Streams: Engineering Issues, State of the Art and Future Prospects'. In: *Underwater Technology* 32.1, pp. 27-37. DOI: [10.3723/ut.32.027](https://doi.org/10.3723/ut.32.027). URL: <http://www.ingentaconnect.com/content/sut/unwt/2014/00000032/00000001/art00004%20http://dx.doi.org/10.3723/ut.32.027>.
- Frost, C. (2016). 'Flow Direction Effects On Tidal Stream Turbines'. Thesis.
- Frost, C., P.S. Evans, M.J. Harrold, A. Mason-Jones, T. O'Doherty and D.M. O'Doherty (2017). 'The Impact of Axial Flow Misalignment on a Tidal Turbine'. In: *Renewable Energy* 113, pp. 1333-1344. ISSN: 0960-1481.
- Frost, C., P.S. Evans, C.E. Morris, A. Mason-Jones, D.M. O'Doherty and T. O'Doherty (2015). 'Flow Misalignment and Tidal Stream Turbines'. In: *European Wave and Tidal Energy Conference 2015*, 09B2-5-1 to 09B2-5-6.
- Funami, Y., Y. Nakanishi, N.J. Lee, B. Huang and T. Kanemoto (2017). 'Counter-Rotating Type Horizontal-Axis Bidirectional Propellers for Tidal Stream Power Unit'. In: *Journal of Power and Energy Engineering* 5.07, p. 34.
- Galal, A.M. and T. Kanemoto (2008). 'Field Tests of Wind Turbine Unit with Tandem Wind Rotors and Double Rotational Armatures'. In: *Journal of Fluid Science and Technology* 3.3, pp. 359-369. ISSN: 1880-5558.
- Gifford, J.S. and R.C. Grace (2013). *CREST - Cost of Renewable Energy Spreadsheet Tool: A Model for Developing Cost-Based Incentives in the United States*. Report. National Renewable Energy Lab.(NREL).
- Gobierno de Costa Rica (2016). *Manual de Instrumentos Técnicos para el Proceso de Evaluación de Impacto Ambiental - Parte IV*. Legal Rule or Regulation.
- Gorle, J.M.R., L. Chatellier, F. Pons and M. Ba (2016). 'Flow and Performance Analysis of H-Darrieus Hydroturbine in a Confined Flow: A Computational and Experimental Study'. In: *Journal of Fluids and Structures* 66, pp. 382-402. ISSN: 0889-9746. DOI: <http://dx.doi.org/10.1016/j.jfluidstructs.2016.08.003>. URL: [//www.sciencedirect.com/science/article/pii/S0889974616301281](http://www.sciencedirect.com/science/article/pii/S0889974616301281).

- Goundar, J.N. and M.R Ahmed (2013). 'Design of a Horizontal Axis Tidal Current Turbine'. In: *Applied Energy* 111, pp. 161–174. ISSN: 0306-2619. DOI: <http://dx.doi.org/10.1016/j.apenergy.2013.04.064>. URL: <http://www.sciencedirect.com/science/article/pii/S0306261913003607>.
- Greaves, Deborah and Gregorio Iglesias (2018). *Wave and tidal energy*. John Wiley & Sons. ISBN: 1119014476.
- Griffin, D.A. (2001). *Windpact Turbine Design Scaling Studies Technical Area 1-Composite Blades for 80- to 120-meter Rotor*. Report. National Renewable Energy Lab., Golden, CO (US).
- Hardisty, J. (2009). 'The Analysis of Tidal Stream Power'. In: DOI: [10.1002/9780470743119](https://doi.org/10.1002/9780470743119).
- Hau, E. and H. Von Renouard (2006). *Wind Turbines: Fundamentals, Technologies, Application, Economics*. 2nd edition. Berlin, Heidelberg: Springer Berlin Heidelberg. DOI: [10.1007/3-540-29284-5](https://doi.org/10.1007/3-540-29284-5).
- Hernandez-Madrigal, T., A. Mason-Jones, T. O'Doherty and D.M. O'Doherty (2017). 'The Effect of Solidity on a Tidal Turbine in Low Speed Flow'. In: *European Wave and Tidal Energy Conference 2017*.
- Hernandez-Madrigal, T., S. Wright-Green, A. Mason-Jones, T. O'Doherty, D.M. O'Doherty and C.M. Johnstone (2016). 'Marine Energy in Costa Rica: Development Procedures Compared to the UK'. In: *Asian Wave and Tidal Energy Conference 2016*.
- Houghton, E.L. and P.W. Carpenter (2003). *Aerodynamics for engineering students*. Elsevier. ISBN: 0080493858.
- Huang, B. and T. Kanemoto (2015a). 'Multi-Objective Numerical Optimization of the Front Blade Pitch Angle Distribution in a Counter-Rotating Type Horizontal-Axis Tidal Turbine'. In: *Renewable Energy* 81, pp. 837–844. ISSN: 0960-1481.
- (2015b). 'Numerical Simulation for Cavitation Around Horizontal-Axis Counter-Rotating Type Propellers in a Tidal Stream Power Unit (In Preparation for Suppressing Cavitation)'. In: *The Twenty-fifth International Ocean and Polar Engineering Conference*. International Society of Offshore and Polar Engineers. ISBN: 1880653893.
- (2015c). 'Performance and Internal Flow of a Counter-Rotating Type Tidal Stream Turbine'. In: *Journal of Thermal Science* 24.5, pp. 410–416. ISSN: 1003-2169.
- Huang, B., Y. Nakanishi and T. Kanemoto (2016a). 'Numerical and Experimental Analysis of a Counter-Rotating Type Horizontal-Axis Tidal Turbine'. In: *Journal of Mechanical Science and Technology* 30.2, pp. 499–505. ISSN: 1738-494X.

- Huang, B., Y. Usui, K. Takaki and T. Kanemoto (2016b). 'Optimization of Blade Setting Angles of a Counter-Rotating Type Horizontal-Axis Tidal Turbine using Response Surface Methodology and Experimental Validation'. In: *International Journal of Energy Research* 40.5, pp. 610–617. ISSN: 0363-907X.
- Huang, B., K. Yoshida and T. Kanemoto (2016c). 'Development of a Model Counter-Rotating Type Horizontal-Axis Tidal Turbine'. In: *IOP Conference Series: Materials Science and Engineering*. Vol. 129. IOP Publishing, p. 012057. ISBN: 1757-899X.
- Huang, B., G.J. Zhu and T. Kanemoto (2016d). 'Design and Performance Enhancement of a Bi-Directional Counter-Rotating Type Horizontal Axis Tidal Turbine'. In: *Ocean Engineering* 128, pp. 116–123. ISSN: 0029-8018. DOI: <http://dx.doi.org/10.1016/j.oceaneng.2016.10.012>. URL: [//www.sciencedirect.com/science/article/pii/S0029801816304462](http://www.sciencedirect.com/science/article/pii/S0029801816304462).
- Hyun, B.S., D.H. Choi, J.S. Han and J.Y. Jin (2012). 'Performance analysis and design of vertical axis tidal stream turbine'. In: *Journal of Shipping and Ocean Engineering* 2.4, p. 191. ISSN: 2159-5879.
- Instituto Costarricense de Electricidad (May 2017). *Plan de Expansión de la Generación Eléctrica 2016 – 2035*. Report. ICE.
- International Energy Agency and Nuclear Energy Agency (2015). *Projected Costs of Generating Electricity; 2015 Edition*. Report.
- Ioannou, A., A. Angus and F. Brennan (2017). 'Stochastic Prediction of Offshore Wind Farm LCOE through an Integrated Cost Model'. In: *Energy Procedia* 107, pp. 383–389. ISSN: 1876-6102.
- IPCC (2012). *Renewable Sources and Climate Change Mitigation*. Report.
- IRENA (2012). *Renewable Energy Technology: Cost Analysis Series - Wind Power*. Report.
- (2014). *Tidal Energy Technology Brief*. Report.
- (2018). URL: <https://www.irena.org/ocean/> (visited on 12/06/2019).
- (2019). *Global Energy Transformation*. Report.
- Jamieson, P. (2011). *Innovation in Wind Turbine Design*. Wiley. ISBN: 9780470699812. URL: <https://books.google.co.uk/books?id=qCAwt6Tgga4C>.
- Jo, C.H., J.H. Lee, Y.H. Rho and K.H. Lee (2014). 'Performance Analysis of a HAT Tidal Current Turbine and Wake Flow Characteristics'. In: *Renewable Energy* 65, pp. 175–182. ISSN: 0960-1481. DOI: <http://dx.doi.org/10.1016/j.renene.2013.08.027>. URL: <http://www.sciencedirect.com/science/article/pii/S0960148113004291>.

- Johnson, K., S. Kerr and J. Side (2013). 'Marine Renewables and Coastal Communities—Experiences from the Offshore Oil Industry in the 1970s and their Relevance to Marine Renewables in the 2010s'. In: *Marine Policy* 38, pp. 491–499. ISSN: 0308-597X. DOI: <http://dx.doi.org/10.1016/j.marpol.2012.08.004>. URL: <http://www.sciencedirect.com/science/article/pii/S0308597X12001716>.
- Johnstone, C.M., D. Pratt, J.A. Clarke and A.D. Grant (2013). 'A Techno-Economic Analysis of Tidal Energy Technology'. In: *Renewable Energy* 49, pp. 101–106. ISSN: 0960-1481.
- Jung, H., T. Kanemoto and P. Liu (2017). 'A Numerical Prediction of Tip Vortices from Tandem Propellers in the Counter-Rotating Type Tidal Stream Power Unit'. In: *Journal of Power and Energy Engineering* 5.12, p. 66.
- Jung, H., T. Kanemoto, P. Liu and T. Murakami (2019). 'A Numerical Study on Performance Improvement of Counter-Rotating Type Tidal Stream Power Unit'. In: *IOP Conference Series: Earth and Environmental Science*. Vol. 240. IOP Publishing, p. 052013. ISBN: 1755-1315.
- Kanemoto, T. and K. Kubo (2010a). 'Intelligent Wind Power Unit with Tandem Wind Rotors'. In: *Wind Power Generation and Wind Turbine Design*. WIT Press, pp. 333–361.
- Kanemoto, T. and T. Suzuki (2010b). 'Counter Rotating Type Hydroelectric Unit Suitable for Tidal Power Station'. In: *IOP Conference Series: Earth and Environmental Science*. Vol. 12. IOP Publishing, p. 012111. ISBN: 1755-1315.
- Kanemoto, T., D. Tanaka, T. Kashiwabara, M. Uno and M. Nemoto (2000). 'Counter-Rotating Type Machine Suitable for Tidal Current Power Generation'. In: *The Tenth International Offshore and Polar Engineering Conference*. International Society of Offshore and Polar Engineers.
- Kawashima, R., T. Kanemoto, I. Samura and K. Kuwano (2017). 'Power Generation by Counter-Rotating Type Tidal Stream Power Unit'. In: *The 27th International Ocean and Polar Engineering Conference*. International Society of Offshore and Polar Engineers. ISBN: 1880653974.
- Kepler Energy (2013). URL: keplerenergy.co.uk (visited on 08/06/2019).
- Kerr, S., K. Johnson and J. C. Side (2014). 'Planning at the Edge: Integrating Across the Land Sea Divide'. In: *Marine Policy* 47, pp. 118–125. ISSN: 0308-597X. DOI: <http://dx.doi.org/10.1016/j.marpol.2014.01.023>. URL: <http://www.sciencedirect.com/science/article/pii/S0308597X14000396>.
- Keysan, O., A. McDonald, M. Mueller, R. Doherty and M. Hamilton (2010). 'C-GEN, a Lightweight Direct Drive Generator for Marine Energy Converters'. In:

- Keysan, O., A.S. McDonald and M. Mueller (2011). 'A Direct Drive Permanent Magnet Generator Design for a Tidal Current Turbine (SeaGen)'. In: *2011 IEEE International Electric Machines & Drives Conference (IEMDC)*. IEEE, pp. 224–229. ISBN: 1457700611.
- Kim, I.C., N.J. Lee, J. Wata, B.S. Hyun and Y.H. Lee (2016). 'Experiments on the Magnetic Coupling in a Small Scale Counter Rotating Marine Current Turbine'. In: *IOP Conference Series: Materials Science and Engineering*. Vol. 129. IOP Publishing, p. 012047. ISBN: 1757-899X.
- Kinsey, T. and G. Dumas (2010). 'Testing and Analysis of an Oscillating Hydrofoils Turbine Concept'. In: *ASME 2010 3rd Joint US-European Fluids Engineering Summer Meeting collocated with 8th International Conference on Nanochannels, Microchannels, and Minichannels*. American Society of Mechanical Engineers, pp. 9–22.
- Kirke, B. and L. Lazauskas (2008). 'Variable Pitch Darrieus Water Turbines'. In: *Journal of Fluid Science and Technology* 3.3, pp. 430–438. ISSN: 1880-5558.
- Kubo, K., Y. Hano, H. Mitarai, K. Hirano, T. Kanemoto and A.M. Galal (2010). 'Intelligent Wind Turbine Unit with Tandem Rotors (Discussion of Prototype Performances in Field Tests)'. In: *Current Applied Physics* 10.2, S326–S331. ISSN: 1567-1739.
- Kubo, K. and T. Kanemoto (2008). 'Development of Intelligent Wind Turbine Unit with Tandem Wind Rotors and Double Rotational Armatures'. In: *Journal of Fluid Science and Technology* 3.3, pp. 370–378. ISSN: 1880-5558.
- LaBonte, A., P. O'Connor, C. Fitzpatrick, K. Hallett and Y. Li (2013). 'Standardized Cost and Performance Reporting for Marine and Hydrokinetic Technologies'. In: *Proceedings of the 1st Marine Energy Technology Symposium (METS13), Washington, DC, USA*, pp. 10–11.
- Lam, W.H. and A. Bhatia (2013). 'Folding Tidal Turbine as an Innovative Concept Toward the new era of Turbines'. In: *Renewable and Sustainable Energy Reviews* 28, pp. 463–473. ISSN: 1364-0321.
- Laurens, J.M., M. Ait-Mohammed and M. Tarfaoui (2016). 'Design of Bare and Ducted Axial Marine Current Turbines'. In: *Renewable Energy* 89, pp. 181–187. ISSN: 0960-1481. DOI: <http://dx.doi.org/10.1016/j.renene.2015.11.075>. URL: <http://www.sciencedirect.com/science/article/pii/S0960148115304912>.
- Laws, N.D. and B.P. Epps (2016). 'Hydrokinetic Energy Conversion: Technology, Research, and Outlook'. In: *Renewable and Sustainable Energy Reviews* 57, pp. 1245–1259. ISSN: 1364-0321.
- Lee, J.H., S. Park, D.H. Kim, S.H. Rhee and M.C. Kim (2012). 'Computational Methods for Performance Analysis of Horizontal Axis Tidal Stream Turbines'. In: *Applied Energy* 98, pp. 512–523.

- ISSN: 0306-2619. DOI: <http://dx.doi.org/10.1016/j.apenergy.2012.04.018>. URL: <http://www.sciencedirect.com/science/article/pii/S0306261912003042>.
- Lee, N.J., M. Inagaki and T. Kanemoto (2019). 'Performance of Counter-Rotating Tandem Propellers at Oblique Flow Conditions'. In: *IOP Conference Series: Earth and Environmental Science*. Vol. 240. IOP Publishing, p. 052004. ISBN: 1755-1315.
- Lee, N.J., I.C. Kim, C.G. Kim, B.S. Hyun and Y.H. Lee (2015). 'Performance Study on a Counter-Rotating Tidal Current Turbine by CFD and Model Experimentation'. In: *Renewable Energy* 79, pp. 122–126. ISSN: 0960-1481. DOI: <http://dx.doi.org/10.1016/j.renene.2014.11.022>. URL: <http://www.sciencedirect.com/science/article/pii/S096014811400737X>.
- Li, H. and Z. Chen (2008). 'Design optimization and Evaluation of Different Wind Generator Systems'. In: *2008 International Conference on Electrical Machines and Systems*. IEEE, pp. 2396–2401. ISBN: 1424438268.
- Li, Y., B.J. Lence and S.M. Calisal (2011). 'An Integrated Model for Estimating Energy Cost of a Tidal Current Turbine Farm'. In: *Energy Conversion and Management* 52.3, pp. 1677–1687. ISSN: 0196-8904.
- Liu, H.W., H.B. Zhou, Y.G. Lin, W. Li and H.G. Gu (2016). 'Design and Test of 1/5th Scale Horizontal Axis Tidal Current Turbine'. In: *China Ocean Engineering* 30.3, pp. 407–420. ISSN: 2191-8945. DOI: [10.1007/s13344-016-0027-5](http://dx.doi.org/10.1007/s13344-016-0027-5). URL: <http://dx.doi.org/10.1007/s13344-016-0027-5>.
- Liu, P. and N. Bose (2012). 'Prototyping a Series of Bi-Directional Horizontal Axis Tidal Turbines for Optimum Energy Conversion'. In: *Applied Energy* 99, pp. 50–66. ISSN: 0306-2619. DOI: <http://dx.doi.org/10.1016/j.apenergy.2012.04.042>. URL: <http://www.sciencedirect.com/science/article/pii/S030626191200339X>.
- Liu, P., N. Bose, R. Frost, G. Macfarlane, T. Lilienthal, I. Penesis, F. Windsor and G. Thomas (2014). 'Model Testing of a Series of Bi-Directional Tidal Turbine Rotors'. In: *Energy* 67, pp. 397–410. ISSN: 0360-5442. DOI: <https://doi.org/10.1016/j.energy.2013.12.058>. URL: <http://www.sciencedirect.com/science/article/pii/S0360544213011286>.
- Liu, P., H. Jung, T. Murakami and T. Kanemoto (2018). 'Scale Effect and Undersea Noise of Counter-Rotating Propellers Installed in Tidal Stream Power Unit'. In: *IOP Conference Series: Earth and Environmental Science*. Vol. 163. IOP Publishing, p. 012043. ISBN: 1755-1315.

- Logan, J., C. Marcy, J. McCall, F. Flores-Espino, A. Bloom, J. Aabakken, W. Cole, T. Jenkin, G. Porro, C. Liu, F. Ganda, R. Boardman, T. Tarka, J. Brewer and T. Schultz (Jan. 2017). *Electricity Generation Baseline Report*. Report. National Renewable Energies Laboratory.
- López, A., J.L. Morán, L.R. Núñez and J.A. Somolinos (2020). 'Study of a Cost Model of Tidal Energy Farms in Early Design Phases with Parametrization and Numerical Values. Application to a Second-Generation Device'. In: *Renewable and Sustainable Energy Reviews* 117, p. 109497. ISSN: 1364-0321.
- Luquet, R., D. Bellevre, D. Fréchou, P. Perdon and P. Guinard (2013). 'Design and Model Testing of an Optimized Ducted Marine Current Turbine'. In: *International Journal of Marine Energy* 2, pp. 61–80. ISSN: 2214-1669. DOI: <http://dx.doi.org/10.1016/j.ijome.2013.05.009>. URL: <http://www.sciencedirect.com/science/article/pii/S2214166913000106>.
- MacGillivray, A., H. Jeffrey, M. Winskel and I. Bryden (2014). 'Innovation and Cost Reduction for Marine Renewable Energy: A Learning Investment Sensitivity Analysis'. In: *Technological Forecasting and Social Change* 87, pp. 108–124. ISSN: 0040-1625.
- Magagna, D. and A. Uihlein (2015). 'Ocean Energy Development in Europe: Current Status and Future Perspectives'. In: *International Journal of Marine Energy* 11, pp. 84–104. ISSN: 2214-1669.
- Malcolm, D.J. and A.C. Hansen (2003). *WindPACT Turbine Rotor Design, Specific Rating Study*. Report. National Renewable Energy Lab.(NREL).
- (2006). *WindPACT Turbine Rotor Design Study*. Report. National Renewable Energy Lab.(NREL).
- Manwell, J.F. (2009). *Wind Energy Explained Theory, Design and Application*. 2nd ed. Chichester, New York: Chichester : John Wiley.
- Marine Energy Research and Innovation Center (Nov. 2018). *Energías Marinas, Estudio de Costo Nivelado de Energía en Chile, Análisis de la Cadena de Suministro*. Report. MERIC.
- Mason-Jones, A. (2010). 'Performance Assessment of a Horizontal Axis Tidal Turbine in a High Velocity Shear Environment'. Thesis.
- Mason-Jones, A., D.M. O'Doherty, C.E. Morris, T. O'Doherty, C.B. Byrne, P.W. Prickett, R.I. Grosvenor, I. Owen, S. Tedds and R.J. Poole (2012). 'Non-dimensional Scaling of Tidal Stream Turbines'. In: *Energy* 44.1, pp. 820–829. ISSN: 0360-5442. DOI: <http://dx.doi.org/10.1016/j.energy.2012.05.010>. URL: <http://www.sciencedirect.com/science/article/pii/S0360544212003891>.

- Masters, I., R. Malki, A.J. Williams and T.N. Croft (2013). 'The Influence of Flow Acceleration on Tidal Stream Turbine Wake Dynamics: A Numerical Study Using a Coupled BEM-CFD Model'. In: *Applied Mathematical Modelling* 37.16–17, pp. 7905–7918. ISSN: 0307-904X. DOI: <http://dx.doi.org/10.1016/j.apm.2013.06.004>. URL: <http://www.sciencedirect.com/science/article/pii/S0307904X13003880>.
- May-Grosser, S. (2020). URL: <https://delfino.cr/2020/01/costa-rica-se-estanca-en-indice-de-percepcion-de-la-corrupcion> (visited on 18/02/2020).
- McAdam, R.A., G.T. Hously and M.L.G. Oldfield (2013). 'Experimental Measurements of the Hydrodynamic Performance and Structural Loading of the Transverse Horizontal Axis Water Turbine: Part 1'. In: *Renewable energy* 59, pp. 105–114. ISSN: 0960-1481.
- Minesto AB (2019). URL: <https://minesto.com> (visited on 08/06/2019).
- Mohamed, M. H. (2013). 'Impacts of Solidity and Hybrid System in Small Wind Turbines Performance'. In: *Energy* 57, pp. 495–504. ISSN: 0360-5442. DOI: <https://doi.org/10.1016/j.energy.2013.06.004>. URL: <http://www.sciencedirect.com/science/article/pii/S0360544213005021>.
- Morris, C.E. (2014). 'Influence of Solidity on the Performance, Swirl Characteristics, Wake Recovery and Blade Deflection of a Horizontal Axis Tidal Turbine'. Thesis.
- Morris, C.E., A. Mason-Jones, D.M. O'Doherty and T. O'Doherty (2015). 'The Influence of Solidity on the Performance Characteristics of a Tidal Stream Turbine'. In: *European Wave and Tidal Energy Conference 2015*, 09B2-3-1 to 09B2-3-7.
- Morris, C.E., D.M. O'Doherty, T. O'Doherty and A. Mason-Jones (2016a). 'Kinetic Energy Extraction of a Tidal Stream Turbine and its Sensitivity to Structural Stiffness Attenuation'. In: *Renewable energy* 88, pp. 30–39. ISSN: 0960-1481.
- Morris, C.E., D.M. O'Doherty, A. Mason-Jones and T. O'Doherty (2016b). 'Evaluation of the Swirl Characteristics of a Tidal Stream Turbine Wake'. In: *International Journal of Marine Energy* 14, pp. 198–214. ISSN: 2214-1669.
- Myers, L.E., B. Keogh and A.S. Bahaj (2011). 'Experimental Investigation of Inter-Array Wake Properties in Early Tidal Turbine Arrays'. In: *OCEANS 2011*, pp. 1–8.
- Myhr, A., C. Bjerkseter, A. Ågotnes and T.A. Nygaard (2014). 'Levelised Cost of energy for Off-shore Floating Wind Turbines in a Life Cycle Perspective'. In: *Renewable energy* 66, pp. 714–728. ISSN: 0960-1481.

- NASA (2019). URL: <https://climate.nasa.gov/resources/about-climate-change> (visited on 12/06/2019).
- National Geographic (2019). URL: <https://www.nationageographic.com/encyclopedia/climate-change/> (visited on 12/06/2019).
- Nautricity Ltd (2019). URL: www.nautricity.com (visited on 08/06/2019).
- Neary, V.S., M. Lawson, M. Previsic, A.E Copping, K.C. Hallett, A. LaBonte, J. Rieks and D. Murray (2014a). *Methodology for Design and Economic Analysis of Marine Energy Conversion (MEC) Technologies*. Report. Sandia National Lab.(SNL-NM), Albuquerque, NM (United States).
- (2014b). ‘Methodology for Design and Economic Analysis of Marine Energy Conversion (MEC) Technologies’. In: *Marine Energy Technology Symposium*.
- Newman, B.G. (1983). ‘Actuator-Disc Theory for Vertical-Axis Wind Turbines’. In: *Journal of Wind Engineering and Industrial Aerodynamics* 15.1-3, pp. 347–355. ISSN: 0167-6105.
- (1986). ‘Multiple Actuator-Disc Theory for Wind Turbines’. In: *Journal of Wind Engineering and Industrial Aerodynamics* 24.3, pp. 215–225. ISSN: 0167-6105.
- Noruzi, R., M. Vahidzadeh and A. Riasi (2015). ‘Design, Analysis and Predicting Hydrokinetic Performance of a Horizontal Marine Current Axial Turbine by Consideration of Turbine Installation Depth’. In: *Ocean Engineering* 108, pp. 789–798. ISSN: 0029-8018. DOI: <http://dx.doi.org/10.1016/j.oceaneng.2015.08.056>. URL: <http://www.sciencedirect.com/science/article/pii/S0029801815004540>.
- Nova Innovation Ltd (2019). URL: <https://www.novainnovation.com> (visited on 08/06/2019).
- O’Doherty, T., A. Mason-Jones, D. M. O’Doherty, P. S. Evans, C. F. Wooldridge and I. Fryett (2010). ‘Considerations of a Horizontal Axis Tidal Turbine’. In: *Proceedings of Institution of Civil Engineers: Energy* 163.3, pp. 119–130. DOI: [10.1680/ener.2010.163.3.119](https://doi.org/10.1680/ener.2010.163.3.119). URL: <http://www.scopus.com/inward/record.url?eid=2-s2.0-77956465124%5C&partnerID=40%5C&md5=25f7f92999488ab8d51b6e75e6e006ce>.
- O’Rourke, F., F. Boyle and A. Reynolds (2010). ‘Tidal Energy Update 2009’. In: *Applied Energy* 87.2, pp. 398–409. ISSN: 0306-2619. DOI: <http://dx.doi.org/10.1016/j.apenergy.2009.08.014>. URL: <http://www.sciencedirect.com/science/article/pii/S030626190900347X>.
- O’Doherty, D.M., A. Mason-Jones, C.E. Morris, T. O’Doherty, C.B. Byrne, P.W. Prickett and R.I. Grosvenor (2011). ‘Interaction of Marine Turbines in Close Proximity’. In: *9th European Wave and Tidal Energy Conference (EWTEC)*. Southampton, UK, pp. 10–14.

- O'Doherty, D.M., A. Mason-Jones, T. O'Doherty, C.B. Byrne, I. Owen and W. Wang (2009). 'Considerations of Improved Tidal Stream Turbine Performance Using Double Rows of Contra-Rotating Blades'. In: *Proceedings of the 8th European Wave and Tidal Energy Conference*. Uppsala, Sweden: IET Renewable Power Generation, pp. 434–442.
- O'Doherty, T., A. Mason-Jones, D.M. O'Doherty, C.B. Byrne, I. Owen and Y. Wang (2009). 'Experimental and Computational Analysis of a Model Horizontal Axis Tidal Turbine'. In: *8th European Wave and Tidal Energy Conference (EWTEC)*, Uppsala, Sweden.
- Ocean Energy Systems and IEA Energy Technology Network (May 2015). *International Levelised Cost of Energy for Ocean Energy Technologies*. Report.
- Official Data Foundation, Alioth LLC (2020). URL: <https://www.officialdata.org/UK-inflation> (visited on 05/01/2020).
- Orbital Marine Power (2019). URL: <https://orbitalmarine.com> (visited on 08/06/2019).
- Ordonez Sanchez, S., K. Porter, C. Frost, M. Allmark, C. Johnstone and T. O'Doherty (2016). 'Effects of Extreme Wave-Current Interactions on the Performance of Tidal Stream Turbines'. In: *Asian Wave and Tidal Energy Conference*.
- ORE Catapult (Sept. 2015). *Marine Energy Electrical Architecture. Report 1: Landscape Map and Literature Review*. Report. ORE Catapult.
- (May 2018a). *Tidal Stream and Wave Energy Cost Reduction and Industrial Benefit*. Report. ORE Catapult.
- (Sept. 2018b). *Tidal Stream and Wave Energy Cost Reduction and Industrial Benefit: Summary Analysis*. Report. ORE Catapult.
- (Feb. 2019). *Tidal Stream: Opportunities for Collaborative Action*. Report. ORE Catapult.
- ORPC Inc. (2019). URL: www.orpc.co (visited on 08/06/2019).
- Ossenbach-Sauter, M., S. Guillén-Grillo and O. Coto-Chinchilla (2010). *Guía para el Desarrollo de Proyectos de Energía Renovable en Costa Rica*. Report. PAMPAGRASS, S.A.
- Pacheco, A. and O. Ferreira (2016). 'Hydrodynamic Changes Imposed by Tidal Energy Converters on Extracting Energy on a Real Case Scenario'. In: *Applied Energy* 180, pp. 369–385. ISSN: 0306-2619. DOI: <http://dx.doi.org/10.1016/j.apenergy.2016.07.132>. URL: <http://www.sciencedirect.com/science/article/pii/S0306261916310790>.
- Polinder, H., F.F.A. Van der Pijl, G.J. De Vilder and P.J. Tavner (2006). 'Comparison of Direct Drive and Geared Generator Concepts for Wind Turbines'. In: *IEEE Transactions on Energy Conversion* 21.3, pp. 725–733. ISSN: 0885-8969.

- Poore, R. and T. Lettenmaier (2003). *Alternative Design Study Report: WindPACT Advanced Wind Turbine Drive Train Designs Study*. Report. National Renewable Energy Lab., Golden, CO (US).
- Porter, K., S. Ordonez-Sanchez, C. Johnstone and S. Conesa (1986). 'Integration of a Direct Drive Contra-Rotating Generator with Point Absorber Wave Energy Converters'. In: *12th European Wave and Tidal Energy Conference*.
- Presidencia de Costa Rica (Dec. 2019). Press Release. URL: <https://presidencia.go.cr/comunicados/2019/12/costa-rica-superara-99-de-generacion-electrica-renovable-en-2019/>.
- REN21 (2018). *Renewables 2018 - Global Status Report*. Report.
- Rezaeiha, A., I. Kalkman and B. Blocken (2017). 'Effect of Pitch Angle on Power Performance and Aerodynamics of a Vertical Axis Wind Turbine'. In: *Applied energy* 197, pp. 132–150. ISSN: 0306-2619.
- Sabella SAS (2019). URL: <https://www.sabella.bzh/en> (visited on 08/06/2019).
- Samura, I., K. Kuwano, R. Kawashima, T. Oda, T. Imakurei, H. Inoue, Y. Tokunaga, T. Kanemoto, K. Miyagawa and T. Miwa (2019). 'Counter-Rotating Type Tidal Stream Power Unit: Excellent Performance Verified at Offshore Test'. In: *IOP Conference Series: Earth and Environmental Science*. Vol. 240. IOP Publishing, p. 052003. ISBN: 1755-1315.
- Sanchez, M., R. Carballo, V. Ramos and G. Iglesias (2014). 'Energy Production from Tidal Currents in an Estuary: A Comparative Study of Floating and Bottom-Fixed Turbines'. In: *Energy* 77, pp. 802–811. ISSN: 0360-5442. DOI: <http://dx.doi.org/10.1016/j.energy.2014.09.053>. URL: <http://www.sciencedirect.com/science/article/pii/S0360544214011098>.
- Saylor Academy (2012). URL: https://saylordotorg.github.io/text%5C_managerial-accounting/s12-04-other-factors-affecting-npv-an.html (visited on 13/04/2020).
- Schlichting, H. (1979). *Boundary-Layer Theory*. Seventh. United States of America: McGraw-Hill Book Company.
- Schluntz, J. and R.H.J. Willden (2015). 'The Effect of Blockage on Tidal Turbine Rotor Design and Performance'. In: *Renewable Energy* 81, pp. 432–441. ISSN: 0960-1481. DOI: <http://dx.doi.org/10.1016/j.renene.2015.02.050>. URL: <http://www.sciencedirect.com/science/article/pii/S0960148115001664>.
- Segura, E., R. Morales, J.A. Somolinos and A. Lopez (2017). 'Techno-Economic Challenges of Tidal Energy Conversion Systems: Current Status and Trends'. In: *Renewable and Sustainable Energy Reviews* 77, pp. 536–550. ISSN: 1364-0321.

- Serrano-González, J., M. Burgos-Payán and J.M. Riquelme-Santos (2011). 'An Improved Evolutive Algorithm for Large Offshore Wind Farm Optimum Turbines Layout'. In: *2011 IEEE Trondheim PowerTech*. IEEE, pp. 1–6. ISBN: 1424484189.
- SETENA (2016). *Document of Environment Evaluation*. Chart or Table.
- Shi, W., D. Wang, M. Atlar and K.C. Seo (2013). 'Flow Separation Impacts on the Hydrodynamic Performance Analysis of a Marine Current Turbine using CFD'. In: *Proceedings of the Institution of Mechanical Engineers, Part A: Journal of Power and Energy* 227.8, pp. 833–846. DOI: [10.1177/0957650913499749](https://doi.org/10.1177/0957650913499749). URL: <http://pia.sagepub.com/content/227/8/833.abstract>.
- Shiono, Mitsuhiro, Katsuyuki Suzuki and Seiji Kiho (2000). 'An Experimental Study of the Characteristics of a Darrieus Turbine for Tidal Power Generation'. In: *Electrical Engineering in Japan* 132.3, pp. 38–47. ISSN: 1520-6416. DOI: [10.1002/1520-6416\(200008\)132:3<38::AID-EEJ6>3.0.CO;2-E](https://doi.org/10.1002/1520-6416(200008)132:3<38::AID-EEJ6>3.0.CO;2-E). URL: [http://dx.doi.org/10.1002/1520-6416\(200008\)132:3%3C38::AID-EEJ6%3E3.0.CO;2-E](http://dx.doi.org/10.1002/1520-6416(200008)132:3%3C38::AID-EEJ6%3E3.0.CO;2-E).
- Shirasawa, K., K. Tokunaga, H. Iwashita and T. Shintake (2016). 'Experimental Verification of a Floating Ocean-Current Turbine with a Single Rotor for Use in Kuroshio Currents'. In: *Renewable Energy* 91, pp. 189–195. ISSN: 0960-1481.
- SI Ocean (May 2013). *Ocean Energy: Cost of Energy and Cost Reduction Opportunities*. Report. SI Ocean.
- SIMEC Atlantis Energy (2019). URL: <https://simecatlantis.com> (visited on 08/06/2019).
- Singh, P.M. and Y.D. Choi (2014). 'Shape Design and Numerical Analysis on a 1 MW Tidal Current Turbine for the South-Western Coast of Korea'. In: *Renewable Energy* 68, pp. 485–493. ISSN: 0960-1481. DOI: <http://dx.doi.org/10.1016/j.renene.2014.02.032>. URL: <http://www.sciencedirect.com/science/article/pii/S0960148114001232>.
- SME Ltd (2019). URL: <https://sustainablemarine.com> (visited on 08/06/2019).
- Smith, K. (2001). *WindPACT Turbine Design Scaling Studies Technical Area 2: Turbine, Rotor, and Blade Logistics*. Report. National Renewable Energy Lab.(NREL).
- Smolders, K., H. Long, Y. Feng and P. Tavner (2010). 'Reliability Analysis and Prediction of Wind Turbine Gearboxes'. In: *European Wind Energy Conference and Exhibition 2010*. Vol. 4, pp. 2660–2682.
- Tatum, S., M. Allmark, C. Frost, D.M. O'Doherty, A. Mason-Jones and T. O'Doherty (2016). 'CFD Modelling of a Tidal Stream Turbine Subjected to Profiled Flow and Surface Gravity Waves'.

References

- In: *International Journal of Marine Energy* 15, pp. 156–174. ISSN: 2214-1669. DOI: <http://dx.doi.org/10.1016/j.ijome.2016.04.003>. URL: <http://www.sciencedirect.com/science/article/pii/S2214166916300157>.
- Tedds, S., R.J. Poole, I. Owen, G. Natjafian, A. Mason-Jones, C.E. Morris, T. O'Doherty and D.M. O'Doherty (2011). 'Experimental Investigation of Horizontal Axis Tidal Stream Turbines'. In: *European Wave and Tidal Conference*.
- The Crown Estate (2010). *A Guide to an Offshore Wind Farm*. Report.
- Thomas, N. (2019-06-23 2019). *Swansea's £1.3bn tidal scheme races to beat 2020 deadline*. Newspaper Article.
- Tidal Sails AS (2019). URL: <https://tidalsails.com> (visited on 08/06/2019).
- Tocardo B.V. (2019). URL: <https://www.tocardo.com> (visited on 08/06/2019).
- Torresi, M., B. Fortunato and S.M. Camporeale (2013). 'Numerical Investigation of a Darrieus Rotor for Low-Head Hydropower Generation'. In: *Procedia Computer Science* 19, pp. 728–735. ISSN: 1877-0509. DOI: <http://dx.doi.org/10.1016/j.procs.2013.06.096>. URL: <http://www.sciencedirect.com/science/article/pii/S1877050913007047>.
- Transparency International (2018). URL: <https://www.transparency.org/cpi2019> (visited on 18/02/2020).
- U.S. Energy Information Administration (2019). *Annual Energy Outlook 2019*. Report. U.S. Department of Energy.
- Uihlein, A. and D. Magagna (2016). 'Wave and Tidal Current Energy : A Review of the Current State of Research Beyond Technology'. In: *Renewable and Sustainable Energy Reviews* 58, pp. 1070–1081. ISSN: 1364-0321.
- UK Government (1989). *Electricity Act 1989*. Legal Rule or Regulation.
- (2008). *Planning Act 2008*. Legal Rule or Regulation.
 - (2009). *The Infrastructure Planning (Environmental Impact Assessment) Regulations 2009*. Legal Rule or Regulation.
 - (2013). URL: <https://www.gov.uk/guidance/wave-and-tidal-energy-part-of-the-uks-energy-mix> (visited on 12/06/2019).
- UK's National Infrastructure Planning (Oct. 2016). *Generating Stations: Tidal Lagoon Swansea Bay*. Web Page. URL: <https://infrastructure.planninginspectorate.gov.uk/projects/wales/tidal-lagoon-swansea-bay/?ipcsection=overview>.

- United Nations (2019). URL: <https://www.un.org/sustainabledevelopment/development-agenda/> (visited on 12/06/2019).
- Usui, Y., T. Kanemoto and K. Hiraki (2013a). 'Counter-Rotating Type Tidal Stream Power Unit Boarded on Pillar (Performances and Flow Conditions of Tandem Propellers)'. In: *Journal of Thermal Science* 22.6, pp. 580–585. ISSN: 1003-2169.
- Usui, Y., T. Kanemoto, T. Kohei and K. Hiraki (2014). 'Counter-Rotating Type Tidal Stream Power Unit Moored by Only One Cable'. In: *Journal of Energy and Power Engineering*, pp. 2089–2025.
- Usui, Y., K. Takaki, T. Kanemoto and K. Hiraki (2013b). 'Counter-Rotating Type Tidal-Stream Power Unit Playing Favorable Features in Various Ocean Circumstances'. In: *ASME 2013 International Mechanical Engineering Congress and Exposition*. American Society of Mechanical Engineers, V06BT07A091–V06BT07A091.
- Vantoch-Wood, A., J. de Groot, P. Connor, I. Bailey and I. Whitehead (May 2012). *National Policy Framework for Marine Renewable Energy within the United Kingdom*. Report. MERiFIC Project.
- Vazquez, A., S. Astariz and G. Iglesias (2018). 'A Method for the Spatial Targeting of Tidal Stream Energy Policies'. In: *International Marine Energy Journal* 1.1 (Aug), pp. 19–26. ISSN: 2631-5548.
- Vazquez, A. and G. Iglesias (2015). 'Device Interactions in Reducing the Cost of Tidal Stream Energy'. In: *Energy Conversion and Management* 97, pp. 428–438. ISSN: 0196-8904.
- (2016a). 'A Holistic Method for Selecting Tidal Stream Energy Hotspots under Technical, Economic and Functional Constraints'. In: *Energy Conversion and Management* 117, pp. 420–430. ISSN: 0196-8904.
- (2016b). 'Capital Costs in Tidal Stream Energy Projects – A spatial Approach'. In: *Energy* 107, pp. 215–226. ISSN: 0360-5442.
- (2016c). 'Grid Parity in Tidal Stream Energy Projects: An Assessment of financial, technological and economic LCOE input parameters'. In: *Technological Forecasting and Social Change* 104, pp. 89–101. ISSN: 0040-1625.
- (2017). 'A Holistic Method for Selecting Tidal Stream Energy Hotspots'. In: *Coastal Engineering Proceedings* 1.35, p. 5. ISSN: 2156-1028.
- Versteeg, H.K. and W. Malalasekera (2007). *An Introduction to Computational Fluid Dynamics: The Finite Volume Method*. Pearson Education. ISBN: 0131274988.

- Walker, S., R. Howell, P. Hodgson and A. Griffin (2015). 'Tidal Energy Machines: A Comparative Life Cycle Assessment Study'. In: *Proceedings of the Institution of Mechanical Engineers, Part M: Journal of Engineering for the Maritime Environment* 229.2, pp. 124–140. ISSN: 1475-0902.
- Wang, S.Q., K. Sun, G. Xu, Y.T. Liu and X. Bai (2017). 'Hydrodynamic Analysis of Horizontal-Axis Tidal Current Turbine with Rolling and Surging Coupled Motions'. In: *Renewable Energy* 102, Part A, pp. 87–97. ISSN: 0960-1481. DOI: <http://dx.doi.org/10.1016/j.renene.2016.10.036>. URL: [//www.sciencedirect.com/science/article/pii/S0960148116309016](http://www.sciencedirect.com/science/article/pii/S0960148116309016).
- Wärtsilä (2019). URL: <https://www.wartsila.com/encyclopedia/term/propeller-pitch> (visited on 05/04/2019).
- Wei, X., B. Huang, P. Liu and T. Kanemoto (2016). 'Performance Research of Counter-rotating Tidal Stream Power Unit'. In: *International Journal of Fluid Machinery and Systems* 9.2, pp. 129–136. ISSN: 1882-9554.
- Wei, X., B. Huang, P. Liu, T. Kanemoto and L. Wang (2015). 'Experimental Investigation into the Effects of Blade Pitch Angle and Axial Distance on the Performance of a Counter-Rotating Tidal Turbine'. In: *Ocean Engineering* 110, pp. 78–88. ISSN: 0029-8018.
- World Energy Council (2016a). *World Energy Resources - Marine Energy*. Report. World Energy Council.
- (2016b). *World Energy Resources - Wind*. Report. World Energy Council.
- X-Rates (2019). URL: <https://www.x-rates.com/> (visited on 24/12/2019).
- Xu, J.A. and H.Y. Sun (2015). 'Fluid Dynamics Analysis of Passive Oscillating Hydrofoils for Tidal Current Energy Extracting'. In: *2015 IEEE International Conference on Mechatronics and Automation (ICMA)*. IEEE, pp. 2017–2022. ISBN: 1479970980.
- Zupone, G.L., M. Amelio, S. Barbarelli, G. Florio, N.M. Scornaienchi and A. Cutrupi (2017). 'LCOE Evaluation for a Tidal Kinetic Self Balancing Turbine: Case Study and Comparison'. In: *Applied energy* 185, pp. 1292–1302. ISSN: 0306-2619.